SCUOLA DI DOTTORATO
UNIVERSITÀ DEGLI STUDI DI MILANO-BICOCCA

Department of

Earth and Environmental Sciences (DISAT)

PhD program in Chemical, Geological and Environmental Sciences
Cycle XXXVIII

Curriculum in Chemical Science

Metal oxide-based catalysts for the catalytic conversion of CO_2 into added-value fuels

Mariani Pietro

Registration number: 831327

Tutor: Prof. Claudio Greco

Supervisor: Prof. Massimiliano D'Arienzo

Coordinator: Prof. Marco Giovanni Malusà

ACADEMIC YEAR 2024-2025

List of abbreviations

2-PET	2-Phenylethanethiol
Au@ZnO	$Au_{25}(2\text{-PET})_{18}$ nanoclusters supported on ZnO
AuNCs	$Au_{25}(2\text{-PET})_{18}$ nanocluster
BZO	$BaZrO_3$
CCS	Carbon Capture and Storage
CCU	Carbon Capture and Usage
CCUS	Carbon Capture Usange and Storag
CHNS	Carbon,Hydrogen, Nitrogen and Sulphur elemental analysis
CuAu@ZnO	$Au_{25-x}Cu_x(2\text{-PET})_{18}$ nanoclusters supported on ZnO
CuAuNCs	$Au_{25-x}Cu_x(2\text{-PET})_{18}$ nanoclusters
CZA	$Cu/ZnO/Al_2O_3$ catalyst
DRIFTS	Diffuse Reflectance InfraRed Fourier Transform Spectroscopy
EDX	Energy Dispersive X-rays
EPR	Elentron Paramagnetic Resonance
EXAFS	Extended X-rays Absorption Fine Sturcture
ICP	Inductively Coupled Plasma
LCF	Linear Combination Fitting
LSPR	Localised Surface Plasmon Resonance
MALDI	Matrix Assistes Lased Desorption/Ionization
MeOH	Methanol
NCs	Nanoclusters
NPs	Nanoparticles
nX-STO	$SrTiO_3$ doped with metal X with a concentration of n% of B-site
(P)-XRD	(Powder) X-Rays Diffraction
RWGS	Reverse Water Gas Shift
SACs	Single Atom Catalysts
SEM	Scanning Electron Microscopy
SSCs	Single Site Catalysts
STO	$SrTiO_3$
(HR)-TEM	(High Resolution) Transmission Electron Microscopy
TGA	ThermoGravimetric Analysis

TMCs	Transition Metal Carbides
TPR	Temperature Programmed Reduction
UV-DRS	UV-Vis Diffuse Reflectance Spectroscopy
$V_O^{\bullet}$	Oxygen Vacancy singly charged
XANES	X-rays Absorption Near Edge Structure
XAS	X-rays Absorption Spectroscopy
XPS	X-rays Photoelectron Spectroscopy
XRF	X-Rays Fluorescence
ZFS	Zero Field Splitting
Zn_i	Zinc interstitials

Preface and structure of the thesis

The escalating concentration of carbon dioxide (CO_2) in the atmosphere represents one of the most pressing challenges of our time, both environmentally and technologically. As a primary greenhouse gas, CO_2 is responsible for driving climate change, and its continuous accumulation underscores the urgent necessity for innovative mitigation and valorisation strategies. Among the various approaches developed to address this issue, Carbon Capture, Utilization, and Storage (CCUS) has emerged as one of the most promising frameworks. This integrated approach not only aims to curb emissions but also redefines CO_2 as a renewable carbon feedstock for sustainable chemical production.

From a chemical standpoint, the transformation of CO_2 into valuable chemicals and fuels is a formidable challenge. Its inherent thermodynamic stability and strong C=O bonds make its activation and reduction energetically demanding, requiring highly efficient catalytic systems. Consequently, catalysis lies at the core of CO_2 valorisation, providing a platform to explore diverse reaction pathways such as hydrogenation to methanol, the Reverse Water Gas Shift (RWGS) reaction, and electrochemical or photocatalytic conversion routes. These processes, if efficiently optimized, could pave the way toward a carbon-neutral circular economy.

The development of catalysts capable of activating CO_2 under mild and sustainable conditions remains a focal point of current research. Conventional $Cu/ZnO/Al_2O_3$ systems, long used in industrial methanol synthesis, have inspired extensive studies to identify their active sites and understand the interplay between structural, electronic, and defect-related properties. However, the complexity and dynamic nature of these systems pose significant challenges, highlighting the necessity for more controllable and structurally defined catalytic materials. Recent advances in materials chemistry have introduced innovative catalytic concepts that go beyond traditional approaches. Perovskite oxides, through defect engineering and redox exsolution, offer robust and recyclable catalysts in which metal nanoparticles emerge from the bulk to the surface in situ, ensuring strong metal–support interactions and enhanced stability. Similarly, atomically precise metal nanoclusters, such as $Au_{25}(SR)_{18}$, bridge the molecular and nanoscale regimes, exhibiting tuneable catalytic and electronic properties with unprecedented structural control. These novel systems open new perspectives for rational catalyst design and for establishing correlations between structure, defects, and catalytic performance.

The theoretical framework of this thesis is lies on the interplay between catalysis, catalyst's composition and structure, as well as advanced spectroscopic characterization of the materials. A unifying theme throughout this work is the role of defects, whether structural, electronic, or surface-

related, which are regarded not as imperfections to be limited, but as active contributors to catalytic reactivity. Electron Paramagnetic Resonance (EPR) spectroscopy was employed extensively due to its exceptional sensitivity to local environments and its ability to provide detailed information on geometry and coordination. The EPR spectra served as unique fingerprints of each material, enabling the correlation of structural features with catalytic behaviour. Complementary spectroscopic methods, including X-ray Absorption Spectroscopy (XAS), X-ray Photoelectron Spectroscopy (XPS), UV–Vis Diffuse Reflectance Spectroscopy (DRS), and in-situ DRIFTS, were employed to build a comprehensive picture of the catalysts' electronic structure, oxidation states, and surface defect populations.

In this context, the research presented herein contributes to the broad scientific effort toward sustainable carbon utilization by integrating fundamental insights into catalyst structure and reactivity with innovative materials design. The theoretical and experimental approaches developed throughout this work aspire to deepen our understanding of CO_2 conversion processes and to provide new pathways for transforming a greenhouse gas into a valuable chemical resource.

For these reasons, the thesis is organized to progressively explore these concepts. Chapter 1 is an introduction to the topic of CO_2 conversion, some possible common paths followed and some innovative routes for CO_2 reduction. Chapter 2 introduces the theoretical background of EPR spectroscopy and presents characteristic spectra relevant to the studied systems. Chapters 3 and 4 examine exsolution processes in $SrTiO_3$-based catalysts, highlighting the formation of monometallic and bimetallic nanoparticles, the reversibility of exsolution, and the influence of co-dopants (Ni and Fe) on structural dynamics and defect formation. Chapter 5 focuses on ZnO-supported Au and CuAu nanoclusters, showing that both metal composition and ZnO defect chemistry critically influence methanol selectivity and reaction kinetics. Chapter 6 expands this analysis to CZA systems and Cu/Zn co-doped $SrTiO_3$, examining the synergistic effect of Cu and Zn in enhancing methanol production.

Chapter 1
Introduction

Index of the chapter

1.1 The issue of CO_2

The rising levels of carbon dioxide (CO_2) in the atmosphere have become an important environmental concern in recent years, as CO_2 is a major greenhouse gas contributing to global warming. This increase is primarily driven by the combustion of fossil fuels for energy production, transportation, and agricultural activities. Therefore, strategies to reduce atmospheric CO_2 are essential to protect the planet and future generations.

It is well established that, since the Industrial Revolution, atmospheric CO_2 concentrations have increased significantly, mainly due to the widespread use of fossil fuels such as coal and oil for energy. The adoption of coal during the Industrial Revolution represented a major turning point in human history. Replacing traditional energy sources like wood, coal enabled rapid industrial growth and technological advancement in Britain and beyond. However, this progress came at a significant environmental cost, including a substantial rise in greenhouse gas emissions, particularly CO_2.

The industrial sector's transition from coal to other fossil fuels, particularly petroleum, marked a new phase in energy production. The discovery of large oil reserves established petroleum as the primary energy source for both industry and transportation. The development of the internal combustion engine, fueled by the extensive use of oil, revolutionized transportation through the advent of the automobile. This event marked the beginning of the era of motorized mobility and further stimulated industrial and commercial growth. However, the rising demand for oil also drove the expansion of extraction and refining activities, contributing to a sustained increase in greenhouse gas emissions, including CO_2. Consequently, the shift from coal to petroleum, coupled with the extensive use of motorized transport, has had a profound environmental impact, intensifying global warming and climate change.

Beyond fossil fuel use, some industrial processes have also significantly contributed to rising atmospheric CO_2 levels. Cement production and steel production are an example of this, as cement manufacturing releases CO_2 as a byproduct of the chemical reaction between limestone and clay, while steel production generates CO_2 as a byproduct in the process of reducing the carbon content in the Iron-Carbon alloy. The rapid expansion of the construction industry, particularly in urban areas, has driven a substantial increase in both of these industrial productions, resulting in higher CO_2 emissions. This process has further exacerbated the persistent rise of atmospheric CO_2 and its impact on global warming and climate change.

Earth as a whole, however, has its natural processes for capturing and repurposing CO_2, which play a crucial role in maintaining the balance of CO_2 concentration in the atmosphere. These processes include photosynthesis in plants, which captures CO_2 and stores it as organic carbon in soils and plants,

and the ocean, which absorbs large amounts of CO_2 from the atmosphere dissolving it in the waters. The carbon cycle between sky, land and oceans, plays a crucial role in regulating the amount of CO_2 in the atmosphere. However, the increase in human activities, such as the burning of fossil fuels, deforestation and heavy industrial production, has led to a persistent increase in atmospheric CO_2 concentration, leading to an unbalance of produced and naturally consumed CO_2.

Despite growing momentum in the transition toward renewable energy to avoid the combustion of fossil fuels for energy production, petroleum-based fuels still dominate the global energy mix, particularly in rapidly developing economies due to low cost of raw materials. This dependence has resulted in annual CO_2 emissions exceeding 37 billion tons in 2023, with projections indicating further increases until at least 2050 if decisive actions are not taken. Such numbers highlight the urgency of developing efficient and scalable CO_2 reduction processes that not only mitigate greenhouse gas accumulation but also provide pathways for sustainable carbon utilization [1].

Conventional strategies have often emphasized carbon capture and storage, where CO_2 is compressed and sequestered in geological formations as a possible solution for the problem. However, even if effective in principle, Carbon storage faces several persistent challenges, including high financial costs, the complexity of long-term monitoring, potential leakage risks, and geographically constrained storage capacities as well as being processes that do not exploit CO- as a potential carbon resource. These limitations have led to increasing interest in carbon capture, utilization, and storage, an approach that combines emission reduction with value creation. Rather than treating CO_2 as a waste product, Carbon Capture Usage and Storage (CCUS) repositions it as a resource that can be integrated into industrial cycles, offering the potential to close the carbon loop and reduce reliance on fossil-derived feedstocks.

The utilization aspect of Carbon usage is particularly attractive because CO_2 is an abundant, low-cost, non-toxic, and renewable C1 building block. Through chemical conversion, CO_2 can be transformed into a wide array of high value-added chemicals and fuels, including methanol, formic acid, olefins, and synthetic fuels. Some of these processes, such as the production of urea and salicylic acid, have already been commercialized at industrial scale, while others remain at the pilot or demonstration level. These routes not only contribute to emissions lowering but also represent a strategic opportunity for shifting the chemical industry toward greener production pathways. However, even if CCUS seems like a promising solution, its impact still remains quite limited. For instance, in 2023 CCUS technologies were applied only to capture 0.1% of global CO_2 emissions, corresponding to roughly 45 million metric tons of CO_2 annually [2]. For this process to be effective in keeping the global warming rate below 1,5°C/year, CCUS should reach 1 billion metric tons by 2030. The improvement needed is remarkable, and the costs to face are no less. For these reasons, study, design and improvements of the process of CO_2 reuse are mandatory in order to meet the needs of the industry and facilitate the migration to CCUS.

Many different CO_2 conversion routes are gaining traction, mainly based on catalytic processes, including thermo and photocatalytic conversion to fuels, electrochemical conversion and enzymatic processes. Each of these approaches offers unique opportunities and challenges, particularly in terms of scalability, efficiency, and compatibility with renewable energy systems. Catalysis research has therefore become a milestone of CO_2 utilization, with scientific and technological efforts directed toward catalyst preparation, plant design, and technology development. From a chemical point of view, the challenge lies in the study of heterogeneous catalysts focusing on improving electronic and chemical properties, increasing the scalability of the synthesis and application of the catalyst, while keeping the synthesis process cost effective and the catalytic process non complicated.

1.1.1 CO_2 reactivity and thermodynamics

One of the main challenges in utilizing CO_2 as a resource originates from its high chemical stability. CO_2 molecules possess a linear, centrosymmetric structure (O=C=O) with strong C=O bonds (~750 kJ/mol), making their activation thermodynamically unfavorable. Overcoming this barrier typically requires high temperatures, high pressures, or the use of highly efficient catalysts to supply the necessary energy.

Furthermore, the carbon atom in CO_2 exists in its maximum oxidation state of +4. Consequently, the full conversion of CO_2 into hydrocarbons demands the transfer of up to eight electrons per molecule. This complexity often leads to multiple possible reaction pathways and the formation of diverse byproducts [3].

For these reasons, CO_2 conversion is generally reliant on catalysis, where an external species reduces the activation energy and directs the reaction toward desired products. To date, various strategies have been explored, including enzymatic catalysis, thermal catalysis, photocatalysis, electrocatalysis, and photoelectrochemical (PEC) processes. These approaches employ heat, light, or electricity to deliver the required energy input. Each method offers distinct advantages and limitations depending on its chemical characteristics, cost, and scalability. A brief overview of these different approaches is provided below.

1.1.2 Possible CO_2 conversion routes

Photocatalysis

Solar energy represents an ideal alternative to fossil fuels, as it is abundant, inexpensive, clean, and sustainable. Consequently, employing photocatalysts to drive solar-powered CO_2 conversion into fuels

or chemicals is a highly promising approach. Similar to natural photosynthesis, photocatalysts generate electron–hole pairs upon exposure to sunlight. The photogenerated electrons then promote CO_2 reduction through redox reactions, leading to hydrocarbon formation.

The photocatalytic conversion of CO_2 generally involves different steps e.g. light absorption; charge separation, charge transfer and catalytic CO_2 reduction etc. A thorough understanding of these processes is essential for the rational design of catalysts with enhanced performance. Most photocatalysts reported in the literature are semiconductors, which are abundant and relatively simple to synthesize, and their main applications are in reduction of CO_2 and production of CO, methane, formic acid, and other short-chain hydrocarbons. To improve efficiency, extensive research has been devoted to optimizing both the chemical composition and the electronic structure of photocatalysts, with the aim of increasing light absorption as well as prolonging the lifetime and availability of photogenerated electron–hole pairs [4]. In addition to inorganic semiconductors, organic photocatalysts have also been investigated, with particular attention to porphyrin-based systems, which are planar macrocyclic compounds composed of four pyrrole units interconnected by methylene bridges, resulting in a highly conjugated framework with delocalized electrons. This molecular structure confers strong absorption in the visible-light region and distinctive redox properties [5].

Despite these advances in photocatalytic reduction of CO_2, several challenges are still open. Current photocatalytic systems often rely on costly transition metals and tend to have poor selectivity towards a desired product as well as competition from H_2 evolution reaction. What is more, rapid recombination of charge carriers tends to generate catalyst with low conversion efficiency, making the upward scalability of these systems quite challenging.

Electrocatalysis

The electrocatalytic conversion of CO_2 into value-added chemicals represents a highly promising approach. In this process, an external electric field serves as the driving energy source, while water functions as the proton donor, and different catalysts are employed to facilitate CO_2 reduction. Compared with thermocatalysis, electrocatalysis is considered more cost-effective because it uses water, instead of molecular hydrogen, as the proton source, what is more, electrocatalysis operates under mild conditions (ambient temperature and pressure), allows fine control over reaction parameters and rates, enables the use of recyclable catalysts and electrolytes, relies on relatively simple equipment, and can achieve noteworthy levels of conversion efficiency [6]. In recent years, researchers have investigated a wide variety of electrode materials for this purpose, including metals [7], transition-metal oxides [8], transition-metal chalcogenides, as well as other advanced materials [9].

Through these systems, various reduction products such as CO, methane, ethanol, and other hydrocarbons can be readily obtained. However, some issues are still present, as for instance, most catalysts employed in CO_2 reduction also catalyse the hydrogen evolution reaction (HER) and, as a result, hydrogen is generated as a side product, which competes with CO_2 reduction and thus diminishes the selectivity toward the desired products. What is more, stability of the catalyst, as well as product separation are still problematic matters for these systems. This makes it challenging to identify electrocatalysts capable of selectively enhancing CO_2 conversion efficiency [10]. In addition to selectivity issues, other intrinsic limitations stem from the multi-electron transfer processes and the slow electron transfer rates associated with CO_2 reduction. These kinetic and thermodynamic barriers make it particularly difficult to design catalysts that combine high activity, excellent selectivity, and long-term stability while overcoming the inherent stability of the CO_2 molecule.

A promising strategy to address these limitations lies in the integration of electrocatalysis with photocatalysis. By combining these two approaches, it is possible to exploit their respective advantages and potentially achieve more efficient and sustainable CO_2 reduction.

Photoelectrocatalysis

Photoelectrocatalysis, which combines the advantages of photocatalysis and electrocatalysis, is considered to be an ideal strategy for the selective conversion of CO_2 into gaseous (such as CO, methane, etc.) and liquid products (such as formic acid, methanol, ethanol, etc.) under sunlight irradiation and for this it has attracted great attention [11], [12]. Photoelectrocatalysis makes the best use of solar energy to produce photoelectrons which are then transferred to the electrode surface under the action of an applied electric field and finally used for the reduction of CO_2. The applied electric field can effectively facilitate charge separation in the photocatalytic process, promote electron migration, and significantly improve the intrinsic activity and energy efficiency of CO_2 molecules. Catalysts usually employed are semiconductors, as TiO_2, WO_3, ZnO, Fe_2O_3 [13]. Nevertheless, this catalytic route, even though appears to be less energy consuming and feasible at milder conditions, hides some still ongoing problems. First of all, the complexity of the set up makes the scalability of the process harder, binding this research to lab scale or pilot plants, secondly, the mechanism of the reaction and the intermediate steps are difficult to fully understand, making difficult to improve the catalysts activity and selectivity by designing a novel catalyst.

Thermal Catalysis

Most thermal catalytic conversion of CO_2 involves the hydrogenation reaction at high temperatures to produce useful fuels such as CO, methane, and methanol. Since CO_2 molecules are thermodynamically and chemically stable, large amounts of energy are required if CO_2 is used as a single reactant. The introduction of more reactive species, such as CO and H_2 as the co-reactants will make the thermodynamic process easier. In the past few decades, great attention has been paid to the thermal catalysis of CO_2 and significant progress has been made. Various catalysts, including metals (e.g. Cu, Fe, etc.) and metal oxides (e.g. ZnO, ZrO_2, etc.) as well as novel nano-sized catalyst metal–organic frameworks (MOFs) have also been designed, prepared, and gradually developed [14]. There are still great challenges in developing catalysts with high catalytic performance and long-term stability, reducing the size of thermal catalytic reactors and decreasing the production costs. In addition, more effective and economical methods to produce H_2 are urgently needed [15][16]. However, among the available options, thermal catalytic hydrogenation remains the most commercially advanced and promising pathway for near-term industrial deployment. The reaction usually takes place in a fluidised bed reactor, where CO_2 and H_2 flow through the catalyst without the need of a liquid or another medium thus facilitating the possibility of increasing pressure and temperature to overcome the energy activation barrier. The relatively easy set up makes the scalability of this process simple, therefore attracting the interests of industries. The Icelandic company Carbon Recycling Company [17] for instance, already scaled up the process of CO_2 reduction to MeOH with a plant in Iceland producing up to 200 thousand tons of MeOH each year using CO_2 captured from the nearby power station.

1.1.3 Some more issues, Hydrogen

One more problem concerning the CCUS which will not be tackled in this dissertation but its worth mentioning, is the availability and the sources of hydrogen. Hydrogen is usually needed as a source of e- for reducing CO_2 to lower oxidation state carbon species. Hydrogen can be produced in multiple ways and its usually called by different names:

- Grey Hydrogen: produced via steam reforming of methane with CO and CO_2 as a byproduct of the reaction;
- Green Hydrogen: produced via water electrolysis where the energy required for the reaction is produced with renewable sources;
- Blue Hydrogen: produced via water electrolysis where the energy required for the reaction is produced via steam reforming but excess CO_2 is captured and stored;

- Turquoise Hydrogen: produced by steam reforming of methane and solid carbon is a byproduct [18].

There also exist other newer processes with slight differences between one another and all of them generate different colours of hydrogen, but the one listed here are the main used.

Nowadays, up to 83% of H_2 used in the world comes from fossil fuels and is mainly grey hydrogen [19]. This process however produces CO_2 as a side product and therefore using it in the frame of CCUS, counterproductive. For this reason, just as many efforts are focused on the production of catalysts for CO_2 reduction, just as many efforts are focused on the development of always better strategies and catalysts for the production of clean hydrogen. Up to date, although still costly, the integration of renewable green hydrogen into CO_2 utilization processes is vital for ensuring genuine climate benefits. Research and pilot projects in recent years have demonstrated the technical feasibility of such integration, and ongoing efforts are directed at improving energy efficiency and reducing production costs[20], [21].

1.2 Strategies for CO_2 conversion

As already seen in the previous paragraphs, CCUS can pass through many different routes and strategies.

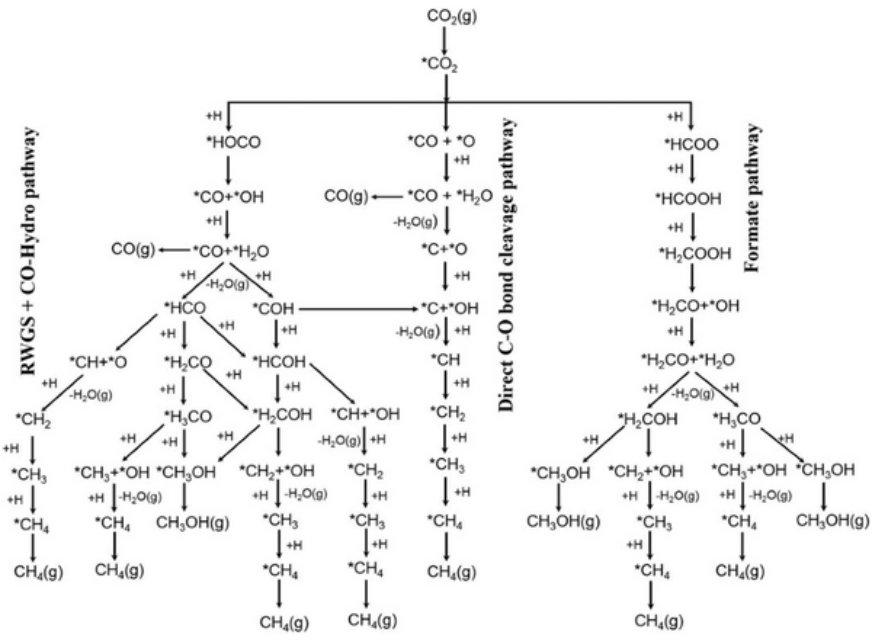

Fig. 1.1: Some possible reaction pathways for CO_2 hydrogenation to CO, CH_4, CH_3OH. Absorbed species are indicated with (*)[22].

Each reaction pathway and intermediate heavily depends on the condition of the reaction (e. g. temperature, pressure and reaction mixture of gas) as well as the catalyst composition. Some substances (either oxides, metals or complexes) are known for being active for a particular reaction and the condition on the catalytic bed can favour a reaction over another. For this reason, it can be possible to decide what reaction to do, nevertheless, reaching 100% selectivity and yield toward the desired product is no easy task and tailoring of catalyst properties as well as reaction conditions are mandatory to maximise the effectiveness of the reaction.

For the sake of this dissertation, we will mainly focus on two different routes both driven via thermocatalysis: CO_2 reduction to MeOH and Reverse Water Gas Shift (RWGS) reaction.

1.2.1 CO_2 Conversion to MeOH

The concept of producing synthetic methanol by reacting CO_2 with hydrogen dates back to 1905, when it was first introduced by the French chemist Paul Sabatier [23]. The first industrial-scale process was later developed by the German chemists Alwin Mittasch and Mathias Pier, who at the time were working for Badische Anilin & Soda-Fabrik (BASF). They discovered a method to convert syngas (a mixture of CO, CO_2, and H_2) into methanol, a process patented by BASF in 1926 under the name *"Synthetic Manufacture of Methanol"* [24]. This first industrial scale process required very harsh operating conditions, with pressures up to 220 bar and temperatures as high as 450 °C and relied on chromium- and manganese-oxide-based catalysts. Subsequent improvements led to the development of catalysts based on chromia and zinc oxide. It was not until the 1960s, however, that methanol synthesis became more efficient, with the introduction of a new class of Cu-based catalysts that enabled operation under significantly milder conditions. This advancement was developed and patented by Imperial Chemical Industries (ICI) [25] and the basics of this discovery still lies under the process used up to our times.

Nowadays MeOH is usually produced from syngas, which can be derived from many different feedstocks, but is frequently derived from gasification of coal or natural gas [26]. However, as already seen on the first part of the introduction, this would produce CO_2 as a waste product and therefore increase its concentration in atmosphere and favour global warming. To overcome this issue a more sustainable conversion involving CO_2 from the atmosphere should be preferred. The hydrogenation of CO_2 to MeOH involves three main reactions [27]:

$$CO_2 + 3H_2 \rightleftarrows CH_3OH + H_2O \qquad \Delta H_{298K} = -49.16 \text{ KJ/mol} \qquad (1)$$

$$CO_2 + H_2 \rightleftarrows CO + H_2O \qquad \Delta H_{298K} = +41.21 \text{ KJ/mol} \qquad (2)$$

$$CO + 2H_2 \rightleftarrows CH_3OH \qquad \Delta H_{298K} = -90.77 \text{ KJ/mol} \qquad (3)$$

Let's for now focus on reactions (1) and (2).

Both the hydrogenation of CO and the hydrogenation of CO_2 are endothermic, and therefore too high temperatures would move the reaction back to the reagents. Nevertheless, temperature of around 220-280°C are needed to overcome the kinetic barrier of the hydrogenation of CO_2 [28]. The lower exothermicity of direct hydrogenation of CO_2 compared with CO reduction, allows to more easily control the heat dissipation in the reactor plant, usually exploiting tubular cooled reactor which can also help to reduce the cost of the set up [29]. The second parameter to consider is pressure, since R1 has four moles of gas as reagents and two moles as products, via increase in the pressure equilibrium can be moved towards the products, therefore these reactions are carried out under high pressure conditions, usually 50-100 bar.

Catalysts used for this reaction are Cu-based catalysts, mainly Cu/ZnO/Al2O3, commonly known as CZA, a mixture of three oxides obtained via coprecipitation of the metal salts, with relative concentrations usually around 60:30:10 respectively. While is commonly known that Cu is the active part of the catalyst, the absence of any of the three metals or a change in composition of the commonly used one, can drastically reduce activity and selectivity of the catalysts. This first note highlights one of the major problems with this system, which will be discussed later in the dissertation, namely the complexity of uniquely identifying the active site for the catalytic reaction. What is more, the latest generation of CZA commercial catalysts are being produced with the addition of little amounts (around 2%) Magnesium Oxide "to maximise the initial dispersion of copper and therefore boost the initial activity of the methanol synthesis catalysts" [30] as well as a small amount of SiO_2 to "slow down the rate of copper and zinc sintering" [30]. The system is therefore pretty complicated already before starting the reaction, and things become even more complicated as the catalysts need to be activated before starting the process. The activation is usually a thermal reduction of CZA used to produce reduced copper species on the surface. However, this reduction process is not as easy as it looks, but few different simultaneous processes happen:

- Cu gets reduced both to Cu(0) and Cu(I) species;
- Zn(II) also gets partially reduced to partially charged Zn species;
- Zn and Cu start interacting producing both a Zn-Cu alloy, as well as Zn-Cu interfaces;
- Crystal phase, particle size and surface area are strongly modified by the activation process.

More in depth analysis of the process will be tackled later on in the discussion.

1.2.2 Reverse Water Gas Shift Reaction (RWGS)

Another possible reaction between CO_2 and H_2 is reaction (2) from the previous paragraph, commonly referred to as the RWGS reaction. Analysing its enthalpy reveals that it is the only endothermic process among the reactions listed above. This means that if temperature is too high this process will take place and start competing with MeOH formation, therefore temperature control and knowledge of both the catalyst and the reaction are mandatory for the success of the process.

The RWGS reaction is an equilibrium process that is promoted at elevated temperatures, as well as under conditions of high H_2: CO_2 ratios and reduced contact times [31]. Fig. 1.2 illustrates the thermodynamic equilibrium compositions of the RWGS products at different H_2/CO_2 ratios. The distribution of products obtained from a given feed stream is strongly dependent on the reaction temperature. In the 100–700 °C range, CH_4 is typically the dominant product. From a thermodynamic perspective, CO becomes the major product only at temperatures above 700 °C. For this reason, it is crucial to employ highly selective catalysts capable of ensuring efficient performance within moderate temperature ranges [32].

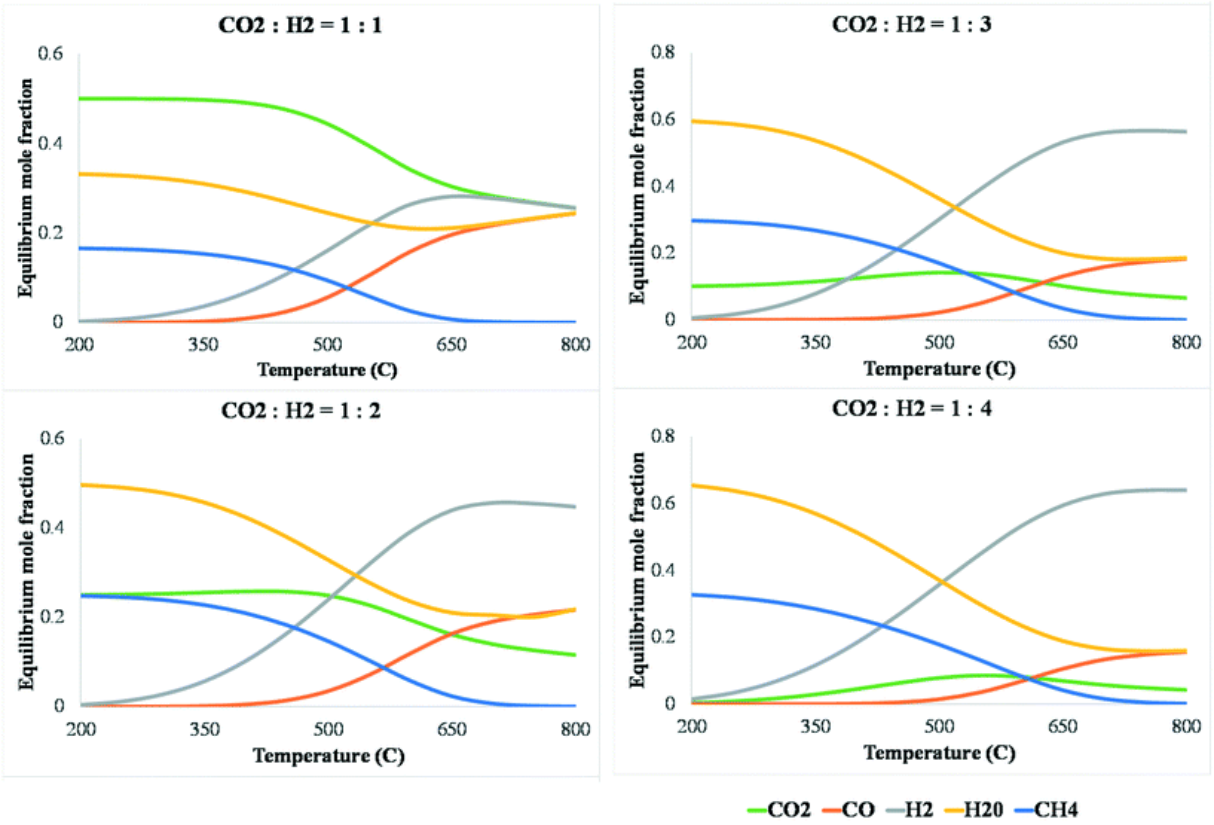

Fig. 1.2: Schematic representation of the influence of temperature on the thermodynamic equilibrium of the RWGS reaction at 1 bar. Modelled in Aspen Plus using an RGibbs reactor and the Peng–Robinson property method [32].

Typical catalysts for this kind of reaction are metal nanoparticles supported on oxide with high surface are. As metals, noble metals are usually preferred (e.g. Pt, Au, Ir, etc.) as for their ability to dissociate H_2 molecules [33], while oxides (e.g. Al_2O_3, TiO_2, perovskite oxides, etc.) favour the breakage of C=O bonds. These catalysts have proven to be excellent in converting CO_2 due to their stability, easy dispersibility and high reactive surface areas. However, owing the high cost of noble metals, the scaling up of the reaction is still an issue, so research moved towards developing non-noble metal supported catalysts. Among them Fe, Ni and Cu based catalysts seems to be the most promising [33]. There are however still some issues with this kind of systems. Ni and Cu, although being very active and selective towards CO, tend to be easily poisoned and coked by carbon deposition over prolongated reaction time; Fe on the other hand, is a very active metal at high temperature, therefore its application in RWGS has been widely studied. The issue however is a lack in comprehension of the actual active site, whether it involves Fe(0) centres or FeO_x centres. What is commonly known, however is Fe ability of being easily oxidised and reduced when is at the surface, making it particularly interesting for studying its redox behaviour.

1.3 Innovative catalysts for CO_2 reduction

Other than the classical materials listed above, in the past few years some novel class of catalysts or innovative and unconventional processes for the catalysts preparation, have attracted the attention of scientist due to their potential in the CO_2 conversion, as well as their advantages in synthetical pathways or reuse. Among them it's worth mentioning perovskite oxide based catalysts, Transition Metal Carbide (TMCs), Single-atom Catalysts (SACs) anchored on oxides and Metal Nanoclusters (NCs).

Perovskite oxide represents a relative wide class of materials, as the term perovskite identifies an extensive class of structures with molecular formula ABX3, where A and B are cations and X is an anion. [34]. These complexes are composed by a large cationic site given by the presence of A and a smaller cationic site due to B's presence, while X usually is an oxygen atom, but can also be a halogen, B, C, N, P, or S. The ideal structure shows A as the central ion with a 12-fold octahedral coordination, occupying a cubic B sublattice, where every six corner-linked octahedral X ions are coordinated to a B cation. The structure of these materials is highly stable and can be easily modified by substituting the cations site A or B with different ionic radius and oxidation state. Considering this and that nearly 90% of elemental metals of the Periodic Table can form stable perovskite oxide structures, the synthesis of substituted multicomponent compounds is something that the literature has soon discovered [35]. The substitution of A and B site of the lattice with other transition metals can also improve the catalytic activity of this

class of materials by inserting defects and new energy level in the energy gap of these materials therefore manipulating the metal oxide band gap. What is more, via doping the perovskite (e.g. $SrTiO_3$, $LaAlO_3$ etc.) with other more reducible transition metals opens the door to the possibility of exploiting exsolution, a novel way to generate meal nanoparticles (either monometallic or bimetallic alloys) on the surface of the oxide with and inside-out route that improves the stability and durability of the catalyst. A more in-depth explanation of this process and its functioning is reported in the next paragraph

Transition metal carbides (TMCs) are a class of intermetallic compounds formed by the interstitial incorporation of carbon atoms into the lattice of parent transition metals. Theoretical studies indicate that three types of chemical bonding coexist in TMCs: (i) covalent bonds arising from electron sharing between metal and carbon atoms, (ii) metallic bonds resulting from the rearrangement of metal atoms, and (iii) ionic bonds generated through electron transfer between metal and carbon atoms [36]. This unique electronic structure imparts TMCs with distinctive physicochemical properties, including high melting points, excellent electrical conductivity, and strong corrosion resistance.

The insertion of carbon atoms into the interstices of the metal lattice increases the density of states near the Fermi level, giving TMCs electronic configurations and catalytic behaviours similar to those of noble metals. In 1973, Levy and Boudart [37] first reported that tungsten carbide (WC) exhibited platinum-like catalytic properties in hydrocarbon isomerization. Since then, numerous TMC catalysts have been studied and shown to deliver high catalytic activity and selectivity in reactions such as dehydrogenation, hydrogenation, and isomerization. More recently, TMCs have attracted significant attention for their promising performance in CO_2 hydrogenation, with many studies investigating the underlying mechanisms and strategies to enhance their catalytic efficiency [38]. One of the possible reasons why TMCs are so active in CO_2 hydrogenation, is due to their peculiar electronic structure that allows them to bind CO_2 non too weakly nor too tight, but with just the right energy to activate it on the surface.

Single-site catalysts (SSCs) are isolated reactive centres on the surface of oxides, carbides or MOF-derived supports considered to be an effective strategy to greatly improve the metal utilization for heterogeneous catalysts. When the isolated centre is a metal atom that is not bind to any other atom of the same type, the material is called Single-Atom Catalysts (SAC). These classes of materials are used to give maximal atom efficiency and to tune selectivity by creating unique active sites that stabilize CO_2 reduction intermediates. The highly dispersed metal sites enable the maximum exposure of active metals at the catalytic interface. Also, the coordination environment of isolated metal sites is more

editable than metal nanoparticles and nanoclusters due to the clear site structure, thereby resulting in the physicochemical properties and catalytic activities of SSCs being highly tuneable. The first study of heterogeneous SSC dates back to 1999 [39] and after its publication, also due to more modern spectroscopic characterization, a rapid growth of the number of paper revolving around SSCs or SACs has been observed in the literature [40]. In 2022, more than 37 metal elements that have successfully been prepared as SSCs and many sophisticated characterization and simulation techniques have been applied to analyse the coordination environments of SSCs in depth [41].

One possible route to produce these kinds of materials is known as Surface Organometallic Chemistry (SOMC), which consists in treating the surface of the support (e.g. the oxide) in order to control its reactivity towards molecular precursors such as coordination complexes. The main advantage of this route is to produce supported catalysts with a known coordination sphere and exploit already known coordination chemistry to produce the catalysts. Different review on this kind of process already exist in the literature and its potential has already been shown both in preparing [42] SACs as well as in developing novel catalysts by exploiting native defectivity of the support. Polshettiwar et al. for instance [43] synthesized highly defective silica nanoparticles and were able to convert CO_2 directly to methane without the addition of any metal atoms. The reactivity of this catalyst has been connected by the authors to nonbridging oxygen hole centres (NBOHCs) which are nothing more than ≡Si-O•, silica native defects.

Though effective and interesting, SACs research still hides great challenges. First, a set of unified guiding principles that govern the formation of SACs is lacking. In particular, because different metallic centres have different chemical and electronic properties, a guiding principle for the synthesis of one SAC cannot be simply extrapolated to another. Second, it remains difficult to regulate local structures of SACs, including bond length, oxidation state, coordination number and coordination anions. This is mainly due to the lack of a comprehensive understanding of SAC formation mechanisms. Third, it is difficult to control the loading of metal single atoms, since single atoms tend to aggregate into nanoclusters/particles due to the Gibbs–Thomson effect, blocking the loading level to around 1-3% mol. [44].

Atomically precise gold-based Nanoclusters (NCs) $Au_n(SR)_m$ are a novel class of ultrasmall sized nanoparticles composed of tens or hundreds of metal atoms surrounded by organic protecting ligands (i. e. thiolated ligands). Metal NCs were firstly discovered in 1994 by Brust et al. [45] and since then have been widely studied for many different applications including, but not limited to, heterogeneous catalysis. Progress in precise synthesis, separation and characterization revealed the possibility to

produce a variety of atomically precise nanostructures including $Au_{25}(SR)_{18}$, $Au_{38}(SR)_{24}$ and $Au_{144}(SR)_{60}$, but other compositions were also reported. These clusters consist of a symmetric metal core protected by multiple gold–thiolate staples $-SR-(Au-SR-)_n$ (n = 1,2) which properties such as photoluminescence, optical activity and catalytic activity are strongly size-dependent [46]. They attracted the attention of scientist due to their small size (in the range of nm or less), well defined structures, and molecule-like quantized electronic structure.

In the past few years, heteroatom doping of gold NCs has been proposed as a viable strategy to modify and tune the physical-chemical properties of the NCs by replacement of a single or few gold atoms by other metals [47]. Several well-defined bimetallic clusters have been studied with single or multiple doping atoms (e. g. Pd [48], Pt [49] Cu [50], Ag [51]). Highly selective synthesis protocols or separation techniques are critical in order to obtain high purity samples of the metal clusters for structure studies.

By tuning the size, staple units and doping, different catalytic activity can be obtained, ranging from electrochemical conversion of CO_2 ([52], [53]) to thermal hydrogenation of CO_2 [54].

In the frame of this PhD project, perovskite oxide-based catalysts and metal NCs were exploited as novel systems for the thermal conversion of CO_2.

1.3.1 Exsolution from perovskite oxide

Perovskite background

As we observed before, perovskite oxides are a wide class of materials containing mainly binary oxides and halides. The interest in their application lies in the variety of different possible combinations of metals that produce a stable system, as a matter of fact, the cations' sites can be substituted by the introduction of metals with different loadings and different oxidation states. The particularity with the intercalation of external elements in the perovskites native lattice sites is the possibility of tuning the stoichiometry and the materials properties [55]. A variety of perovskites with different molar concentration ratios can be generated and the most common charges combination involve A^{+} B^{5+}, A^{2+} B^{4+}, A^{3+} B^{3+} [56], [57]. Since the substitution of a cation with a different charge element modifies the systems stoichiometry, either vacancies in A or B site, or the modification of oxygen site occupancy can restore the charge neutrality. The structural versatility of these materials can be also empirically understood by using the tolerance factor t also called the Goldschmidt factor:

$$t = \frac{(r_A + r_O)}{[\sqrt{2}(r_B + r_O)]} \qquad [1.1]$$

Where r_A, r_B and r_O are respectively the cation's radius in site A, in site B and the oxygen radius. In an ideal perovskite, the tolerance factor t equals 1, giving rise to a cubic unit cell with space group *Pm-3m*, as exemplified by SrTiO3. For values of t close to unity, typically within 0.9 < t < 1, the structure retains its (pseudo)cubic symmetry. When the A-site cation is considerably smaller relative to the B-site cation (0.71 < t < 0.9), the BO6 octahedra undergo tilting, which lowers the symmetry. Equal, out-of-phase tilts of these octahedra along the *a*, *b*, and *c* axes of the cubic lattice produce a rhombohedral structure, whereas restricting the out-of-phase tilts to the *b* and *c* axes yields an orthorhombic phase. Conversely, when t exceeds unity due to oversized A-site cations, the perovskite tends to stabilize in hexagonal or tetragonal symmetries. This high tolerance in structure modifications makes this class of material applicable to multiple different fields.

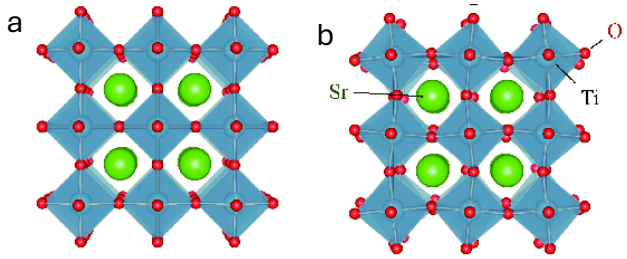

Fig. 1.3: a) cubic and b) tetragonal structure of $SrTiO_3$

One way to finely tune the chemical and physical properties of this kind of materials is via doping, that is the "the action of adding a small amount of foreign atoms to form a *solid solution* in the lattice of a non-metallic catalyst" [58]. In heterovalent doping, host cations within the perovskite lattice are substituted by atoms of different valence states, creating charge imbalances. These imbalances are typically compensated by the formation of oxygen vacancies or by changes in cation oxidation states, which in turn enhance ionic and/or electronic conductivity. Conversely, when lattice cations are replaced by heteroatoms of the same valence, no charge imbalance occurs; instead, the process, known as isovalent doping, primarily influences lattice distortions and structural properties. The substitution of an atom with a different one, therefore generates a defect, which influences the properties of the final material.

Among all the possible perovskite oxide, Strontium titanate, $SrTiO_3$ (STO), was chosen as the base oxide for the development of the work. It is a semiconductor, with a band gap of 3.2 eV [59]. Semiconductors are a class with appealing properties due to the ability to absorb UV light radiation and to generate e^--h^+ pairs, which are highly reactive and can therefore increase the catalytic and photocatalytic activity of the system. At room temperature $SrTiO_3$ crystalizes in the cubic perovskite structure with a lattice parameter of 3.905 Å [25]. This perovskite has elevated thermal stability, high dielectric constant and remarkable physical properties, such as mechanical stability, as well as chemical stability due to the

fact that Sr and Ti have highly positive reduction potentials, which makes them highly stable under reduction conditions [19]. These reasons, together with its well-known defect chemistry, made it the perfect choice for this PhD work.

One of the most researched topics for STO is in catalysis, especially photo- and- thermo-catalysis. However, this oxide alone does not have good enough properties to compete with commercial or commonly used catalysts, to overcome this issue doping is often use for two reasons, on the one hand doping STO ensures the intercalation of new energy levels inside its band gap, favouring optical and photo responsive properties, on the other hand doping can also be a way unconventionally generate metal nanoparticle on the surface. This process, called redox exsolution, was firstly discovered in 2002 using Pd and a perovskite based on Lanthanum and Iron/Cobalt doped in 5% of the B site with Palladium [60]. What the authors showed is the ability of the catalytic metal (Pd) to migrate from the bulk of the host material to the surface when exposed to a reducing environment, as well as its reintegration into the matrix under an oxidizing atmosphere.

This novel "inside-out" route for producing metal nanoparticles at the surface of the oxide, has rapidly gained great interest by the scientific community due to its several advantages. The first advantage lies in its synthetic route: a solid-state, solvent-free process that minimizes environmental toxicity. Moreover, the synthesis is carried out in a single step, facilitating easier implementation for scale-up. The second reason of the increasing interest in this process is due to the fact that, since the NPs are generated from the bulk, when they reach the surface they remain "socketed" in the matrix. In such a way, 1/3 of their volume remains below the surface [56]. Consequently, the NPs obtained are strongly anchored to the supported oxide and thus the catalyst is ensured with greater resistance to processes degradation, such as coarsening and particle migration, compared to the same catalyst synthesized by classical wet-chemistry methods [62].

Exsolution process

As anticipated, the process happens when a doped perovskite oxide is put under a reducing atmosphere and high temperatures. These conditions are necessary to let the reticular oxygen, starting from the superficial oxygen atoms (α-oxygen) and then the bulk oxygen (β-oxygens), react with hydrogen. From this interaction, water is produced, thus leaving behind electrons that reduces the metal dopant from its cationic form to M^0. The reaction scheme is the following:

$$H_2 + O_2\text{-} \rightarrow H_2O + V_O + 2e^-$$

$$M^{2+} + 2e^- \rightarrow M^0$$

Specifically, the exsolution process is composed of four main processes:

- Diffusion
- Reduction
- Nucleation
- Growth

Diffusion phenomena in a crystal lattice occur through the hopping process, which consists of ions jumping from one lattice site to another. The process is activated because the defect must pass through a "bottleneck" in order to move, i.e., a region of space where the ions of the lattice are at a minimum distance, and consequently the passage of the defect generates a structural deformation in the crystal. This process therefore requires activation energy provided by the high temperature at which the process takes place. This process is also the reason why the oxygen vacancies generated are essential for the migration of the ions, both O^{2-} and M^{n+} ions, as they generate free space in the lattice making the hopping process easier.

If we look at the conductivity of the solid by considering, as a first approximation, that it depends only on the presence of vacancies in the solid, to observe the effect of these defects on the system, we have:

$$\sigma = z_V e n_V u_V \qquad [1.2]$$

Considering Arrehnius' definition of mobility, conductivity can therefore be derived as a function of the activation energy of the process and as a function of temperature as follows:

$$u_V = \frac{z_V e}{KT} f_V e^{-(\frac{\Delta G_{att,u}}{KT})} \qquad [1.3]$$

$$\sigma = \frac{(z_V e)^2}{KT} n_V f_V e^{\frac{-\Delta G_{att,u}}{KT}} \qquad [1.4]$$

Here, fv represents the oscillation frequency of an ion around its equilibrium position, indicating the probability of an O^{2-} ion making a jump. This relationship clearly shows that both the vacancy concentration and temperature have a strong influence on conductivity, emphasizing the essential role of defects in facilitating the exsolution process. Oxygen vacancies enhance both the mobility and release of oxygen ions within the lattice. These vacancies can be introduced either through B-site acceptor doping [63] or by inducing Sr deficiency, which generates Sr vacancies, that, for charge compensation, consequently, produces oxygen defects, thereby promoting ionic species diffusion [64], [65].

Using Kröger-Vink notation, we can write these two different phenomena as:

$$Sr_{Sr}^{X} + O_O^X \rightarrow V_{Sr}'' + V_O^{\bullet\bullet} \qquad [1.5]$$

While the insertion of a dopant (e.g. Cu ion) with an oxidation number different from that of the site (i.e. Ti site) where it is inserted can be written like:

$$CuO \xrightarrow{SrTiO_3} Sr_{Sr}^{X} + Cu_{Ti}'' + O_O^X + V_O^{\bullet\bullet} + TiO_2 \qquad [1.6]$$

Consequently, it can be observed that for each copper atom inserted into the lattice at a Ti site, an oxygen vacancy is generated to balance the charge. It can thus be noted that doping not only introduces substitutional defects but also generates vacancies, thereby facilitating the exsolution process through enhanced cation migration along pre-existing lattice pathways [59].

Reduction of the metal chosen mainly depends on the choice of the oxide metals and the dopant metal. Particularly, the selected dopant should have a reduction potential ΔG close to zero at high temperatures, to be thermodynamically favoured. For instance, since Ni(II)-Ni(0) has a negative ΔG, but close to 0, it can be an easily exsolvable metal, whereas iron has a more complex behaviour. In fact, Fe has an ambivalent character, with ΔG > 0 at low temperature and ΔG < 0 at elevated temperature [66] which means that can be both used as a non-reducible B-site element [67] as well as a possible exsolved metal at higher temperatures [65]. However, when a hard to reduce metal is chosen to be exsolved, what can also be done is to add a second metal (co-doping) with lower ΔG of reduction. The addition of the second metal lowers the overall reduction potential of the material, and a bimetallic exsolution can happen, where both the metals are exsolved generally producing an alloy nanoparticle on the surface. This process, though chemically simple, is still being studied in literature as the profound reason why it works are still unclear. What is certain is that two possible processes might happen: either a "bulk alloy formation" or a "surface alloy formation". The main difference between these two situations is due to where the two metals react together and bond, whether on the surface or in the bulk of the material before migrating to the surface [68]. The exploitation of bimetallic or multimetallic exsolution can therefore produce innovative materials with mixed properties and compositions for a wider plethora of applications.

Aside of doping metal choice, also the choice of the matrix is crucial, as the matrix metals should be stable enough not to get reduced during the exsolution process, and therefore not pollute the exsolved nanoparticles. That is why SrTiO3 is a good choice for this process, as both Sr(II) and Ti(IV) have high enough reduction potentials not to be easily disturbed by hydrogen treatment.

According to classical nucleation theory, the **nucleation** of the nanoparticles is explained by the Gibbs free energy of nucleation of the nuclei, and their growth is only favoured when the size of the nuclei reaches a critical r*. However, classical nucleation theory is an approximate description of the real processes, as cannot fully describe the complexity of the system due to its modification during the process. However, what seems to be experimentally demonstrated is that NPs are more easily

generated on grain boundaries or surface defects of the oxide support, probably due to higher stabilization of the surface [66]. What has also been observed is that nucleation can happen either at the surface or in the bulk of the material, but the active nucleation site is still unclear and the monitoring of the first nucleus to be generated is still complicated due to highly sensitive and fast in situ characterization techniques needed [69].

In the moments right after the nucleation starts, **growth** process begins, where ions from the lattice are drawn towards the nucleation centre and the particle enlarges in order to minimize the surface energy. The growth rate is determined by rate determining steps (e.g., diffusion and reduction). It has been suggested that [66]the growth of exsolved particles is limited by strain, reactant, and diffusion. However, a clear-cut explanation on how the process happens, the energetics involved and the parameters to tune in order to control growth, are still missing. Nevertheless, again there are some agreed on phenomena that can happen. Both Endogenous and Exogenous growth can happen, and what has experimentally been seen is that when reduction conditions are strong (e.g. H2 conditions) endogenous exsolution tend to happen more [68], the reason for this might be in the fact that, upon strong reduction conditions, the rate determining step is usually ion diffusion and not reduction. This however is not always true as the overall system, the thickness of the sample, doping level, reduction temperature and conditions, are still unclear parameter that can greatly affect the growth of the particles [70].

Exsolution process is therefore very complicated, and a full understanding of all the steps and modifications of the system is still lacking, nevertheless, the product of the exsolution process i.e. metal NPs supported on the oxide, are good catalysts and can be applied in a variety of different reaction. What is more, the NPs generated via this process, tend to be more stable and more durable compared to classical impregnation techniques, making their application interesting and worth of studying.

The last interesting property of exsolved materials is their recyclability. Since the process to obtain them is a reduction process, via exposure to oxidative conditions the catalyst can be restored to its original form and therefore be used again [71]. This peculiar property opens the door also to smart catalyst and innovative materials that can be recycled multiple times. What is more, when exploiting both bimetallic exsolution and reoxidation of the catalyst, the same material can be tuned and different NPs can be generated as needed, thus producing a catalyst with different applications from the same pristine material [72]

1.3.2 Thiol protected Metal NCs

Thiol-protected metal nanoclusters (NCs), and particularly gold nanoclusters (AuNCs), have emerged over the past three decades as a distinct class of nanomaterials with molecular precision and unique physicochemical properties. These ultrasmall entities, generally composed of a few to several hundred metal atoms, bridge the gap between energy discrete molecular complexes and larger nanoparticles with continuous energy bands. Their core sizes, typically less than 2 nm, provide them with pronounced quantum confinement effects that impart a discrete electronic structure, molecule-like optical transitions, and size-dependent properties [73].

Generally speaking, these class of materials are composed of a metal core, that is an ordered arrange of zero-valent metal atoms, which is then protected by the so called staple units i.e. $-SR-(Au-SR-)_n$ (n = 1,2) units that protect the core and impart a chirality to the cluster, and finally the ligand layer, a layer composed of the organic protecting ligands which allow the cluster not to coalesce together and stabilize them .

The synthesis of this class of materials has been historically challenging, often connected with low yields of the reaction, multiple different synthetical steps and impure products due to the uncontrolled growth of the metal cores. Following the seminal Brust–Schiffrin method reported in 1994, substantial progress has been made in developing synthetic strategies that afford better control over size, and purity of the NCs. Ligand-mediated approaches, such as size-focusing, have proven particularly effective in generating highly uniform nanoclusters with well-defined compositions. These methods highlight the central role of the ligand shell: ligands not only stabilize the metal core and prevent aggregation, but also modulate surface reactivity, dictate solubility, and tune optical properties. The dynamic interaction between ligands and the gold core is at the base of the structural diversity of AuNCs, and careful selection of ligands, ranging from small thiols to peptides, proteins, etc., is mandatory for selecting the desired functionality for a certain application [53].

Clusters alone can be used as homogeneous catalysts [74] directly in solution, or can be supported, for example on an oxide. The deposit of the cluster on solid support impregnation techniques are usually preferred due to the easiness of the process and the quality of the result. However, after the deposition, the organic protecting ligands prevent direct interaction between oxide surface and the cluster, limiting the possible strong metal support interaction and the synergistic effect of metal/oxide interphases. To solve this issue a two-step pretreatment is usually needed, where firstly the ligands are burn off in an oxidative atmosphere and afterwards the metals are reduced again in a reducing atmosphere to directly bind the zerovalent core to the surface of the oxide.

The $Au_{25}(SR)_{18}$ Nanocluster

Nanoclusters (NCs) occupy the intermediate regime between nanoparticles and molecules, where discrete electronic states emerge and unique physicochemical properties can be observed. Clusters with core diameters below ~1.6 nm exhibit a HOMO–LUMO gap, as well as unusual optical, magnetic, and electrochemical behaviors distinct from bulk metals.

Among these systems, **$Au_{25}(SR)_{18}$** is the most extensively studied molecular NC. It consists of 25 gold atoms stabilized by a protective organic monolayer of 18 ligands, primarily thiolates. From the crystallization of this specimen, and the subsequent diffraction pattern, it was demonstrated that the metal framework is organized into an icosahedral 13-atom gold core, with the central atom symmetrically embedded [75]. The surrounding ligands arrange into repeating $–Au_2(SCH_2CH_2Ph)_3–$ moieties, known as "staples." Taking the organic shell into account, the cluster's overall diameter is under 1 nm, enabling molecular-like properties.

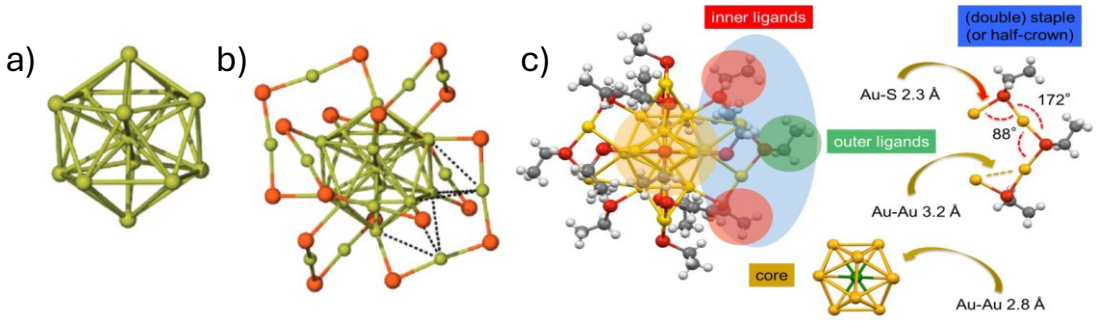

Fig. 1.4: a) icosahedral Au 13 core; b) **$Au_{25}(SR)_{18}$** 3D structure representation, in red the S atoms of the six orthogonal staples units; c) crystal structure of $Au_{25}(SEt)_{18}^0$. Au = yellow, S = red, C = gray, H = white, together with the staple units and the identification of inner and outer ligands [76], [77], [78].

More recently, a more "naked" Au25 species has been successfully crystallized, i.e. $Au_{25}(SC_2H_5)_{18}$ in its neutral charge state (with no counterion). These crystals provided more accurate and detailed structural insights. The 18 thiolate ligands can be divided into two distinct categories: 12 inner ligands in which sulfur bridges one core Au atom and one staple Au atom, and 6 outer ligands that bind exclusively to staple Au atoms. Each staple follows the $Au_2(SR)_3$ stoichiometry and has the form $Au_{core}–(–SR–Au–SR–Au–SR–)–A_{ucore}$. It comprises two gold atoms located outside the icosahedral core and three thiolate ligands, two directly linked to the core and one not directly connected [79].

1.4 Open problems for catalysis

The main problem in producing an innovative catalyst is knowing which site is active in the chosen reaction. However, identifying the active site is not so simple.

As we saw in the previous paragraph, CZA catalysts are active for methanolation of CO_2, however the profound reason of its high reactivity still lies undetected. A deep investigation on the composition of the catalyst is enough to understand the complexity of the system. Multiple phases, different morphologies and various Zn/Cu interfaces are generated when coprecipitation synthesis is used. This inhomogeneity of the system makes its study difficult. What is more, recent publications underlined that upon changing the conditions of the reaction (mainly temperature and pressure) the active phase changes [80]. What is unanimously recognized as true is the fact that Cu is needed, but what oxidation state, coordination and structures of these metals are needed is still under debate. Schlögl called this hard to define copper active phase "methanol copper" [81]. Reduced Cu centres (either zero valent or monovalent) are needed, but it is not enough, defects in Cu particles (e.g. twin boundaries or stacking faults) are also needed as they stabilize intermediate and favour the dissociation of hydrogen molecules [82]. Also, punctual defects as oxygen vacancies and interstitials have been demonstrated to increase the activity of the catalysts, and their generation at the interface between Cu and ZnO help binding reaction intermediate with the correct energy for promoting the products [83].

Also, the role of ZnO is still under debate, on the one hand upon reaction conditions Zn/Cu alloy forms at the surface and multiple publication (both experimental and theoretical) studied the importance of this phenomenon. Some calculations indicate that alloying Zn into the Cu surface strengthens the bonding of key intermediates, thereby lowering activation barriers and enhancing the rate of methanol synthesis [84]. However, alloying is not the only process that can happen between ZnO and Cu, Stong Metal-Support Interaction (SMSI) can also happen. SMSI is a process that happens when the support oxide, under reaction condition, covers the metal nanoparticles with a thick layer deactivating it [85]. However, if this process is done under mild reaction conditions, what happens is that firstly Zn(0) species and ZnO NPs generate on the surface of metallic Cu generating the so-called inverse catalyst, then Zn species gets partially oxidised to $Zn^{\delta+}$ and only at the end a thin layer of ZnO is formed. Nevertheless, the oxide layer before growing to be thick and deactivating the catalyst can stay "graphitic like", just few layers, not completely blocking the metal activity. This phenomenon can therefore promote MeOH production in the first stages, before completely covering the metallic Cu as generates Zn defects on Cu surfaces [86]. Different reaction conditions can therefore give rise to different phenomena either enhancing or reducing the catalytic activity of the system.

Lastly, Al_2O_3 is usually called the structural promoter of the catalyst, and its low overall concentration (around 10%) seems to be indicative of its little importance in the reaction. However, when alumina is replaced with other oxides, the activity or the selectivity of the catalyst decreases [87],[88]. One possible explanation is that alumina promotes CO_2 activation via favouring RWGS reaction and reacting with Zn to form a new spinel phase. Therefore, the presence of Al ions induces some defects in the ZnO_x sites at the interface with Cu, enhancing the activity [89].

1.5 Objectives

The above listed issues are just some of the open questions that the wide literature on the topic proposes. What is clear is that the dynamicity and the inhomogeneity of this system make it difficult to study this system and very complicated to identify the active site of the catalyst via spectroscopic tools. For this reason, the work of this PhD has been developed as follows:

- Characterization and testing of a commercially available CZA catalyst compared with an in-house synthesized one, to evaluate the state of the art and assess any issues with the characterization and monitoring of the catalysts;
- Production of a model system for CO_2 conversion to MeOH based on ZnO supported thiol-protected metal nanocluster;
- Provide an alternative approach to catalyst preparation: metal NPs supported on SrTiO3 produced via unconventional exsolution method.

As we already mentioned in the past paragraphs, defects and defect chemistry seems to play a crucial role in the catalytic conversion of CO_2, for this reason the common thread underneath the overall discussion will be the monitoring of defects and their modifications during reactions or pseudo catalytic conditions. To do this Electron Spin Resonance (ESR) has been used due to its high sensitivity and to its ability to give information about both the geometry and coordination of the centre of interest. What is more, due to the vast quantity of information retrievable from a single spectrum, and due to the high sensitivity of this technique, the spectrum obtained is usually a fingerprint characteristic of the specific system in analysis and can therefore be used as a concise technique to gain insight of multiple aspects of the materials composition and properties in one.

1.6 Structure of the thesis

Chapter 2 will focus on explaining the theoretical background, as well as the working of an EPR spectrometer. The understanding of the physical background of this technique is mandatory to know what to expect in the different systems one is experimenting with. In the last part of this chapter, some useful characteristic spectra of system used in the frame of this PhD work are presented in order to anticipate what will be seen in the other chapters.

Chapter 3 will present the first unconventional system studied for this PhD, Cu-doped $SrTiO_3$ with particular focus on the monitoring of the exsolution process and its reversibility giving particular attention to the possibility of monitoring the process and the defectivity of the material via EPR spectroscopy

Chapter 4 will deal once again with exsolution process, but in this chapter bimetallic exsolution will be analysed involving Fe and Ni co-doped $SrTiO_3$. The mutual influence of Ni and Fe has been studied with all the conventional techniques as well as with EPR to monitor the defects modification of the materials. Finally, some preliminary catalytic tests have been performed on these materials to detect any relationship between co-doping and reactivity.

Chapter 5 will focus on the preparation of model systems for CO_2 conversion to MeOH exploiting nanocluster chemistry developed during my period abroad at the Technische Universität Wien in Vienna in the group of Prof. Barrabés. In short, Au and CuAu NCs have been synthesized and deposited on ZnO NPs and used for catalytic conversion of CO_2. Finally, an in-depth defects monitoring and characterization has been carried out exploiting both EPR and in-situ DRIFTS spectroscopies to detect any defects-reactivity correlations.

Chapter 6 presents other case studies analysed during these three years of PhD, mainly focusing on the characterization and testing of CZA systems (a commercial one and a synthesised one) that was the first approach to CO_2 to MeOH and was necessary to understand the dynamic behaviour of these catalysts. Another system analysed in this chapter is Cu, Zn co-doped $SrTiO_3$ that has been used as a meeting point between the advantages of the exsolution process (analysed and studied in chapters 3 and 4) and the necessity of having strong interactions between Cu and Zn (as seen in chapter 5).

Bibliography

[1] "Statista - Global Carbon Budget." Accessed: Sep. 10, 2025. [Online]. Available: https://www.statista.com/statistics/276629/global-co2-emissions/

[2] Katie Lebling, Karl Hausker, Ankita Gangotra, and Zachary Byrum, "7 Things to Know About Carbon Capture, Utilization and Sequestration." Accessed: Sep. 10, 2025. [Online]. Available: https://www.wri.org/insights/carbon-capture-technology

[3] J. H. Park, J. Yang, D. Kim, H. Gim, W. Y. Choi, and J. W. Lee, "Review of recent technologies for transforming carbon dioxide to carbon materials," Jan. 01, 2022, *Elsevier B.V.* doi: 10.1016/j.cej.2021.130980.

[4] H.-L. Chen *et al.*, "Photoreduction of carbon dioxide and photodegradation of organic pollutants using alkali cobalt oxides MCoO2 (M = Li or Na) as catalysts," *J Environ Manage*, vol. 313, p. 114930, 2022, doi: https://doi.org/10.1016/j.jenvman.2022.114930.

[5] S. Gu, A. N. Marianov, T. Lu, and J. Zhong, "A review of the development of porphyrin-based catalysts for electrochemical CO2 reduction," *Chemical Engineering Journal*, vol. 470, p. 144249, 2023, doi: https://doi.org/10.1016/j.cej.2023.144249.

[6] Lin S *et al.*, "Covalent organic frameworks comprising cobalt porphyrins for catalytic CO_2 reduction in water," *Science (1979)*, no. 349, Sep. 2015, doi: https://doi.org/10.1126/science.aac8343.

[7] W. Zhang *et al.*, "Progress and Perspective of Electrocatalytic CO2 Reduction for Renewable Carbonaceous Fuels and Chemicals," *Advanced Science*, vol. 5, no. 1, p. 1700275, Jan. 2018, doi: https://doi.org/10.1002/advs.201700275.

[8] L. Zhang, Z.-J. Zhao, and J. Gong, "Nanostructured Materials for Heterogeneous Electrocatalytic CO2 Reduction and their Related Reaction Mechanisms," *Angewandte Chemie International Edition*, vol. 56, no. 38, pp. 11326–11353, Sep. 2017, doi: https://doi.org/10.1002/anie.201612214.

[9] M. Asadi *et al.*, "Nanostructured transition metal dichalcogenide electrocatalysts for CO2 reduction in ionic liquid," *Science (1979)*, vol. 353, no. 6298, pp. 467–470, Jul. 2016, doi: 10.1126/science.aaf4767.

[10] Z. Sun, T. Ma, H. Tao, Q. Fan, and B. Han, "Fundamentals and Challenges of Electrochemical CO2 Reduction Using Two-Dimensional Materials," *Chem*, vol. 3, no. 4, pp. 560–587, Oct. 2017, doi: 10.1016/j.chempr.2017.09.009.

[11] Y. Wang, J. Liu, Y. Wang, A. M. Al-Enizi, and G. Zheng, "Tuning of CO2 Reduction Selectivity on Metal Electrocatalysts," Nov. 20, 2017, *Wiley-VCH Verlag*. doi: 10.1002/smll.201701809.

[12] W. Tu, Y. Zhou, and Z. Zou, "Photocatalytic conversion of CO2 into renewable hydrocarbon fuels: State-of-the-art accomplishment, challenges, and prospects," Jul. 16, 2014, *Wiley-VCH Verlag*. doi: 10.1002/adma.201400087.

[13] P. Wang, S. Wang, H. Wang, Z. Wu, and L. Wang, "Recent Progress on Photo-Electrocatalytic Reduction of Carbon Dioxide," Jan. 01, 2018, *Wiley-VCH Verlag*. doi: 10.1002/ppsc.201700371.

[14] L. Xu, Y. Xiu, F. Liu, Y. Liang, and S. Wang, "Research progress in conversion of CO2to valuable fuels," Aug. 01, 2020, *MDPI AG*. doi: 10.3390/molecules25163653.

[15] X. Jiang, X. Nie, X. Guo, C. Song, and J. G. Chen, “Recent Advances in Carbon Dioxide Hydrogenation to Methanol via Heterogeneous Catalysis,” Aug. 12, 2020, *American Chemical Society*. doi: 10.1021/acs.chemrev.9b00723.

[16] B. M. Tackett, E. Gomez, and J. G. Chen, “Net reduction of CO2 via its thermocatalytic and electrocatalytic transformation reactions in standard and hybrid processes,” *Nat Catal*, vol. 2, no. 5, pp. 381–386, May 2019, doi: 10.1038/s41929-019-0266-y.

[17] “Carbon Intenational Company.” Accessed: Sep. 10, 2025. [Online]. Available: https://carbonrecycling.com/

[18] J. Incer-Valverde, A. Korayem, G. Tsatsaronis, and T. Morosuk, “‘Colors’ of hydrogen: Definitions and carbon intensity,” Sep. 01, 2023, *Elsevier Ltd*. doi: 10.1016/j.enconman.2023.117294.

[19] I. - International Energy Agency, “Global Hydrogen Review 2022,” 2022. [Online]. Available: www.iea.org/t&c/

[20] M. T. Khalil *et al.*, “Recent advancements in catalytic CO2 conversion to methanol: strategies, innovations, and future directions,” Jul. 28, 2025, *Royal Society of Chemistry*. doi: 10.1039/d5gc01906k.

[21] F. Zhang, W. Chen, and W. Li, “Recent advances in the catalytic conversion of CO2 to chemicals and demonstration projects in China,” *Molecular Catalysis*, vol. 541, Apr. 2023, doi: 10.1016/j.mcat.2023.113093.

[22] S. Kattel, P. Liu, and J. G. Chen, “Tuning Selectivity of CO2 Hydrogenation Reactions at the Metal/Oxide Interface,” *J Am Chem Soc*, vol. 139, no. 29, pp. 9739–9754, Jul. 2017, doi: 10.1021/jacs.7b05362.

[23] G. Bozzano and F. Manenti, “Efficient methanol synthesis: Perspectives, technologies and optimization strategies,” Sep. 01, 2016, *Elsevier Ltd*. doi: 10.1016/j.pecs.2016.06.001.

[24] ALWIN MITTASCE and MATHIAS PIER, “Synthetic Manufacture of Methanol,” 1926.

[25] Alan Edward and Alford Gent, “METHANOL PRODUCTION,” 1976

[26] D. Sheldon, “Methanol production - A technical history,” Jul. 01, 2017, *Johnson Matthey Public Limited Company*. doi: 10.1595/205651317X695622.

[27] A. C. Dimian, C. S. Bildea, and A. A. Kiss, “Methanol,” in *Applications in Design and Simulation of Sustainable Chemical Processes*, Elsevier, 2019, pp. 101–145. doi: 10.1016/B978-0-444-63876-2.00003-6.

[28] G. Pacchioni, “From CO2 to Methanol on Cu/ZnO/Al2O3 Industrial Catalyst. What Do We Know about the Active Phase and the Reaction Mechanism?,” Feb. 16, 2024, *American Chemical Society*. doi: 10.1021/acscatal.3c05669.

[29] D. S. Marlin, E. Sarron, and Ó. Sigurbjörnsson, “Process Advantages of Direct CO2 to Methanol Synthesis,” *Front Chem*, vol. 6, Sep. 2018, doi: 10.3389/fchem.2018.00446.

[30] Y. Cul *et al.*, “Latest catalyst provides more methanol for longer,” 2022.

[31] J. E. Whitlow, “Operation, Modeling and Analysis of the Reverse Water Gas Shift Process,” AIP Publishing, Feb. 2003, pp. 1116–1123. doi: 10.1063/1.1541409.

[32] M. González-Castaño, B. Dorneanu, and H. Arellano-García, “The reverse water gas shift reaction: A process systems engineering perspective,” Jun. 01, 2021, *Royal Society of Chemistry*. doi: 10.1039/d0re00478b.

[33] C. Zhou, J. Zhang, Y. Fu, and H. Dai, “Recent Advances in the Reverse Water–Gas Conversion Reaction,” Nov. 01, 2023, *Multidisciplinary Digital Publishing Institute (MDPI)*. doi: 10.3390/molecules28227657.

[34] H. Arandiyan *et al.*, “Defect engineering of oxide perovskites for catalysis and energy storage: Synthesis of chemistry and materials science,” Sep. 21, 2021, *Royal Society of Chemistry*. doi: 10.1039/d0cs00639d.

[35] M. A. Peña and J. L. G. Fierro, “Chemical structures and performance of perovskite oxides,” Jul. 2001. doi: 10.1021/cr980129f.

[36] J. G. Chen, “Carbide and Nitride Overlayers on Early Transition Metal Surfaces: Preparation, Characterization, and Reactivities,” 1996. [Online]. Available: https://pubs.acs.org/sharingguidelines

[37] R. B. LEVY and M. BOUDART, “Platinum-Like Behavior of Tungsten Carbide in Surface Catalysis,” *Science (1979)*, vol. 181, pp. 547–548, 1973.

[38] L. Wang, H. Wang, H. Huang, T. Yun, C. Song, and C. Shi, “Transition Metal Carbides: Emerging CO2 Hydrogenation Catalysts, from Recent Advance to Future Exploration,” Feb. 12, 2024, *John Wiley and Sons Inc*. doi: 10.1002/adfm.202309850.

[39] K. Asakura, H. Nagahiro, N. Ichikuni, and Y. Iwasawa, “Structure and catalytic combustion activity of atomically dispersed Pt species at MgO surface,” 1999.

[40] H. Wang, T. Yang, J. Wang, Z. Zhou, Z. Pei, and S. Zhao, “Coordination engineering in single-site catalysts: General principles, characterizations, and recent advances,” Jan. 11, 2024, *Elsevier Inc.* doi: 10.1016/j.chempr.2023.08.014.

[41] L. Han *et al.*, “A single-atom library for guided monometallic and concentration-complex multimetallic designs,” *Nat Mater*, vol. 21, no. 6, pp. 681–688, Jun. 2022, doi: 10.1038/s41563-022-01252-y.

[42] C. Copéret *et al.*, “Surface Organometallic and Coordination Chemistry toward Single-Site Heterogeneous Catalysts: Strategies, Methods, Structures, and Activities,” Jan. 27, 2016, *American Chemical Society*. doi: 10.1021/acs.chemrev.5b00373.

[43] A. K. Mishra, R. Belgamwar, R. Jana, A. Datta, and V. Polshettiwar, “Defects in nanosilica catalytically convert CO 2 to methane without any metal and ligand,” *PNAS*, vol. 117, no. 12, 2020, doi: 10.1073/pnas.1917237117/-/DCSupplemental.

[44] Y. Duan *et al.*, “Large-Scale Synthesis of High-Loading Single Metallic Atom Catalysts by a Metal Coordination Route,” *Advanced Materials*, vol. 36, no. 32, Aug. 2024, doi: 10.1002/adma.202404900.

[45] M. Brust, M. Walker, D. Bethell, D. J. Schiffrin, and R. Whyman, “Synthesis of Thiol-derivatised Gold Nanoparticles in a Two-phase Liquid-Liquid System,” 1994.

[46] N. Barrabés, B. Zhang, and T. Bürgi, “Racemization of chiral Pd2Au36(SC2H4Ph)24: Doping increases the flexibility of the cluster surface,” *J Am Chem Soc*, vol. 136, no. 41, pp. 14361–14364, Oct. 2014, doi: 10.1021/ja507189v.

[47] B. Zhang *et al.*, "Pd2Au36(SR)24 cluster: Structure studies," *Nanoscale*, vol. 7, no. 40, pp. 17012–17019, Oct. 2015, doi: 10.1039/c5nr04324g.

[48] R. Jin and K. Nobusada, "Doping and alloying in atomically precise gold nanoparticles," 2014, *Tsinghua University Press*. doi: 10.1007/s12274-014-0403-5.

[49] H. Qian *et al.*, "Monoplatinum doping of gold nanoclusters and catalytic application," *J Am Chem Soc*, vol. 134, no. 39, pp. 16159–16162, Oct. 2012, doi: 10.1021/ja307657a.

[50] Y. Negishi, K. Munakata, W. Ohgake, and K. Nobusada, "Effect of copper doping on electronic structure, geometric structure, and stability of thiolate-protected Au 25 nanoclusters," *Journal of Physical Chemistry Letters*, vol. 3, no. 16, pp. 2209–2214, Aug. 2012, doi: 10.1021/jz300892w.

[51] Y. Negishi, T. Iwai, and M. Ide, "Continuous modulation of electronic structure of stable thiolate-protected Au25 cluster by Ag doping," *Chemical Communications*, vol. 46, no. 26, pp. 4713–4715, Jul. 2010, doi: 10.1039/c0cc01021a.

[52] C. Zhu *et al.*, "Arylation of gold nanoclusters and insights into structure-related CO2 reduction reaction performances," *Chem Sci*, vol. 16, no. 23, pp. 10273–10281, May 2025, doi: 10.1039/d5sc01200g.

[53] J. Zhao, A. Ziarati, and T. Bürgi, "Tuning Atomically Precise Gold Nanoclusters for Selective Electroreduction of CO2," Jun. 24, 2025, *John Wiley and Sons Inc*. doi: 10.1002/anie.202504320.

[54] S. Pollitt *et al.*, "Engineering Catalytic Efficiency by Thiolate-Protected Trimetallic (Cu, Pd, Au) Nanoclusters: Single-Atom Alloy Catalysts for Water–Gas Shift," *ACS Catal*, vol. 15, no. 17, pp. 15459–15474, Sep. 2025, doi: 10.1021/acscatal.5c04165.

[55] R. J. H. Voorhoeve, D. W. Johnsoi, J. P. Remeika, and P. K. Gall, "Perovskite oxides, long known in solid-state chem and physics, find new applications in catal," 1977. [Online]. Available: www.sciencemag.org

[56] A. S. Bhalla, Ruyan Guo, and Rustum Roy, "The perovskite structure – a review of its role in ceramic science and technology," *Materials Research Innovations*, vol. 4, pp. 3–26, 2000.

[57] R. I. Walton, "Perovskite Oxides Prepared by Hydrothermal and Solvothermal Synthesis: A Review of Crystallisation, Chemistry, and Compositions," Jul. 27, 2020, *Wiley-VCH Verlag*. doi: 10.1002/chem.202000707.

[58] "Doping," in *The IUPAC Compendium of Chemical Terminology*, Research Triangle Park, NC: International Union of Pure and Applied Chemistry (IUPAC), 2014. doi: 10.1351/goldbook.D01834.

[59] M. Cardona, "Optical Properties and Band Structure of SrTiO& and BaTiO&f," 1965.

[60] Y. Nishihata *et al.*, "Self-regeneration of a Pd-perovskite catalyst for automotive emissions control," *Nature*, vol. 418, no. 6894, pp. 164–167, Jul. 2002, doi: 10.1038/nature00893.

[61] D. Neagu *et al.*, "Nano-socketed nickel particles with enhanced coking resistance grown in situ by redox exsolution," *Nat Commun*, vol. 6, Sep. 2015, doi: 10.1038/ncomms9120.

[62] S. P. Jiang, "Nanoscale and nano-structured electrodes of solid oxide fuel cells by infiltration: Advances and challenges," 2012, *Elsevier Ltd*. doi: 10.1016/j.ijhydene.2011.09.067.

[63] B. Rudolph, "Understanding nickel exsolution by morphology and composition variation of the perovskite host oxide."

[64] D. Neagu *et al.*, “Demonstration of chemistry at a point through restructuring and catalytic activation at anchored nanoparticles,” *Nat Commun*, vol. 8, no. 1, Dec. 2017, doi: 10.1038/s41467-017-01880-y.

[65] D. Neagu, G. Tsekouras, D. N. Miller, H. Ménard, and J. T. S. Irvine, “In situ growth of nanoparticles through control of non-stoichiometry,” *Nat Chem*, vol. 5, no. 11, pp. 916–923, Nov. 2013, doi: 10.1038/nchem.1773.

[66] Y. Gao, D. Chen, M. Saccoccio, Z. Lu, and F. Ciucci, “From material design to mechanism study: Nanoscale Ni exsolution on a highly active A-site deficient anode material for solid oxide fuel cells,” *Nano Energy*, vol. 27, pp. 499–508, Sep. 2016, doi: 10.1016/j.nanoen.2016.07.013.

[67] R. I. Eglitis, S. Piskunov, E. Heifets, E. A. Kotomin, and G. Borstel, “Ab initio study of the SrTiO 3 , BaTiO 3 and PbTiO 3 (0 0 1) surfaces,” in *Ceramics International*, 2004, pp. 1989–1992. doi: 10.1016/j.ceramint.2003.12.176.

[68] O. Kwon *et al.*, “Self-assembled alloy nanoparticles in a layered double perovskite as a fuel oxidation catalyst for solid oxide fuel cells,” *J Mater Chem A Mater*, vol. 6, no. 33, pp. 15947–15953, 2018, doi: 10.1039/c8ta05105d.

[69] D. Neagu *et al.*, “In Situ Observation of Nanoparticle Exsolution from Perovskite Oxides: From Atomic Scale Mechanistic Insight to Nanostructure Tailoring,” *ACS Nano*, vol. 13, no. 11, pp. 12996–13005, Nov. 2019, doi: 10.1021/acsnano.9b05652.

[70] Y. H. Kim *et al.*, “Nanoparticle Exsolution on Perovskite Oxides: Insights into Mechanism, Characteristics and Novel Strategies,” Dec. 01, 2024, *Springer Science and Business Media B.V.* doi: 10.1007/s40820-023-01258-4.

[71] A. López-García, L. Almar, S. Escolástico, A. B. Hungría, A. J. Carrillo, and J. M. Serra, “Tuning Ternary Alloyed Nanoparticle Composition and Morphology by Exsolution in Double Perovskite Electrodes for CO2Electrolysis,” *ACS Appl Energy Mater*, vol. 5, no. 11, pp. 13269–13283, Nov. 2022, doi: 10.1021/acsaem.2c01829.

[72] J. H. Kim *et al.*, “Nanoparticle Ex-solution for Supported Catalysts: Materials Design, Mechanism and Future Perspectives,” Jan. 26, 2021, *American Chemical Society*. doi: 10.1021/acsnano.0c07105.

[73] A. Baghdasaryan and H. Dai, “Molecular Gold Nanoclusters for Advanced NIR-II Bioimaging and Therapy,” Jun. 11, 2025, *American Chemical Society*. doi: 10.1021/acs.chemrev.4c00835.

[74] R. Banu *et al.*, “Synergistic effect of ligand-cluster structure and support in gold nanocluster catalysts for selective hydrogenation of alkynes,” *Nanoscale*, vol. 17, no. 9, pp. 5098–5105, Jan. 2025, doi: 10.1039/d4nr03865g.

[75] M. W. Heaven, A. Dass, P. S. White, K. M. Holt, and R. W. Murray, “Crystal structure of the gold nanoparticle [N(C8H 17)4][Au25(SCH2CH 2Ph)18],” *J Am Chem Soc*, vol. 130, no. 12, pp. 3754–3755, Mar. 2008, doi: 10.1021/ja800561b.

[76] S. Agnoli, “THE PIVOTAL ROLE OF LIGANDS DETERMINING THE PROPERTIES OF ATOMICALLY PRECISE GOLD NANOCLUSTERS.”

[77] M. W. Heaven, A. Dass, P. S. White, K. M. Holt, and R. W. Murray, “Crystal Structure of the Gold Nanoparticle [N(C8H17)4][Au25(SCH2CH2Ph)18],” *J Am Chem Soc*, vol. 130, no. 12, pp. 3754–3755, Mar. 2008, doi: 10.1021/ja800561b.

[78] T. Dainese *et al.*, “Au25(SEt)18, a Nearly Naked Thiolate-Protected Au25 Cluster: Structural Analysis by Single Crystal X-ray Crystallography and Electron Nuclear Double Resonance,” *ACS Nano*, vol. 8, no. 4, pp. 3904–3912, Apr. 2014, doi: 10.1021/nn500805n.

[79] T. Dainese *et al.*, “Au25(SEt)18, a nearly naked thiolate-protected Au25 cluster: Structural analysis by single crystal X-ray crystallography and electron nuclear double resonance,” *ACS Nano*, vol. 8, no. 4, pp. 3904–3912, Apr. 2014, doi: 10.1021/nn500805n.

[80] A. Urakawa, “Mind the gaps in CO2-to-methanol,” Jun. 01, 2021, *Nature Research*. doi: 10.1038/s41929-021-00638-6.

[81] R. Schlögl, “Chemical Batteries with CO2,” Feb. 07, 2022, *John Wiley and Sons Inc*. doi: 10.1002/anie.202007397.

[82] Malte Behrens et al., “The Active Site of MethanolSynthesis over Cu/ZnO/Al 2 O3Industrial Catalysts,” *Science (1979)*, vol. 336, no. 6083, pp. 893–897, May 2012, doi: 10.1126/science.1219468.

[83] A. Ruiz Puigdollers, P. Lamoureux, S. Tosoni, and G. Pacchioni, “Increasing Oxide Reducibility: The Role of Metal/Oxide Interfaces in the Formation of Oxygen Vacancies,” *ACS Catal*, vol. 7, Aug. 2017, doi: 10.1021/acscatal.7b01913.

[84] M. Behrens, “Promoting the Synthesis of Methanol: Understanding the Requirements for an Industrial Catalyst for the Conversion of CO2,” *Angewandte Chemie International Edition*, vol. 55, no. 48, pp. 14906–14908, Nov. 2016, doi: https://doi.org/10.1002/anie.201607600.

[85] S. J. Tauster, “Strong metal-support interactions,” *Acc Chem Res*, vol. 20, no. 11, pp. 389–394, Nov. 1987, doi: 10.1021/ar00143a001.

[86] T. Lunkenbein, J. Schumann, M. Behrens, R. Schlögl, and M. G. Willinger, “Formation of a ZnO Overlayer in Industrial Cu/ZnO/Al2O3 Catalysts Induced by Strong Metal–Support Interactions,” *Angewandte Chemie International Edition*, vol. 54, no. 15, pp. 4544–4548, Apr. 2015, doi: https://doi.org/10.1002/anie.201411581.

[87] G. Bonura, M. Cordaro, C. Cannilla, F. Arena, and F. Frusteri, “The changing nature of the active site of Cu-Zn-Zr catalysts for the CO2 hydrogenation reaction to methanol,” *Appl Catal B*, vol. 152–153, pp. 152–161, 2014, doi: https://doi.org/10.1016/j.apcatb.2014.01.035.

[88] L. Angelo, K. Kobl, L. M. M. Tejada, Y. Zimmermann, K. Parkhomenko, and A.-C. Roger, “Study of CuZnMOx oxides (M = Al, Zr, Ce, CeZr) for the catalytic hydrogenation of CO2 into methanol,” *Comptes Rendus. Chimie*, vol. 18, no. 3, pp. 250–260, 2015, doi: 10.1016/j.crci.2015.01.001.

[89] Z. Cheng *et al.*, “Insights into the Inducing Effect of Aluminum on Cu–ZnO Synergy for Methanol Steam Reforming,” *Ind Eng Chem Res*, vol. 61, no. 32, pp. 11699–11707, Aug. 2022, doi: 10.1021/acs.iecr.2c01790.

Chapter 2
Electron Paramagnetic Resonance

Index of the chapter

This chapter contains a brief theoretical and instrumental introduction to EPR spectroscopy, to help to understand the main principles behind this technique, as well as to help understand the signals reported throughout this manuscript. At the end of the chapter are some information about the main systems analysed in this thesis and their typical EPR signals.

2.1 Introduction

Electron Spin Resonance (ESR), also known as Electron Paramagnetic Resonance (EPR), is a powerful technique for studying paramagnetic species in chemistry, physics, and biology. This methodology has high sensitivity, and it is capable of measurements at concentrations down to 10^{-8} M [1], thus making the amount of information obtainable from a single spectrum considerable. The utility of this spectroscopy lies in its ability to monitor both the generation of paramagnetic defects in the material and the variation in coordination and environment of the chosen centre contained in the system. This specific capacity permits the generation of a “fingerprint” of the material in a sole spectrum, which is characteristic of the type of defects and paramagnetic centres present in the system of interest.

A clear limitation of the method, already implied in its definition, is that diamagnetic systems, which make up the majority of substances, cannot be examined using EPR. Yet this limitation is also advantageous: reactive paramagnetic intermediates in complex environments or paramagnetic centres embedded within intricate systems (e.g., a metal ion in a protein) can be investigated without interference from diamagnetic components.

Before introducing the principles of EPR spectroscopy, some of which overlap with the more widely known nuclear magnetic resonance (NMR), it is helpful to recall the magnetic properties of matter. A paramagnetic body placed in a magnetic field increases the density of the field lines (the magnetic flux density) within its volume, whereas a diamagnetic substance decreases it. Diamagnetism, present in all substances, arises from electron circulation in atoms, ions, or molecules with closed electron shells. Paramagnetism, by contrast, is characteristic of systems containing one or more unpaired electrons, which carry intrinsic angular momentum (spin) and an associated magnetic moment. These centres behave largely independently and therefore do not display cooperative magnetic phenomena such as ferromagnetism or antiferromagnetism. In an external magnetic field, their magnetic moments tend to align with the field and with each other, although thermal motion acts against this ordering. In the absence of a field, the unpaired electrons remain randomly oriented.

Electron magnetic resonance occurs when electromagnetic radiation of appropriate frequency (usually in the microwave region) interacts with a sample in a magnetic field, causing the free electron spins and

their magnetic moments to “flip,” thereby absorbing energy. From a quantum mechanical standpoint, this corresponds to the behaviour of a single unpaired electron experiencing the Zeeman effect—that is, the splitting of its spin states in an external magnetic field. Under these conditions, a photon of suitable energy can promote the electron from the lower-energy state to the higher-energy state.

EPR (and similarly NMR) differs from classical spectroscopies that use electromagnetic waves in two key respects. First, whereas most spectroscopic methods probe the interaction between the electric field of radiation and molecular electric dipoles, magnetic resonance techniques rely on the interaction between the magnetic field of the radiation and the magnetic dipoles of paramagnetic centres. Second, the experimental setup is distinct: instead of employing a tuneable radiation source and monochromator, EPR uses a nearly monochromatic source of radiation in combination with a variable magnetic field. In a typical continuous-wave EPR (CW-EPR) experiment, the sample is irradiated with fixed-frequency microwaves while the magnetic field is swept across a defined range to identify the resonance condition. The resulting CW-EPR spectrum plots microwave absorption (or, more commonly, its first derivative, as discussed in Section 2.2) as a function of the applied magnetic field [2].

2.1.1 Origin of the technique

The earliest reported research for a dependence of magnetic susceptibility on frequency was carried out by Belz in 1922 [3] for solutions of a variety of paramagnetic salts, but no frequency dependence was found. After this first trial, the origins of the molecular beam magnetic resonance method can be traced back to early theoretical speculations and experiments on the change in the quantum mechanical space quantization when the direction of a magnetic field is changed. The problem was first posed and partially solved in 1927 by C. G. Darwin [4] and subsequently by P. Gutinger [5] and E. Majorana [6], but it was not until 1937 that Rabi et al. [7] studied transitions between levels induced by an oscillating magnetic field. This experiment was the first observation of magnetic resonance. The first observation of an electron paramagnetic resonance peak was however made by Yevgeny Zavoisky’s discovery in 1945 [8], when he detected a radiofrequency absorption line from a $CuCl_2 \bullet 2H_2O$ sample. In the years immediately after this breakthrough, progress in the field was largely driven by the development of microwave technology for RADAR systems during World War II that made the components for a spectrometer cheaper. The earliest chemical applications of EPR involved studies of transition metal ions, while spectra of organic radicals were first recorded later, in 1952.

2.2 Instrumental set up

Before diving into the theoretical aspects of this technique is worth mentioning the main components of an EPR spectrometer to analyse their function and fully grasp how the system works, but before doing that, two general annotations are needed.

Firstly, among the various experimental modalities, continuous-wave EPR (CW-EPR) remains the most widely employed, and since this technique is also the basis of the investigations presented in this PhD work, the following discussion will primarily focus on CW-EPR, though more recent and complex experimental approaches in the field have been developed.

Secondly, it is useful to highlight the two main methodological approaches to EPR:

- **Spin-probe or spin-label method**: In this approach, the system under investigation is typically diamagnetic (EPR silent). A stable paramagnetic probe—such as a nitroxide radical—is introduced, enabling the study of the system through its interaction with the added paramagnetic species.
- **Direct investigation of paramagnetic centres**: Here, the technique is applied directly to species that inherently possess unpaired electrons, such as stable organic radicals or transition metal ions in oxidation states that allow at least one unpaired electron.

We can now analyse the main parts that make up an EPR instrument. Not all parts of the instrument will be described in full in this thesis, but only the main parts necessary to understand how the instrument works in its simplest form. For a more detailed explanation of how the instrument works and for a more detailed description, the reader is referred to the reference texts that were used to produce this discussion, which certainly describe the experimental set-up better and in greater depth [2], [9], [10], [11].

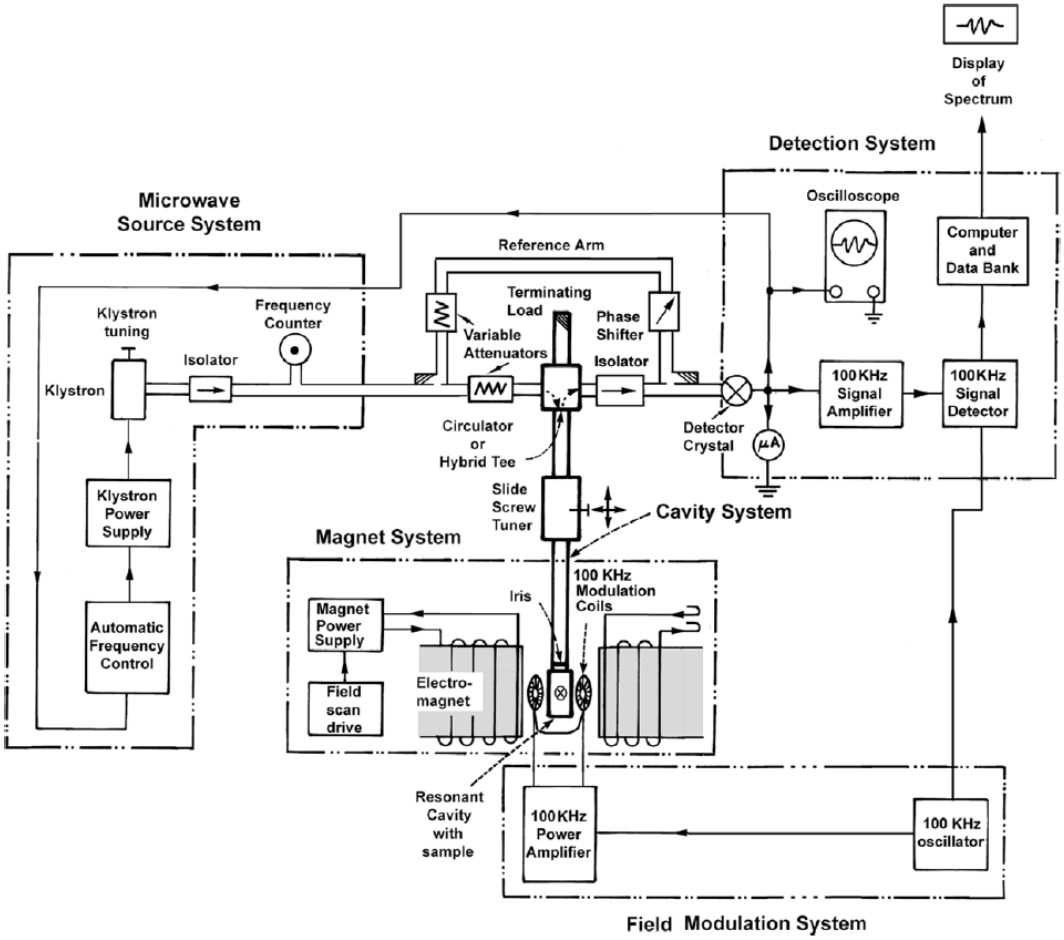

Fig. 2.1: Block diagram of a typical X-band continuous-wave (CW) 100KHz modulated, electron paramagnetic resonance (EPR) spectrometer [10]

Source. Most EPR spectrometers operate at a frequency of around 9.5 GHz, known as the X-band, which lies in the medium-frequency microwave region and corresponds to a wavelength of about 32 mm. Microwaves are typically generated using a klystron source, a vacuum tube recognized for its low-noise performance. The magnetic field B_1 arises from oscillations within a tuneable cavity. Frequencies in the range of 1–100 GHz are transmitted either through specialized coaxial cables or more commonly through waveguides. In conventional instruments, microwave power is applied to the sample continuously (continuous-wave EPR, or CW-EPR), whereas in some modern spectrometers, the power is delivered in pulsed mode.

The **Resonator** is usually considered the heart of the EPR spectrometer, and it's the region where the sample is contained. Even if nowadays also exists EPR systems where the resonator is missing and the instrument works in transmission, they are still a little slice of the whole EPR world. The idea behind this piece of instrument is basically the same of a resonator for acoustic waves like the pipes of an organ. All the waves interfere together inside the pipe and the one that are not submultiples of one dimension of the resonator die out due to destructive interference. The frequency at which one-half of a wavelength

corresponds to a cavity dimension is called the fundamental resonant frequency; this frequency increases with decreasing dimensions of the cavity. A cavity may be excited to produce more than one type of standing-wave pattern or resonant 'mode'. The energy density associated with a traveling wave (say, in a waveguide) is usually small; by comparison, considerable acoustical energy may be stored in the standing waves of a resonant cavity. One can readily observe acoustical resonance because the wavelengths of sound are in the range of a few centimetres to a few meters. The same phenomenon also occurs with electromagnetic waves. For microwaves, the wavelength is also typically of the order of centimetres (3 cm at X band). Hence the dimensions of a resonant cavity are convenient. The cavity walls are of highly conducting metal, and the effective electric current (associated with the electromagnetic waves in the cavity) flows within only a thin portion on the inner surface adjacent to this space (skin effect) [12]. The design and construction of the cavity is therefore crucial to select a priory the useful cavity mode, which are usually kept perpendicular to the external magnetic field B.

Magnetic Field. In magnetic resonance experiments, the static magnetic field B must be precisely controlled and highly stable, since fluctuations directly cause variations in the energy separation of spin states. The usual source of the static magnetic field B is an. This field should be stable and uniform over the sample volume, and field variations should be kept within ±1 mT to resolve very narrow EPR lines and to obtain the correct line shapes [13]. The direction of B in the cavity region between the pole caps is generally of no importance. Stability is achieved by energizing the magnet with a highly stable regulated power supply, which precision is mandatory for the success of a good experiment. The simplest procedure to monitor it is to place a Hall-effect probe, which gives an output voltage proportional to field B, at a fixed location in the gap. It should temperature-compensated to avoid drift with changing probe temperature. A feedback system adjusts the magnet current to maintain a fixed Hall-probe voltage.

Field Modulation. A serious disadvantage of the EPR spectrometer is the contribution of the noise components to the output signal. To overcome this issue, phase-sensitive amplitude detection technique is used via the application of small-amplitude sinusoidal magnetic-field modulation superimposed on the external field B. The effect of the modulation is depicted in Fig. 2.2. This technique allows

- the amplification of the EPR signal,
- elimination of most of the noise-contributing components,
- enhanced spectral resolution.

Modulation of the magnetic field B at the commonly used frequency of 100 kHz is achieved by placing small Helmholtz coils on each side of the cavity along the axis of the static field. The cavity walls in the

region of the modulation coils must consist of very thin conductive layers the cavity walls to allow penetration of the 100 kHz magnetic field, yet these layers must be thick (several skin depths) enough to retain the microwaves and must not vibrate. The magnitude of the modulated field at the sample may be measured by inserting a suitably calibrated pick-up coil into the appropriate region in the resonator. The magnetic field modulation and phase sensitive detection at the modulation frequency improves the signal to noise ration and stabilizes the baseline. However, this technique can cause line shape distortion. For instance, if the amplitude of the modulated field is small enough the spectrum measured looks is just a collection of the slopes of the absorption curve, therefore looks like the first derivative of the absorbance spectrum, however, if the amplitude is too high and therefore the approximation of the slope is bad, the shape of the absorption gets modified and distorted, risking the loss of information if the spectral line is of the same magnitude of the amplitude. Usually, the choice of amplitude is done for it to be 10% of the amplitude of the thinnest line.

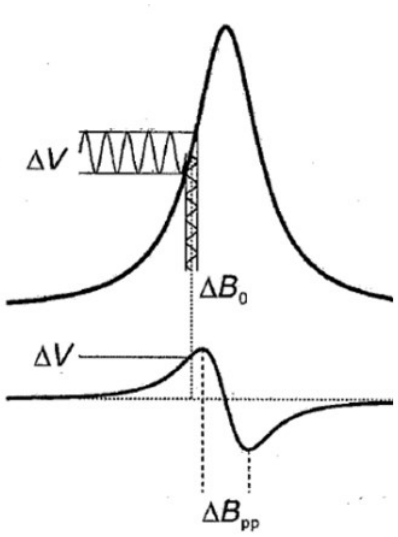

Fig. 2.2: Schematic representation of the field modulation of EPR signal

Detector. Various solid-state diodes are capable of detecting microwave energy. In an EPR spectrum, absorption lines appear when the energy difference between two levels matches (or nearly matches) the quantum energy hv of an incoming microwave photon. This absorption is revealed as a change in the detector current. Direct absorption detection is effective only for samples with unusually high concentrations of unpaired electrons, since noise spanning a wide frequency range can obscure the signal [10].

In a single-source EPR system, three key components transmit microwave power from the source to the resonator containing the sample: the isolator, the attenuator, and the circulator. Significant backward reflections of microwave energy from the system can cause serious perturbations in the source frequency. These reflections are minimized by the **isolator**, a non-reciprocal device—meaning its

behaviour differs for waves traveling forward versus backward. It allows microwave energy to pass in the forward direction while strongly attenuating any reflected power returning to the source. Modern spectrometers typically use three-port circulators as isolators, with one port terminated by a matched load, often a wedge that converts the radiation into heat.

The **attenuator** controls the microwave power reaching the sample. It contains an absorptive element, analogous to a neutral-density filter in optical absorption measurements, allowing precise adjustment of the incident power.

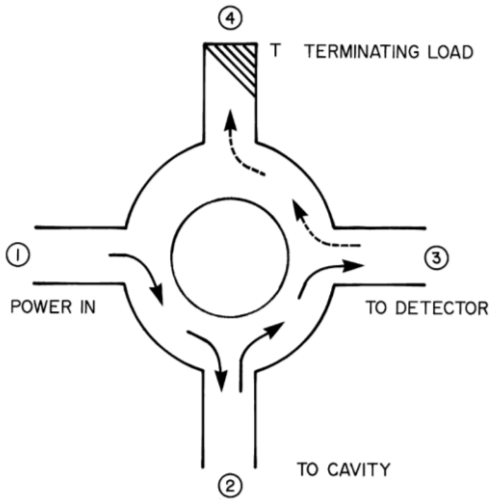

Fig. 2.3: Schematic representation of a circulator

A **circulator**, like an isolator, is a non-reciprocal device that directs microwave power to the resonator while simultaneously routing any power reflected from the cavity to the detector. The function of a four-port circulator is illustrated in Fig. 2.3. It is essentially composed of two three-port circulators combined into a single unit to enhance directional performance. A terminating load on the fourth port absorbs any power reflected from the detector arm. Since the operation of a circulator relies on a magnetic field, it is sensitive to stray fields; therefore, both circulators and isolators must be positioned away from the main magnet.

2.3 Theoretical background

The physical principles of this technique see the use of a magnetic field and electromagnetic radiation, in the microwave range, to observe the presence of unpaired electrons. For the theoretical background we chose a semi-classical description as it keeps the interpretation simple while keeping in consideration the quantum nature of the system.

The magnetic field strength leads to the separation of the electronic spin levels α (spin up, m_s = +1/2) and β (spin down, m_s = -1/2) through the Zeeman effect. By the splitting into two energy levels, an electronic transition can then occur by absorbing a photon hv that has the same energy as the energy gap generated by the Zeeman splitting of the levels. If we consider a free electron, the formula that describes this relation is:

$$h\nu = g\mu_B B \qquad [2.1]$$

Where μ_B is called the Bohr magneton and g is a "constant" called Lande's Factor, that for a free electron is 2.0023. This "constant" will be better described further in this work.

The instrument registers the spectra by keeping the microwave source fixed at a certain frequency (e.g. 9,45 GHz for X-Band spectrometers) and swiping the magnetic field. When the field intensity is such to generate a separation in the energy levels equal to the radiation energy, the transition occurs with the relative absorption of energy, and the correspondent peak can be recorded. The data that the instrument reads is the absorption of the photon, when it has the same energy as the energy gap.

However, the external magnetic field imposed by the electromagnet is not the only field the paramagnetic system experiences. If we consider a simple electron, in a semiclassical perspective it is a particle with a mass and a charge, which moves around an orbit, and therefore it will possess angular momentum L, defined as the function of a quantum number l, for which:

$$L = \sqrt{l(l+1)}\,\hbar \qquad [2.2]$$

Describing this moment in terms of a vector, it can be depicted by its projections along the lx, ly, lz axes. For the purposes of this system, the most interesting and useful projection will be the projection along z, which will only assume certain possible values, which depend on ml (magnetic quantum number) defined as between -l < ml < +l. Considering systems with d orbitals (and therefore l = 2), ml can be -2, -1, 0, 1, 2, as shown in Fig. 2.4.

$$L_z = \hbar m_l \qquad [2.3]$$

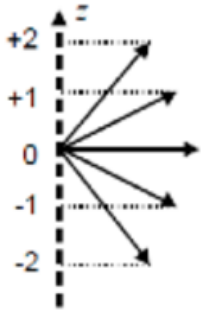

Fig. 2.4: possible orientation of m_l along z axes

The electron possesses also the spin angular momentum S, classically perceived as the rotation of the particle on its own axis and with the value ½ for an electron, defined similarly as the angular momentum was defined before:

$$|S| = \hbar\sqrt{S(S+1)} = \hbar\sqrt{\frac{3}{4}} \quad [2.4]$$

$$S_z = \hbar m_s \quad [2.5]$$

S_z being the projection of S along the z axes. This property will have the characteristic properties of the angular momentum and a spin quantum number, m_s, with values between $-S<m_s<+S$, and with the condition that $\Delta m_s = 1$. Consequently, the possible values of m_s are ± ½, thus spin up and spin down, or α and β.

Being the electron a charged particle with angular momentum, a magnetic spin moment μ_S will be generated, that can (classically speaking) be visualized as the magnetic moment generated by a small magnet. Therefore:

$$\mu_S = -g_e\frac{|e|\hbar}{2me}S = -g_e\mu_B S = -\gamma_e S \quad [2.6]$$

Defining μ_B as Bohr's magneton and γ_e as the electron's gyromagnetic factor. This magnetic moment is what actually interacts with the surrounding environment, generating couplings and interactions between electrons and the environment. In particular, the magnetic moment μ_S will interact with the external magnetic field B_0, generating a difference in energy between the spin levels. If we consider, by convention, a magnetic field directed along the z-axis, we will have a splitting of the levels only along the z-axis, generating two energy levels:

$$E_{ms} = g_e\mu_e m_s B_0 = \pm \tfrac{1}{2}\, g_e\mu_e B_0 \quad [2.7]$$

This energy difference is what was previously defined as the Zeeman effect, and it the fundamental principle of operation of EPR spectroscopy. However, the electron will also experience the presence of the chemical environment, thus an effective magnetic field B_{eff} will be experienced by the electron:

$$B_{eff} = B_0 + \delta B \quad [2.8]$$

where the term δB includes all the variations of the local magnetic field due to the interactions of the electron with the environment. Therefore, by uniting eq. [2.7] and [2.8], we find:

$$h\nu = g_e\mu_B(B_0 + \delta B) \quad [2.9]$$

which can be rewritten as

$$h\nu = (g_e + \delta g)\,\mu_B B_0 = g_{eff}\mu_B B_0 \quad [2.10]$$

where the g_{eff} holds all the information about the chemical environment of the electron we are looking at. Therefore, each unpaired electron will experience a different chemical environment, meaning it will also resonate at different magnetic fields, generating a shift in the position, which therefore produce a value of g which can be both bigger and smaller than the g_e = 2,0023. What is more, since g depends on the chemical environment, if the electron is in a non-spherically symmetric (or octahedral) geometry the g factor will also depend on the orientation of the sample in respect with the external B, making g a 3X3 tensor. The discrepancy between the electron value of g and the effective g value can be described as a first approximation due to the interaction of the electronic spin angular momentum S and orbital angular momentum L, resulting in the so-called Spin-Orbit interaction. Through the hypothesis that this interaction comports a minor correction compared to the Zeeman effect energy separation, the correspondent total Hamiltonian can be obtained considering second-order perturbation theory:

$$\mathcal{H} = g_e \mu_B BS + \mu_B BL + \lambda LS \qquad [2.11]$$

By resolving the equation using the perturbation theory, it can be shown that:

$$g_{ij} = g_e \delta_{ij} + 2\lambda \sum_{n=0} \frac{\langle 0|L_i|n\rangle\langle n|L_j|n\rangle}{E_n - E_o} \qquad [2.12]$$

Where δ_{ij} is the Kronecker delta which equals to 0 if i≠j and equals to 1 if i = j L_i and L_j are the components of the orbital angular momentum operator, 0 represents the ground state and n is the different excited states and E_0 and E_n are the energies of the ground state and the excited states respectively. The g tensor can therefore be written as:

$$\boldsymbol{g} = \begin{matrix} g_{xx} & g_{xy} & g_{xz} \\ g_{yx} & g_{yy} & g_{yz} \\ g_{zx} & g_{zy} & g_{zz} \end{matrix} \qquad [2.13]$$

And can be diagonalized via changing the reference system to just g_{xx}, g_{yy} and g_{zz}, and their relative values can give information about the geometry of the centre. When the system under analysis is in a solid, but with high symmetry (spherical or octahedral symmetry) or a liquid, the values of the g tensor are all equal and the system will respond uniquely to the external field, generating a single EPR signal with g:

$$g_{avg} = \frac{g_{xx} + g_{yy} + g_{zz}}{3} \qquad [2.14]$$

However, if the symmetry of the system is lower, the response of the sample will be different if the field B is oriented along the x, y or z axis. This therefore leads to different responses based on the orientation of the sample with respect to the field. The lower the symmetry, the greater the number of components of g with a different response, the greater the number of lines observed on the spectrum.

Before looking at the possible shapes of the spectrum, it is worth noting that the typical EPR solid state sample could be a single crystal, but more often is a polycrystalline material called powder, which is constituted by a large number of microcrystals randomly oriented, so that all the possible orientation of the crystal are equally probable. However, since the sample is solid, and therefore the centres do not have the ability to move like in a solution, the anisotropy of the various interactions influences the spectrum, and the resulting spectrum is an envelope of the single crystal spectra corresponding to all possible crystal orientations.

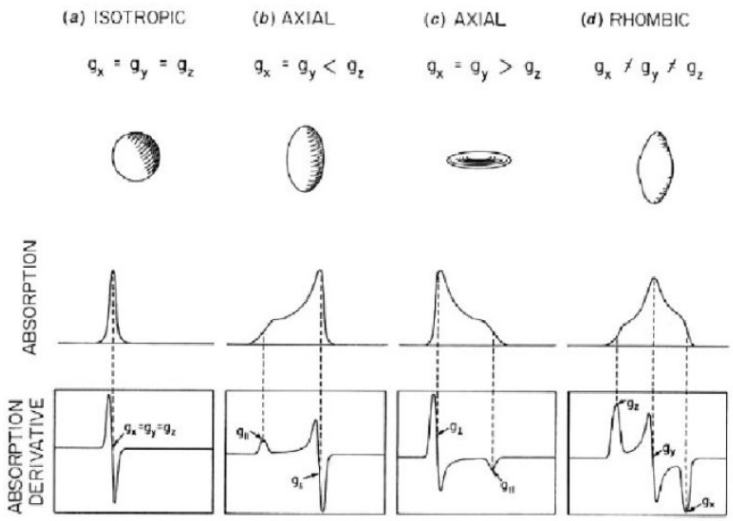

Fig. 2.5: Schematic representation of g tensors in the EPR spectra for systems with different geometries

2.3.1 Contribution to the Hamiltonian

Nonetheless, the Spin-Orbit interaction is not the only interaction that a generic electron experiences in a system and often is not even the most prominent one. Typical interactions of an electron can be included in a series of terms that can be expressed through the following total Hamiltonian:

$$\hat{\mathrm{H}} = -\gamma_e \hat{S} B_0 + \gamma_N \hat{I} B_0 + \hat{S}\boldsymbol{A}\hat{I} + \hat{S}\boldsymbol{D}\hat{S} + \hat{I}\boldsymbol{Q}\hat{I} \qquad [2.15]$$

where, the terms are in order called: electron Zeeman Interaction, Nuclear Zeeman Interaction, Hyperfine Interaction, Dipolar interaction and Quadrupolar Interaction. The spin-orbit interaction seems to not be present anymore just because for convention its influence is concentrated in the terms of g and D. For the discussion to be carried out in this dissertation, not all the terms will be completely expanded and resolved, but only the terms that have a noticeable impact in this thesis work will be tackled.

The second and third terms of the Hamiltonian are related to the nucleus of the atom on which the electron lies but as for the second term it is proportional to γ_N which is in turn proportional to g_N and μ_N.

However, this last term for nuclei is 10^3 times smaller than for electrons and therefore can be considered not influent on the overall energetic of the system. Nevertheless, the nucleus of an atom can deeply affect the shape of an EPR signal due to the third term $\hat{S}\boldsymbol{A}\hat{I}$ which introduces the term of hyperfine coupling. This term is in turn composed of dipole coupling and Fermi interaction. The latter is a purely quantum term and we will analyse it briefly later on, while the former is a term for which we can find a classical analogue. In particular, the hyperfine dipole interaction is the e^- - nucleus coupling, due to the interaction between two spins, described by the term $S \cdot A \cdot I$, which comes into play when the unpaired electron under consideration is located on a nucleus that has a non-zero nuclear magnetic moment. To understand what these elements are, we must consider the number of protons and neutrons, in particular:

- If the number of protons and the number of neutrons are equal, then the atom has zero nuclear spin and does not couple with unpaired electrons.
- If the number of protons is even and the number of neutrons is odd (or vice versa), then the nucleus has half-integer spin and couples with unpaired electrons.
-If the number of protons and the number of electrons are odd, then the nucleus has integer spin and couples with unpaired electrons.

Therefore, within the nuclei that couple with unpaired electrons, we find all those nuclei with nuclear spin other than zero, and in this category, we can find the common isotopes of elements (such as ^1H) or the less common isotopes of other elements (such as ^{13}C).

When an electron and a nucleus couple, they generate a multiplet of lines, i.e., the signal that should be a single peak at a certain B value is instead split into multiple peaks that remain symmetrically spaced from the B value at which the electron would resonate if it did not couple with the nucleus. In particular, the number of EPR lines observed will depend on the value of the nuclear spin in this way: number of lines = 2I + 1, where I is the nuclear spin. The number of lines thus obtained represents all possible permutations of nuclear and electron spin numbers.

The distance between lines deriving from the same signal is constant and is called A, the coupling constant, and while the multiplicity of the signal provides information on how many and, in a certain sense, which nuclei couple with the electron, the distance between the peaks, i.e. the coupling constant A, provides information on which peaks are linked to each other and, in a second analysis, on the geometry of the system. It is important to note, however, that since the hyperfine dipole interaction is an interaction that occurs between two particles with a specific position in space, when we consider a solid and not a rapidly moving system such as a liquid, this interaction will not necessarily be isotropic and identical in every direction, as in a paramagnetic centre with a non-spherical but distorted and asymmetrical coordination geometry. There will therefore be directions in which the interaction is

favoured and therefore greater, and others in which it is unfavoured and smaller. This leads us to conclude that the hyperfine dipole interaction will therefore be represented by a 3x3 tensor called tensor **T.** This classical term depends, as seen above, on the interaction between the nucleus and the electron density outside the nucleus, and will therefore scale classically with $1/r^3$. However, the hyperfine interaction does not depend solely on a classical term, but there is also a purely quantum term, called contact interaction, which describes the e^- - nucleus interaction, due to the non-zero probability that the electron is at a certain moment at zero distance from the nucleus, and therefore exactly on the nucleus [9]. However, this probability is not zero when the orbital is an s orbital, and therefore isotropic. This interaction is also known as isotropic hyperfine coupling and can be represented by a constant a_0, or a_{iso} with the following formula:

$$a_{iso} = \frac{8\pi}{3} g_e g_n \mu_e \mu_n |\Psi(0)|^2 \qquad [2.16]$$

Where g_e and μ_e are the constants introduced previously for electrons, and g_n μ_n are the analogues for nuclei. The term $|\Psi(0)|^2$, on the other hand, represents the square modulus of the wave function in (0,0,0), i.e. the probability that the electron wave function has coordinates (0,0,0), or the probability that the electron resides on the nucleus at a given moment [10].

The two terms of the hyperfine coupling can therefore be combined into a single operator **A** with matrix form:

$$A = A_0 \cdot I + T = A_0 \begin{pmatrix} 1 & 0 & 0 \\ 0 & 1 & 0 \\ 0 & 0 & 1 \end{pmatrix} + \begin{pmatrix} T_{xx} & T_{xy} & T_{xz} \\ T_{yx} & T_{yy} & T_{yz} \\ T_{zx} & T_{zy} & T_{zz} \end{pmatrix} \qquad [2.17]$$

Considering now the fourth correction term of the Hamiltonian, $\hat{S}\boldsymbol{D}\hat{S}$, it represents the e^--e^- coupling interaction that occurs when two or more electrons interact with each other. Considering two electrons, we can identify four possible spin combinations, which can be grouped into symmetric and antisymmetric functions. In particular, naming the first electron 1 and the second electron 2, we have:

Symmetric	**Antisymmetric**
$\alpha(1)\alpha(2)$	
$\frac{1}{\sqrt{2}}[\alpha(1)\beta(2) + \beta(1)\alpha(2)]$	$\frac{1}{\sqrt{2}}[\alpha(1)\beta(2) - \beta(1)\alpha(2)]$
$\beta(1)\beta(2)$	
Triplet state, $S = 1$	**Singlet state, $S = 0$**

We therefore define the triplet state as the three possible spin combinations that produce a total spin S = 1, and the singlet state as the only possible spin combination that produces a total spin S = 0. These states represent both the multiplicities and the possible arrangements of two electrons in a state. For example, if two electrons must occupy the same orbital, according to the Pauli principle, they must be

arranged in an antiparallel manner, obtaining a total spin S = 0 with multiplicity 1 (only one possible arrangement) and therefore a singlet state. Conversely, if I have two levels available, the two electrons can be arranged in three possible ways: both spin up, both spin down, one spin up and the other spin down (multiplicity 3 and therefore a triplet state) [14].

The first interaction that can occur between two electrons is called Electron-Exchange interaction represented by the spin Hamiltonian

$$\widehat{H}_{exc} = \sum_{ij} J_{ij} \hat{S}_{1i} \hat{S}_{2j} \qquad [2.18]$$

Where S1 and S2 are the electron-spin operators for the two electrons and J is a 3x3 matrix that takes into account the electric (Columbian) interaction between the electrons but not the electron-electron dipole interaction which is the second type of interaction that can occur between two electrons [15]. The composition of this interaction is not of easy understanding and discussion, and for the sake of this dissertation it is enough just to know it exists and is in turn made up of two different contribution, one isotropic and one anisotropic. While the electron exchange splits the states into singlet and triplet, there is another contribution that greatly affects the spectra of multiple electron systems which is the dipole-dipole interaction which can also remove the removal of degeneracy even when the external magnetic field is zero, the so called Zero Field Splitting (ZFS).

The e^--e^- dipole interaction is a classical dipole interaction to which correspond the following Hamiltonian:

$$\widehat{H_{ss}}(r) = \frac{\mu_0}{4\pi} \left(\frac{\hat{\mu}_1^T \hat{\mu}_2}{r^3} - \frac{3(\hat{\mu}_1^T \cdot r)(\hat{\mu}_2^T \cdot r)}{r^5}\right) \qquad [2.19]$$

Where r is the inter-electron vector. If we resolve the equation above by explicating μ and expand the equation, we can obtain:

$$\widehat{H}_{ss} = \hat{S}\boldsymbol{D}\hat{S} \qquad [2.20]$$

Where **D** is a 3x3 matrix where each term is dependent by the vector r and its projection on the x, y, z axes. **D** is a diagonalizable and traceless, and by convention its diagonalisation is done so that D_z is set to be the biggest of all the parameters and D_y to be the smallest. We can write that:

$$E_{dip} = (D_{xx} S_x^2 + D_{yy} S_y^2 + D_{zz} S_z^2) \qquad [2.21]$$

with

$$D_{xx} + D_{yy} + D_{zz} = 0 \qquad [2.22]$$

The dipole energy equation can therefore be rewritten using for convention two independent energy parameters, defined as:

$$D = -3/2D_{zz} \quad [2.23]$$

$$E = 1/2(D_{yy} - D_{xx}) \quad [2.24]$$

Therefore, we can rewrite the Hamiltonian as:

$$\widehat{H}_{ss} = D(\hat{S}_z^2 - \frac{1}{3}\hat{S}^2) + E(\hat{S}_y^2 + \hat{S}_x^2) \quad [2.25]$$

Where D is a term that, as before, depends on the inverse of the distance between the two interacting electrons cubed, while E is a measure of the deviation of the electron distribution from axial symmetry, and is therefore an anisotropy factor [81]. Therefore, the values of D and E strongly depend on the reference system and the choice of the axes, as seen in eq. [2.21] the convention is to choose the axes so that |D|/3 ≥ |E|, therefore often the sign of D and E are unknown, and the values are used as absolute quantities. However, often D and E are used in energy unit by defining them $\overline{\overline{D}}$ = D/hc and the same for E.

The effect of this interaction is to modify the spacing between the sublevels, generating two distinct lines in the EPR spectrum, whose shape describes the geometry of the system in terms of matrix D and matrix E.

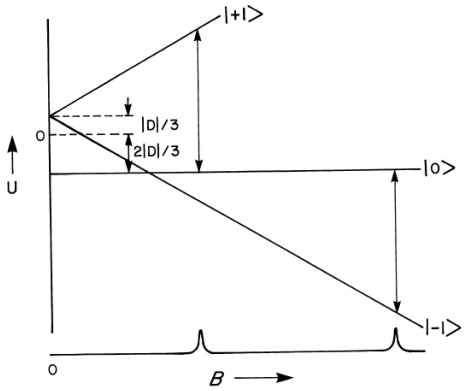

Fig. 2.6: Energy states as a function of applied magnetic field B for a system of spin S = 1 and B || Z, shown for D>0 and E=0. The two primary transitions of type ΔM_s=+1, are indicated for a constant-frequency spectrum.

The symmetry of the system, and therefore the values of E and D, change the energy states at B=0. For instance, if E≠0, and therefore the y and x components of D are different from one another, the geometry of the centre is rhombic, the degeneracy at B=0 is broken, and the corresponding energies vs B vary nonlinearly [14], [16].

It is worth noticing that the considerations made up till now consider a two-spin system, but this is not the only possibility, as when dealing with transition metals systems with more than two unpaired electrons are often found (e. g. Fe(III), Cr(III), Mn(II), etc). The discussion made is still valid, just the math a bit more complicated.

However, the matter does not end there. There are more terms that are included in the Hamiltonian and further modify its form, making it more complicated (e.g. or the presence of quadrupole spin systems, which introduce new interactions [11]). For the purposes of this dissertation, however, the addition of these terms are not necessary for understanding the results and would complicate the discussion.

2.4 EPR systems of interests

During the work of this PhD, EPR was employed mainly on inorganic solids composed of transition metals oxide and is therefore worthy spending few words on what to expect for the main systems analysed in this work.

Cu(II)

Cu(II) ions are one of the most studied EPR centre due to the fact that they have an external shell electronic configuration of $4s^0 3d^9$, and therefore in the outer most layer have an unpaired electron which can be useful in EPR monitoring. The peculiar property if copper lies also in the fact that when Cu^{2+} occurs within an octahedral site, due to the crystal field and elongation along the z axis (i.e. Jahn Teller effect), it loses the degeneration of the d orbitals, resulting in splitting of the energy levels and placement of the uncoupled electron in the $dx^2\text{-}y^2$ orbital.

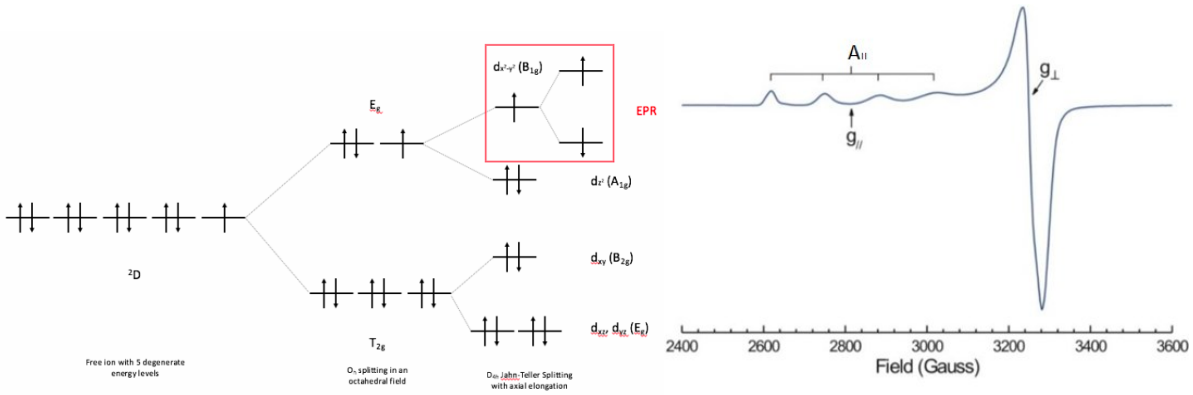

Fig. 2.7: schematic representation of Cu(II) electron configuration in an octahedral field and its typical EPR spectrum

The Jahn–Teller effect leads to a system with axial symmetry, which in turn causes anisotropy in the g-factor, giving rise to distinct parallel and perpendicular components. In addition, since copper nuclei have a spin of I=3/2, there is hyperfine coupling between the unpaired electron and the nucleus. This interaction produces a splitting into four lines (2I+1) along both the parallel and perpendicular directions. However, in practice, the hyperfine constant A associated with the perpendicular region is usually very small. As a result, the splitting often becomes unresolved and merges into the overall signal, while the parallel component typically appears as four distinct lines.

In 1974 Peisach and Blumberg [17] collected spectra of multiple copper containing proteins in order to analyse whether there is a relation between the structure of the copper site in the protein and the values of $A_{||}$ and $g_{||}$ of the relative EPR signal. What they were able to conclude is that by looking at the values of $A_{||}$ and $g_{||}$ one can understand the ligand neighbouring environment. Thanks to their pioneering work more recently R. A. Eichel [18], [19], constructed the same plot to find a correlation between $A_{||}$ and $g_{||}$ and the coordination of Cu ions in an oxide structure. In particular, the work done by Eichel helps to understand the number of oxygen vacancies that are close to the detectable Cu centre as well as its coordination when Cu ions are used as dopants inside an oxide (mainly a perovskite) lattice.

One last thing to point out when looking at Cu(II) EPR spectrum is that Cu atom has two different isotopes ^{63}Cu and ^{65}Cu with isotopic abundance of respectively 69% and 31%, and both centres have nuclear spin of 3/2, therefore each of them will present a different quadruplet of signals. Luckily though usually only the first (and sometimes the second) signal of the parallel part of the signal present the double resonances due to the two isotopes. The signals at higher field are usually broad enough so that the two components fuse together.

Fe(II) & Fe(III)

Iron has an electronic configuration [Ar] $4s^2$ $3d^6$, while its most commonly possible corresponding ionic species have the following configurations:

$$Fe^{2+}: [Ar]\ 4s^0\ 3d^6$$

$$Fe^{3+}: [Ar]\ 4s^0\ 3d^5$$

As a matter of fact, for the Fe^{2+} and Fe^{3+} ions the d-orbitals electrons can be in a high spin or a low spin configuration, as can be visualized for Fe^{3+} in Fig. 2.8, therefore giving rise to different possible EPR spectra. This filling of d-orbitals normally depends on two quantities: the crystal field splitting energy (Δ) and the pairing energy (P), where the first is the separation in the energy of the d-orbital and the latter is the energetic cost for having two electrons in the same orbital, which result in repulsion between electrons.

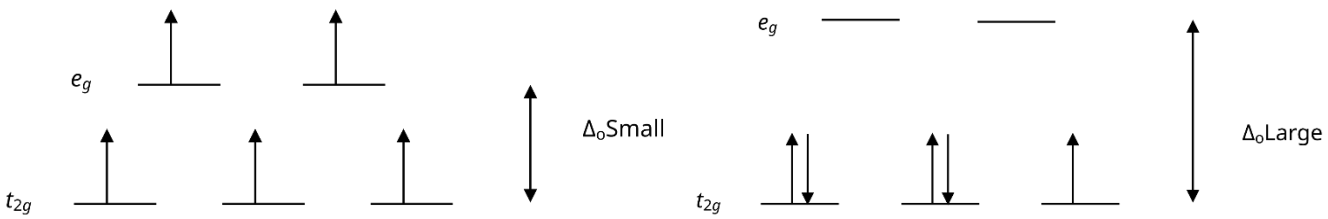

Figure 2.8: Configuration of a d^5 transition metal in an octahedral field with a) high spin state and b) low spin state.

Therefore, the specific configuration in transition metal complexes is determined by the relationship between crystal field splitting energy and electron pairing energy:

- **Low spin state:** in this case the crystal field splitting is bigger than the pairing energy thus electrons will prioritize filling the lower-energy orbitals completely before pairing.
- **High spin state:** contrary to before, the crystal field splitting is smaller than the pairing energy, meaning that electrons follow Hund's rule, for which the electrons distribute themselves across all available orbitals, maximizing their spin multiplicity, before pairing begins.

The relative magnitudes of crystal field splitting and pairing energy are fundamental parameters to know the spin state of the system, which influences the geometries of the complex as well. This explains why Fe^{2+}, even though is a d^6 element, could have both unpaired electrons (and thus being EPR-active) and paired electron (thus being diamagnetic and EPR-silent). If Fe(III) is present in the high spin state, it has a total spin S = 5/2, and the presence of this many electrons near each other generates ZFS, basically meaning that the resonances of each transition (5/2↔3/2; 3/2↔1/2; 1/2↔-1/2; -1/2↔-3/2; -3/2↔-5/2) will be scattered from low field (100 G) to high field producing spectral features of few thousands Gauss, thus leading to broad and complex spectra which often require low temperatures to resolve individual features.

In addition to ZFS, the spectrum may exhibit anisotropy of g due to deviations from perfect octahedral symmetry (e. g. tetrahedral or rhombic symmetry). The g-tensor may have distinct components corresponding to different orientations of the magnetic field relative to the molecular axis. This anisotropy reflects the influence of the ligand environment and can provide information about the geometry of the coordination site.

Furthermore, if the iron nucleus possesses a non-zero spin ^{57}Fe = 1/2 hyperfine interactions between the unpaired electron and the nuclear spin can occur. These interactions split the electronic resonance into multiple hyperfine lines, whose number and intensity depend on the nuclear spin and the hyperfine coupling constant. In practice, hyperfine splitting in Fe systems is often partially unresolved due to the

large ZFS and broad lines, but in some cases, careful measurement at low temperatures or in frozen solutions can reveal fine structure.

In summary, an EPR spectrum of an iron-containing system is expected to exhibit broad signals, often with anisotropic g-values, possible hyperfine splitting (depending on the isotope and resolution), and features influenced by zero-field splitting and dipolar interactions. By analysing the position, width, and splitting of these signals, one can extract valuable information about the oxidation state, spin state, and local geometry of the iron centres in the sample.

Ni(II) & Ni(III)

In the most common oxidation states, Ni is charged +2 and is therefore a d^8 system, is typically found with two unpaired electrons in the e_g orbitals. However, distortions of the field and lower symmetry of the coordination environment can lead to a further separation in energy of the e_g and therefore favour a S=0 system which is EPR silent [20], [21]. For the S=1 system of Ni EPR transitions are observed generally at low temperatures (e.g liquid helium temperature range) due to the fast relaxation rates of electrons on the excited state [22], and are often not observed due to the fact that ZFS parameters D and E are too large and common low field EPR (e. g. X and Q-band) are not enough to observe them [23].

Ni(I) and Ni(III) respectively d^9 and d^7 are also EPR active. Ni(I) only has one unpaired electron and therefore total spin of S=1/2, as well as Ni(III) in low spin configuration with S=1/2. This species usually give rise to an isotropic signal at g=2, but due to spin orbit coupling and low symmetry of the coordination environment can present anisotropy of g thus splitting the signal.

When inserted in an oxide like $SrTiO_3$ Ni is usually stable in the Ni(III) form and has an oxygen vacancy in the surroundings formed due to charge compensation (Ni(II) or Ni(III) are substituent of Ti(IV) and therefore generate V_o to compensate for the charge difference). This peculiar situation has been reported in literature since 1969 [24] and what the authors point out is that this conformation generates axially symmetric centres with g values around $g_{||} \approx 2.01\text{-}2.03$ and $g_{\perp} \approx 2.25\text{-}2.35$. The presence of Ni(III)-V_o couple, however, does not prevent the existence of other species as Ni(II) or other coordination of Ni(III).

ZnO

Contrary to the previous metal, Zn is the only that in its stable electronic configuration is a d^{10} element, and thus does not have any unpaired electrons, nor does the O^{2-} in the ZnO lattice. However, when the oxide is prepared, native defects (e.g. oxygen and zinc vacancies, interstitials etc.) appear in the

structure and since these defects can present unpaired electron they will be EPR active and monitorable.

Usually, two main signals are observed in ZnO EPR, one at g ≈ 1.95-1.96 and one at g ≈ 1.99-2.004, though the fair attribution of these signals is still being discussed in the literature there are different possible interpretations for these signals. Generally speaking, these signals are attributed by determining their depth in the band gap of the semiconductor (i. e. shallow or deep acceptor and donor defects), via the coupled use of EPR and of other techniques e. g. Photoluminescence (PL) measurements [25], irradiation of the sample [26] or gas contact in the EPR cavity [27].

Giamello et al. [25], for instance, via coupling EPR measurements with PL, and by exploiting irradiation measurements on bare ZnO particle, agreed with one attribution which is commonly found in literature [28], [29], where the defects at g = 1,96 is attributed to electrons present in the Conduction Band (or in a donor defect's band just below the latter) deriving from the ionization of unintentional dopants of the solid such as hydrogen or from ionization of interstitial Zn_i defects acting as shallow donors [30]. They also assigned the other defect, in the region 1.99–2.02, to paramagnetic zinc vacancy centres V_{Zn}^- due to the presence of V_{Zn} defects that act as deep acceptor of either one or two electrons (respectively V_{Zn}^- and V_{Zn}^{2-}).

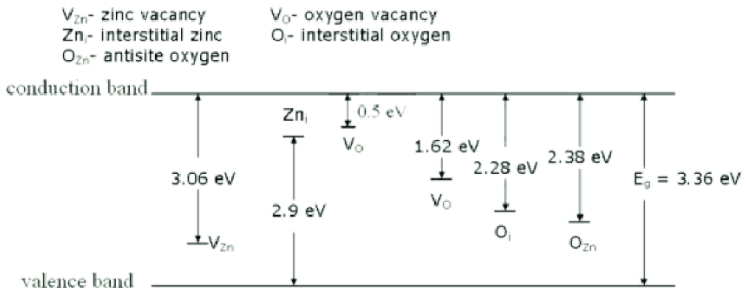

Fig. 2.9: Schematic representation of commonly found native defects in ZnO [31]

It is however worth citing also one theory that has been proposed few years ago about the explanation of these defects and that brought a new possible interpretation in the vast word of ZnO defects.

Core shell theory was introduced by Erdem et al. in 2011 [32] and then further described in other papers from the same authors [33], [34]. What they monitored in the first paper was the signal modification as a function the size of ZnO nanocrystals, and what they found out was that by reducing the size of the nanoparticles the defect at 1.96 decreased, while the defect at 2.004 increased. What the authors propose is that the defect at 2.004 are characteristic of $V_o^{\bullet}$ defects localised in the external shell of the ZnO NPs, while signal at 1.96 was attributed to deeper defects like V_{zn}^- localized in the core of the ZnO nanocrystal.

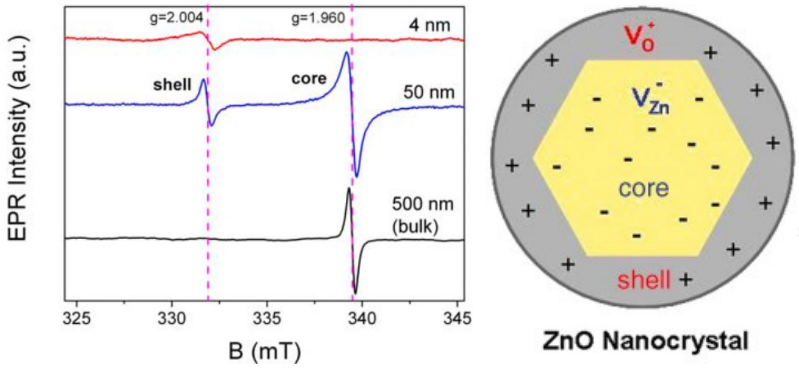

Fig. 2.10: Erdem et al. results of size dependent EPR signals (left); schematic representation of core shell model proposed by the authors (right) [32]

2.5 Conclusions

Electron Paramagnetic Resonance (EPR) spectroscopy represents one of the most powerful and selective techniques for the investigation of paramagnetic centres in solid materials. Through its ability to detect and characterise unpaired electrons, EPR provides direct insight into the local electronic and structural environment of transition metal ions and defect sites that often govern the reactivity and catalytic behaviour of oxide-based systems. Every measurement constitutes a unique spectroscopic fingerprint capable of distinguishing between chemically similar species, thereby making EPR a particularly valuable tool in heterogeneous catalysis, where multiple oxidation states and coordination environments may coexist. Using EPR not merely as a diagnostic tool, but as a quantitative probe of defect chemistry and transition-metal speciation in catalytic oxides could give some new information or shed novel light onto already known systems.

In conclusion, despite the complexity of this technique, both instrumentally and theoretically speaking, there are hardly any other techniques that provide such a deep and detailed insight into the investigated systems as EPR.

Bibliography

[1] G. Feher, “Sensitivity considerations in microwave paramagnetic resonance absorption techniques,” *The Bell System Technical Journal*, vol. 36, no. 2, pp. 449–484, 1957, doi: 10.1002/j.1538-7305.1957.tb02406.x.

[2] M. Chiesa and E. Giamello, “Electron Spin Resonance Spectroscopy,” in *Encyclopedia of Analytical Chemistry*, John Wiley & Sons, Ltd, 2000, pp. 1–34. doi: 10.1002/9780470027318.a6104.pub2.

[3] M. H. Belz, “XLV. The heterodyne beat method and some applications to physical measurements,” *The London, Edinburgh, and Dublin Philosophical Magazine and Journal of Science*, vol. 44, no. 261, pp. 479–501, Sep. 1922, doi: 10.1080/14786440908565190.

[4] C. G. Darwin, “Free motion in the wave mechanics,” *Proceedings of the Royal Society of London. Series A, Containing Papers of a Mathematical and Physical Character*, vol. 117, no. 776, pp. 258–293, Jan. 1927, doi: 10.1098/rspa.1927.0179.

[5] I. I. Rabi, “On the Process of Space Quantization,” *Physical Review*, vol. 49, no. 4, pp. 324–328, Feb. 1931, doi: 10.1103/PhysRev.49.324.

[6] E. Majorana, “Atomi orientati in campo magnetico variabile,” *Il Nuovo Cimento (1924-1942)*, vol. 9, no. 2, pp. 43–50, 1932, doi: 10.1007/BF02960953.

[7] I. I. Rabi, J. R. Zacharias, S. Millman, and P. Kusch, “A New Method of Measuring Nuclear Magnetic Moment,” *Physical Review*, vol. 53, no. 4, p. 318, Feb. 1938, doi: 10.1103/PhysRev.53.318.

[8] E Zavoisky, “Paramagnetic absorption in some salts in perpendicular magnetic fields,” *J. Phys.*, vol. 9, 1945.

[9] Marina Brustolon and Elio Giamello, *ELECTRON PARAMAGNETIC RESONANCE, A practitioner’s toolkit*, 1st ed. Wiley, 2009.

[10] J. A. Weil and J. R. Bolton, *Electron Paramagnetic Resonance, Elementary Theory and Practical Applications*, 1st ed. Wiley, 2007.

[11] A. Abragam and B. Bleaney, *Electron Paramagnetic Resonance of Transition Metal Ions*. 1970.

[12] G. S. Smith, “On the skin effect approximation,” *Am J Phys*, vol. 58, no. 10, pp. 996–1002, Oct. 1990, doi: 10.1119/1.16266.

[13] J. A. Burt, “Experimental and theoretical analysis of spurious EPR line features caused by field inhomogeneity,” *Journal of Magnetic Resonance (1969)*, vol. 37, no. 1, pp. 129–139, 1980, doi: https://doi.org/10.1016/0022-2364(80)90098-0.

[14] P. Atkins and R. Friedman, “MOLECULAR QUANTUM MECHANICS, FOURTH EDITION,” 2005.

[15] A. Bencini and D. Gatteschi, *EPR of exchange coupled systems*. Mineola, New York: Dover Publications, INC, 1990.

[16] R. F. Howe, “Electron paramagnetic resonance spectroscopy of catalytic surfaces,” 1993.

[17] J. Peisach and W. E. Blumberg, “Structural implications derived from the analysis of electron paramagnetic resonance spectra of natural and artificial copper proteins,” *Arch Biochem Biophys*, vol. 165, no. 2, pp. 691–708, 1974, doi: https://doi.org/10.1016/0003-9861(74)90298-7.

[18] R. A. Eichel *et al.*, “Defect structure and formation of defect complexes in Cu 2+-modified metal oxides derived from a spin-Hamiltonian parameter analysis,” *Mol Phys*, vol. 107, no. 19, pp. 1981–1986, Jun. 2009, doi: 10.1080/00268970903084920.

[19] R. A. Eichel, “Structural and dynamic properties of oxygen vacancies in perovskite oxides - Analysis of defect chemistry by modern multi-frequency and pulsed EPR techniques,” Jan. 14, 2011. doi: 10.1039/b918782k.

[20] R. D. Smyth *et al.*, “High- versus Low-Spin Ni2+ in Elongated Octahedral Environments: Sr2NiO2Cu2Se2, Sr2NiO2Cu2S2, and Sr2NiO2Cu2(Se1–xSx)2,” *Chemistry of Materials*, vol. 34, no. 21, pp. 9503–9516, Nov. 2022, doi: 10.1021/acs.chemmater.2c02002.

[21] H. Ohtsu and K. Tanaka, “Equilibrium of Low- and High-Spin States of Ni(II) Complexes Controlled by the Donor Ability of the Bidentate Ligands,” *Inorg Chem*, vol. 43, no. 9, pp. 3024–3030, May 2004, doi: 10.1021/ic035486+.

[22] K. Amrutha and V. Kathirvelu, “Interpretation of EPR and optical spectra of Ni(II) ions in crystalline lattices at ambient temperature,” *Magnetic Resonance in Chemistry*, vol. 60, no. 3, pp. 414–421, Mar. 2022, doi: https://doi.org/10.1002/mrc.5237.

[23] D. Maganas *et al.*, “Investigating Magnetostructural Correlations in the Pseudooctahedral trans-[NiII{(OPPh2)(EPPh2)N}2(sol)2] Complexes (E = S, Se; sol = DMF, THF) by Magnetometry, HFEPR, and ab Initio Quantum Chemistry,” *Inorg Chem*, vol. 51, no. 13, pp. 7218–7231, Jul. 2012, doi: 10.1021/ic300453y.

[24] K. A. Müller, W. Berlinger, and R. S. Rubins, “Observation of Two Charged States of a Nickel-Oxygen Vacancy Pair in SrTiO3 by Paramagnetic Resonance,” *Physical Review*, vol. 186, no. 2, pp. 361–371, Oct. 1969, doi: 10.1103/PhysRev.186.361.

[25] E. Cerrato, M. C. Paganini, and E. Giamello, “Photoactivity under visible light of defective ZnO investigated by EPR spectroscopy and photoluminescence,” *J Photochem Photobiol A Chem*, vol. 397, p. 112531, 2020, doi: https://doi.org/10.1016/j.jphotochem.2020.112531.

[26] E. Cerrato and M. C. Paganini, “Mechanism of visible photon absorption: unveiling of the C3N4–ZnO photoactive interface by means of EPR spectroscopy,” *Mater Adv*, vol. 1, no. 7, pp. 2357–2367, 2020, doi: 10.1039/D0MA00451K.

[27] M. D’Arienzo *et al.*, “Insight into the Influence of ZnO Defectivity on the Catalytic Generation of Environmentally Persistent Free Radicals in ZnO/SiO2 Systems,” *The Journal of Physical Chemistry C*, vol. 123, no. 35, pp. 21651–21661, Sep. 2019, doi: 10.1021/acs.jpcc.9b06900.

[28] D. M. Hofmann *et al.*, “Hydrogen: A Relevant Shallow Donor in Zinc Oxide,” *Phys Rev Lett*, vol. 88, no. 4, p. 45504, Jan. 2002, doi: 10.1103/PhysRevLett.88.045504.

[29] J. M. Smith and W. E. Vehse, “ESR of electron irradiated ZnO confirmation of the F+ center,” *Phys Lett A*, vol. 31, no. 3, pp. 147–148, 1970, doi: https://doi.org/10.1016/0375-9601(70)90199-4.

[30] A. Janotti and C. G. Van de Walle, “Native point defects in ZnO,” *Phys Rev B*, vol. 76, no. 16, p. 165202, Oct. 2007, doi: 10.1103/PhysRevB.76.165202.

[31] G. Valverde Aguilar, M. Jaime Fonseca, A. Mantilla Ramírez, and A. G. Juárez Gracia, “Photoluminescence Studies on ZnO Thin Films Obtained by Sol-Gel Method,” in *Recent Applications in Sol-Gel Synthesis*, U. Chandra, Ed., London: IntechOpen, 2017. doi: 10.5772/intechopen.68529.

[32] P. Jakes and E. Erdem, “Finite size effects in ZnO nanoparticles: An electron paramagnetic resonance (EPR) analysis,” *physica status solidi (RRL) – Rapid Research Letters*, vol. 5, no. 2, pp. 56–58, Feb. 2011, doi: https://doi.org/10.1002/pssr.201004450.

[33] E. Erdem, “Microwave power, temperature, atmospheric and light dependence of intrinsic defects in ZnO nanoparticles: A study of electron paramagnetic resonance (EPR) spectroscopy,” *J Alloys Compd*, vol. 605, pp. 34–44, 2014, doi: https://doi.org/10.1016/j.jallcom.2014.03.157.

[34] H. Kaftelen, K. Ocakoglu, R. Thomann, S. Tu, S. Weber, and E. Erdem, “EPR and photoluminescence spectroscopy studies on the defect structure of ZnO nanocrystals,” *Phys Rev B*, vol. 86, no. 1, p. 14113, Jul. 2012, doi: 10.1103/PhysRevB.86.014113.

Chapter 3
Exsolution of Cu from $SrTiO_3$

Index of the chapter

This chapter provides a comprehensively description of the materials, syntheses procedures, and characterization techniques used to investigate copper-doped $SrTiO_3$. A particular focus is given on monitoring the exsolution process and its reversibility, with emphasis on using EPR spectroscopy as unconventional technique to track the process and assess the material defect's structure. The copper-based system was selected as it is a model low-cost material for a variety of catalytic applications, including water–gas shift reaction, and CO_2 hydrogenation. Moreover, Cu (II) ions are paramagnetic, producing a distinctive signature in EPR spectra that depends on their local coordination environment, providing a sensitive probe for monitoring exsolution dynamics.

3.1 Introduction

Supported metal nanoparticles play a crucial role in catalysis due to their high surface area and reactivity, which allow for increased reaction rates and greater process efficiency [1]. Typically, these supported catalysts are synthesized via impregnation methods. However, this approach inherently produces weakly bound nanoparticles that can migrate across the substrate, leading to coalescence or sintering under high-temperature or long-term operation, ultimately causing catalyst deactivation [2]. Catalyst ageing can also occur through surface poisoning, where carbon or sulphur species deposit on the surface and diminish catalytic activity [3]. Since both sintering and poisoning are largely irreversible, recycling or replacing such catalysts remains a costly challenge [4].

These issues are particularly critical for perovskite oxides (ABO_3), a versatile class of materials extensively employed in photovoltaics, heterogeneous (photo)catalysis, and energy storage [5,6]. To address these challenges, a novel design strategy has emerged over the past decade. This method offers a relatively straightforward, single-step route to synthesize supported nanoparticles on perovskite oxide matrices [7–9]. Under oxidizing conditions, catalytic cations can be incorporated into the B-site of the perovskite lattice, and subsequent reduction promotes their partial exsolution, leading to the controlled formation of nanoparticles.

This process, commonly referred to as redox exsolution [10], was first demonstrated for Pd nanoparticles [11] and later extended to a wide range of noble and non-noble transition metals, including Ni, Co, Fe, Cu, Mn, and Pt, which has sparked significant interest within the scientific community [12].

A key feature of exsolved nanoparticles is their crystallographic alignment with the host lattice and their partial embedding ("socketing") within the oxide support. This configuration produces nanoparticles that are highly resistant to sintering and capable of redissolving back into the perovskite lattice under oxidizing conditions. The resulting reversibility enables catalyst regeneration through redox cycling, mitigating agglomeration and prolonging operational lifetime [13–15].

Additionally, the socketed geometry and strong lattice anchoring confer protection against common deactivation mechanisms, such as surface poisoning, sintering, and coalescence, thereby further enhancing catalyst durability [16].

$SrTiO_3$-based parent structures have been extensively employed for exsolution due to their high chemical stability and well-characterized defect chemistry [17,18]. Several factors have been identified as key drivers of exsolution in these materials, including composition [19], morphology [20], exposed crystallographic surfaces [13], and particularly, the degree of non-stoichiometry. As highlighted by Irvine et al., exsolution preferentially occurs at the surface of highly A-site-deficient perovskites (A/B < 1) [19].

Upon reduction of an A-site-deficient perovskite, oxygen vacancies ($V_O^{\bullet\bullet}$) are introduced. For instance, in $A_{1-\alpha}BO_{3-\delta}$ (where α represents the A-site deficiency and δ the number of oxygen atoms removed per formula unit), the generation of $V_O^{\bullet\bullet}$ destabilizes the perovskite lattice, locally promoting the spontaneous exsolution of B-site species as a mechanism to restore stoichiometry. Similarly, intentional doping with acceptor-type metal cations enhances this effect by generating additional $V_O^{\bullet\bullet}$, which act as preferential nucleation sites for the formation of exsolved nanoparticles [21].

Thus, engineering and monitoring the defect chemistry of the host oxide remains a major challenge, as it requires bridging nanoscale phenomena with the macroscopic manifestation of nanoparticle exsolution. To date, most studies have focused on screening exsolution in host oxides with tailored compositions and, consequently, varying degrees of non-stoichiometry [19]. Ex-situ imaging methods, such as conventional and high-resolution transmission electron microscopy (TEM) or scanning electron microscopy (SEM), have been extensively applied [22,23]. More advanced in-situ techniques, including X-ray diffraction (XRD) and X-ray absorption spectroscopy (XAS), often relying on synchrotron radiation, have also been employed [24,25]. Nevertheless, because the exsolution process itself can induce structural changes in the host oxide, such as Sr segregation [26] or additional defect formation [27,28], these methods inherently carry a degree of uncertainty in pinpointing the generation and evolution of point defects.

In this context, electron paramagnetic resonance (EPR) offers a sensitive spectroscopic approach to monitor the defect structure of transition-metal-doped perovskite oxides, providing insights into the coordination environment and aggregation state of exsolving metal ions [29]. EPR can also monitor dynamic processes involving oxygen and strontium vacancies within these materials [30]. Moreover, given that the detection limit of a standard X-band EPR setup is typically on the order of 10^{11} spins [31], well below the dopant concentrations relevant for exsolution (0.5–10.0 mol%) [32,33], this technique represents a powerful strategy to assess the reversibility of the exsolution process.

Previous studies on Cu-doped perovskites by Eichel et al. demonstrated the feasibility of identifying by EPR the coordination environments of metal centers within various perovskite lattices [30, 34, 35],

providing new insights into the potential monitoring of Cu centers during exsolution processes. Specifically, the authors tracked the changes in the coordination of Cu(II) centers by employing different parent oxide structures for Cu intercalation. The use of multiple host lattices enabled the investigation of several key parameters, such as bond covalency, bond length, and center geometry, and, combined with theoretical calculations, allowed the construction of a correlation map of $g_{||}$and $A_{||}$values as functions of Cu-centre coordination and the number of oxygen vacancies in their first coordination sphere. The resulting map (Fig. 3.1) effectively depicts Cu centers in various coordination states and with differing numbers of neighbouring oxygen atoms, represented in terms of $g_{||}$versus $A_{||}$.

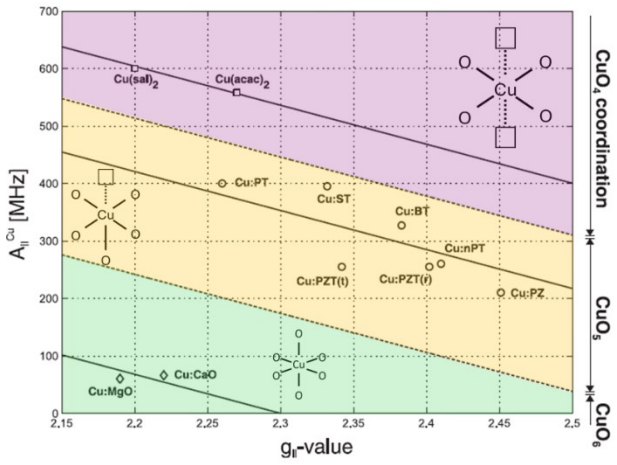

Fig. 3.1: map of Cu coordination and geometry as a function of $g_{||}$ and $A_{||}$. Modified from [30]

Additionally to EPR, UV–Vis diffuse reflectance spectroscopy (UV-DRS) serves as a valuable tool to characterize the local titanium environment and oxygen defectivity, as well as to provide further information on the coordination and aggregation of dopant metal species in the perovskite lattice [36]. For instance, Kittilstved et al. [37] employed UV-DRS coupled with EPR to monitor native point defects, such as oxygen vacancies or Ti^{3+} centres, in metal (Cr, Fe, Mn)-doped $SrTiO_3$, which are known to contribute to visible-light absorption in bulk $SrTiO_3$. Specifically, they suggested that the broad absorption feature extending from the visible to near-infrared region in Cr-doped $SrTiO_3$ arises from electronic transitions involving different oxygen vacancy species (i.e. V_O^X, $V_O^\bullet$ and $V_O^{\bullet\bullet}$) formed during synthesis and that the broad transition in the IR region is ascribable to Ti^{3+} centres. Moreover, they also monitored the modifications of the metals during reduction and oxidation conditions both in terms of UV-DRS spectra and EPR spectra. They foun out that an EPR signal associated with Ti^{3+} centres appears only after strong reduction conditions and is not easily re-oxidized during subsequent oxidative treatments. Similar behaviour has also been observed in $SrTiO_3$ after vacuum annealing.

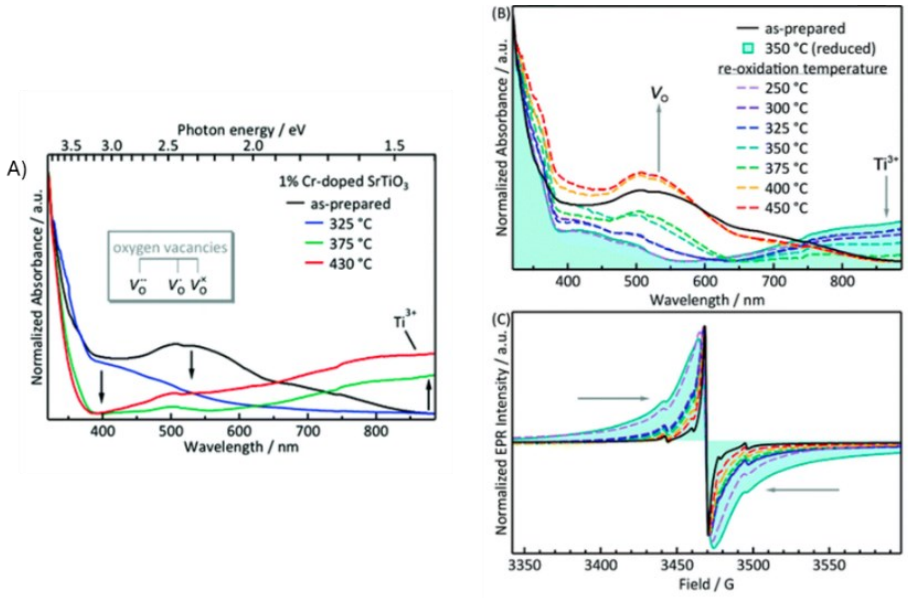

Fig. 3.2: UV-DRS spectra of Cr:STO A) at different reduction temperatures; B) after reoxidation of the samples; C) EPR spectra of reoxidized Cr:STO [37]

Despite the potential of EPR and UV–Vis diffuse reflectance spectroscopy (UV-DRS) to monitor changes in the electronic structure of both intrinsic defects and extrinsic dopants in perovskite materials, to the best of the author knowledge, no studies have yet employed these techniques to track metal exsolution in doped $SrTiO_3$ systems.

In this context, the present chapter focuses on the monitoring of surface transformation and defect evolution of Cu-doped $SrTiO_3$ during metallic copper exsolution, with particular emphasis on the application of UV-DRS and EPR measurements [34, 35, 38–41]. Specifically, A-site-deficient perovskite oxides of the type $Sr_{0,95}Ti_{1-\alpha}Cu_{\alpha}O_{3-\delta}$ (α = 0, 0.005, 0.05, 0.15) were successfully synthesized via a tailored sol–gel approach, and surface decoration with metallic copper nanoparticles was achieved through exsolution.

A multi-technique approach combining temperature-programmed reduction (TPR), X-ray absorption spectroscopy (XAS), X-ray photoelectron spectroscopy (XPS), and high-resolution transmission electron microscopy (HR-TEM) was employed to investigate the exsolution of Cu species. Notably, these well-established techniques were complemented with unconventional methods like EPR and UV–Vis diffuse reflectance spectroscopy (UV-DRS) which proved to be original and effective strategies for gaining deeper insights into the phenomenon. These techniques allowed direct monitoring of changes in the inner-sphere of copper coordination and the evolution of oxygen and oxygen defects during the exsolution process. The results not only revealed a heterogeneous chemical environment for the exsolvable species and more complex behavior than initially anticipated but also provide a foundation for a novel methodological approach for more effective evaluation of exsolution in doped perovskite materials.

3.2 Materials and methods

3.2.1Materials

Strontium nitrate (99%, Acros Organics), titanium (IV) isopropoxide (97%, Alfa Aesar), copper (II) acetate (98%, Alfa Aesar), anhydrous citric acid (99.6%, Acros Organics), glycerol (99%, Alfa Aesar), and glacial acetic acid (99.7%, Fischer Scientific) were used as received without further purification.

3.2.2 Synthesis

A modified Pechini synthesis [42] was used for the preparation of the $Sr_{0.9}Ti_{1-\alpha}Cu_{\alpha}O_{3\pm\delta}$ (Cu-STO) perovskite nanoparticles. Instead of the conventionally used ethylene glycol, glycerol was selected as the polyol, due to its better chelating and cross-linking ability [42, 43]. In a typical synthesis, titanium(IV) isopropoxide ($Ti(OCH(CH_3)_2)_4$) was dissolved in 15 mL of glycerol and stirred at room temperature for 60 minutes. Subsequently, 7.82 g of citric acid was added, and the mixture was heated to 60°C in an oil bath and stirred for an additional 60 minutes. $Sr(NO_3)_2$ and $Cu(CO_2CH_3)_2$ were then dissolved in 1–2 mL of water and added consecutively to the titanium solution at 60-minute intervals under continuous stirring. The final molar ratio of total metal cations to glycerol to citric acid was set to 1:8:33.3. After 2 more hours of stirring, the solution temperature was raised to 130°C and maintained for 2 hours to promote the polycondensation reaction between glycerol and citric acid, resulting in the formation of a sticky polyester gel.

The gel precursor was then calcined in a muffle furnace at 400°C for 2 hours, followed by 900°C for 2 hours with a ramp rate of 2°C/min. The final perovskite powders were labeled xCu-STO, where x corresponds to the nominal molar percentage of Cu dopant in the B-site.

3.2.3 Exsolution procedure

Exolution

Exsolution/reduction treatments were carried out using a U-shaped quartz tube filled with 80 mg of each sample. 5% H_2/Ar was chosen as the reducing gas, and the flow rate was set at 20 mL/min. A ramping rate of 10 °C min^{-1} was employed to reach the final temperatures of 200°C, 400°C, 600°C, 800°C or 900°C with a dwell time of 1 h. Samples which underwent the reduction treatment at 900°C were labelled as *x*Cu-STO_r, where r stands for the reducing procedure.

Reoxidation process

The re-oxidation process was operated by putting the sample in a round bottom quartz tube inserted in a tubular oven, under O_2 flow of around 100 ml/min. The process was operated at a temperature of 50°C

higher than the reduction temperature and were kept at this temperature for 2 hours to allow the complete reoxidation and redispersion of the metal in the lattice. Samples which underwent re-oxidation at 950°C were labelled as *x*Cu-STO_ox, where ox stands for the re-oxidation treatment.

3.2.4 Characterization

Powder X-ray Diffraction (PXRD) patterns were recorded using a Rigaku Miniflex 600 diffractometer with a Cu Kα source (40 kV, 15 mA). Data were collected over the 2θ range of 20–90°, with a step size of 0.01° and an angular velocity of 3.0° min^{-1}. Patterns were compared with reference data from the ICDD database using Rigaku PDXL-2 software. Mean crystallite sizes were estimated from the full width at half-maximum (FWHM) of the most intense reflection using the Scherrer equation.

Inductively Coupled Plasma Optical Emission Spectroscopy (ICP-OES) was employed to detect the concentrations of Sr, Ti, and Cu in the powders using an Optima 7000 DV (Perkin Elmer, MA, USA).

Temperature-Programmed Reduction (H_2-TPR) experiments were performed with a vertical oven with a U-shaped quartz vessel inserted. Approximately 100 mg of catalyst was pretreated under a 5% H_2/Ar stream (20 mL min^{-1}) at room temperature for 2 h. The sample was then heated to 120 °C at 10 °C min^{-1} and held for 1h, followed by heating to 950 °C at the same rate with a second 1 h isotherm. H_2 consumption and H_2O production was monitored using a Mass spectrometer.

UV-Diffuse Reflectance Spectroscopy (UV–Vis DRS) spectra were collected over 300–1400 nm using a PerkinElmer Lambda 1050+ UV/Vis/NIR spectrophotometer equipped with a 10 cm integrating sphere. Measurements were performed on powdered samples as-prepared, after thermal reduction at each target temperature, and after re-oxidation at 950 °C.

X-ray Photoelectron Spectroscopy (XPS) was used to analyse the surface chemical composition on powder samples mounted on UHV-compatible carbon tape. The reduced 5Cu-STO_r sample (900 °C) was handled under nitrogen to minimize atmospheric oxidation. Spectra were acquired under ultrahigh vacuum (~5 × 10^{-10} mbar) at room temperature using a Mg Kα source (hv = 1253.6 eV) and a hemispherical analyzer (120 mm; total energy resolution ~0.8 eV). Binding energies were calibrated to the Ti $2p_{3/2}$ peak of STO at 458.3 eV [44]. Survey scans (0–1100 eV) and high-resolution scans for O 1s, C 1s, Sr 3d, Ti 2p, and Cu 2p were recorded. Spectra were fitted using an integral background and Voigt functions to account for different oxidation states and chemical environments. Atomic ratios were calculated from peak areas and instrumental sensitivity factors.

High-resolution transmission electron microscopy (HRTEM) was performed on a ThermoFisher Talos F200X G2 microscope operated at 200 kV, with a resolution of 4096 × 4096 pixels and without the use of objective apertures. Energy dispersive X-ray spectroscopy (EDX) maps were acquired using Super X spectrometers equipped with 30 mm^2 silicon drift detectors and a collection angle of 0.7 sr.

X-ray absorption spectra (XAS) at the Cu K-edge (ECu = 8979 eV) were collected at the P64 beamline of the Deutsches Elektronen Synchrotron (DESY, Hamburg, Germany) [45]. A Si(111) double-crystal monochromator was employed to perform the energy scans around the Cu absorption edge. The XAFS spectra were recorded in fluorescence mode using gas ionization chambers to monitor the photon intensities before and after the samples. For the measurements, the powders were diluted in cellulose, pressed into pellets of about 28 μm thickness, and sealed with Kapton tape prior to insertion in the beam path. Normalization of the obtained XAFS data was carried out in Athena using the AUBACK algorithm for pre-edge and post-edge background subtraction [46].

EPR measurements were carried out on a Bruker EMX spectrometer operating at X-band frequency (9,43 GHz), equipped with an Oxford cryostat for temperature control in the 4–298 K range. A custom-built setup was employed, allowing the sample, placed directly in the EPR tube, to be heated and connected to both a high-vacuum system and a controlled gas feed (Ar/H_2 95/5 vol% or O2), enabling experiments under reducing or oxidizing conditions. Spectra were recorded at microwave powers between 5 and 63 mW, under vacuum ($p < 10^{-5}$ mbar), and at 130 K on both as-prepared powders and samples subjected to thermal treatments at 200, 400, 600, 800, and 900 °C in Ar/H2. To assess the reversibility of the process, additional measurements were performed after re-oxidation in O2 at 950°C.

3.3 Results and discussion

3.3.1 Structural and morphological characterization of the oxide support

The crystalline phase structures of the as-prepared materials were assessed by PXRD patterns and summarized in Fig. 3.3.

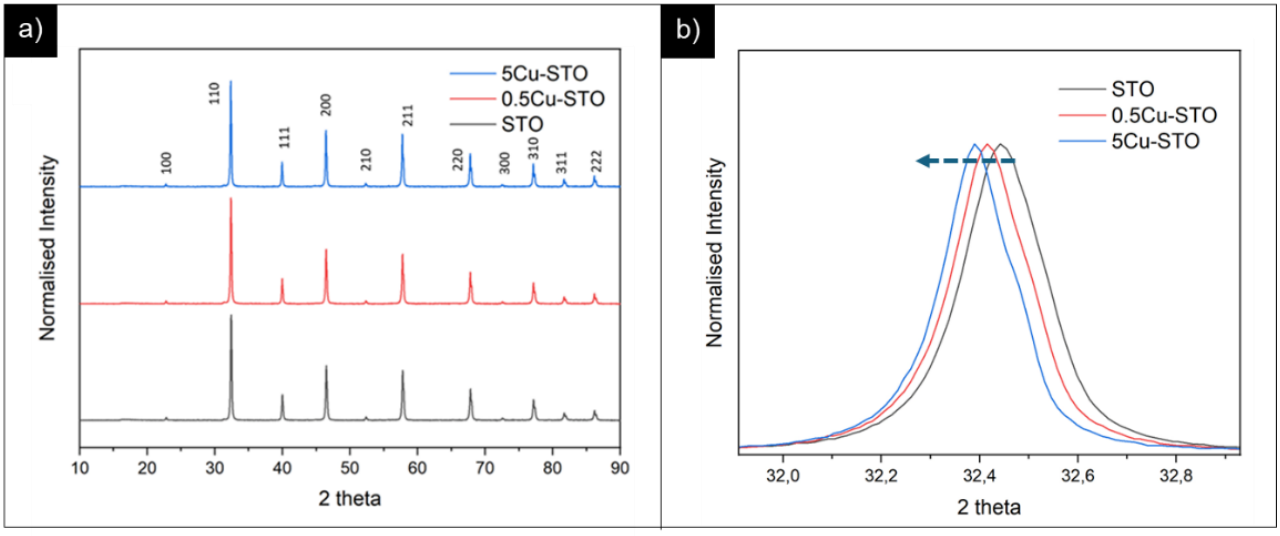

Fig. 3.3: a) PXRD patterns of pristine STO and of copper doped perovskite parental structures, b) Highlight on main reflection shift before and after copper doping.

All samples exhibit diffraction patterns consistent with the cubic $Pm\bar{3}m$ structure of $SrTiO_3$ perovskite oxide, with no evidence of secondary phase segregation. Notably, the diffraction peaks of the doped samples are slightly shifted toward lower angles compared with pristine $SrTiO_3$, indicating an expansion of the unit cell due to the incorporation of larger Cu^{2+} ions into the smaller Ti^{4+} lattice sites (Cu^{2+} = 0.73 Å > Ti^{4+} = 0.61 Å) [47]. Quantitative analysis of the PXRD data, via Rietveld refinement confirmed this trend, showing an increase of the lattice parameter *a* from 3.904 Å for pristine STO to 3.910 Å for 5Cu-STO. These results demonstrate that Cu doping into the $SrTiO_3$ lattice was successfully achieved.

To further investigate the oxidation state and coordination of Cu, X-ray absorption spectroscopy (XAS) measurements were performed around the Cu K-edge (E = 8979 eV) on as-prepared 0.5Cu-STO and 5Cu-STO samples (Fig. 3.4). For 0.5Cu-STO, the absorption edge closely matches that of CuO, confirming that Cu is predominantly present as Cu(II). In contrast, 5Cu-STO shows a noticeable blue shift of the edge, indicating that the average Cu oxidation state is slightly higher than +2. The overall shape of the XANES spectra for both doped samples is consistent with previous reports on Cu-doped $SrTiO_3$ [48]. However, a detailed comparison with reference spectra suggests that Cu does not completely substitute Ti in the perovskite lattice, and minor impurity phases are present. Specifically, the pre-edge feature at 8983 eV in 0.5Cu-STO reveals traces of Cu_2O, while the pronounced shoulder at 8987 eV in 5Cu-STO is indicative of residual CuO.

Further insights were obtained from Fourier-transformed EXAFS analysis (not shown). The data for both 0.5Cu-STO and 5Cu-STO can be fitted with a single coordination shell, giving a Cu–O bond distance of ~1.95 Å, in agreement with Cu–O bonds in CuO. However, the coordination number is significantly reduced, with values of 1.85 for 0.5Cu-STO and 3.45 for 5Cu-STO, compared to the expected 4. This reduction suggests the presence of substitutional copper species ($Cu_{Ti}^{2'}$ or $Cu_{Ti}^{3'}$) associated with one or more neighbouring oxygen vacancies ($V_O^{\bullet\bullet}$).

SEM imaging of 0.5Cu-STO and 5Cu-STO are reported in Fig. 3.4b-c. 0.5Cu-STO display grains of around couple of hundreds of nm, while larger particles (length ranging from ~200 to ~400 nm) were detectable for 5Cu-STO powders.

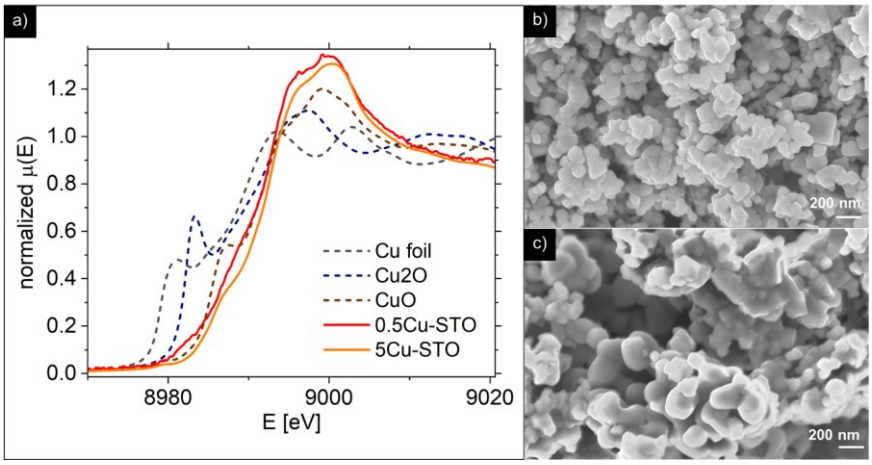

Fig. 3.4: a) X-ray absorption spectra; b-c) SEM images of the 0.5Cu-STO and 5Cu-STO parental structures, respectively.

3.3.2 Monitoring copper exsolution from $SrTiO_3$

The exsolution process was initially monitored by mass spectrometry to track the reduction behavior of the materials during high-temperature hydrogen treatment. Specifically, the evolution of the water signal was followed (Fig. 3.5a), as it directly reflects the release of lattice oxygen and, consequently, the stepwise reduction of copper ions according to the following reaction

$H_2 + O^{2-} \rightarrow H_2O + 2e^-$

$Cu^{2+}\ e^- \rightarrow Cu^+$

$Cu^+\ e^- \rightarrow Cu^0$

For reference, before measuring the doped STO samples, undoped $SrTiO_3$ and a physical mixture of CuO (5 mol%) with commercial alumina were first analyzed as control systems. All samples exhibited a pronounced water desorption during the isothermal treatment at 120 °C, which can be attributed to the release of adsorbed environmental moisture.

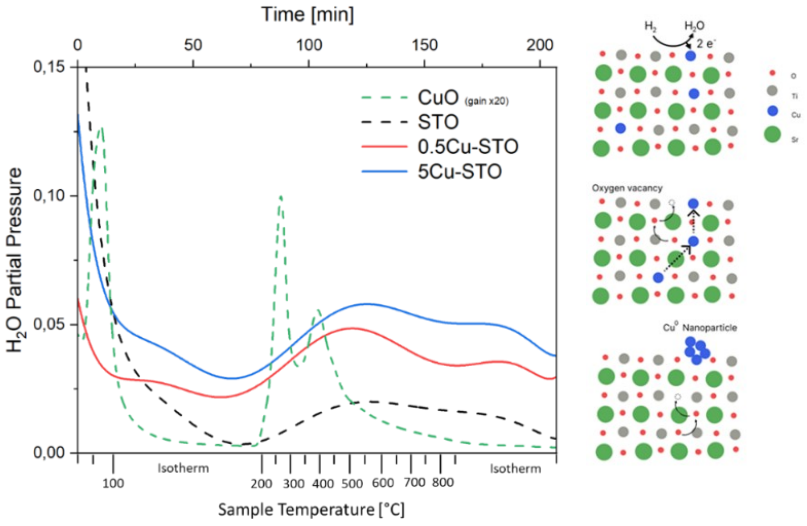

Fig. 3.5: a) Water evolution during exsolution from mass spectrometry for Cu-STO powders, CuO-alumina and bare STO reference samples. b) Schematical representation of Cu exsolution from $SrTiO_3$.

The H_2-TPR profile of the reference CuO sample exhibits two main peaks at approximately 270°C and 420°C, corresponding to the reduction of Cu^{2+} species in distinct chemical environments. Literature reports generally indicate that CuO undergoes a first reduction from Cu(II) to Cu(I) between 210 and 270 °C, followed by a second reduction from Cu(I) to metallic Cu at higher temperatures [49,50].

For the Cu-STO materials, two broad features are observed over the temperature range of 250–870 °C. Comparison with the CuO reference suggests that the first main signal arises from surface Cu species with varying coordination environments, reflecting different reduction tendencies. The second shoulder, appearing during the isothermal step at 870 °C, is likely associated with the release of lattice oxygen from the perovskite matrix [51]. Interestingly, a similar reduction pattern is observed for the bare A-site-deficient undoped STO, where the lower-temperature signal (250–600 °C) corresponds to oxygen release from the surface, while the high-temperature feature at 870 °C reflects lattice oxygen evolution, likely as part of the perovskite's attempt to restore stoichiometry.

The reduction behavior of the copper species was further investigated using XAS (Fig. 3.6). After the reduction treatments, both 0.5Cu-STO and 5Cu-STO exhibit shifts of the spectral half-maximum positions toward lower energies, indicating that the Cu dopants in both samples are partially reduced to Cu^+ or even to metallic Cu. Upon re-oxidation in O_2 at 950 °C, 0.5Cu-STO (Fig. 4.4a) displays only a slight shift relative to the as-prepared sample, suggesting that the exsolved Cu is not easily re-oxidized, likely because reduction also occurs within the bulk of the $SrTiO_3$ matrix [25,52]. In contrast, for re-oxidized 5Cu-STO, the XANES spectrum (Fig. 3.6b) closely matches that of the as-prepared sample, indicating that the exsolution process in this material is largely reversible and predominantly occurs at the surface.

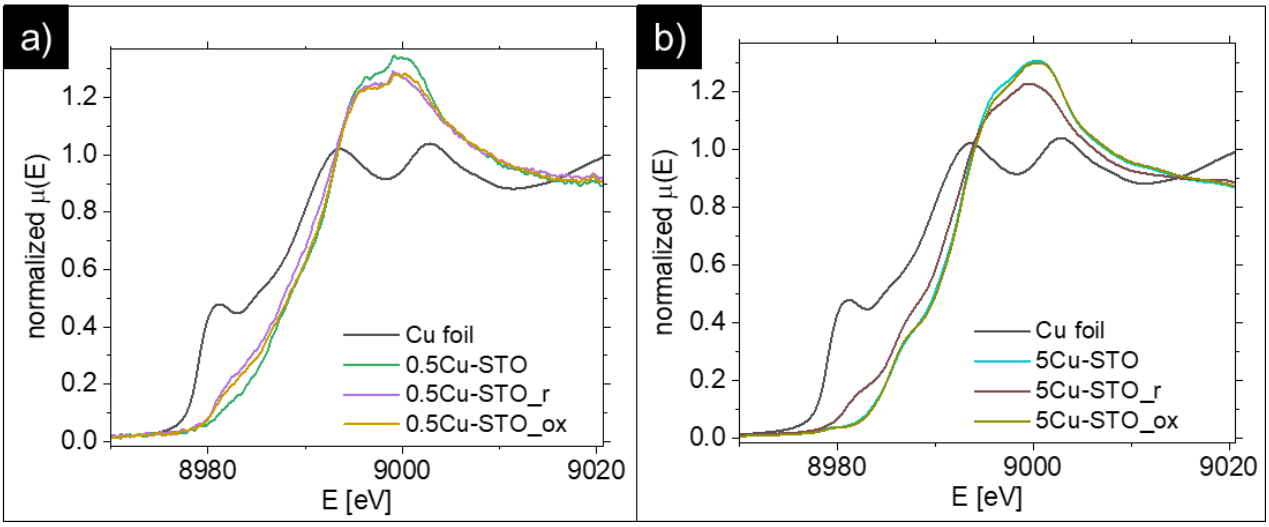

Fig. 3.6: Comparison of the XANES spectra of metallic Cu foil and a) 0.5Cu-STO and b) 5Cu-STO before and after reduction or re-oxidation.

During reduction, the Cu dopants in the as-prepared samples are partially converted to Cu^+ or metallic Cu. Quantitative analysis was performed by fitting the XANES spectra using a linear combination of the as-prepared sample, metallic Cu, Cu_2O, and CuO reference spectra. The results from the best fits are summarized in Table 4.1. For 0.5Cu-STO, approximately 71% of the Cu remains in the as-prepared state after reduction, while 9% is reduced to metallic Cu and 13.4% to Cu_2O. In 5Cu-STO, a similar trend is observed, but with a higher fraction of metallic Cu relative to Cu_2O. Upon re-oxidation, 0.5Cu-STO shows only slight changes in the fractions of metallic Cu, Cu_2O, and CuO, whereas in 5Cu-STO about 95% of Cu returns to the as-prepared state, with only ~6% remaining as CuO. These results indicate that 5Cu-STO is more readily reduced and re-oxidized than 0.5Cu-STO.

EXAFS analysis (not shown) corroborates these findings, confirming that Cu in as-prepared 0.5Cu-STO, 5Cu-STO, and re-oxidized 5Cu-STO is in the Cu^{2+} state, while reduction partially converts it to Cu^+. Consistent with XANES results, 0.5Cu-STO shows incomplete re-oxidation compared to 5Cu-STO. The Cu–Cu distances could not be determined from EXAFS due to insufficient data quality for reliable fitting.

Table 3.1: Comparison of the relative composition of the 0.5Cu-STO and 5Cu-STO after reduction and re-oxidation from XANES fitting.

Sample	xCu-STO	Metallic Cu	Cu_2O	CuO
0.5Cu-STO_ap	1.000	/	/	/
0.5Cu-STO_r	0.712	0.090	0.134	0.064
0.5Cu-STO_ox	0.816	0.070	0.077	0.037
5Cu-STO_ap	1.000	/	/	/
5Cu-STO_r	0.686	0.131	0.090	0.093
5Cu-STO_ox	0.938	0.000	0.000	0.062

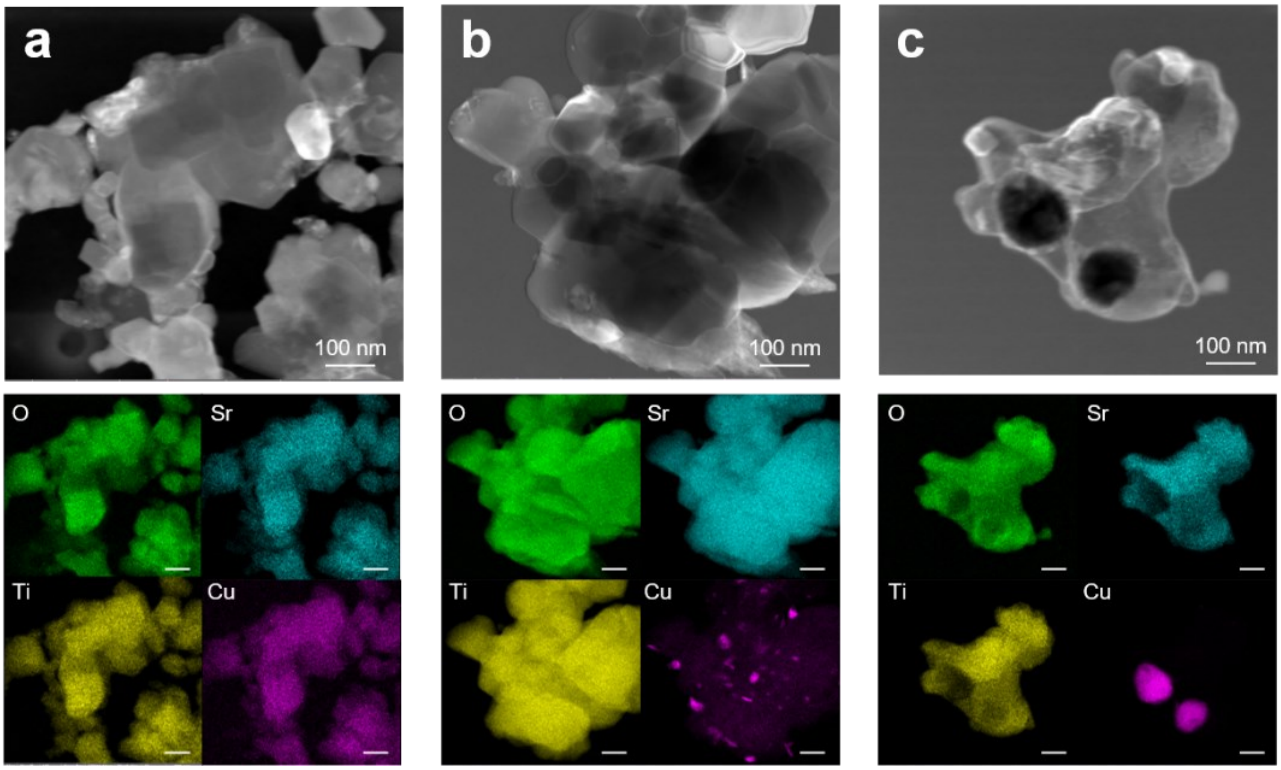

Fig. 3.7: TEM images and corresponding EDX elemental maps of 5Cu-STO powders: a) as prepared and after exsolution at b) 600 and c) 900 °C.

TEM-EDX characterization was employed to monitor the morphological evolution of Cu-STO powders during the exsolution process. HRTEM images and EDX elemental maps of the 5Cu-STO sample before and after thermal reduction in H_2/Ar at 600 °C and 900 °C are shown in Fig. 3.7. The pristine sample exhibits irregular aggregates of cubic-like nanoparticles a few hundred nanometers in size, with EDX mapping confirming a homogeneous distribution of all elements, including the Cu dopant, throughout the matrix (Fig. 3.7a). After exsolution at 600 °C, Cu segregation begins, as evidenced by the formation of irregularly shaped Cu-rich nanoparticles on the surface of the $SrTiO_3$ aggregates (Fig. 3.7b). Increasing the reduction temperature to 900 °C promotes further migration of Cu to the surface, resulting in larger nanoparticles. This behavior is attributed to enhanced ionic diffusion and additional oxygen release from the perovskite matrix as well as to a sort of sintering process happening, where the small nanoparticles of Cu fuse together in bigger particles at higher temperatures [53,54] (Fig. 3.7c). A similar investigation was carried out for 0.5Cu-STO powders, but the results are not shown here as it confirms the findings of higher Cu concentration samples, just less clearly visible owing the lower Cu concentration.

The elemental compositions and oxidation states of the elements in bare and Cu-doped $SrTiO_3$ perovskites were inspected by XPS, measuring the Sr 3*d*, Ti 2*p*, Cu $2p_{3/2}$, and O 1*s* (SI) XPS core levels before, after reduction and upon re-oxidation in air, as shown in Fig. 3.8.

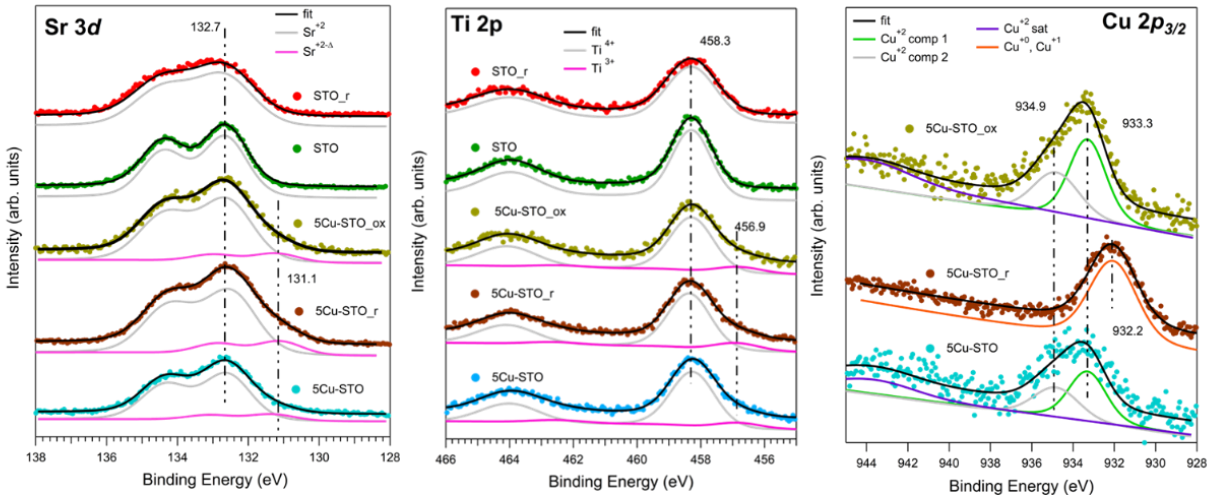

Fig. 3.8: XPS core levels spectra of: Sr 3*d* (Left), Ti 2*p* (Center) and Cu 2$p_{3/2}$ (Right). The intensities of all the spectra have been normalized to the total Ti 2*p* intensity. Superimposed to the experimental data (dots) are shown the fit results (black line) and the fit components, all including the background signal. To better visualize the results, an offset has been summed to all components. See text for more details.

The reference STO sample exhibits the characteristic XPS features of this material (Fig. 3.8, green spectra). The Sr 3d and Ti 2p core levels each consist of a single doublet, with Sr 3$d_{3/2}$ and Ti 2$p_{3/2}$ binding energies (BEs) at 132.7 eV and 458.3 eV, respectively, corresponding to Sr^{2+} and Ti^{4+} in $SrTiO_3$ [44]. Upon reduction (STO_r, Fig. 3.8, red spectra), both core levels show significant broadening (FWHM increasing from 1.3 to 1.8 eV for Sr 3d and from 1.3 to 1.6 eV for Ti 2p), while the BEs remain essentially unchanged. This behavior is consistent with increased structural disorder and the coexistence of multiple chemical environments, such as the possible segregation of Sr species at the surface [26,54].

Cu doping introduces an additional low-BE component in both Sr 3d and Ti 2p spectra, observed in all investigated samples: as-prepared (5Cu-STO, light blue spectra), after reduction (5Cu-STO_r, brown spectra), and after re-oxidation in air (5Cu-STO_ox, yellow spectra). In this case, the Sr 3$d_{3/2}$ level shifts to 131.1 eV, while Ti 2$p_{3/2}$ is observed at 456.9 eV, consistent with the formation of Ti^{3+} species [55].

The Cu 2$p_{3/2}$ core level spectra provide direct evidence of Cu reduction. Consistently with the XAS analysis, the spectra of the as-prepared sample (5Cu-STO) and the re-oxidized sample (5Cu-STO_ox) are very similar, showing a broad peak around 933.5 eV and corresponding satellite features near 944 eV. These spectra were fitted using two components at 933.3 and 934.9 eV, with satellites at 944.0 eV (5Cu-STO) and 943.8 eV (5Cu-STO_ox), indicative of Cu^{2+} species [56]. Upon reduction, the copper spectrum changes: the satellite peaks disappear, and the main peak shifts to 932.2 eV, reflecting the presence of Cu reduced species i.e. Cu^0 and Cu^+ species [56]. The relatively broad FWHM (≈2.3 eV) likely arises from different chemical environments of the Cu atoms, consistent with TPR data. After re-oxidation, the spectral line shape closely resembles that of the as-prepared sample, supporting the XAS

results. These observations suggest that the doped perovskite partially recovers its initial characteristics, indicating a degree of reversibility in the exsolution process.

The atomic ratios of the metal elements were measured via ICP analysis and are summarized in Table 3.2. For 5Cu-STO_r and 5Cu-STO_ox, the relative intensities of Sr and Ti suggest partial segregation of Sr to the perovskite surface, resulting in an apparent increase in its signal. The formation of Sr surface segregation (i.e. generation of strontium vacancies, V_{Sr}'') in STO is well documented in the literature [57] and appears to occur only in the presence of Cu. The measured Cu content for both 5Cu-STO and 5Cu-STO_r is 4±1%, consistent with the nominal doping levels used during synthesis, as well as with the ICP results presented below.

Table 3.2: ICP results

Sample	Cu ICP counts	Nominal absolute Cu content (% m/m)	Measured Cu content (% m/m)
Blank	0.0731	n. a.	0.1
5Cu-STO	0.9482	1.76	1.5
STO	0.0706	0	0.1

UV-DRS provides a complementary approach to probe both the coordination and aggregation state of Cu species in the perovskite, as well as to investigate the local titanium environment and oxygen defectivity. To this end, diffuse-reflectance (DR) spectra were collected for both undoped and 5Cu-STO powders as a function of reduction and re-oxidation treatments. The spectra are presented in Fig. 3.9 in terms of –log(DR), which enhances the visibility of little spectral features.

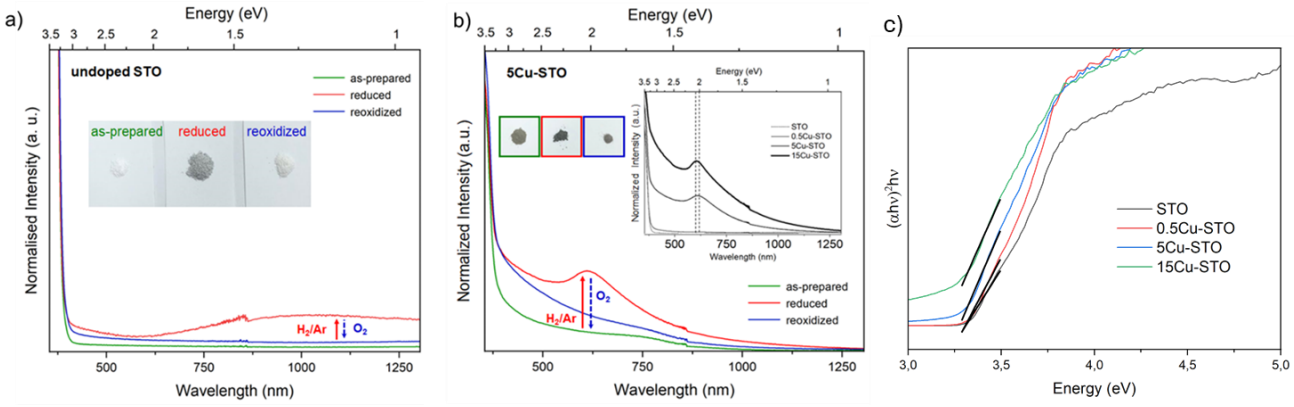

Fig. 3.9: Diffuse reflectance (DR) spectra of a) undoped STO and b) 5Cu-STO samples as prepared (green lines), after reduction in H_2/Ar at 900°C (red lines) and after subsequent re-oxidation in O_2 at 950°C (blue lines). Inset in b) shows the evolution of the spectra upon reduction as a function of dopant level in Cu-STO powders. The noisy signal and the step around 860 nm are unavoidable instrumental artefacts: c) Tauc plot of the four different samples

In Fig. 3.9a, the UV-DRS spectrum of the bare STO sample (green line) is dominated by the $SrTiO_3$ band edge at 3.31 eV, as determined from the Tauc plot Fig. 3.9c. After reduction in H_2/Ar at 900 °C, a broad feature emerges across the near-IR region, centered around ~1.2 eV (~1000 nm) (Fig. 3.9a, red line). Based on previous studies on chemically reduced and vacuum-annealed undoped $SrTiO_3$ and TiO_2 [27,34,58], this feature can be attributed to Ti^{3+} lattice defects and oxygen vacancies. Reduction also induces a visible color change of the powder from white to grey (inset, Fig. 3.9a), consistent with the decreased diffuse reflectance across the visible spectrum. Upon re-oxidation in O_2, the broad near-IR signal disappears entirely (blue line), and the spectrum returns to a featureless profile, identical to that of the as-prepared powders, with the powder regaining its original white color.

For the Cu-doped materials, no significant spectral features were observed for 0.5Cu-STO. In contrast, the as-prepared 5Cu-STO sample exhibits, in addition to the $SrTiO_3$ band edge slightly red-shifted to 3.27 eV (from the Tauc plots Fig. 3.9c), a broad absorption band in the visible region cantered around 750 nm that extends into the near-infrared (Fig. 3.9b, green line). This feature is clearly associated with the presence of copper in the perovskite matrix and can be primarily attributed to the d–d transition ($^2E_g \rightarrow {}^2T_{2g}$) of octahedral Cu^{2+} species [59,60].

Upon thermal reduction at 900 °C to induce copper exsolution, a new absorption band appears around 610 nm (Fig. 3.9b, red line), accompanied by a colour change of the powder from light to dark grey. This behaviour is likely due to the enhanced formation of Ti^{3+} lattice defects and oxygen vacancies during reduction, combined with the simultaneous formation of Cu^0 nanoparticles at the perovskite surface, as confirmed by XAS and TEM analyses. These metallic nanoparticles can contribute to a localized surface plasmon resonance (LSPR) effect [61,62].

To validate this interpretation, a 15Cu-STO sample (nominal 15 mol% Cu in the B-site) was synthesized and subjected to the same reduction and oxidation treatments as the other perovskite powders. The spectrum of 15Cu-STO shows a sharpening and slight blue shift of the absorption band to ~600 nm (inset, Fig. 3.9b), further supporting the presence of metallic Cu nanoparticles at the material surface [63]. After re-oxidation, the spectral profile gradually returns to its original shape (Fig. 3.9b, blue line).

These observations demonstrate the feasibility of using diffuse reflectance (DR) spectroscopy to detect changes in both the electronic structure and intrinsic defectivity of the samples.

3.3.4 EPR monitoring

To further investigate the evolution of the defect structure during the exsolution process in both undoped and Cu-doped $SrTiO_3$ samples, a comprehensive X-band electron paramagnetic resonance (EPR) study was carried out. Spectra were recorded under high vacuum ($p < 10^{-5}$ mbar) at 130 K, following thermal reduction treatments in H_2/Ar at various temperatures (200–900 °C) and subsequent re-oxidation at 950 °C in an oxygen atmosphere. These measurements provide valuable insights into

the coordination environment and aggregation state of the copper ions, as well as into the dynamic processes associated with oxygen and strontium vacancy formation.

The EPR spectra of the undoped STO samples are shown in Fig. 3.10. The as-prepared powders exhibit a very weak high-field signal at g ≈ 1.97, attributable to residual Ti^{3+} centres, along with overlapping resonances in the g = 1.99–2.01 range, corresponding to various paramagnetic species whose precise assignment remains controversial due to the limited EPR literature on $SrTiO_3$ [64–79]. Ti^{3+} centres are usually axial, thus two components should be noticed when looking at its signal, however in this case the perpendicular component of the signal is not well defined and can only be noticed as a broad band at 344 mT.

Thermal treatment under a reducing atmosphere allows for better discrimination and tentative assignment of these superimposed species (Fig. 3.10a). With increasing reduction temperature, all spectral features intensify, and notably, a sharp isotropic line at g ≈ 2.0 (labelled *) emerges. The g-values and the relative contributions of the individual species (calculated as percentages of the total intensity of the overlapping signals at g = 1.99–2.01) were determined via signal simulation (Table 3.3 and Fig. 3.10b).

Two distinct paramagnetic defects were identified in the EPR spectra: an axial signal (center I) and an isotropic line (center II). Based on previous studies [54, 70] and corroborated by the UV-DRS results, both features are attributed to paramagnetic defects located near the surface of the $SrTiO_3$ particles. Specifically, species I, exhibiting axial symmetry, can be associated either with O^- centers in proximity to Ti^{4+} ions or with oxygen ions surrounding V_{Sr}'',consistent with the A-site deficiency of the parental perovskite and the Sr surface segregation observed via XPS. The isotropic species II is attributed to singly ionized oxygen vacancies ($V_O^{\bullet}$) likely formed through the removal of lattice oxygen during thermal reduction, which also aligns with the observed increase of the Ti^{3+} signal at g ≈ 1.97.

Interestingly, re-oxidation in an oxygen atmosphere almost completely restores the original spectral features, with the exception of Ti^{3+} centres, which appear more stable (Fig. 3.10a). This behaviour mirrors the trends observed in the diffuse reflectance spectra.

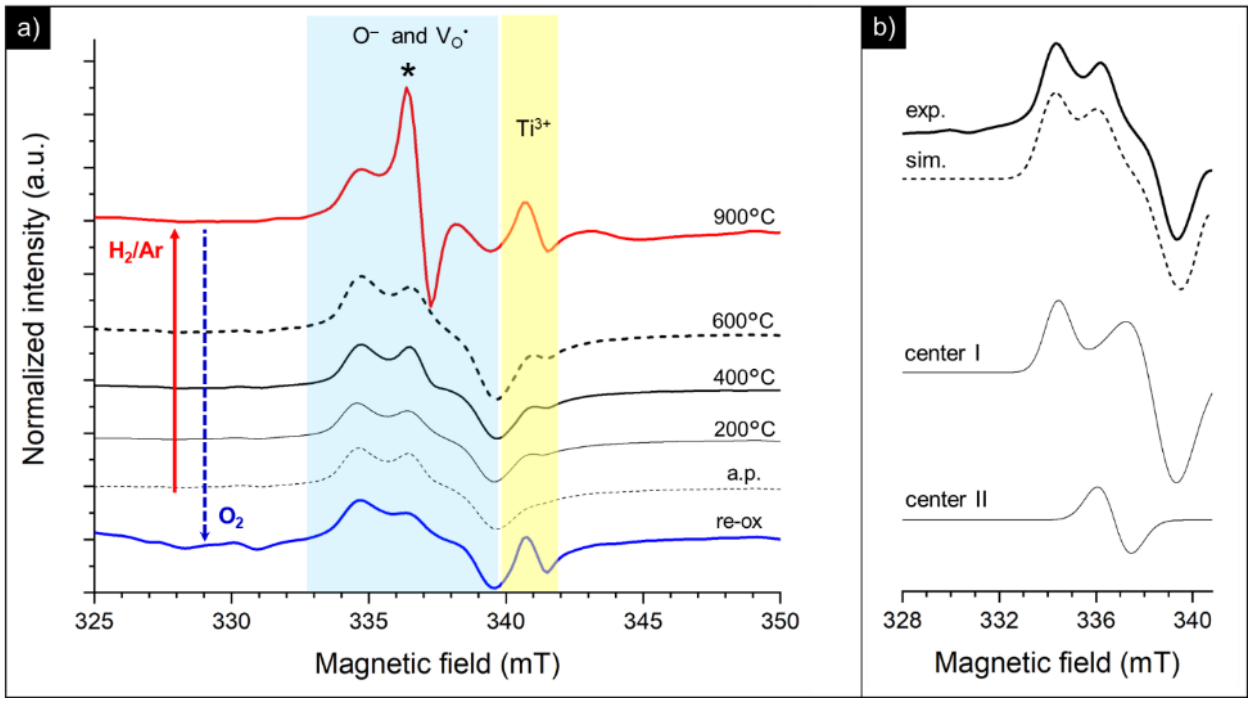

Fig. 3.10: a) EPR spectra at 130 K of as prepared (a.p.) STO nanopowders, after thermal reduction at different temperatures in H_2/Ar and subsequent re-oxidation (re-ox) in O_2 atmosphere at 950°C. b) Experimental (exp.) and simulated (sim.) EPR spectrum at 130 K of as prepared STO powders in the high field region and deconvolution of signals into centers I–II.

Table 3.3: *g* tensor values of the paramagnetic defects detected on pristine $SrTiO_3$ sample determined by simulation of the EPR features.

Center		Contribution (%)	*g* value
I	O^-	70.0 %	$g_\perp$ = 2.0124, $g_\parallel$ = 1.9865
II	($V_O^\bullet$)	30.0 %	g_{iso} = 1.9988

By introducing a small amount of copper into the perovskite (0.5Cu-STO), in addition to the increased intensity of the resonances corresponding to O^- centres, singly ionized oxygen vacancies, and Ti^{3+} defects, a complex set of signals attributable to various Cu^{2+} species emerges in the EPR spectra (Fig. 3.11a). A closer view of the Cu^{2+} spectral region is shown in Fig. 3.11b. The spectrum of the as-prepared sample (a.p.) is characterized by at least four overlapping signals: i) a broad, asymmetric, and unstructured line cantered at $g \approx 2$, typical of dipolar-coupled Cu^{2+} species in a disordered coordination environment [71–74], likely related to the CuO traces detected by XANES in Cu-STO; ii) at least three superimposed signals from distinct isolated copper centres (labeled i, ii, and iii), each showing a well-resolved "parallel" (z) hyperfine structure, with the corresponding g-tensor and hyperfine tensor (A‖) values reported in Table 3.4. It is worth noting the differences in the hyperfine constant values among

the three Cu centres. These differences likely arise because the centres occupy distinct sites in the lattice, either being intercalated at different lattice positions or incorporated as interstitial defects. The "perpendicular" (x, y) hyperfine features consist of multiple overlapping and broadened lines, making precise determination of the individual components through spectral simulation very challenging.

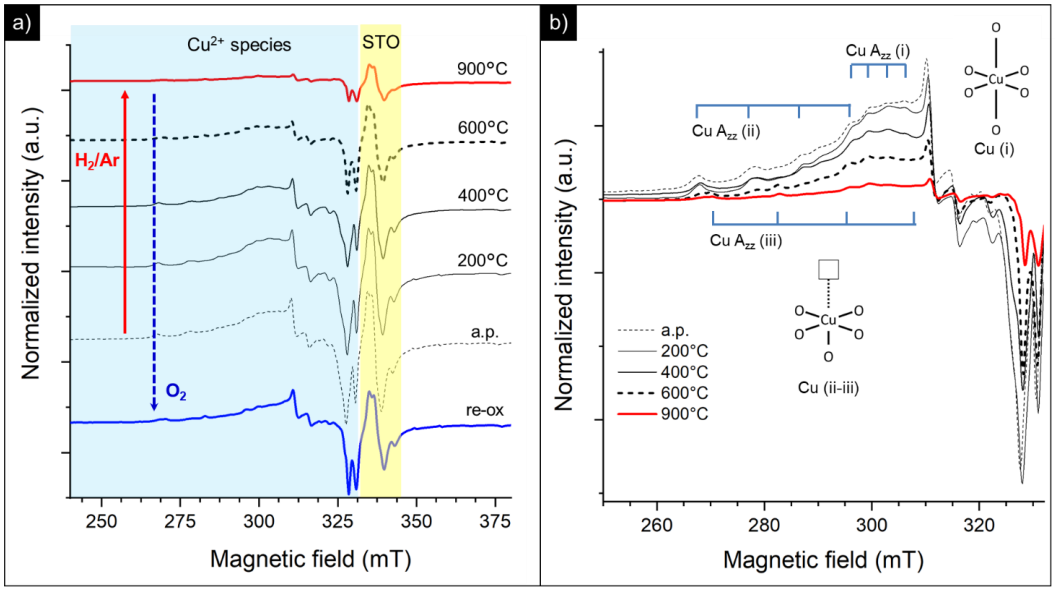

Fig. 3.11: a) EPR spectra at 130 K of as prepared (a.p.) 0.5Cu-STO nanopowders, after thermal reduction at different temperatures in H_2/Ar and subsequent re-oxidation (re-ox) in O_2 atmosphere at 950°C. b) Highlight of the Cu^{2+} spectral region: i, ii, and iii indicate three types of isolated copper centers, whose corresponding structures are depicted in inset.

Based on the g and A‖ parameters, these Cu^{2+} species can be attributed to substitutional defects in the perovskite lattice, each with distinct coordination environments with surrounding oxygen atoms [30, 37, 39, 75]. Specifically, center (i) corresponds to a copper site with slightly distorted octahedral symmetry, whereas centers (ii) and (iii) can be assigned to octahedrally coordinated Cu^{2+} ions associated with an oxygen vacancy (i.e. $(Cu''_{Ti} - V_O^{\bullet\bullet})^x$), or more generally, to Cu^{2+} centers experiencing a pronounced Jahn-Teller tetragonal distortion (see schematic of the possible structures in the inset of Fig. 3.11b) following the model proposed by Eichel et al. [30, 37, 39, 76, 77].

Table 3.4: *g*-tensor and hyperfine tensor ($A_{||}$) values determined from the experimental spectra of 0.5Cu-STO nanopowders.

Species	$g_{||}$ value	$A_{||}$ value (MHz)
Center *i*	2.234	118.2
Center *ii*	2.373	349.7
Center *iii*	2.326	408.9

Thermal annealing under a reducing atmosphere provided clearer insights into the evolution of the copper centers during the exsolution process. As the reduction temperature increased, the broad line lacking hyperfine structure, attributed to coupled Cu^{2+} species, rapidly decreased in intensity and ultimately disappeared at 900°C, leaving only weak signals corresponding to isolated copper sites in the final spectrum (red line in Fig. 3.11b, H_2/Ar, 900°C). This behavior suggests that Cu^{2+} centers with a disordered coordination environment, likely located at the perovskite surface, migrate first and undergo selective reduction to Cu^{+} or zero-valent diamagnetic species. In contrast, other lattice defects require higher thermal energy to gain mobility and reduce, displaying a sort of "delay." Re-oxidation in oxygen partially restores the initial resonances (re-ox spectrum in Fig. 3.11a), indicating that the exsolution process is feasible but only partially reversible.

These observations are consistent with the quantitative compositional changes obtained from XANES, which show that, in addition to the reduction of Cu^{2+} to Cu^{+} and metallic Cu, a significant fraction of 0.5Cu-STO remains in its as-prepared state during exsolution (Fig. 3.6, Table 3.1). Furthermore, these findings align with the TPR results, where signals from lattice oxygen species, which may facilitate the mobility and reduction of substitutional Cu sites, appear only at higher temperatures (Fig. 3.5).

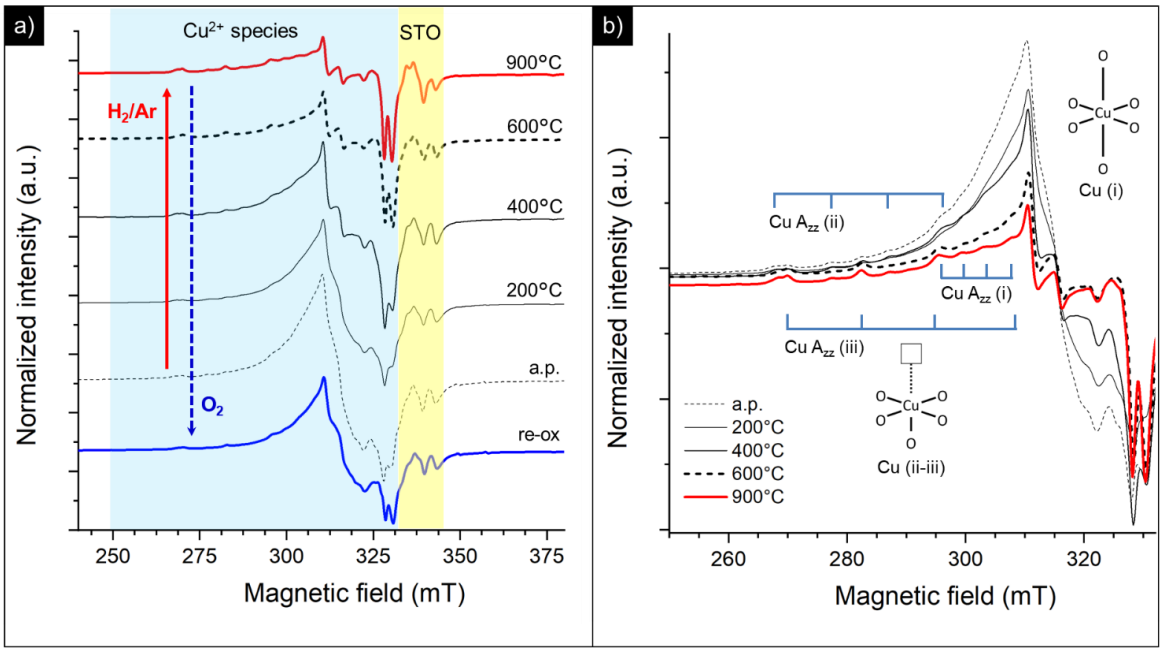

Fig. 3.12: a) EPR spectra at 130 K of as prepared (a.p.) 5Cu-STO nanopowders, after reduction in H_2/Ar and subsequent re-oxidation (re-ox) at 950°C. b) Highlight of the Cu^{2+} spectral region: i, ii, and iii indicate three types of isolated Cu centers, whose structures are depicted in inset.

With an increased copper dopant concentration (i.e., 5Cu-STO), a similar behaviour is observed (Fig. 3.12). In this case, the broad signal attributed to dipolar-coupled Cu^{2+} species is significantly more

intense and dominates the spectrum of the as-prepared material (Fig. 3.12a). Nevertheless, the distinct hyperfine structure of the isolated Cu^{2+} centres (i, ii, and iii) remains clearly observable (Fig. 3.12b). As in 0.5Cu-STO, a pronounced depletion of the copper resonances occurs upon reduction, leaving only the features corresponding to the isolated centres in the final spectrum. This supports the idea of a preferential and faster reduction of disordered Cu^{2+} species. Similarly, re-oxidation in an oxygen atmosphere allows the recovery of nearly the original spectral features (re-ox spectrum in Fig. 3.12a).

In conclusion, the EPR analysis provides valuable insights into the evolution of Cu coordination and speciation during exsolution, even at low doping levels, and offers high-resolution information that complements the results obtained from more complex techniques such as XAS.

3.4 Conclusion

In this chapter, the combination of multiple spectroscopic techniques (XAS, XPS, UV-DRS, and EPR) provided new insights into the exsolution and reincorporation processes of copper nanoparticles in $SrTiO_3$. Although standard characterization methods, such as XRD and TEM-EDX, indicate a homogeneous distribution of the copper dopant within the perovskite matrix, our analyses revealed that copper exists in at least two distinct configurations. Regardless of the dopant concentration (0.5 and 5 wt.%), copper was found both in a distorted octahedral environment, corresponding to amorphous Cu_2O and CuO likely located at the material surface, and as substitutional acceptor species (Cu''_{Ti}) within the lattice, as evidenced by the combination of XANES and EPR. Surface oxide species were reduced at much lower temperatures (200–400 °C) than lattice species (>800 °C). This heterogeneity in the local environment and reduction behaviour of copper is expected to be reflected in the properties of the exsolved nanoparticles (e.g., sintering resistance and support anchoring), potentially affecting their catalytic performance.

EPR spectroscopy, in agreement with XPS, also revealed that both copper doping and high-temperature reduction induce the formation of oxygen defects and modify the oxidation state not only of copper but also of titanium in the lattice. These findings indicate that electrons released from lattice oxygen reduction contribute to the reduction of the parent matrix itself, not just the aliovalent defects, which may have implications for catalytic applications, including photocatalysis. UV-DRS was shown to be a valuable complementary technique to TEM for detecting nanoparticle segregation via plasmon resonance effects. Interestingly, while XANES suggested a complete restoration of the copper oxidation state upon re-oxidation, EPR and UV-DRS demonstrated that the original local environment of copper is not fully recovered, resulting in a highly disordered structure.

The use of these less conventional spectroscopic techniques revealed that the chemical environment of exsolvable species is far more heterogeneous and the exsolution process more complex than commonly assumed. Therefore, we advocate that standard techniques such as XRD and TEM should not be solely relied upon to characterize exsolution; instead, a broader approach incorporating laboratory-scale spectroscopic methods can provide a more accurate and comprehensive understanding of these systems.

Bibliography

[1] B. Yan, Q. Wu, J. Cen, J. Timoshenko, A. I. Frenkel, D. Su, X. Chen, J. B. Parise, E. Stach, A. Orlov, J. G. Chen, *Appl Catal B* **2018,** *237,* 1003

[2] M. D. Argyle, C. H. Bartholomew, *Catalysts* **2015**, *5*, 145

[3] D. K. Niakolas, *App. Catal. A* **2014**, *486*, 123–142

[4] M. Miceli, P. Frontera, A. Macario, A. Malara, *Catalysts* **2021,** *11*, 591

[5] D. Mateo, J. Albero, H. García, *Joule* **2019**, *3*, 1949–1962

[6] C. Yang, J. Li, Y. Lin, J. Liu, F. Chen, M. Liu, *Nano Energy*, **2015**, 11, 704–710

[7] Y. F. Sun, Y. L. Yang, J. Chen, M. Li, Y. Q. ZZhang, J.H. Li, B. Hua, J. L. Luo, *Chem. Commun.* **2018**, *54*, 1505-1508

[8] A. J. Carrillo, K. J. Kim, Z. D. Hood, A. H. Bork, J. L. M. Rupp, *ACS Appl. Energy Mater.* **2020** *3*, 4569

[9] D. Neagu, E. I. Papaioannou, W. K. W. Ramli, D. N. Miller, B. J. Murdoch, H. Ménard, A. Umar, A. J. Barlow, P. J. Cumpson, J. T. S. Irvine, I. S. Metcalfe, *Nat. Commun*. **2017**, *8*, 1855

[10] K. Kousi, C. Tang, I. S. Metcalfe, D. Neagu, *Small* **2021**, *17*, 2006479

[11] Y. Nishihata, J. Mizuki, T. Akao, H. Tanaka, M. Uenishi, M. Kimura, T. Okamoto, N. Hamada, *Nature* **2002**, *418*, 6894

[12] Y. Gao, J. Wang, Y. Q. Lyu, K. Lam, F. Ciucci, *J. Mater. Chem. A* **2017**, *5*, 14

[13] D. Neagu, T. Oh, D. N. Miller, H. Ménard, S. M. Bukhari, S. R. Gamble, R. J. Gorte, J. M. Vohs, J. T. S. Irvine, *Nat. Commun.* **2015**, *6*, 8120

[14] D. Burnat, R. Kontic, L. Holzer, P. Steiger, D. Ferri, A. Heel, *J. Mater. Chem. A* **2016**, *30*, 11939

[15] S. Li, Q. Qin, K. Xie, Y. Wang, Y. Wu, *J. Mater. Chem. A* **2013**, *1*, 8984

[16] Y. R. Jo, B. Koo, M. J. Seo, J. K. Kim, S. Lee, K. Kim, J. W. Han, W. Jung, B. J. Kim, *J Am Chem Soc*. **2019**, *141*, 6690

[17] Y. Gao, D. Chen, M. Saccoccio, Z. Lu, F. Ciucci, *Nano Energy*, **2016**, *27*, 499

[18] T. S. Oh, E. K. Rahani, D. Neagu, J. T. S. Irvine, V. B. Shenoy, R. J. Gorte, J. M. Vohs, *J. Phys. Chem. Lett.* **2015**, *6*, 24

[19] D. Neagu, G. Tsekouras, D. N. Miller, H. Ménard, J. T. S. Irvine, Nat. Chem. **2013**, *5*, 11

[20] T. Ruh, D. Berkovec, F. Schrenk, C. Rameshan, *Chem. Commun.* **2023**, *59*, 3948

[21] D. Neagu, J. T. S. Irvine, J. Wang, B. Yildiz, A. K. Opitz, J. Fleig, Y. Wang, J. Liu, L. Shen, F. Ciucci, B. A. Rosen, Y. Xiao, K. Xie, G. Yang, Z. Shao, Y. Zhang, J. Reinke, T. A. Schmauss, S. A. Barnett, R. Maring, V. Kyriakou, U. Mushtaq, M. N. Tsampas, Y. Kim, R. O'Hayre, A. J. Carrillo, T. Ruh, L. Lindenthal, F. Schrenk, C. Rameshan, E. I. Papaioannou, K. Kousi, I. S. Metcalfe, X. Xu, G. Liu, *J. Phys. Energy* **2023**, *5*, 031501.

[22] D. Neagu, V. Kyriakou, I. L. Roiban, M. Aouine, C. Tang, A. Caravaca, K. Kousi, I. Schreur-Piet, I. S. Metcalfe, P. Vernoux, M. C. M. van de Sanden, M. N. Tsampas, *ACS Nano* **2019**, *13*, 11

[23] E. Calì, M. P. Thomas, R. Vasudevan, J. Wu, O. G. Diaz, K. Marquardt, E. Saiz, D. Neagu, R. R. Unocic, S. C. Parker, B. S. Guiton, D. J. Payne *Nat. Commun.* **2023,** *14*, 1754

[24] S. Shah, J. Hong, L. Cruz, S. Wasantwisut, S. R. Bare, K. L. Gilliard-AbdulAziz, *ACS Catal.* **2023***, 13*, 6

[25] B. Rudolph, A. I. Tsiotsias, B. Ehrhardt, P. Dolcet, S. Gross, S. Haas, N. D. Charisou, M. A. Goula, S. Mascotto, *Adv. Sci.* **2023**, *10*, 6

[26] B. Kayaalp, K. Klauke, M. Biesuz, A. Iannaci, V. Sglavo, M. D'Arienzo, H. Noei, S. Lee, W. Jung, S. Mascotto, *J. Phys. Chem. C*. **2019**, *123*, 27

[27] H. Tan, Z. Zhao, W. Zhu, E. N. Coker, B. Li, M. Zheng, W. Yu, H. Fan, Z. Sun, *ACS Appl. Mater. Interfaces* **2014**, *6*, 21

[28] B. Liu, V. R. Cooper, H. Xu, H. Xiao, Y. Zhang, and W. J. Weber, *Phys. Chem. Chem. Phys*. **2014**, *16*, 15590

[29] Y. Gao, Z. Lu, T. L. You, J. Wang, L. Xie, J. He, F. Ciucci *J. Phys. Chem. Lett.* **2018**, *9*, 13

[30] R. A. Eichel, E. Erünal, M .D. Drahus, D. M. Smyth, J. van Tol, J. Acker, H. Kungl, M. J. Hoffmann**,** *Phys. Chem. Chem. Phys*. **2009**, *11*, 8698

[31] G. Feher, *Bell System Technical Journal* **1956,** *36*, 2.

[32] S. A. Horlick, Y. L. Huang, I. A. Robinson, E. D. Wachsman, *Nano Energy* **2021**, *87* 106193

[33] E. Calì, G. Kerherve, F. Naufal, K. Kousi, D .Neagu, E. I. Papaioannou, M. P. Thomas, B. S. Guiton, I. S. Metcalfe, J. T. S. Irvine, D. J. Payne, *ACS Appl. Mater. Interfaces* **2020**, *12*, 3

[34] R. A. Eichel, *J. Electroceram*. **2007**, *19*, 1

[35] R. A. Eichel**,** *Phys. Chem. Chem. Phys*. **2011**, *13*, 368

[36] W. L. Harrigan, K. R. Kittilstved, *J. Phys. Chem. C* **2018**, *122*, 46

[37] K. A. Lehuta, K. R. Kittilstved, *Dalton Trans.* **2016**, *45*, 10034

[38] R. F. Howe, *Colloids Sur. A* **1993**, *72*, 353.

[39] R. A. Eichel, P. Erhart, P. Träskelin, K. Albe, H. Kungl, M. J. Hoffmann, *Phys Rev Lett*, **2008**, *100*, 9

[40] K. A. Schönau, L. A. Schmitt, M. Knapp, H. Fuess, R. A. Eichel, H. Kungl, M. J. Hoffmann *Phys. Rev. B* **2007**, *75*, 18

[41] E. Garribba, G. Micera, *J. Chem. Educ*. **2006**, *83*, 8

[42] B. Kayaalp, S. Lee, K. Klauke, J. Seo, L. Nodari, A. Kornowski, W. Jung, S. Mascotto, *Appl Catal B*, **2019**, *245*, 536

[43] E. Poffe, H. Kape, B. Ehrhardt, L. Gigli, D. Aubert, L. Nodari, S. Gross, S. Mascotto, ACS *Appl Mater Interfaces*, **2021**, *13*, 21

[44] R. P. Vasquez, *Surf. Sci. Spectra*, **1992**, *1*, 1

[45] W. A. Caliebe, V. Murzin, A. Kalinko, and M. Görlitz, *AIP Conf. Proc.* 2019, 2054, 06003

[46] B. Ravel, M. Newville, *J. Synchrotron Radiat.* **2005**, *12*, 537

[47] L. Rizzato, J. Cavazzani, A. Osti, M. Scavini, A. Glisenti, *Catalysts*, **2023**, *13*, 10

[48] Z. Bao, V. Fung, J. Moon, Z. D. Hood, M. Rochow, J. Kammert, F. Polo-Garzo, Z. Wu, *Catal. Today*, **2023**, *416*, 113672

[49] J. J. Rodriguez, J. Y. Kim, J. C. Hanson, M. Pérez, A. I. Frenkel, *Catal. Lett.* **2003**, *85*, 247

[50] P. Gwóźdź, A. Łącz, A. Mizera, E. Drożdż, *J. Therm. Anal. Calorim.* **2022***, 147*, 18

[51] B. Rudolph, A. I. Tsiotsias, B. Ehrhardt, P. Dolcet, S. Gross, S. Haas, N. D. Charisou, M. A.Goula, S. Mascotto, *Adv. Sci.* **2023**, *10*, 2205890

[52] K. Kousi, D. Neagu, L. Bekris, E. I. Papaioannou, I. S. Metcalfe, *Angew. Chem. Int. Ed.* **2020**, *59*, 2510

[53] A. I. Tsiotsias, B. Ehrhardt, B. Rudolph, L. Nodari, S. Kim, W. Jung, N. D. Charisiou, M. A. Goula, S. Mascotto, *ACS Nano* **2022**, *16*, 6

[54] K. Klauke, B. Kayaalp, M. Biesuz, A. Iannaci, V. M. Sglavo, M. D'Arienzo, S. Lee, J. Seo, W. Jung, S. Mascotto, *ChemNanoMat* **2019**, *5*, 948

[55] M. de Simone, E. Snidero, M. Coreno, G. Bongiorno, L. Giorgetti, M. Amati, C. Cepek, *Thin Solid Films* **2012**, *520*, 14

[56] M. C. Biesinger, B. P. Payne, A. P. Grosvenor, L. W.M. Lau, A. R. Gerson, R. St. C. Smart, *Appl. Surf. Sci.* **2011**, *257*, 7

[57] A. G. Shard, *Surf. Interface Anal.* **2014**, *46*, 175

[58] F. Zuo, L. Wang, T. Wu, Z. Zhang, D. Borchardt, P. Feng, *J. Am. Chem. Soc.* **2010**, *132*, 34

[59] R. Hierl, H. Knözinger, H. P. Urbach, *J. Catal.* **1981**, *69*, 475

[60] B. R. Strohmeier, D. E. Leyden, R. S. Field, D. M. Hercules, *J. Catal.* **1985**, *94*, 514.

[61] M. J. Kale, T. Avanesian, P. Christopher, *ACS Catal.* **2014**, *4*, 1

[62] Z. Li, G. Zhu, W. Zhang, L. Zhu, B. Cao, J. Gao, X. Shi, Y. Huang, P. Liu, M. Hojamberdiev, *Chemical Engineering Journal*, **2023**, *452*, 139378

[63] G. Y. Yao, Z. Y. Zhao, Q. L. Liu, X. D. Dong, Q. M. Zhao, *Sol. Energy Mater. Sol. Cells*, **2020**, *208*, 110385

[64] K. Xie, N. Umezawa, N. Zhang, P. Reunchan, Y. Zhang, J. Ye, *Energy Environ. Sci.*, **2011**, *4*, 4211

[65] A. Troup, J. Mort, S. Grammatica, D.J. Sandman, *Solid State Commun.***1980***, 33,* 91

[66] I. Bykov, M. Makarova, V. Trepakov, A. Dejneka, L. Yurchenko, A. Jäger, L. Jastrabik, *Phys. Status Solidi B* **2013**, *250*, 4

[67] C. Oliva, L. Bonoldi, S. Cappelli, L. Fabbrini, I. Rossetti, L. Forni, *J. Mol. Catal. A: Chem.* **2005**, *226*, 33

[68] X. Zhou, N. Liu, T. Yokosawa, A. Osvet,M. E. Miehlich, K. Meyer, E. Spiecker, P. Schmuki, *ACS Appl. Mater. Interfaces* **2018**, *10*, 35

[69] Z. Wei, M. Zhao, Z. Yang, X. Duan, G. Jiang, G. Lia, F. Zhanga, Z. Hao, *PNAS* **2023**, *120*, 3

[70] B. Kayaalp, K. Klauke, M. Biesuz, A. Iannaci, V. M. Sglavo, M. D'Arienzo, H. Noei, S. Lee, W.Jung, S. Mascotto, *J. Phys. Chem. C* **2019**, *123*, 27

[71] S. Fujiwara, S. Katsumata, T. Seki, *Phys. Chem.* **1967**, *71*, 1

[72] J. P. Donoso, C. J. Magon, J. F. Lima, O. R. Nascimento, E. Benavente, M. Moreno, G. Gonzalez, *J. Phys. Chem. C* **2013**, *117*, 45

[73] S. Radhakrishnan, S. Smet, C. V. Chandran, S. P. Sree, K. Duerinckx, G. Vanbutsele, J. A. Martens, E. Breynaert, *Molecule*s **2023**, *28*, 6456

[74] J. F. Boas, R. H. Dunhill, J. R. Pilbrow, R. C. Srivastava, T. D. Smith, *J. Chem. Soc. A*, **1969**, 94-108

[75] P. Politzer, J. Martinez, J. S. Murray, M. C. Concha, A. Toro-Labbé, *Molecular Physics*, **2009**, *107*, 19

[76] S. Maurelli, M. Ruszak, S. Witkowski, P. Pietrzyk, M. Chiesa, Z. Sojka, *Phys. Chem. Chem. Phys.* **2010**, *12*, 10933

[77] A. Godiksen, F. N. Stappen, P. N. R. Vennestrøm, F. Giordanino, S. B. Rasmussen, L. F. Lundegaard, S. Mossin, *J. Phys. Chem. C* **2014**, *118*, 23126

Chapter 4

Fe-Ni doped $SrTiO_3$ for RWGS

Index of the chapter

This chapter provides a comprehensive description of the synthesis procedures, characterization techniques, and testing methods employed to investigate Ni and Fe doped and co-doped STO systems. Particular focus is given on monitoring the exsolution process with emphasis on using EPR spectroscopy as unconventional technique to track the process and assess the material defect's structure. Finally, the monometallic and bimetallic catalysts were tested in RWGS reaction.

4.1 Introduction

In recent years, the redox exsolution process in doped perovskites has attracted significant attention from the scientific community, owing to its ability to produce customizable, highly stable, selective, and regenerable catalysts [1]. Exsolution takes place when a doped perovskite oxide is subjected to reduction at high temperature under oxygen-deficient conditions. As oxygen is released from the crystal lattice, the transition metal dopants are reduced to their metallic state. Through spontaneous nucleation and growth, these metal nanoparticles migrate from the bulk to the oxide surface, forming "socketed" metal catalysts. Such exsolved nanoparticles exhibit enhanced stability, reduced susceptibility to deactivation, and the potential for regeneration compared to conventional impregnated catalyst systems [2], [3], [4]. It is worth noting that certain metals, such as Fe, are unlikely to exsolve when they are the sole B-site cation in the perovskite lattice due to their high segregation energy. However, co-exsolution can be achieved by incorporating a second, more reducible metal—such as Ni or Co—with a lower segregation energy [5]. In mixed B-site systems, the Gibbs free energy of reduction depends on the metal–oxygen bond strengths of both cations. Thus, incorporating a more reducible element decreases the overall energy barrier and facilitates exsolution [6]. This process typically results in the formation of alloy nanoparticles on the surface, as supported by both modelling and experimental evidence [7], [8], [9]. Exsolution is driven by oxygen vacancies generated during reduction, which tend to migrate from the bulk toward the surface, thus, this migration promotes the segregation of reducible metal species in association with oxygen vacancies, as it requires less energy [8].

For what concerns Fe–Ni bimetallic systems, Irvine et al. [10] demonstrated that in the stoichiometric perovskite $(La_{0.75}Sr_{0.25})(Cr_{0.5}Fe_{0.5-x}Ni_x)O_3$, Fe–Ni alloy nanoparticles exsolve from the B-site, leading to the formation of a Ruddlesden–Popper (RP) phase similar to $(La,Sr)_{m+1}(Cr,Fe)_mO_{3m+1}$. The exsolution process initiates near the surface, where reduction induces cation diffusion from subsurface layers outward. As a result, an RP-type shell forms around the perovskite particles.

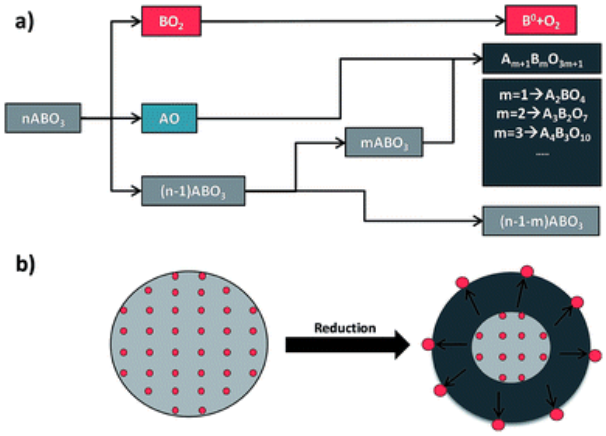

Fig. 4.1: Schematic representation of a) mechanism of the chemical reactions, b) surface modification of ABO_3 type perovskite during reduction process. In dark blue is the Ruddlesden Popper phase [10]

Their study also revealed that the exsolved alloy nanoparticles were richer in Ni than Fe. This observation was attributed to the lower Gibbs free energy associated with the reduction of NiO to metallic Ni compared to that of Fe_2O_3 to metallic Fe, as reported by Neagu et al. [11]. Consequently, the reduction of Ni^{2+} to Ni^0 is thermodynamically more favourable than that of Fe^{3+} to Fe^0. More recent investigations [12] of Fe–Ni bimetallic exsolution in heavily doped LSTO systems have reported similar trends. Ni was observed to reduce more readily than Fe, with XRD and TEM analyses confirming the formation of a Ni_3Fe intermetallic phase. Based on these findings, it has been proposed that metallic Ni initially exsolves from the parent perovskite, generating cation and oxygen vacancies. These defects subsequently facilitate Fe exsolution, ultimately leading to the formation of Fe–Ni alloy nanoparticles.

Beyond these mechanistic insights, most studies on Fe–Ni bimetallic exsolution have focused on application-oriented research. Such works highlight not only the enhanced performance arising from Ni–Fe interfacial synergy but also the limited reversibility of the exsolution process, which remains a major challenge for practical applications. Beyond their widespread use as electrocatalytic materials [13], [14], exsolved Fe–Ni alloy systems have also been employed as catalysts for various thermochemical reactions, including methane reforming [15], CO oxidation [16], and, to a lesser extent, the reverse water–gas shift (RWGS) reaction [17].

In the case of methane reforming, the influence of A-site cations on catalytic performance has been systematically examined in a series of $LnFe_{0.7}Ni_{0.3}O_{3-\delta}$ (Ln = La, Pr, Sm) perovskites. Among these, the $PrFe_{0.7}Ni_{0.3}O_{3-\delta}$ composition exhibited the highest catalytic activity and stability, attributed to the optimized composition of exsolved Fe–Ni nanoparticles, which displayed a higher Fe content [15]. Furthermore, increasing the Ni doping level was found to enhance the oxygen nonstoichiometry of the perovskite lattice. This effect was linked to the reduction of Fe^{3+}/Fe^{4+} and Ni^{2+} to lower oxidation states,

which promoted Fe–Ni nanoparticle exsolution and led to significantly improved catalytic activity for CH_4 conversion [10].

For CO oxidation, exsolved Fe–Ni nanoparticles derived from $La_{0.5}Sr_{0.4}Fe_{0.1}Ni_{0.1}Ti_{0.6}O_3$ demonstrated not only high catalytic activity but also exceptional long-term stability over 170 hours, along with notable sulphur tolerance [16].

Finally, in the case of the RWGS reaction, Orsini et al. [17] recently investigated the structural evolution and redox behaviour of the double perovskite $Sr_2FeMo_{0.6}Ni_{0.4}O_{6-\delta}$ under H_2/CO_2 redox cycling, with a particular focus on its performance in the Reverse Water–Gas Shift Chemical Looping (RWGS-CL) process. The study revealed that both the reduction and oxidation steps were significantly enhanced, a result attributed to the exsolution of Ni–Fe alloy nanoparticles and the concurrent formation of the Ruddlesden–Popper (RP) phase $Sr_3FeMoO_{7-\delta}$. This improvement was ascribed to the synergistic interaction between the exsolved Ni–Fe alloy nanoparticles, responsible for the adsorption and activation of H_2 and CO_2, and the RP phase, which facilitates rapid oxygen exchange during redox cycling.

Despite the extensive literature on bimetallic exsolution, only a limited number of studies have systematically explored the individual and synergistic roles of Ni and Fe during their co-exsolution from A-site-deficient perovskites, particularly with regard to their specific contributions to the RWGS reaction. A valuable foundation for deeper analysis of these aspects is provided by the work of Lindenthal et al. [18]. In their investigation of various doped and co-doped perovskite materials under RWGS conditions, the authors observed that the highest catalytic activity was achieved when metallic nanoparticles were exsolved *in situ* during the reaction. This enhancement was attributed to a Mars–van Krevelen-type mechanism, wherein dissociative H_2 adsorption occurs on the surface of the exsolved metal particles. The resulting active hydrogen species subsequently migrate via spillover into the perovskite lattice, promoting lattice reduction and generating oxygen vacancies that, in turn, facilitate CO_2 activation. Furthermore, the study suggested that introducing an easily reducible dopant (e.g., Co or Ni) at the B-site, alongside a less reducible primary component such as Fe, not only promotes the formation of metallic nanoparticles on the surface but also drives the preferential exsolution of the more reducible species. Concurrently, the presence of the more stable, less reducible host cation preserves the structural integrity of the perovskite lattice under reducing conditions. This structural robustness enables effective anchoring of the exsolved nanoparticles, mitigating sintering and maintaining a high density of gas/metal/oxide three-phase boundaries that are crucial for catalytic activity.

Building upon these insights, we undertook a detailed investigation into the individual and cooperative effects of Ni and Fe during bimetallic exsolution from A-site-deficient $SrTiO_3$-based perovskites.

Specifically, perovskite oxides with the nominal composition $Sr_{0.95}Ti_{1-y-x}Fe_xNi_yO_{3\pm\delta}$ (x, y = 0, 0.01, 0.05, 0.15) were successfully synthesized via a tailored sol–gel method, followed by redox-driven exsolution to achieve surface decoration with finely dispersed (bi)metallic nanoparticles. By exploiting the low doping levels and employing complementary characterization techniques, particularly X-ray Absorption Spectroscopy (XAS) and Electron Paramagnetic Resonance (EPR) spectroscopy, the distinct yet interconnected roles of Ni and Fe in the exsolution process were analysed.

The findings demonstrate that the behaviour of these dopants is intrinsically governed by dynamic changes in their coordination environments and oxidation states during reduction. These transformations directly impact both the selectivity and CO_2 conversion efficiency in the RWGS reaction. Overall, the methodological approach adopted in this study provides a transferable framework for investigating other exsolvable dopants (e.g., Co), thereby enabling the rational design of intermetallic exsolved functional materials with tuneable structure and composition for optimized catalytic performance.

4.2 Materials and methods

Synthesis of perovskite materials

Strontium nitrate (99%, Acros Organics), Titanium(IV) isopropoxide (97%, Alfa Aesar), Iron(III) nitrate (98%, Alfa Aesar), Ni(II) nitrate, (98%, Alfa Aesar), anhydrous citric acid (99.6%, Acros Organics), glycerol (99%, Alfa Aesar), were used as received without further purification. Four samples have been produced following a synthetic route reported in the previous chapter. In particular, the general formula $Sr_{0,95}Ti_{1-x+y}Fe_xNi_yO_{3-d}$ was followed to obtain 5Ni-STO, 5Fe-STO, 5Fe5Ni-STO, 1Ni-STO, 1Fe-STO, 1Ni1Fe-STO, 5Fe0,1Ni-STO, where the number represent the molar fraction of the B-site doping of the metal.

Exsolution procedure

Exsolution/reduction treatments were carried out using a U-shaped quartz tube filled with 70 mg of each sample. 5% H_2/Ar was chosen as the reducing gas, and the flow rate was set at 100 mL/min. A ramping rate of 10 °C/min was employed to reach the final temperatures of 400 °C, 600 °C, or 900 °C with a dwell time of 1 h.

Characterization

Powder X-ray powder diffraction (PXRD) patterns were recorded using a Rigaku Miniflex 600. The acquisition was performed using a Cu source (40 kV, 15 mA), scanning in the 20–80° 2θ range, with a step size of 0.01 degrees and an angular velocity of 3.0 degree per minute. Instrumental HighScore Plus software was used for the sake of comparison with reference diffraction patterns from the ICDD database. The concentration of the metal ions (Sr, Ti, Ni and Fe) was determined with an inductively coupled plasma optical emission spectrometer (ICP-OES, Optima 7000 DV, PerkinElmer, MA, United States) The temperature-programmed reduction measurements under a H_2 environment (H_2-TPR) were performed with a Micromeritics AutoChem 2920 analyzer. The catalyst (~100 mg) was pretreated under a 5% H_2 stream balanced in Ar (20 mL min−1) at room temperature for 2 h. Then, the sample was heated up to 120 °C with a ramp rate of 10 °C min−1 and a dwell time of 1 h. Then the temperature was increased up to 950 °C at a heating rate of 10 °C min−1 and a second isotherm of 1 h was performed. The amount of consumed H2 was measured using a thermal conductivity detector (TCD).

The surface chemical composition of the sample powders was investigated by X-ray photoelectron spectroscopy (XPS). The measurements were performed on the samples in powder form, fixed on the sample holder using UHV-compatible carbon tape. The XPS measurements were performed at room temperature under ultrahigh vacuum conditions (base pressure ≈ 5×10^{-10} mbar) in normal emission geometry, using a conventional Mg Kα X-ray source (hv = 1253.6 eV) and a hemispherical electron energy analyzer (120 mm, PSP; total energy resolution ≈ 0.8 eV). To compensate for sample charging effects, all binding energies (BE) were calibrated by setting the Ti $2p_{3/2}$ core level of STO to 458.3 eV. Survey spectra were collected over the 0–1100 eV binding energy range, while high-resolution spectra were acquired for the O 1s, C 1s, Sr 3d, Ti 2p, Ni 2p, and Fe 2p core levels. The spectra were analyzed by fitting the experimental data with an integral background and Voigt line shapes, accounting for distinct oxidation states and local chemical environments. Further details on the fitting methodology and parameters are provided in the ESI. Atomic ratios were determined from the peak areas corrected by the instrument sensitivity factors.A Thermo Fisher Talos F200X G2 was used for high-resolution scanning transmission electron microscopy (STEM) imaging with an acceleration voltage of 200 kV and a resolution of 4096 × 4096 pixels without any objective apertures. Super X spectrometers equipped with silicon drift detectors of 30 mm2 were used to collect energy dispersive X-ray analysis (EDX) maps with a collection angle of 0.7 s rad.

The measurements at the Fe and Ni K-edges (7112 and 8333 eV, respectively) were carried out at the Italian CRG Beamline Lisa (BM08) at the European Synchrotron Radiation Facility (ESRF, Grenoble, France) [19]. The Fluorescence yield was collected through a 4-element Peltier-cooled SDD detector [20]. To provide an accurate energy calibration, reference metal foils of Fe and Ni, placed in a second

experimental chamber, located downstream from the first one, were measured concurrently. The beam flux before and after the sample, and before and after the reference metal foil, was measured using N_2-filled ionization chambers.

The energy of the X-ray beam was selected by a fixed exit monochromator with a pair of Si (111) crystals (energy resolution $\Delta E/E \approx 1.1 \times 10^{-4}$). At the same time, Si mirrors were used for harmonics rejection (E_{cutoff} ≈15 KeV). Spectral acquisitions were set up to provide a significant energy resolution in the X-ray Absorption Near Edge Structure (XANES) and Extended X-ray Absorption Fine Structure (EXAFS). Accordingly, the step size in the XANES region was 0.5 eV, and the post-edge EXAFS region of the spectrum was acquired with a fixed k-step width of 0.05 $Å^{-1}$. Measurements were carried out at room temperature and in low vacuum conditions (10^{-2}mbar).

The structure and local arrangement of Fe and Ni were examined using X-ray Absorption Spectroscopy (XAS) in both fluorescence and transmission modes. Spectra were collected from 28 samples, which were pelletized with microcrystalline cellulose. The analysis of the XAS spectra was performed using Athena and Artemis software, part of the Demeter package [21] and Larch [22]. The XAS spectrum energy was first calibrated using the reference foil, then its background was subtracted, and it was normalized using the Athena software. Finally, the XANES and EXAFS spectra were extracted. The normalized XANES were investigated through Linear Combination Fitting (LCF) using the Larch package; the as prepared samples' spectra, and the metal foils were employed as endmembers. This procedure was performed in the energy range of -20 to +90 eV (with respect to the metal edge position). The reference spectra were used as primary components, and their weights were constrained to vary between 0 and 1, while the total weights sum was left free to vary. Theoretical EXAFS paths of iron and nickel were calculated using feff6 [23] tarting from the models of $SrTiO_3$ reported by [24] (with a Ti substituted with Fe and Ni), using Muffin Tin potentials and the Hedin–Lundqvist approximation. The edges were analyzed in the R range, using a k^2-weight. The FT window was chosen considering the EXAFS signal-to-noise ratio to include as much oscillation as possible.

Temperature-programmed reduction (TPR) measurements were carried out using a BELCAT II catalytic analyzer (Microtrac Retsch GmbH). For each measurement, a sample mass of at least 40 mg was used. Prior to the experiment, the thermal conductivity detector (TCD) was stabilized at room temperature for a minimum of 90 min. The TPR measurements were performed with a gas flow of 5% H 2 in N 2 at a flow of 20 sccm, applying a heating ramp of 10 K/min up to 900°C. The target temperature was maintained for 30 min. A baseline correction was applied to the TCD signal, and the resulting curves were normalized for data visualization. Hydrogen consumption was quantified using the ChemMaster II software (Microtrac Retsch GmbH).

EPR measurements were performed by using a Bruker EMX spectrometer operating at the X-band frequency and equipped with an Oxford cryostat working in the temperature range of 4–298 K. A tailored home-made system was utilized, where the sample in the EPR tube can be measured in vacuum conditions ($p < 10^{-5}$ mbar). Spectra were collected with MW power of 20 mW, at 130 K after their thermal treatment at 400 °C, 600 °C, or 900 °C under an Ar/H2 atmosphere. Undoped sample measurements are reported in the previous chapter.

The catalytic performance of the prepared samples was tested for the CO_2 hydrogenation reaction in a fixed-bed quartz reactor (I.D. 0.9 cm) within a temperature range of 400–750 °C, under conditions of H_2/CO_2 = 4/1, WHSV = 25,000 mL h^{-1} g^{-1}, and P = 1 atm. A total of 0.24 g of catalyst was mixed with an equal mass of quartz sand and placed in the reactor above a quartz wool layer. A thermocouple was inserted into the catalyst bed to monitor the reaction temperature, and a cold trap was positioned at the reactor outlet to collect the produced water vapor.

Prior to testing, all catalysts were reduced *in situ* under a 5 % H_2/Ar flow (50 mL min^{-1}), with a heating rate of 10 °C min^{-1} up to 900 °C, followed by a 2 h dwell at that temperature. The reactor was then cooled to 400 °C under an Ar flow. Subsequently, the feed gas composition was switched to CO_2/H_2/Ar = 1/4/5, with Ar serving as an internal standard. The total gas flow was maintained at 100 mL min^{-1}, and measurements were taken at 50 °C intervals under steady-state conditions (two readings per temperature). The reactor effluent was analysed using an online gas chromatograph (Agilent 8890 GC) equipped with TCD and FID detectors, revealing CO and CH_4 as the only detectable products.

4.3 Results and discussion

4.3.1 Structural and morphological characterization

The crystalline phase structures of the synthesized materials were characterized using powder X-ray diffraction (PXRD), and the results are summarized in Figure 1. All the samples display the same crystalline structure corresponding to the cubic $Pm\bar{3}m$ structure of the $SrTiO_3$ perovskite oxide with only small impurities of $SrCO_3$, which are reported as typical impurities for this kind of materials [25], [26].

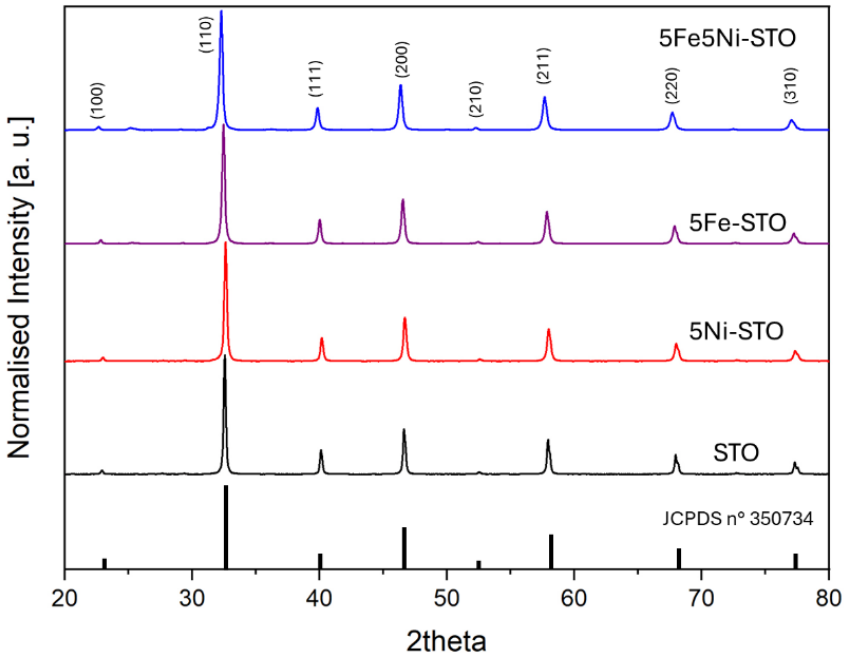

Fig. 4.2: PXRD patterns of $SrTiO_3$ with high levels of doping

To further clarify the oxidation state and local coordination environment of the Fe and Ni dopants, X-ray absorption spectroscopy (XAS) analyses were performed. The spectra of the as-prepared Fe-STO, Ni-STO, and co-doped FeNi-STO samples were collected at the Fe and Ni K-edges (7112 and 8333 eV, respectively). Comparison of the XANES spectra (Fig. 4.3a) with reference data from the literature [27] confirms that both Fe and Ni are incorporated into the perovskite lattice, substituting for Ti.

For Fe, two main peaks (A and B) at 7129.3 and 7136.8 eV are observed, characteristic of the perovskite structure. A pre-edge feature (P1) at 7114.4 eV corresponds to the 1s→3d quadrupole transition of Fe(III), while a shoulder (S1) at 7122 eV is attributed to the 1s→4d dipole transition [27]. The spectral shape remains essentially unchanged with varying dopant concentrations, indicating that Fe maintains a consistent local environment.

The Ni spectra exhibit a similar profile, with two main peaks (A and B) at 8348.7 and 8353 eV, confirming Ni substitution at the Ti site within the perovskite structure. A pre-edge feature (P1) at 8333.5 eV, less intense than in the Fe spectra, and a shoulder (S1) at 8339 eV are also present. However, Ni displays a higher degree of variability in the XANES region. Among the as-prepared (AP) samples, 1Ni-STO most closely reproduces the characteristic perovskite spectrum, with well-resolved A and B peaks, whereas the other samples show less pronounced features, indicating partial structural deviation.

A comparison of the Ni spectra from the as-prepared samples further highlights structural ordering differences: the EXAFS signal intensity at S1 (left) is strongest for the sample containing 1% Ni and decreases with increasing Fe and Ni content. The only exception is the 5Fe0,1Ni-STO sample, where the low Ni concentration prevented acquisition of a spectrum with an adequate signal-to-noise ratio. This

trend is further supported by the Fourier Transform analysis (not reported), which reveals a progressive reduction in signal intensity corresponding to the first coordination shell (Ni–O), and an even greater decrease for the second and third shells (Ni–Sr and Ni–Ti/Ni bonds).

Representative TEM images of 5Fe-STO and 5Fe5Ni-STO samples are shown in Figures 4.3b and 4.3c. The powders display large nanoparticles with grain sizes ranging from approximately 50 to 100 nm. No significant variations in morphology or particle size were observed for the other perovskite compositions.

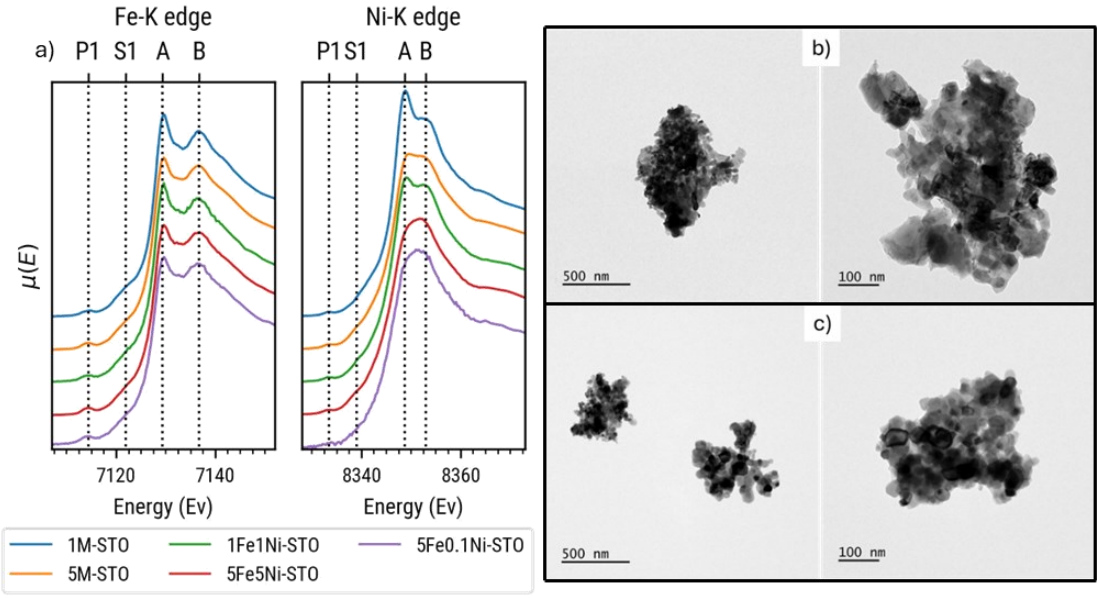

Figure 4.3. a) XAS spectra of all the doped and co-doped STO. M in the legend generically stands for "metal" indicating the mono doped samples. b-c) TEM images of the 5Fe-STO and 5Fe5Ni-STO parental structures, respectively.

4.3.2 Exsolution monitoring

The exsolution process was initially investigated using temperature-programmed reduction (TPR) analysis. The TPR profiles of the Ni-doped and Fe-doped samples, compared with the undoped STO reference, are presented in Figure 4.4. The pristine perovskite lattice exhibits a broad reduction feature between 530 °C and 790 °C, with a maximum at 770 °C, corresponding to hydrogen consumption by the bare lattice. In this case, the total hydrogen uptake is 0.219 mmol g^{-1}. Upon Ni doping (Fig. 4.4a), although the contribution of the STO matrix remains evident, additional reduction features appear that overlap with those of the dopant species. The TPR profile of 1Ni-STO shows a reduction peak at 440 °C that reaches a maximum at 590 °C, which can be attributed to the reduction of Ni(III) to Ni(II), with a total

hydrogen consumption of 0.181 mmol g^{-1}. The most pronounced reduction event occurs near 790 °C and corresponds to the Ni(II) → Ni(0) transition, associated with a hydrogen uptake of 0.300 mmol g^{-1}.

In contrast, the 5Ni-STO sample displays an additional minor reduction peak at 280 °C (0.019 mmol g^{-1} H_2 consumed), probably due to some amorphous like NiO species. A broad feature extending from about 405 °C to a maximum near 565 °C is observed, which corresponds to the reduction of Ni(III) to Ni(II) with a hydrogen consumption of 0.505 mmol g^{-1}. The reduction step around 785 °C, assigned to the Ni(II) → Ni(0) transition, appears slightly shifted to lower temperatures and broader in profile, while its hydrogen uptake remains comparable to that of 1Ni-STO (0.284 mmol g^{-1}). Overall, the total hydrogen consumption increases from 0.488 mmol g^{-1} for 1Ni-STO to 0.807 mmol g^{-1} for 5Ni-STO.

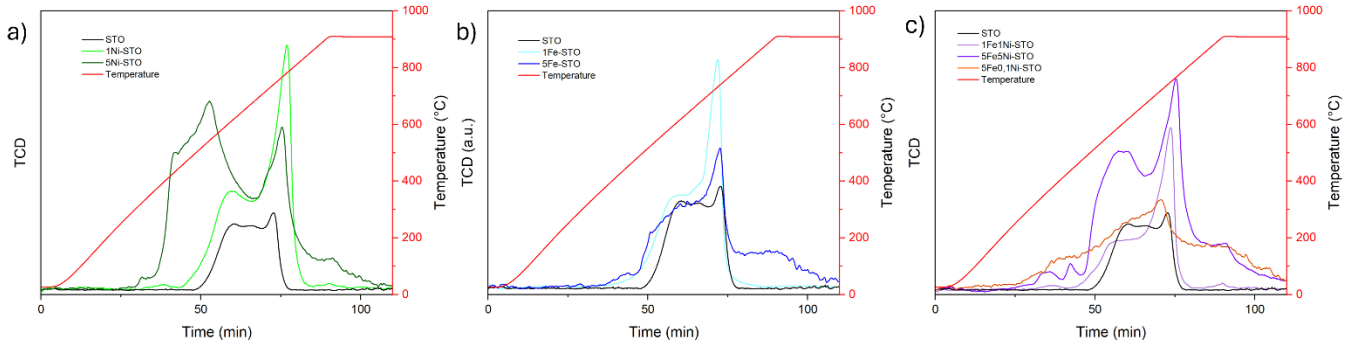

Fig. 4.4: TPR profiles for a) Ni doped; b) Fe doped; c) Ni, Fe co-doped $SrTiO_3$

The TPR profiles of the Fe-STO samples are presented in Figure 4.4b. Similar to the Ni-doped systems, the reduction peaks of the Fe-doped compounds overlap with those of the STO lattice. For both 1Fe-STO and 5Fe-STO, reduction begins at approximately 410 °C, which can be mainly attributed to the Fe(III) → Fe(II) transition. In the case of 5Fe-STO, an additional broad peak appears around 900 °C, likely corresponding to the reduction of Fe(II) to metallic Fe, an event not observed in the 1Fe-STO sample. Increasing the Fe content results in a general broadening of the reduction features. However, in contrast to the Ni-doped samples, the total hydrogen uptake increases only slightly, from 0.306 mmol g^{-1} for 1Fe-STO to 0.357 mmol g^{-1} for 5Fe-STO.

The TPR profiles of the FeNi co-doped systems are shown in Fig. 4.4c. In these samples, the reduction peaks associated with Ni and Fe overlap with those of the pristine STO lattice, making precise assignments difficult. Nonetheless, the introduction of Ni into the 5Fe-STO matrix shifts the onset of reduction toward lower temperatures, beginning at approximately 370 °C. As the Ni content increases up to 5%, the weak shoulder observed at around 610 °C in the 5Fe0.1Ni-STO sample develops into a broader, more intense feature, indicating higher hydrogen consumption and a progressive shift to lower temperatures. Additionally, a peak at approximately 790 °C is observed in all co-doped samples, with

its intensity increasing proportionally with Ni content. All TPR profiles also exhibit a broad shoulder around 900 °C, suggesting that reduction processes continue at higher temperatures.

The reduction behaviour of the iron and nickel species in doped and co-doped STO samples was further investigated using X-ray absorption spectroscopy (XAS), as shown in Figure 4.5. For Fe (Fig. 4.5a), no significant structural changes are evident with varying dopant concentration or reduction temperature. However, subtle variations in the metal-edge region, particularly for 5Fe-STO upon heating at 900°C, suggest the onset of metallic Fe formation facilitated by the higher Fe content in the perovskite matrix. This result seems in agreement with the TPR results where the occurrence of a weak and broad band appears around 900 °C, ascribable to the reduction of Fe(II) to Fe(0).

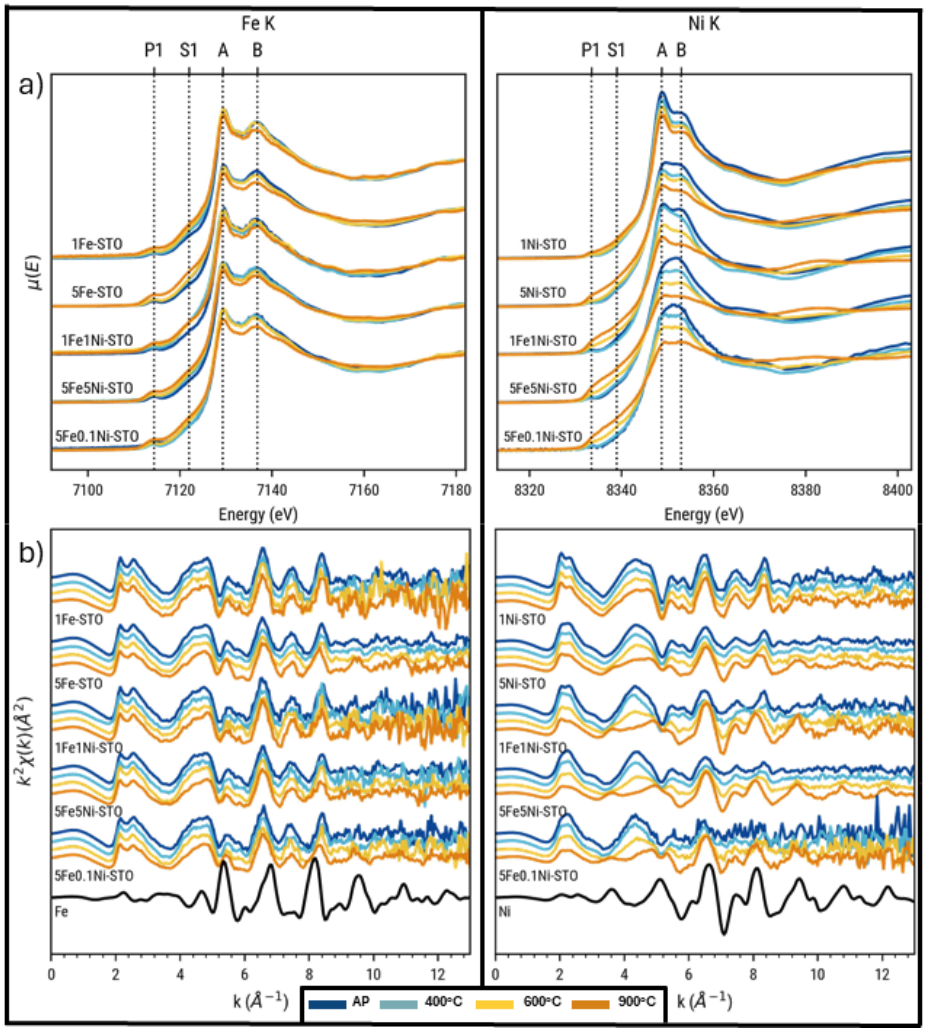

Figure 4.5: a) XANES spectra of the undoped and doped perovskite samples recorded at the Fe K-edge (left) and Ni K-edge (right); b) EXAFS spectra of the perovskite samples recorded at the Fe K-edge (left column) and Ni K-edge (right column). (e0 set for both at the metal edges, 7112 and 8333 eV). In black the spectra of the corresponding doping metal.

In contrast, the Ni-STO samples (Fig. 4.5b) display greater variability in the XANES region. In accordance with TPR, metallic Ni formation is observed at 600 °C and 900 °C in all samples, as evidenced by the

increased intensity at 8333 eV. This effect is significantly enhanced in the presence of Fe: at 900 °C, the fraction of metallic Ni increases from approximately 21% (in Ni-only samples) to about 62% when Fe is co-doped, highlighting a strong synergistic interaction between the two metals during reduction.

The concentration of the metallic fraction of Ni and Fe has been calculated using the LCF. The results indicate that for iron, the formation of the metal phase begins at a lower temperature, with a concentration of 4-11% of Fe at 400°C; it remains stable until 600°C and then increases until 900°C, approximately doubling (21-28%). Nickel data, however, show that the formation of the metallic phases begins above 400°C, and their concentration increases with temperature at a much higher rate than Fe. The rate of conversion of Ni in its metallic phase is proportional to the Fe and Ni concentrations in the structure: 1Ni-STO and 5Ni-STO display a final conversion of 23% and 45%, respectively, while samples containing also Fe show a conversion in the range of 58-70%.

The analysis of EXAFS spectra (Figure 4.5b) supports these conclusions, revealing that the profiles of Fe do not show changes apart from a new oscillation appearing at 9.4 Å, more pronounced in the samples heated at 900°C, related to the formation of the metallic phase (Fig. 4.5b, left). For the Ni edge, instead, it is possible to observe the high conversion from the perovskite structure to the metallic Ni structure (Fig. 4.5b, right).

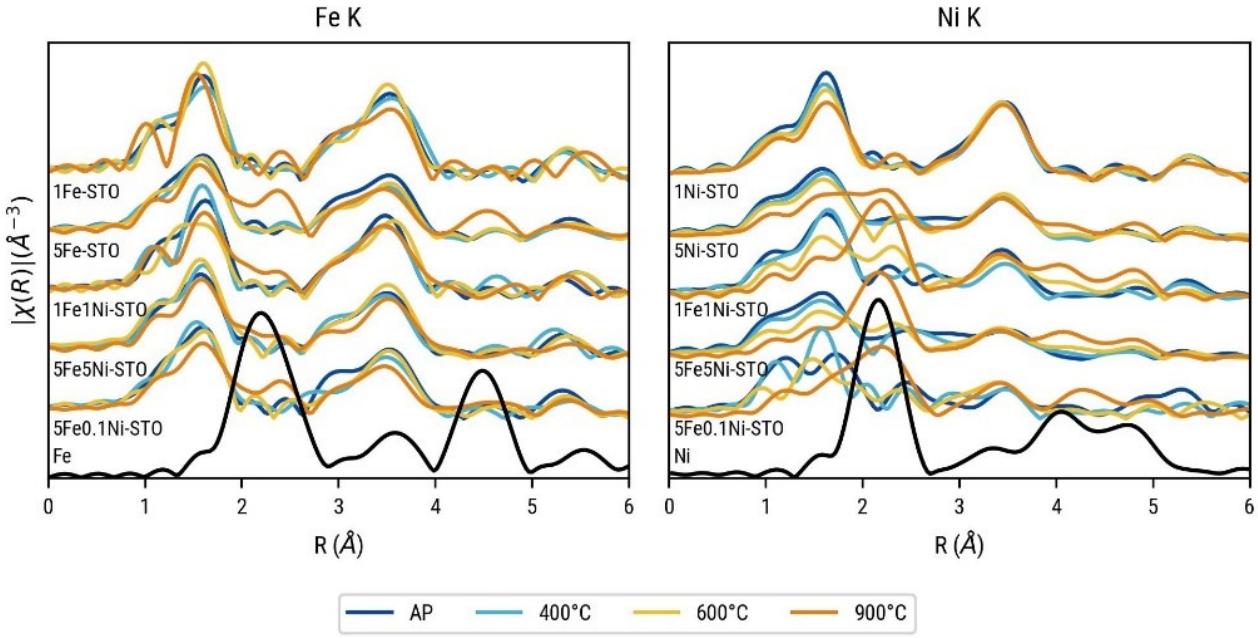

Figure 4.6. Fourier Transform of the EXAFS region of the 28 samples recorded for all the samples at the Fe K-edge (column left) and Ni K-edge (column on the right). In black the spectra of the single the metals.

Figure 4.6 shows the effects of the temperature pre-treatment on the Fourier Transform. Here, the formation of the metallic bond is marked by the appearance of the peak at 2.2 Å, related to the metallic first shell. As concerns the iron species (Fig. 4.6 left), the bond is barely visible in the 1Fe-STO sample, while it is mostly detectable in 5Fe-STO where the LCF also shows a higher iron reduction. Interestingly,

this feature becomes more evident in co-doped perovskites and, specifically in 5Fe0.1Ni-STO after reduction at 900°C, suggesting that even a tiny presence of Ni seems to enhance the iron exsolution. In the Ni spectra (Fig.4.6, right), besides an obvious peak related to the generation of Ni(0) in the materials with the highest metal doping (i.e. 5Ni-STO), the presence of Fe in the perovskites promotes the formation of the metallic phase after heating, regardless of the Ni concentration.

From the fit, we can observe that the distances of Ni inside the perovskite structure are stable regardless of the heat treatment, as can be observed from the results Table 4.1. The same conclusion can be drawn from the data of Fe: the perovskite structure remains stable regardless of the temperature, and at high temperature the structure of metallic Fe is the same as the metallic BCC structure.

Table 4.1: EXAFS fit results in terms of first neighboring distances

Ni Edge

Sample	Distance (Å)						
	Ni-O	Ni-Sr	Ni-Ti	Ni-Ni	Ni-Ni (2)	Ni-Ni (3)	Ni-Ni (4)
N1 AP	2.03(2)	3.35(2)	3.87(2)	-	-	-	-
N1 400	2.03(2)	3.37(2)	3.85(2)	-	-	-	-
N1 600	2.03(2)	3.37(2)	3.86(2)	-	-	-	-
N1 900	2.02(2)	3.36(2)	3.86(2)	2.48(2)	-	-	-
N5 900	2.03(2)	3.3(2)	3.9(1)	2.48(2)	3.51(4)	4.30(4)	-
F1N1 900	2.02(2)	3.3(2)	3.9(1)	2.49(2)	3.53(4)	4.32(4)	-
F5N5 900	-	-	-	2.49(2)	3.52(4)	4.31(4)	4.98(6)
F5N01 900	-	-	-	2.49(2)	3.53(4)	4.32(4)	-

Fe Edge

Sample	Distance (Å)					
	Fe-O	Fe-Sr	Fe-Ti	Fe-Fe	Fe-Fe (2)	Fe-Fe (3)
F1 AP	1.99(2)	3.36(3)	4.0(1)			
F1 400	1.99(2)	3.38(3)	3.9(1)			
F1 600	1.99(2)	3.34(3)	3.9(1)			
F1 900	2.00(2)	3.35(2)	3.9(1)	2.4(2)		
F5 900	1.96(2)	3.35(2)	3.88(2)	2.45(2)	2.83(2)	4.00(3)
F1N1 900	2.0(1)	3.4(2)	3.9(2)	2.5(2)		
F5N5 900	1.97(2)	3.35(3)	3.9(1)	2.48(2)	2.86(2)	4.0(1)
F5N01 900	1.96(2)	3.35(2)	2.89(2)	2.45(2)	2.83(4)	4.00(4)

Beyond the previously mentioned analysis, STEM investigations enabled a detailed study of the morphological changes in Fe-STO, Ni-STO, and co-doped powders during the exsolution process.

Figure 4.7 presents STEM images and the corresponding EDX elemental mapping of Fe and Ni for the differently doped $SrTiO_3$ samples after exsolution at 900°C. A comparative analysis of the images indicates that nearly all samples exhibit localized regions of increased dopant metal concentration, which are attributed to the presence of metal nanoparticles on the surface. Notably, the 5Fe-STO (Fig. 4.7a) displays a lower particle density compared to the other samples, as well as particles with less defined boundaries. This observation suggests that the exsolution process in this case may be incomplete, potentially reflecting a state of incipient segregation rather than fully developed nanoparticle formation. To further investigate the oxidation state of the surface Fe species, X-ray photoelectron spectroscopy (XPS) was employed, as detailed in the following section.

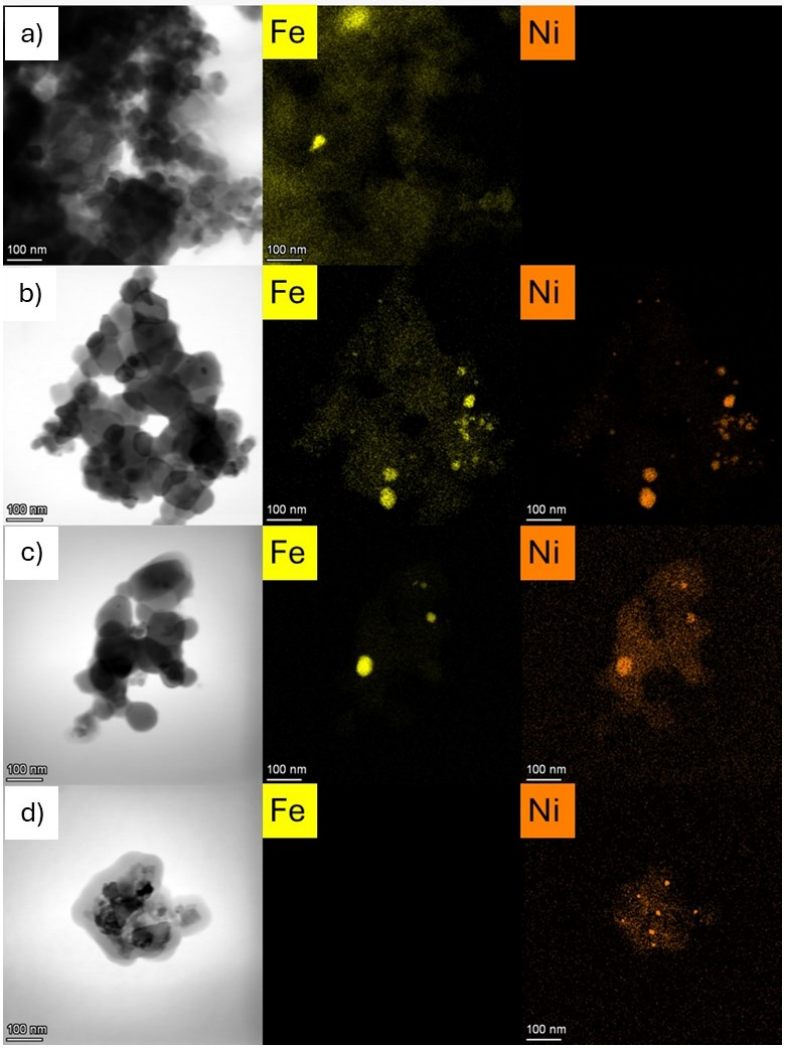

Figure 4.7. STEM images and corresponding Fe and Ni EDX elemental maps of: a) 5Fe-STO; b) 5Fe5Ni-STO: c) 5Fe0.1Ni-STO; d) 5Ni-STO after exsolution at 900°C.

In agreement with XAS findings, the Fe-Ni co-doped samples (Fig. 4.7b and 4.7c) demonstrate a markedly enhanced exsolution behaviour. TEM micrographs and corresponding EDX elemental maps reveal in fact well-defined nanoparticles anchored to the perovskite surface. The overlap of Fe and Ni regions confirms their co-localization, indicating the formation of bimetallic or co-exsolved nanoparticles. According to PXRD and XAS, no alloy generation can be inferred. The observed high particle density and uniform dispersion suggest a synergistic interaction between Fe and Ni that facilitates accelerated exsolution kinetics and improved nanoparticle stabilization. Remarkably, this effect is evident even at low Ni doping levels (e.g., 5Fe0.1Ni-STO), where discrete surface nanoparticles are still clearly present, underscoring the pronounced sensitivity of the exsolution process to dopant composition.

Finally, consistent with previous reports in the literature [28], [29], [30], Ni is capable of exsolving under reducing conditions even in the absence of Fe (Fig. 4.7d). The TEM image reveals isolated nanoparticles on the surface, and EDX analysis confirms that these regions contain only Ni, indicating the formation of pure Ni nanoparticles.

The elemental composition and oxidation states of 5Fe-STO and 5Ni-STO perovskites were analysed by XPS, examining specifically the Fe 2p3/2 and Ni 2p3/2core levels before and after reduction (Fig. 4.8).

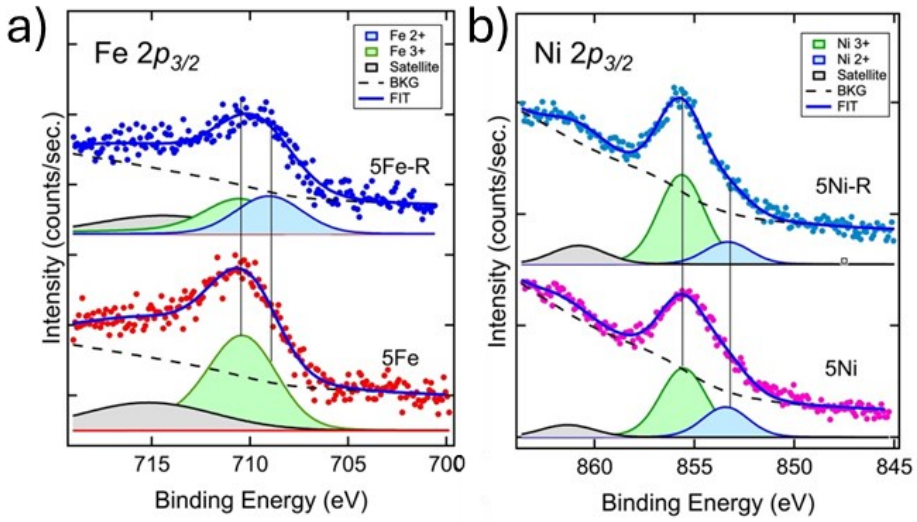

Fig. 4.8: XPS core levels spectra of: a) 5Fe-STO in the Fe 2p3/2 region; b) 5Ni-STO respectively in the and Ni 2p3/2 region before (top) and after redox exsolution (bottom, labelled as 5Fe-STO_R and 5Ni-STO_R, respectively). The intensities of all the spectra have been normalized to the total Ti 2p intensity. Superimposed to the experimental data (dots) are shown the fit results (blue line) and the fit components, all including the background signal (BKG).

For 5Fe-STO, the spectrum registered before exsolution (Fig. 4.8a, bottom) shows only the contribution of Fe^{3+}species, consistent with the XAS results (see Fig. 4.3a). After reduction, no metallic Fe (0) is detected; instead, an increase in the reduced iron components is clearly observed (Fig. 4.8b, top).

The same analysis on the 5Ni-STO sample in the Ni 2p region reveals spectral components corresponding to Ni^{2+} and Ni^{3+} species (Fig. 4.8b, bottom), which appear substantially unaffected by the reduction process (Fig. 4.8b, top), despite the formation of Ni-based nanoparticles on the surface as detected by TEM investigation (see Fig. 4.7d).

However, when the metals are used together as dopants in the perovskite, the situation changes (Fig. 4.9).

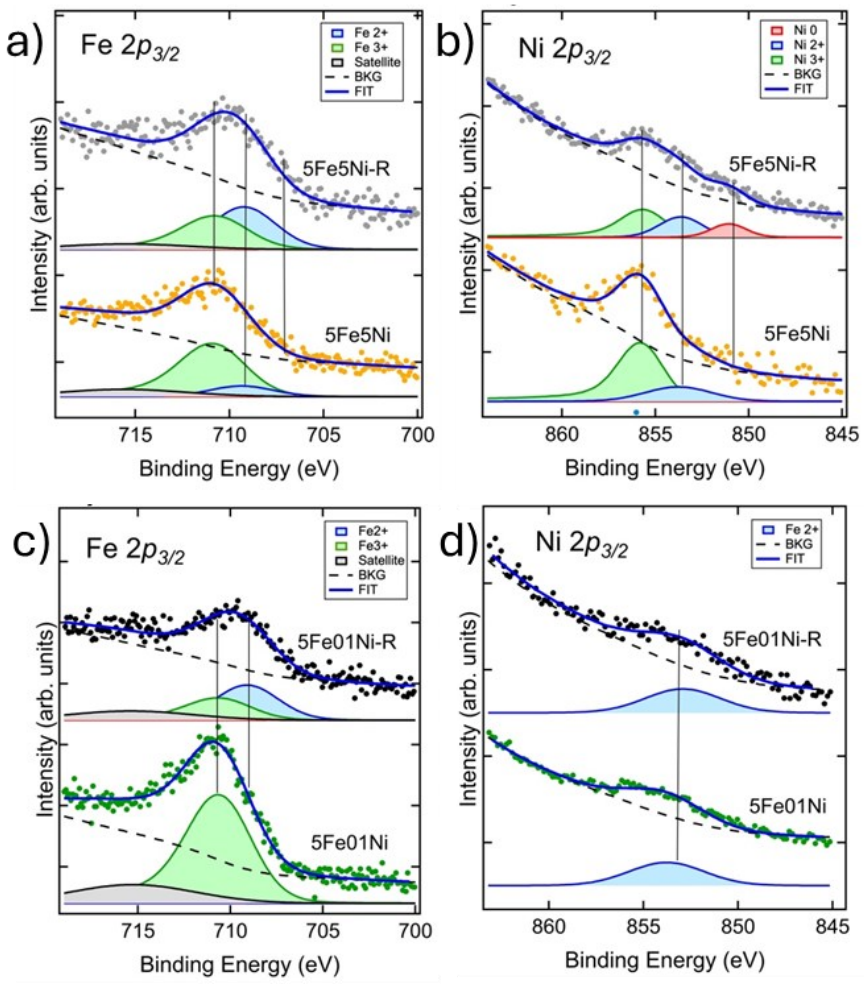

Fig. 4.9: XPS core levels spectra of a) and b) 5Fe5Ni-STO and c, d) 5Fe0.1Ni-STO in the in the Fe 2p3/2 region and Ni 2p3/2 region, respectively. Spectra were acquired before (top) and after redox exsolution (bottom, labelled as 5Fe5Ni-STO_R and 5Fe0.1Ni-STO_R, respectively). The intensities of all the spectra have been normalized to the total Ti 2p intensity. Superimposed to the experimental data (dots) are shown the fit results (blue line) and the fit components, all including the background signal (BKG).

In the Fe 2p3/2 spectral region, the 5Fe5Ni-STO sample displays a behaviour very similar to that of the single-doped perovskite (Fig. 4.9a) with no Fe(0) species detectable on the surface of the catalyst after reduction. Examining the Ni behavior, a weak but discernible metallic Ni signal appears upon exsolution (Fig. 4.9b) suggesting, in agreement with XAS, that the co-presence in the sample of iron promotes partial Ni reduction and exsolution, unlike what is observed in 5Ni-STO.

Finally, in the 5Fe0.1Ni sample, a similar trend of the iron species is observed after exsolution (Fig. 4.9c), while only minor changes appear in the Ni signal. Nevertheless, a reduction effect cannot be excluded, although the slight shift of the Ni 2p3/2 peak toward lower binding energies may fall within experimental uncertainty.

Overall, these outcomes suggest that Fe enhances Ni reducibility, likely by inducing oxygen vacancies or altering the local electronic environment. Conversely, Fe remains mainly in mixed Fe^{2+}/Fe^{3+} states,

undergoing only minor reduction after treatment, even in the presence of Ni. It is however worth noticing that these results are not in contrast with XAS data nor with existing literature. In fact, while the XPS is a surface technique, with a detection limit in the range of 1-0.1 atom % [31] in the first few layers of the sample surface, the XAS can reach ppm sensitivity [32] in the whole bulk of the material, thus providing information on the surface and on the bulk of the materials, simultaneously, with greater precision. Finally, for what concerns the literature studies, it should be noted that articles on this topic commonly involve much higher doping concentration [12], [33] as well as higher A-site deficiency degree [5], [34] both contributing to easier ions mobility, thus favouring exsolution.

4.3.3 EPR monitoring

To explore the evolution of defect structures in both mono-doped and co-doped STO samples during the exsolution process, an extensive X-band EPR study was carried out. The spectra were recorded under vacuum conditions ($p < 10^{-5}$ mbar) at 130 K, following a reducing treatment in H_2/Ar at temperatures ranging from 400 to 900 °C. These measurements provide valuable insights into the coordination environment and aggregation state of metal ions, as well as the dynamic processes associated with the modification of the metal ions.

Results for all the samples are reported below. The EPR spectrum of as prepared 1Fe-SrTiO3 (Fig. 4.10) enlightens the presence of different Fe species in the sample. In particular, multiple peaks can be detected in the low field region (g = 9,8-8,8, g = 6.02, g = 4.84, g = 4.33, insert of Fig. 4.10a) as well several spectral lines arise in the medium field region (g = 2.24-2.21, g = 1.99, g = 1.78 – 1.83, Fig. 4.10a). This great number of signals is ascribable to the fact that Fe ions inside the $SrTiO_3$ lattice can be present in different oxidation states as well as with different coordination environment. In particular, from a deep literature survey the following attributions can be suggested (Table 4.2) [35], [36], [37], [38], [39], [40], [41], [42], [43], [44], [45], [46], [47], [48].

Table 4.2: g-values and tentative attributions of the different Fe-centers in 1FeSTO sample as obtained from literature survey.

Metal species	Coordination	g value
Fe (II) high spin	Tetrahedral	$g_{\|\|} = 9.54$ $g_{\perp} = 4.33$
Fe (III) high spin - V_O	Axial	$g_{\|\|} = 6.02$ $g_{\perp} = 2$
Fe (III) high spin	Rhombic distortion	g = 4.84
Fe (III) high spin	Cubic	$g^{iso} \sim 2$ with two satellites at A=350 G

The spectral complexity is further highlighted by the evolution of the signal during treatment under a reducing atmosphere. After thermal treatment at 400 °C, a moderate decrease in the intensity of the main resonance at g ≈ 2 is observed, whereas no additional significant changes occur upon further heating to higher temperatures (Fig. 4.10a). This behavior indicates that, during exsolution in 1Fe-STO, only a small fraction of iron species—likely situated near the surface of the perovskite lattice and possibly associated with amorphous or interstitial Fe–O_x-like impurities—undergo selective reduction and migration, resulting in the formation of zero-valent or diamagnetic Fe species. In contrast, the majority of Fe atoms, presumably incorporated as substitutional defects within the perovskite lattice, remain unreduced even after treatment at 900 °C. This observation points to the presence of highly stable defect sites that require substantially higher thermal activation energies to become mobile and undergo reduction.

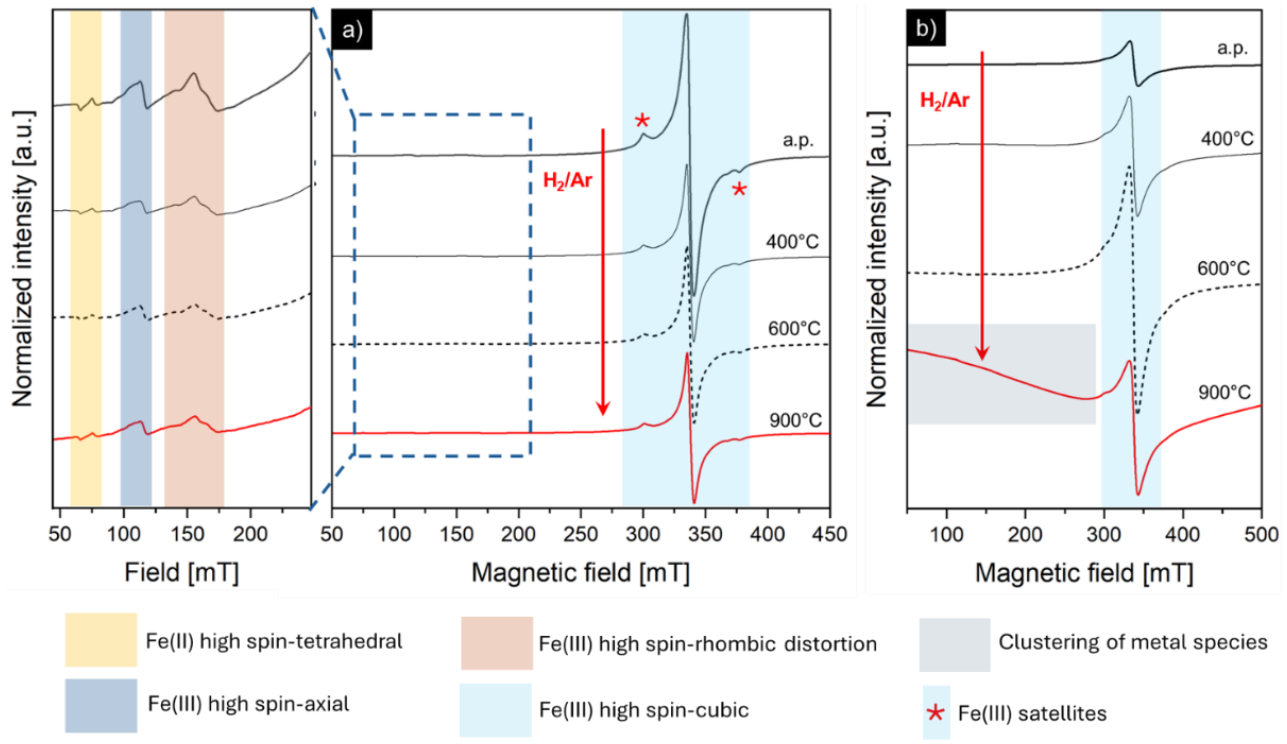

Fig. 4.10: EPR spectra recorded at 130 K of (a) 1Fe–STO and (b) 5Fe–STO nanopowders, both as prepared (a.p.) and after thermal reduction at various temperatures under an H_2/Ar atmosphere. The left panel highlights the iron-related signals observed at low magnetic fields.

Upon increasing the iron dopant concentration (5Fe-STO sample), a broadly similar behavior is observed (Fig. 4.10b). In this case, the EPR spectrum of the as-prepared material is dominated by broad features, which can be attributed to strong dipolar interactions between closely spaced iron species. In contrast to 1Fe-STO, a pronounced increase in the intensity of the iron-related resonances is already evident upon reduction of 5Fe-STO at 400 °C. According to Drahus et al. [46], this behavior may be

associated with changes in the oxidation state of iron, whereby a fraction of the EPR-silent Fe^{4+} or Fe^{5+} species—commonly observed in highly doped perovskites [49] is converted into paramagnetic Fe^{3+}.

When the reduction temperature is further increased to 900 °C, reduction of lattice oxygen in the perovskite framework occurs, which in turn promotes the reduction of the dopant ions and leads to a substantial depletion of the EPR signal. In addition, the extensive broadening of the spectral features across the entire field range indicates the presence of strongly dipolarly coupled iron species, consistent with Fe-ion migration followed by aggregation into clustered or interacting structures.

Overall, these findings demonstrate that the chemical environment of iron species in Fe-STO is considerably more heterogeneous and that the exsolution process is far less straightforward than initially anticipated.

A comparable analysis was also performed for Ni-doped samples. Ni(II), a d^8 ion, contains two unpaired electrons and thus exhibits a total spin state of S = 1, making it susceptible to zero-field splitting (ZFS). When Ni(II) substitutes for Ti(IV) in the perovskite lattice, charge compensation typically occurs through the formation of oxygen vacancies (V_O). These vacancies may reside in the vicinity of Ni centers, leading to the formation of defect complexes such as $(Ni_{Ti}''\text{-}V_O^{\bullet\bullet})^X$ or $(Ni_{Ti}'\text{-}V_O^{\bullet\bullet})^{\bullet}$. The results obtained are the following.

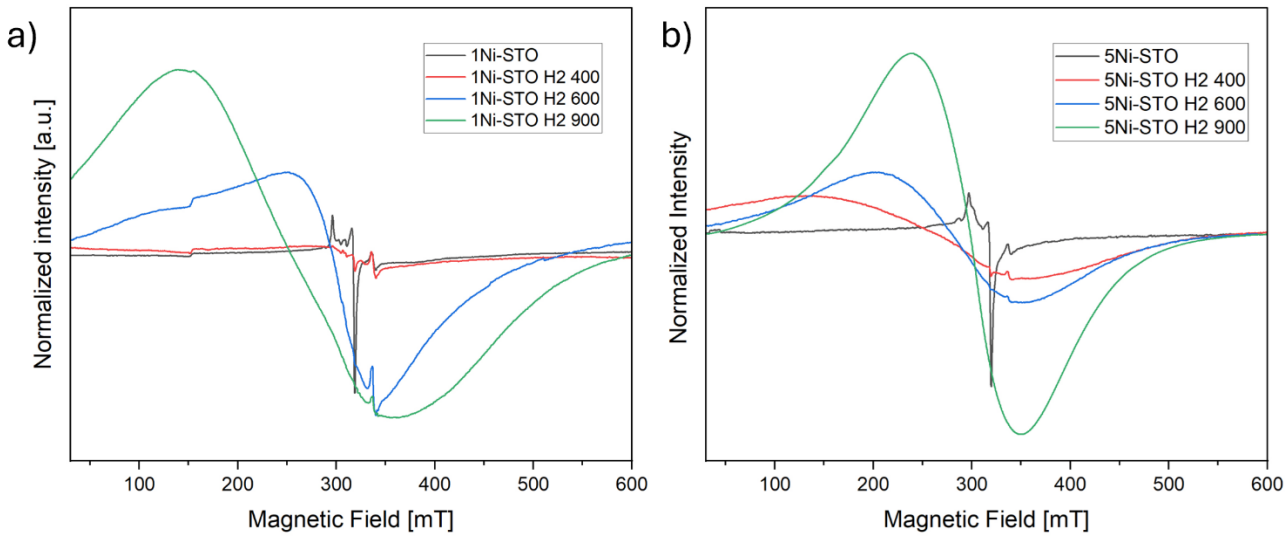

Fig. 4.11: EPR spectra of: a) 1Ni-STO as prepared and reduced at different temperature; b) 5Ni-STO as prepared and reduced at different temperatures.

The low loading Ni doped sample show the presence of few different Ni species, again due to the intercalation of Ni in the perovskite lattice (Fig. 4.11a). When this intercalation occurs, Ni (II) can also be oxidised to Ni (III) as already seen in XPS (Fig. 4. 8) and the centres present can be different. In particular, three different centres can be observed, two signal at g ≈ 2.20 due to the presence of Ni (II)

and Ni (III) in an octahedral site and a signal which can be attributed to an axial centre with $g_{||} = 2.31$ and $g_{\perp} = 2.12$ [50]. The attribution to this last centre is still uncertain due to its shift at lower field compared to the ones reported in the literature [50], [51] but it might be due to the presence of a $(Ni_{Ti}'\text{-}V_O^{\bullet\bullet})^{\bullet}$ pair or a Ni(I) centre with axial symmetry in which the strong crystal field of the perovskite as well as the Jahn-Teller distortion shifts the signal at lower fields. Upon reduction the signal intensity initially decreases due to the reduction of Ni (II) and Ni (III) to probably some EPR-silent species (i.e Ni(I) and Ni(0)).

When the temperature reaches 600°C, the signal increases in intensity increases again, but it broadens as well. This indicates the presence of multiple several coupled Ni-Ni species, however, even when the signal broadens even if the fingerprint of some isolated Ni centres remains present ($g \approx 2$) and can be seen as sharp signals at $g \approx 2$ under the wide band (Fig. 4.11a). This further highlights the occurrence in 1Ni-STO of metal species exhibiting distinct redox behaviour, likely resulting from differences in coordination environment or lattice intercalation. This again underline the presence of some Ni species with different redox behaviour compared to the others, probably due to the different coordination or intercalation in the lattice. The same type of information can also be retrieved by the 5Ni-STO (Fig. 4.11b). However, at higher loading, the coupling among the paramagnetic centres is boosted and therefore broadened features dominate the spectrum (Fig. 4.11b). Once again, this phenomenon makes more difficult the identification of the species in the material.

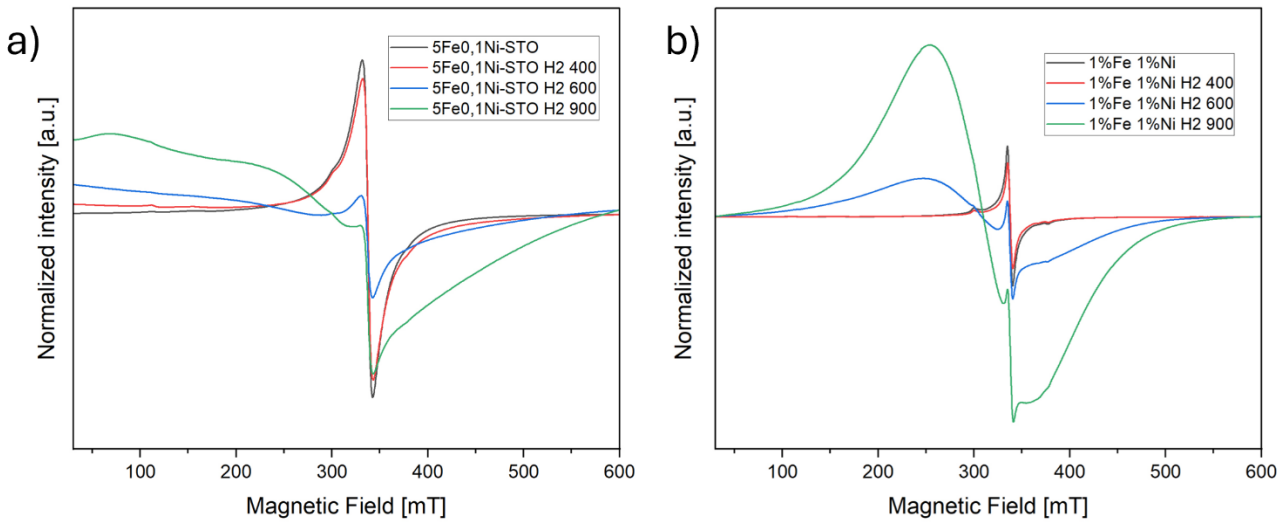

Fig. 4.12: EPR spectra of the as-prepared and exsolved materials for the co-doped a) 5Fe0.1Ni-STO and b) 1Fe1Ni-STO perovskites.

Finally, the behavior of co-doped perovskite samples containing both Fe and Ni was investigated. Irrespective to Ni concentration, the EPR spectra of the as-prepared materials are dominated by features characteristic of Fe(III). However, upon reduction, the samples exhibit markedly different

behaviors. In particular, for the 1Fe1Ni-STO sample (Fig. 9b), thermal treatment at 600 °C results in the occurrence of a broad and intense feature associated with metal–metal coupling, similar to that observed in the Ni-doped samples. Notably, a strong signal at g ≈ 2 remains visible, suggesting the presence of isolated, non-reduced metal centres.

In contrast, when the Fe loading in the perovskite is significantly higher than that of Ni (i.e. 5Fe0.1Ni-STO sample), the spectral response changes considerably. Compared to the sample with only 5% Fe, the EPR signal intensity begins to decrease already at 600 °C, indicating the onset of Fe(III) reduction. Concurrently, the observed signal broadening suggests increased magnetic coupling between metal centres, consistent with the migration and spatial clustering of reduced metal ions. Upon further temperature increase, the overall signal continues to decrease while broadening intensifies, reinforcing the interpretation of progressive metal aggregation and reduction.

In summary, EPR monitoring completes the picture drawn by XAS and XPS analyses, unveiling additional insights on the redox behaviour of the investigated metals. Fe ions, when individually incorporated into the perovskite lattice, are difficult to get reduced and exsolved, probably due to the high energy input required. Conversely Ni ions are more easily reduced and mobile. When both Ni and Fe are introduced as dopants in the perovskite, a synergistic action between the two metal is evident, with the promotion, even at low Ni content, of Fe exsolution.

4.3.4 Catalytic tests

The synthesized perovskite catalysts were tested for CO_2 hydrogenation, focusing on CO production via the reverse water–gas shift (RWGS) reaction. The corresponding results are shown in Figure 4.13. As CO_2 hydrogenation to CO is an endothermic process, elevated temperatures are necessary to attain appreciable CO_2 conversion and CO selectivity. Moreover, operating under lower pressure conditions further favours the reaction [52].

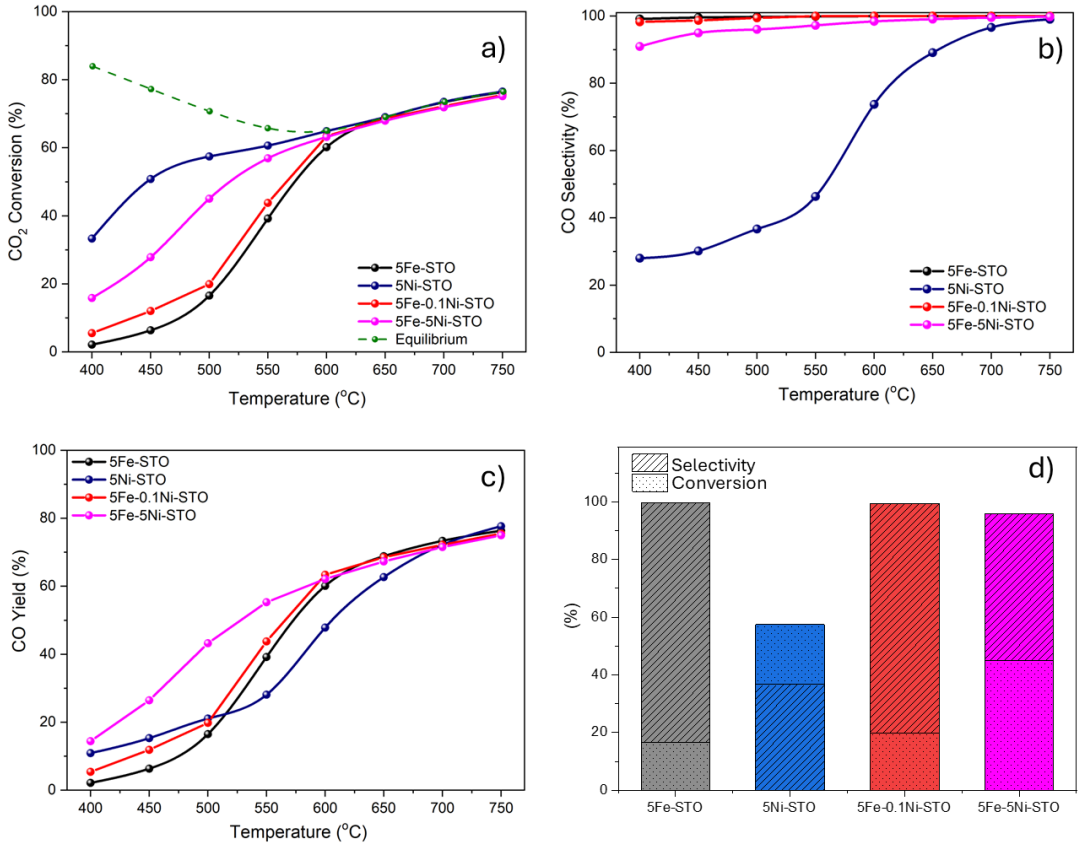

Fig. 4.13: Catalytic performance of Fe- and Ni-doped $SrTiO_3$ (a) CO_2 conversion, (b) CO selectivity, and (c) CO yield.

As a general trend, the catalytic activity, expressed in terms of CO_2 conversion (Fig. 4.13a), increases with increasing temperature for all catalysts, with equilibrium values being reached between 600 °C and 750 °C. As expected, the monometallic Fe–STO catalyst exhibits the lowest activity among all samples, which is attributed to the limited extent of Fe reduction at the catalyst surface, as confirmed by XPS analysis. Consequently, the predominance of FeO_x species results in low CO_2 conversion and high CO selectivity, considering that metallic Fe is the active phase for CO_2 methanation. Notably, even the introduction of small amounts of Ni (as low as 0.1%) into Fe–STO significantly enhances the overall catalytic activity, leading to higher CO_2 conversion across the entire temperature range investigated. The performance of Ni–Fe bimetallic catalysts supported on various oxides has been widely studied for CO_2 hydrogenation and compared with that of monometallic Ni catalysts. It is well established that catalytic activity and product distribution (CH_4 versus CO) strongly depend on metal composition, oxidation states, and the formation of alloy phases [53]. In particular, several studies report that fully reduced Ni–Fe bimetallic systems outperform monometallic Ni catalysts in terms of CO_2 conversion, with CH_4 as the predominant product. Conversely, the presence of metal oxides—especially FeO_x—tends to steer the reaction toward CO formation, typically at the expense of CO_2 conversion relative to monometallic Ni catalysts [54], [55].

In the present study, the highest CO_2 conversion was achieved with the monometallic Ni catalyst rather than the Ni–Fe materials. Nickel, known for its strong hydrogenation capability, directed the reaction predominantly toward CH_4 formation in the temperature range of 400–550 °C. In contrast, both Ni–Fe bimetallic catalysts exhibited lower CO_2 conversion than monometallic Ni and showed high selectivity toward CO, despite the presence of Ni within the perovskite lattice. These findings are consistent with the work of Piano *et al.* [56], who reported reduced methanation activity for Ni_5Fe_5 catalysts supported on SiO_2 or CeO_2–ZrO_2 compared to monometallic Ni or Ni–Fe systems with higher Ni loadings (e.g., Ni_9Fe_1, $Ni_{7.5}Fe_{2.5}$).

The superior methanation performance of certain Ni–Fe bimetallic catalysts reported in the literature has been attributed to the formation of Ni–Fe alloy phases (often Ni_3Fe) and metallic Fe species formed via the reduction reaction $Fe_3O_4 + Ni \rightarrow Fe + Ni_{1-x}Fe_x$ [57] [58]. These phases constitute the active sites responsible for enhanced CO_2 conversion and CH_4 selectivity relative to monometallic Ni. In contrast, although the addition of Ni in the present catalysts promotes Fe exsolution and reduction, CO remains the dominant product for all Fe-containing samples, with CO selectivity ranging from ~90% for 5Fe–5Ni–STO to nearly 100% for undoped 5Fe–STO, even at the low reaction temperature of 400 °C. This behavior is attributed to the persistence of a large fraction of unreduced Fe oxides, likely incorporated within the lattice as $SrFeTiO_3$, even after high-temperature treatment at 900 °C. Consistently, PXRD and XAS analyses reveal the absence of Ni–Fe alloy phases, highlighting the intrinsic role of Fe oxides in selectively catalyzing CO_2 reduction to CO (Fig. 4.13b).

Similar conclusions were reported by Liu *et al.* [59], who demonstrated that incorporating Ni into a $LaSrFeO_3$ catalyst (Ni/Fe = 1) using a hybrid DBD plasma–catalysis system resulted in improved metal dispersion, smaller particle sizes, and stronger metal–support interactions. The high CO selectivity observed was attributed to incomplete reduction of Fe species retained in the perovskite lattice, which promoted oxygen vacancy formation and active oxygen mobility—key parameters for the reverse water–gas shift (RWGS) reaction proceeding via a redox mechanism. This behavior is also evident in the present results (Fig. 10c), where the CO yield is significantly higher for the co-doped catalysts. In particular, 5Fe–5Ni–STO outperforms both 5Fe–0.1Ni–STO and 5Fe–STO in the low-temperature range of 400–550 °C, indicating an optimal balance between activity and selectivity and underscoring its potential as a highly efficient RWGS catalyst.

Studies addressing the synergistic effects of Fe and Ni in perovskite structures for thermocatalytic CO_2 conversion remain scarce. One notable example is the work of Martin *et al.* [61], who investigated $Ln_{0.5}Ba_{0.5}Fe_{1-x}Ni_xO_3$ (Ln = Pr, Sm; x = 0, 0.1) catalysts and observed a decrease in reactivity upon Ni doping relative to monometallic Fe catalysts. As noted by the authors, this finding is somewhat unexpected given the high intrinsic activity of Ni and the increased oxygen vacancy concentration upon reduction. They attributed this behavior to depletion of lattice oxygen in the Ni-doped, exsolved materials.

In summary, the enhanced catalytic performance of the Fe–Ni co-doped samples reported herein can be ascribed to a synergistic interaction between the two metals: Fe facilitates oxygen vacancy formation and enhances redox activity and CO selectivity, while Ni promotes H_2 dissociation and improves overall CO_2 conversion (Fig. 4.13d).

4.4 Conclusion

In this chapter, the systematic synthesis, characterization, and catalytic evaluation of Ni- and Fe-doped $SrTiO_3$ perovskites have been presented, with particular emphasis on elucidating the mechanisms governing their exsolution behaviour. Through the combination of complementary analytical techniques like XAS, XPS, TEM/EDX, and, notably, EPR spectroscopy the distinct redox dynamics and coordination environments of Fe and Ni within the perovskite lattice were examined in detail. The results demonstrate that while Ni readily exsolves to form metallic nanoparticles at comparatively low temperatures, Fe remains more strongly stabilized within the lattice and requires higher thermal energy to exsolve. moreConversely, when both metals coexist in the lattice, a cooperative effect arises: the presence of Ni lowers the energy barrier for Fe migration, enabling the formation of co-exsolved bimetallic nanoparticles even at low Ni concentrations, while Fe promotes the exsolution of metallic Ni (Fig. 4.8). This highlights the synergy between the two metals and their mutual facilitation in reduction and exsolution., when both metals are present in the lattice, a cooperative effect emerges: the presence of Ni lowers the energetic barrier for Fe migration, enabling the formation of co-exsolved bimetallic nanoparticles, even at low Ni concentrations, and the presence of Fe allows the exsolution of metallic Ni (Fig. 4.8) thus underlining the synergy between the two metals and the reciprocal help in being reduced and exsolve. Finally, EPR spectroscopy proved particularly valuable in tracking the evolution of defect structures during this process, offering insights into the coexistence of isolated, lattice-anchored metal centres and increasingly coupled metallic species as reduction progresses.

The surface-decorated perovskites obtained through controlled exsolution were subsequently evaluated in the reverse water–gas shift (RWGS) reaction. The catalytic results underscore the relevance of the exsolution-driven interface between metal nanoparticles and the oxide support, which provides highly active sites for H_2 activation and facilitates CO_2 conversion probably through a Mars–van Krevelen-type mechanism. Moreover, the co-doped systems exhibited enhanced catalytic performance relative to their monometallic counterparts, confirming the beneficial synergy between Fe and Ni in stabilizing active interfacial regions and promoting efficient redox cycling. Overall, the combined synthetic and analytical approach adopted here not only clarifies the mechanistic basis of Ni–Fe co-exsolution but also establishes design principles for tuning the structure, composition, and functionality of exsolved catalysts for applications in CO_2 conversion and related energy-relevant processes.

Bibliography

[1] K. Kousi, C. Tang, I. S. Metcalfe, and D. Neagu, “Emergence and Future of Exsolved Materials,” May 01, 2021, *John Wiley and Sons Inc*. doi: 10.1002/smll.202006479.

[2] D. Neagu *et al.*, “Nano-socketed nickel particles with enhanced coking resistance grown in situ by redox exsolution,” *Nat Commun*, vol. 6, Sep. 2015, doi: 10.1038/ncomms9120.

[3] S. Li, Q. Qin, K. Xie, Y. Wang, and Y. Wu, “High-performance fuel electrodes based on NbTi0.5M 0.5O4 (M = Ni, Cu) with reversible exsolution of the nano-catalyst for steam electrolysis,” *J Mater Chem A Mater*, vol. 1, no. 31, pp. 8984–8993, Aug. 2013, doi: 10.1039/c3ta10404d.

[4] Y. R. Jo *et al.*, “Growth Kinetics of Individual Co Particles Ex-solved on SrTi0.75Co0.25O3-δ Polycrystalline Perovskite Thin Films,” *J Am Chem Soc*, vol. 141, no. 16, pp. 6690–6697, Apr. 2019, doi: 10.1021/jacs.9b01882.

[5] Y.-F. Sun *et al.*, “A-site-deficiency facilitated in situ growth of bimetallic Ni–Fe nano-alloys: a novel coking-tolerant fuel cell anode catalyst,” *Nanoscale*, vol. 7, no. 25, pp. 11173–11181, 2015, doi: 10.1039/C5NR02518D.

[6] Y. Lv *et al.*, “High-Efficiency Perovskite Solar Cells Enabled by Anatase TiO2 Nanopyramid Arrays with an Oriented Electric Field,” *Angewandte Chemie*, vol. 132, no. 29, pp. 12067–12074, Jul. 2020, doi: https://doi.org/10.1002/ange.201915928.

[7] O. Kwon *et al.*, “Self-assembled alloy nanoparticles in a layered double perovskite as a fuel oxidation catalyst for solid oxide fuel cells,” *J Mater Chem A Mater*, vol. 6, no. 33, pp. 15947–15953, 2018, doi: 10.1039/c8ta05105d.

[8] Y. Wang, X. Lei, Y. Zhang, F. Chen, and T. Liu, “In-situ growth of metallic nanoparticles on perovskite parent as a hydrogen electrode for solid oxide cells,” *J Power Sources*, vol. 405, pp. 114–123, 2018, doi: https://doi.org/10.1016/j.jpowsour.2018.10.023.

[9] Y. Jiang *et al.*, “Highly Efficient B-Site Exsolution Assisted by Co Doping in Lanthanum Ferrite toward High-Performance Electrocatalysts for Oxygen Evolution and Oxygen Reduction,” *ACS Sustain Chem Eng*, vol. 8, no. 1, pp. 302–310, Jan. 2020, doi: 10.1021/acssuschemeng.9b05344.

[10] D. Papargyriou, D. N. Miller, and J. T. Sirr Irvine, “Exsolution of Fe–Ni alloy nanoparticles from (La,Sr)(Cr,Fe,Ni)O3 perovskites as potential oxygen transport membrane catalysts for methane reforming,” *J Mater Chem A Mater*, vol. 7, no. 26, pp. 15812–15822, 2019, doi: 10.1039/C9TA03711J.

[11] D. Neagu, G. Tsekouras, D. N. Miller, H. Ménard, and J. T. S. Irvine, “In situ growth of nanoparticles through control of non-stoichiometry,” *Nat Chem*, vol. 5, no. 11, pp. 916–923, Nov. 2013, doi: 10.1038/nchem.1773.

[12] A. I. Tsiotsias *et al.*, “Bimetallic Exsolved Heterostructures of Controlled Composition with Tunable Catalytic Properties,” *ACS Nano*, vol. 16, no. 6, pp. 8904–8916, 2022, doi: 10.1021/acsnano.1c11111.

[13] A. Anantha Krishnan *et al.*, “Multifunctional Na-enriched Ni–Fe/Ni–P plates for highly efficient photo- and electrocatalytic water splitting reactions,” *New Journal of Chemistry*, vol. 46, no. 46, pp. 22256–22267, 2022, doi: 10.1039/D2NJ04389K.

[14] W. Cheng, P. Fan, and W. Jin, “Visualizing the Structure and Dynamics of Transition Metal-Based Electrocatalysts Using Synchrotron X-Ray Absorption Spectroscopy,” *ChemSusChem*, vol. 18, no. 4, p. e202401306, Feb. 2025, doi: https://doi.org/10.1002/cssc.202401306.

[15] L. Kapokova *et al.*, “Dry reforming of methane over LnFe0.7Ni0.3O3−δ perovskites: Influence of Ln nature,” *Catal Today*, vol. 164, no. 1, pp. 227–233, 2011, doi: https://doi.org/10.1016/j.cattod.2010.10.086.

[16] E. I. Papaioannou, D. Neagu, W. K. W. Ramli, J. T. S. Irvine, and I. S. Metcalfe, “Sulfur-Tolerant, Exsolved Fe–Ni Alloy Nanoparticles for CO Oxidation,” *Top Catal*, vol. 62, no. 17, pp. 1149–1156, 2019, doi: 10.1007/s11244-018-1053-8.

[17] F. Orsini *et al.*, “Exsolution-enhanced reverse water-gas shift chemical looping activity of Sr2FeMo0.6Ni0.4O6-δ double perovskite,” *Chemical Engineering Journal*, vol. 475, p. 146083, 2023, doi: https://doi.org/10.1016/j.cej.2023.146083.

[18] L. Lindenthal *et al.*, “Novel perovskite catalysts for CO2 utilization - Exsolution enhanced reverse water-gas shift activity,” *Appl Catal B*, vol. 292, p. 120183, 2021, doi: https://doi.org/10.1016/j.apcatb.2021.120183.

[19] F. d’Acapito *et al.*, “The LISA beamline at ESRF,” *J Synchrotron Radiat*, vol. 26, no. 2, pp. 551–558, Mar. 2019, doi: 10.1107/S160057751801843X.

[20] G. Bellotti *et al.*, “ARDESIA Detection Module: A Four-Channel Array of SDDs for Mcps X-Ray Spectroscopy in Synchrotron Radiation Applications,” *IEEE Trans Nucl Sci*, vol. 65, no. 7, pp. 1355–1364, 2018, doi: 10.1109/TNS.2018.2838673.

[21] B. Ravel and M. Newville, “ ATHENA, ARTEMIS, HEPHAESTUS: data analysis for X-ray absorption spectroscopy using IFEFFIT,” *J Synchrotron Radiat*, vol. 12, no. 4, pp. 537–541, Jul. 2005, doi: 10.1107/S0909049505012719.

[22] M. Newville, “Larch: An Analysis Package for XAFS and Related Spectroscopies,” *J Phys Conf Ser*, vol. 430, no. 1, p. 012007, 2013, doi: 10.1088/1742-6596/430/1/012007.

[23] A. L. Ankudinov, B. Ravel, J. J. Rehr, and S. D. Conradson, “Real-space multiple-scattering calculation and interpretation of x-ray-absorption near-edge structure,” *Phys Rev B*, vol. 58, no. 12, pp. 7565–7576, Sep. 1998, doi: 10.1103/PhysRevB.58.7565.

[24] R. J. Nelmes, G. M. Meyer, and J. Hutton, “Thermal motion in SrTiO3 at room temperature: Anharmonic or disordered?,” *Ferroelectrics*, vol. 21, no. 1, pp. 461–462, Jan. 1978, doi: 10.1080/00150197808237297.

[25] B. Kayaalp *et al.*, “Surface Reconstruction under the Exposure of Electric Fields Enhances the Reactivity of Donor-Doped SrTiO3,” *Journal of Physical Chemistry C*, vol. 123, no. 27, pp. 16883–16892, Jul. 2019, doi: 10.1021/acs.jpcc.9b04620.

[26] B. Koo, K. Kim, J. K. Kim, H. Kwon, J. W. Han, and W. Jung, “Sr Segregation in Perovskite Oxides: Why It Happens and How It Exists,” *Joule*, vol. 2, no. 8, pp. 1476–1499, 2018, doi: https://doi.org/10.1016/j.joule.2018.07.016.

[27] M. Vračar *et al.*, “Jahn-Teller distortion around Fe(IV) in Sr(FexTi1-xO3-d) from x-ray absorption spectroscopy, x-ray diffraction, and vibrational spectroscopy,” *Phys Rev B*, vol. 76, no. 17, p. 174107, Nov. 2007, doi: 10.1103/PhysRevB.76.174107.

[28] C. Tang, K. Kousi, D. Neagu, and I. S. Metcalfe, “Trends and Prospects of Bimetallic Exsolution,” *Chemistry – A European Journal*, vol. 27, no. 22, pp. 6666–6675, Apr. 2021, doi: https://doi.org/10.1002/chem.202004950.

[29] S. Joo, O. Kwon, S. Kim, H. Y. Jeong, and G. Kim, “Ni-Fe Bimetallic Nanocatalysts Produced by Topotactic Exsolution in Fe deposited PrBaMn1.7Ni0.3O5+δ for Dry Reforming of Methane,” *J Electrochem Soc*, vol. 167, no. 6, p. 064518, 2020, doi: 10.1149/1945-7111/ab8390.

[30] S. Joo *et al.*, “Highly active dry methane reforming catalysts with boosted in situ grown Ni-Fe nanoparticles on perovskite via atomic layer deposition,” *Sci Adv*, vol. 6, no. 35, p. eabb1573, Oct. 2025, doi: 10.1126/sciadv.abb1573.

[31] A. G. Shard, “Detection limits in XPS for more than 6000 binary systems using Al and Mg Kα X-rays,” *Surface and Interface Analysis*, vol. 46, no. 3, pp. 175–185, Mar. 2014, doi: https://doi.org/10.1002/sia.5406.

[32] F. Porcaro, S. Roudeau, A. Carmona, and R. Ortega, “Advances in element speciation analysis of biomedical samples using synchrotron-based techniques,” *TrAC Trends in Analytical Chemistry*, vol. 104, pp. 22–41, 2018, doi: https://doi.org/10.1016/j.trac.2017.09.016.

[33] B. Kayaalp *et al.*, “Template-free mesoporous La0.3Sr0.7FexTi1-xO3±Δ with superior oxidation catalysis performance,” *Appl Catal B*, vol. 245, pp. 536–545, May 2019, doi: 10.1016/j.apcatb.2018.12.077.

[34] Y. Gao, D. Chen, M. Saccoccio, Z. Lu, and F. Ciucci, “From material design to mechanism study: Nanoscale Ni exsolution on a highly active A-site deficient anode material for solid oxide fuel cells,” *Nano Energy*, vol. 27, pp. 499–508, Sep. 2016, doi: 10.1016/j.nanoen.2016.07.013.

[35] N. Pathak, S. K. Gupta, K. Sanyal, M. Kumar, R. M. Kadam, and V. Natarajan, “Photoluminescence and EPR studies on Fe3+ doped ZnAl2O4: an evidence for local site swapping of Fe3+ and formation of inverse and normal phase,” *Dalton Transactions*, vol. 43, no. 24, pp. 9313–9323, 2014, doi: 10.1039/C4DT00741G.

[36] Y. J. Park *et al.*, “A mixed-valent Fe(II)Fe(III) species converts cysteine to an oxazolone/thioamide pair in methanobactin biosynthesis,” *Proceedings of the National Academy of Sciences*, vol. 119, no. 13, p. e2123566119, Mar. 2022, doi: 10.1073/pnas.2123566119.

[37] R. Merkle and J. Maier, “Defect association in acceptor-doped SrTiO3: case study for Fe'TiV˙˙O and Mn"TiV˙˙O,” *Physical Chemistry Chemical Physics*, vol. 5, no. 11, pp. 2297–2303, 2003, doi: 10.1039/B300205P.

[38] E. S. Kirkpatrick, K. A. Müller, and R. S. Rubins, “Strong Axial Electron Paramagnetic Resonance Spectrum of ${\mathrm{Fe}}^{3+}$ in SrTi${\mathrm{O}}_{3}$ Due to Nearest-Neighbor Charge Compensation,” *Physical Review*, vol. 135, no. 1A, pp. A86–A90, Jul. 1964, doi: 10.1103/PhysRev.135.A86.

[39] C. Lenser *et al.*, “Spectroscopic study of the electric field induced valence change of Fe-defect centers in SrTiO3,” *Physical Chemistry Chemical Physics*, vol. 13, no. 46, pp. 20779–20786, 2011, doi: 10.1039/C1CP21973A.

[40] J. Dashdorj, M. E. Zvanut, and L. J. Stanley, “Iron-related defect levels in SrTiO3 measured by photoelectron paramagnetic resonance spectroscopy,” *J Appl Phys*, vol. 107, no. 8, p. 083513, Apr. 2010, doi: 10.1063/1.3372760.

[41] R. W. Kedzie, D. H. Lyons, and M. Kestigian, “Paramagnetic Resonance of the Fe3+ Ion in CaWO4 (Strong Tetragonal Crystal Field),” *Physical Review*, vol. 138, no. 3A, pp. A918–A924, May 1965, doi: 10.1103/PhysRev.138.A918.

[42] S. Anderson, “Paramagnetic Resonance of Iron in Glass,” *J Chem Phys*, vol. 50, no. 6, pp. 2783–2784, Mar. 1969, doi: 10.1063/1.1671460.

[43] H. H. Wickman, M. P. Klein, and D. A. Shirley, “Paramagnetic Resonance of Fe3+ in Polycrystalline Ferrichrome A,” *J Chem Phys*, vol. 42, no. 6, pp. 2113–2117, Mar. 1965, doi: 10.1063/1.1696253.

[44] Y. J. Li, Y. Y. Ma, S. Ye, G. P. Hu, and Q. Y. Zhang, “Site-related near-infrared luminescence in MAl12O19 (M=Ca, Sr, Ba):Fe3+ phosphors,” *Mater Res Bull*, vol. 51, pp. 1–5, 2014, doi: https://doi.org/10.1016/j.materresbull.2013.11.008.

[45] M. Nayak and T. R. N. Kutty, “Luminescence of Fe3+ doped NaAlSiO4 prepared by gel to crystallite conversion,” *Mater Chem Phys*, vol. 57, no. 2, pp. 138–146, 1998, doi: https://doi.org/10.1016/S0254-0584(98)00209-0.

[46] M. D. Drahus, P. Jakes, E. Erdem, and R.-A. Eichel, “Defect structure of the mixed ionic–electronic conducting Sr[Ti,Fe]Ox solid-solution system — Change in iron oxidation states and defect complexation,” *Solid State Ion*, vol. 184, no. 1, pp. 47–51, 2011, doi: https://doi.org/10.1016/j.ssi.2010.09.045.

[47] R. Merkle and J. Maier, “Defect association in acceptor-doped SrTiO3: case study for Fe'TiV˙˙O and Mn"TiV˙˙O,” *Physical Chemistry Chemical Physics*, vol. 5, no. 11, pp. 2297–2303, 2003, doi: 10.1039/B300205P.

[48] M. Knight, I. Reimanis, A. Meyer, J.-H. Preusker, and W. Rheinheimer, “Dilute iron-doped polycrystalline strontium titanate: Tracking iron valence and local interactions,” *Journal of the American Ceramic Society*, vol. 106, no. 8, pp. 4740–4751, Aug. 2023, doi: https://doi.org/10.1111/jace.19111.

[49] E. Poffe *et al.*, “Understanding Oxygen Release from Nanoporous Perovskite Oxides and Its Effect on the Catalytic Oxidation of CH4and CO,” *ACS Appl Mater Interfaces*, 2021, doi: 10.1021/acsami.1c02281.

[50] B. Faughnan and Z. Kiss, “Optical and EPR studies of photochromic SrTiO3doped with Fe/Mo and Ni/Mo,” *IEEE J Quantum Electron*, vol. 5, no. 1, pp. 17–21, 1969, doi: 10.1109/JQE.1969.1075665.

[51] K. A. Müller, W. Berlinger, and R. S. Rubins, “Observation of Two Charged States of a Nickel-Oxygen Vacancy Pair in SrTi${\mathrm{O}}_{3}$ by Paramagnetic Resonance,” *Physical Review*, vol. 186, no. 2, pp. 361–371, Oct. 1969, doi: 10.1103/PhysRev.186.361.

[52] C. Zhou, J. Zhang, Y. Fu, and H. Dai, “Recent Advances in the Reverse Water–Gas Conversion Reaction,” Nov. 01, 2023, *Multidisciplinary Digital Publishing Institute (MDPI)*. doi: 10.3390/molecules28227657.

[53] P. Yan *et al.*, “Unlocking the role of Ni-Fe species in CO2 methanation,” *Fuel*, vol. 374, p. 132373, 2024, doi: https://doi.org/10.1016/j.fuel.2024.132373.

[54] A. Z. Md Azmi *et al.*, “The impact bimetallic Ni–Fe deposit configuration has on accessing synergy during plasma-catalytic CO2 methanation††Electronic supplementary information

(ESI) available. See DOI: https://doi.org/10.1039/d5cy00036j," *Catal Sci Technol*, vol. 15, no. 11, pp. 3372–3384, 2025, doi: https://doi.org/10.1039/d5cy00036j.

[55] B. Mutz *et al.*, "Potential of an Alumina-Supported Ni3Fe Catalyst in the Methanation of CO2: Impact of Alloy Formation on Activity and Stability," *ACS Catal*, vol. 7, no. 10, pp. 6802–6814, Oct. 2017, doi: 10.1021/acscatal.7b01896.

[56] G. De Piano, J. J. A. Gamboa, A. M. Condó, S. Bengió, and F. C. Gennari, "Bimetallic Ni-Fe catalysts for methanation of CO2: Effect of the support nature and reducibility," *Appl Catal A Gen*, vol. 634, p. 118540, 2022, doi: https://doi.org/10.1016/j.apcata.2022.118540.

[57] D. Pandey and G. Deo, "Promotional effects in alumina and silica supported bimetallic Ni–Fe catalysts during CO2 hydrogenation," *J Mol Catal A Chem*, vol. 382, pp. 23–30, 2014, doi: https://doi.org/10.1016/j.molcata.2013.10.022.

[58] P. Wu, J. Sun, M. Abbas, P. Wang, Y. Chen, and J. Chen, "Hydrophobic SiO2 supported Fe-Ni bimetallic catalyst for the production of high-calorie synthetic natural gas," *Appl Catal A Gen*, vol. 590, p. 117302, 2020, doi: https://doi.org/10.1016/j.apcata.2019.117302.

[59] L. Liu *et al.*, "Low temperature catalytic reverse water-gas shift reaction over perovskite catalysts in DBD plasma," *Appl Catal B*, vol. 265, p. 118573, 2020, doi: https://doi.org/10.1016/j.apcatb.2019.118573.

[60] L. Lindenthal *et al.*, "Novel perovskite catalysts for CO2 utilization - Exsolution enhanced reverse water-gas shift activity," *Appl Catal B*, vol. 292, p. 120183, 2021, doi: https://doi.org/10.1016/j.apcatb.2021.120183.

[61] A. M. Martin, S. Saini, D. Neagu, W. Hu, I. S. Metcalfe, and K. Kousi, "Tailoring the A and B site of Fe-based perovskites for high selectivity in the reverse water-gas shift reaction," *Journal of CO2 Utilization*, vol. 83, p. 102784, 2024, doi: https://doi.org/10.1016/j.jcou.2024.102784.

Chapter 5

ZnO decorated with CuAu Nanoclusters: a model platform for investigating the CO_2 conversion to methanol.

Index of the chapter

This chapter provides a comprehensive description of the synthesis procedures, characterization techniques, and testing methods employed to investigate Au and Au/Cu nanoclusters (NCs) supported on ZnO catalysts. Particular attention is given to monitoring defect modifications during pretreatment and catalysis, with an emphasis on using EPR spectroscopy to detect changes in the defect structure of the ZnO support. Special effort is devoted to establishing a correlation between the defectivity and the reactivity in the CO_2 to methanol conversion process.

5.1 Introduction

The conversion of CO_2 into methanol, through both direct and indirect pathways, has attracted considerable attention both from academia and industry. This approach not only offers a route to valorise CO_2 but also serves as a mean of storing renewable energy in liquid form, thereby advancing the concept of a circular carbon economy. On an industrial scale, methanol is commonly synthesized from syngas, a mixture of H_2, CO_2, and CO, under elevated pressures (50–100 bar) and moderate temperatures (200–300 °C), typically employing copper-based catalysts such as Cu/ZnO, Cu/ZnO–Al_2O_3, and Cu/ZnO–ZrO_2 [1]. Furthermore, catalysts based on Cu and Pd nanoparticles, and more recently Au nanoparticles supported on ZnO, have shown notable activity and selectivity for this reaction [2].

The literature on this subject is extensive, but despite numerous studies and valuable insights, the precise role of ZnO in the methanol synthesis reaction remains a matter of debate. In Cu/ZnO systems, several hypotheses have been put forward. These include reverse hydrogen spillover from ZnO to Cu [3], the role of ZnO as a physical spacer that enhances Cu nanoparticle (NP) dispersion and increases the catalyst's specific surface area [4], as well as its possible involvement as a direct component of the active site [5]. It has also been reported that ZnO–Cu interactions can induce defective Cu surfaces through lattice strain generated by ZnO coverage [6]. Moreover, partial reduction of ZnO may produce ZnO_x species and promote the formation of CuZn alloys, while Zn migration toward the Cu surface has been observed [7], giving rise to an "inverse catalyst" configuration in which the oxide phase is supported on the metal, an illustrative case of strong metal, support interaction (SMSI) [8]. Additionally, the basic sites of ZnO in direct contact with metallic Cu nanoparticles are believed to contribute to the hydrogenation of CO and CO_2. Collectively, these findings underscore that the true nature and function of Zn species under reaction conditions remain unresolved, owing to their dynamic structural and chemical transformations [9].

Similar effects have also been reported for Au NP supported on ZnO catalysts [2]. Recent investigations have highlighted the pivotal role of partial ZnO reduction in enhancing catalytic reactivity [10]. Specifically, Strunk et al. [11] demonstrated that increasing the Au loading from 1 to 3 wt.%, while

keeping the metal particle size and overall catalyst surface area constant, resulted in a higher concentration of oxygen vacancies (V_O) associated with ZnO. This increase was accompanied by enhanced CO conversion in a 15% CO/H_2 mixture. Based on these observations, the authors proposed that V_O sites, most likely located at the perimeter of the Au nanoparticles, act as the active centers for methanol formation. Furthermore, the presence of Au nanoparticles was shown to promote the generation of additional V_O in Au/ZnO catalysts compared with pristine ZnO under identical reaction conditions.

More recently, Behm et al. [2] investigated the partial reduction of ZnO under CO/H_2 and its subsequent re-oxidation in the presence of CO_2/H_2 over Au/ZnO catalysts using in situ Diffuse Reflectance FTIR spectroscopy (DRIFTS), X-ray photoelectron spectroscopy (XPS), and electron paramagnetic resonance (EPR). Their findings further confirmed the central role of oxygen vacancy (V_O) species in CO_2 conversion to methanol. They monitored V_O paramagnetic defects via EPR (Fig. 5.1a) and catalytic activity (Fig. 5.1c) as a function of ZnO particle size while keeping the Au loading constant. Notably, they found out that the increase in ZnO NPs size led to a continuous rise in selectivity toward methanol formation [12]. In contrast, the methanol yield displayed a volcano-type trend.

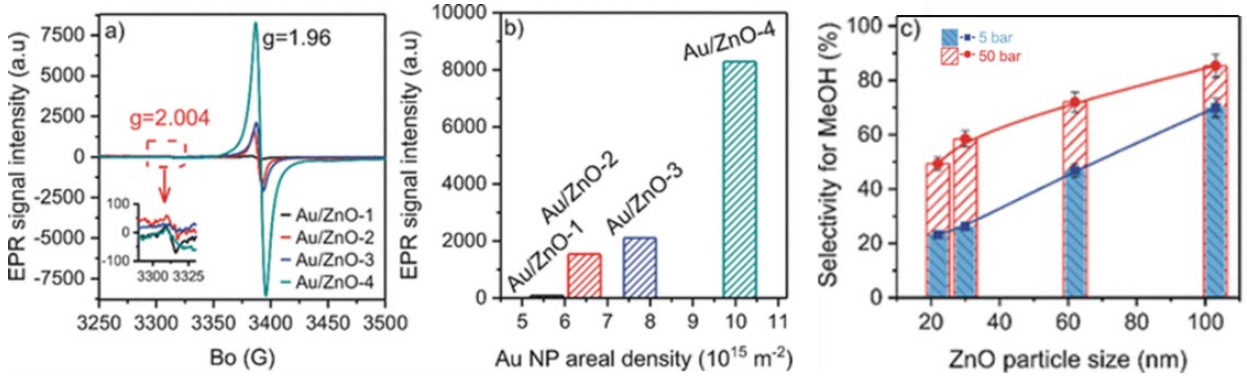

Fig. 5.1: a) EPR signals of Au@ZnO samples with increasing ZnO size; b) Au NPs density on ZnO surface; c) selectivity for MeOH generation as a function of ZnO particle size under different pressures [2]

This unusual reactivity was attributed to the interplay between electronic metal–support interactions (EMSIs), arising from charge transfer between V_O in ZnO_x and adjacent Au sites, and strong metal–support interactions (SMSIs), involving the partial overgrowth of ZnO_x layers on Au nanoparticles [12], [13]. In summary, these studies unequivocally demonstrate that ZnO particle size and specific surface area as well as Au NPs loading and dimensions, are key factors in methanol synthesis primarily due to their influence on the generation of defects in ZnO, which can behave as additional and more selective active sites for the reaction.

In recent years, advances along these lines have enabled the controlled synthesis not only of well-defined nanoparticles (NPs) but also of tailored nanoclusters (NCs) comprising a few to several hundred

atoms, and even single-atom catalysts (SACs). This progression has enhanced catalytic reactivity per unit volume by increasing the number of active sites while simultaneously ensuring atomic economy.

In particular, metal NCs have emerged as a distinct class of nanocatalysts that bridges the gap between metal NPs and SACs, owing to their unique, molecule-like discrete electronic structures, which fundamentally differ from those of both NPs and SACs [14], [15]. Compared with their larger counterparts (i.e., NPs), metal NCs possess smaller dimensions, resulting in improved atom economy and a higher proportion of surface atoms with unsaturated coordination that act as active sites [16]. In addition, metal NCs provide exceptional tunability in catalytic performance; at the sub-nanometre scale, even the addition or removal of even a single atom can induce pronounced changes in their reactivity [17]. In the broad category of precise NCs, thiolate protected Au NCs stand out due to their improved stability and excellent solubility in several solvents, with crucial fallouts in their practical application in catalytic processes [18]. Additionally, their relatively easy preparation, high yields, and versatile surface functionalization further establish Au-based NCs as outstanding candidates for catalysis [19]. Among the various strategies for tailoring their properties, heteroatom doping has proven particularly effective. This approach significantly expands the compositional and structural diversity of NCs and can induce synergistic effects that enhance catalytic performance by modulating the electronic structure, creating additional active sites, and improving structural stability [20]. In this context, Hutchings et al. demonstrated the potential of CuAu nanoalloys in several reactions, including CO and benzyl alcohol oxidation, as well as epoxidation [21]. Similarly, Murayama et al. [22] reported the use of CuAu nanoalloys supported on ZnO for the selective hydrogenation of CO_2 to methanol under CO_2/H_2 conditions. These studies highlight that fine-tuning the Cu/Au molar ratio is a powerful strategy to enhance both the activity and selectivity of CO_2 conversion. With regard to CuAu NCs specifically, several computational studies have demonstrated that their high structural flexibility, originating from their binary composition, can enable remarkable catalytic activity [23] [24].

According to this background and with the aim to attain some further insights into the role of the ZnO defects and metal/ZnO interfaces in the CO_2 methanolation reaction, we developed and tested model catalysts constituted of Au and CuAu NCs supported onto ZnO NPs.

Well-known thiolate-protected clusters, specifically $Au_{25}(SR)_{18}$, were utilized and Cu was then introduced as doping atom. Upon structural and compositional characterization by UV-Vis and Matrix-Assisted Laser Desorption/Ionization (MALDI) analysis, the NCs were loaded on ZnO NPs and the obtained catalysts were tested in CO_2 methanolation at ambient pressure. The catalysts were characterized before and after the reaction using EPR to track changes in defect density and electronic transitions. Additionally, in situ DRIFTS experiments were performed to monitor surface modifications

during the reaction and, through CO dosing experiments, to identify the binding sites of the active gas molecules within the reaction mixture.

These combined studies aimed to establish a persuasive relationship between the local structure of Zn species and their role in the CO_2 hydrogenation reaction, which will be beneficial in exploring complex interactions of multi-component catalysts.

5.2 Experimental

5.2.1 Preparation procedures

Synthesis of Au25-xCux(2-PET)18 (CuAu NCs)

The clusters have been synthesized following procedures reported elsewhere [25], [26], with little modifications. Briefly, 5.58 mL (0.484 mmol) of a solution of HAuCl4 (0.0449 g per mL) was evaporated to eliminate the excess water with rotavapor until a concentrated solution was obtained. Then it was redispersed in 33 mL of MeOH and stirred. After this, a solution of $CuCl_2$ in MeOH (27,5 mg of $CuCl_2$ dihydrate in 13 mL of MeOH) was added together with another solution of 475 mg of tetraoctyl ammonium bromide (TOAB) dissolved in 19 mL of MeOH. The solutions were left to react for 15 minutes and then 1266 µL of 2-Phenylethanethiol (2-PET) and left to react for 15 more minutes. Finally, an ice-cold solution of 297.44 mg of $NaBH_4$ in 13 mL of water was added. The reaction mixture is allowed to react for 3 h after which the product was washed as follows, drying off the solvent after each washing: with MeOH 4 times, with Acetonitrile and finally with DCM. Once dispersed in DCM the product is also filtered through a Teflon filter (pore size 0,2 µm) to remove any solid residues. Finally, after DCM evaporation the products are dispersed in THF and prepared for size exclusion chromatography.

Synthesis of $Au_{25}(2\text{-PET})_{18}$ (Au NCs)

5,571 mL of a 0,228 M solution of $AuHCl_4 \cdot 3H\,2\,O$ was evaporated to eliminate the excess water, then 50 mL of THF were added together with 1.52 mmol of TOAB and the solution was stirred for 15 minutes. After this, 850.54 µL of 2-PET were added to the solution and left to react until the solution clears up. Finally, the reduction was operated by adding a solution of 10 mL of ice-cold water with 480 mg of $NaBH_4$ dissolved inside. The final solution was left under strong stirring for 72 hours. After three days the product is decanted and then washed with methanol 3 times and then with DCM. After the last dispersion in DCM the product is filtered with a Teflon filter (pore size 0,2 µm) and, after drying, is dispersed one last time in THF and prepared for size exclusion chromatography.

Deposition of clusters on ZnO

After purification the clusters were deposited on ZnO nanoparticles synthesized with the polyol method reported elsewhere [27]. For the deposition, 400 mg of ZnO were sonicated in few mL of Toluene together with 3 mg of AuNCs or 3,1 mg of CuAuNCs corresponding to the 0,5% wt of metal to ZnO. The dispersion was left to stir for 24h at the end of which the precipitation was forced via evaporation of the solvent through the use of rotavapor in order to not increase the temperature and just lowering the pressure. After this, the sample were dried in oven at 80°C for one hour and respectively samples Au@ZnO and CuAu@ZnO were produced.

5.2.2 Spectroscopic characterization

MALDI & UV-Vis

All Matrix-Assisted Laser Desorption Ionization Mass Spectrometry (MALDI-MS) measurements were performed using a reflectron (RTOF) mass spectrometer (Shimadzu). For analytical experiments, 2,4,6-trihydroxyacetophenone (Sigma-Aldrich) was selected as MALDI-MS matrix. MALDI-RTOF mass spectra were acquired near threshold laser irradiance to obtain mass spectra of sufficient mass spectrometric resolution [3000–5000 at full width half-maximum (FWHM)]. All displayed mass spectra were based on averaging 300– 600 single and unselected laser pulses (λ = 337 nm at 50 Hz).

UV-Vis spectra of nanoclusters were collected by dissolving the clusters in THF and recorded on a Perkin Elmer Lambda 750 UV-Vis spectrometer

UV-DRS

UV-DRS spectra were recorded in the spectral range from 400 to 1000 nm using a PerkinElmer Lambda 1050+ UV/Vis/NIR spectrophotometer equipped with a 10 cm diameter integrating sphere on the as-prepared powdered samples, after the thermal pretreatment and after catalysis at 500°C.

DRIFTS

Operando infrared studies (transmission FTIR) were conducted using a Bruker Vertex 70 spectrometer. The catalyst, approximately 10 mg, was transferred into the flow cell (PIKE Technologies DiffusIR). The gas flow was controlled by a mks Multi gas controller 647C and the temperature was controlled with X and a Liquid Recirculator (PIKE Technologies). The IR spectra were recorded during all the measurements in a 3-minute interval. The system was flushed with a flow of 10 mL/min of Ar and then

pretreated as described in the catalytic activity studies with PretO2 (5 % O2 in Ar, 10 mL/min total gas flow) and with PretH2 (5 % H2 in Ar, 10 mL/min total gas flow). After the pretreatment took place a CO adsorption experiment was performed. The sample was exposed to 1 mL/min of CO in Ar (10 mL/min total flow rate) until the IR band of CO stopped changing substantially. Next, 10 mL/min of Ar was circulated through the cell until there were no more changes in the IR spectra. After completing the CO adsorption experiment the catalyst was measured while undergoing the gas mixture containing (both of the pretreatment and of the actual catalytic reaction). After each step of the reaction finished and the system was then flushed again with Ar and cooled to room temperature the CO adsorption experiment was repeated.

Pretreatment conditions

Each catalyst would first undergo the oxidative pretreatment (pretO2) with a gas flow of 5% O2 in Ar (total gas flow of 10 mL/min) and a temperature ramp of 10°C/min up to 350°C. The maximum temperature was then maintained for 40 minutes before the sample was cooled to RT in Ar (20 mL/min). then CO dsing experiments were performed before the catalyst would undergo the reductive pretreatment (pretH2) with a gas flow of 5% H2 in Ar (total gas flow of 10 mL/min) and a temperature ramp of 10°C/min up to 350°C. The maximum temperature was again maintained for 40 minutes before cooling the sample to RT in Ar (20 mL/min). Finally, one last CO dosing measurement was performed.

Reaction conditions

After the pretreatments the gas flow composition was then changed to reaction conditions (1 mL/min of CO_2 3 mL/min of H_2 and 1 mL/min Ar) and held for 20 minutes at RT for equilibration. The temperature was then increased to 200°C, 300°C, 400°C and 500°C with a ramp of 5°C/min and was held there for 30 min. Finally, the catalyst was cooled to RT under Argon (20 mL/min).

5.2.3 Pretreatment and preliminary catalytic tests

A flow reactor coupled to a micro-gas chromatograph (Micro-GC, Fusion 3000 A, Inficon) was employed for both catalyst pretreatment and reaction studies. The temperature was monitored and controlled using a Ni/NiCr thermocouple connected to a PID-controlled tubular oven. For each experiment, 100 mg of catalyst powder was loaded into a quartz reaction tube, with the ends secured using glass wool, and the tube was placed in the tubular oven. The system was initially flushed with Ar gas at 50 mL/min. All catalysts underwent sequential oxidative and reductive pretreatments using a 10 °C/min ramp to 350 °C. The oxidative pretreatment ($PretO_2$: 5% O_2 in Ar, 50 mL/min) was applied to remove surface contaminants and residual ligands from synthesis. This was followed by a reductive pretreatment ($PretH_2$: 5% H_2 in Ar, 50 mL/min) to restore the metal to its zero-valent state. At the target temperature

of 350 °C, the catalysts were held for 30 minutes under the respective gas flow, after which they were cooled to room temperature under Ar (50 mL/min).

For the reaction the sample was soaked with the reaction mixture (36 mL/min H_2, 12 mL/min CO_2 and 2 mL/min Ar, 50 mL/min total gas flow) for 20 min at room temperature for equilibration, then heated up with a ramp rate of 10°C/min and then soaked for 1 h at 400 °C and then 5°C/min till 500°C and isotherm for another hour. After reaction, the set-up was cooled down again to room temperature with a flow of 50 mL/min of Ar gas.

5.2.4 EPR investigation

EPR studies of were carried out using a Bruker EMX spectrometer operating in X-band, with a frequency modulation of 100 kHz, a microwave power of 0.2 − 10 mW, a magnetic field modulation of 1−5 G, and equipped with an Oxford cryostat operating in a range of temperatures between 4 and 298 K. Spectra on were registered both at 130 K, mostly in vacuum ($p < 10^{-4}$ mbar).

5.3 Results and discussion

5.3.1 Spectroscopic characterization

MALDI & UV-Vis

Both the UV-vis spectrum of Au and CuAu show the distinct absorption bands at 1.8, 2.8, and 3.1 eV which are in line with the reported values for 25 atoms clusters [28], [26], confirming the correct synthesis. Moreover, the band at 1.8 eV appears to be red shifting a little when copper is intercalated in the cluster structure, underlining the modification of the optical properties of the cluster.

Further investigation on the purity of the clusters and on the doping level of copper was done by matrix-assisted laser desorption ionization mass spectroscopy (MALDI-MS).

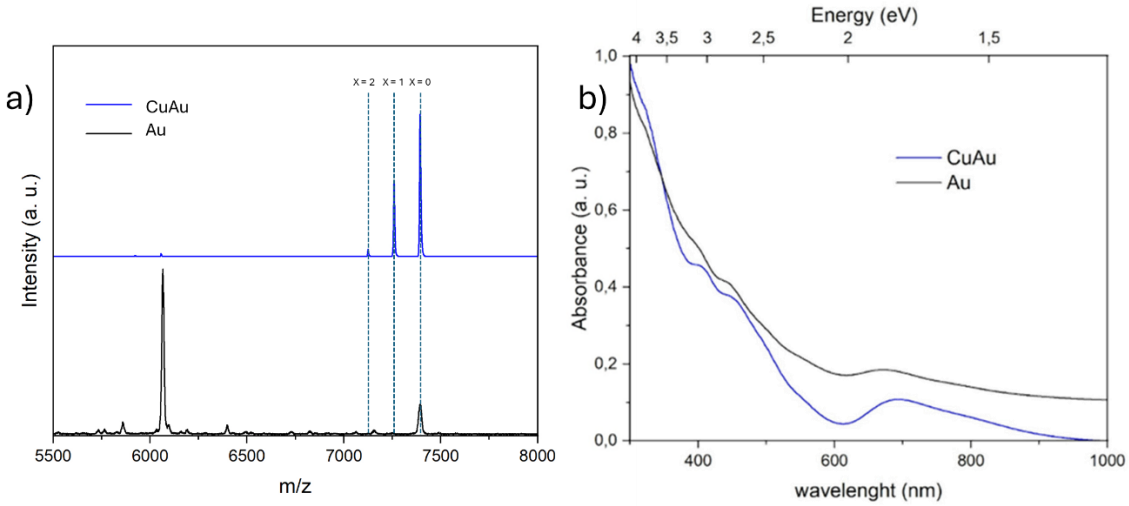

Fig. 5.2: a) MALDI-MS spectra of Au and CuAu NCs. x represents the degree of substitution of Cu in Au NCs with general formula $Au_{25-x}Cu_x(2\text{-PET})_{18}$; b) UV-Vis spectra of CuAu and Au NCs in THF

The MALDI spectrum of the pure $Au_{25}(2\text{-PET})_{18}$ (Fig 5.2a in black) cluster displays two main peaks at m/z 7393 and 6057 which can be attributed to the intact $Au_{25}(2\text{-PET})_{18}$ cluster and its main fragment $Au_{21}(2\text{-PET})_{14}$ [29], underlining the purity of the produced sample. Upon Cu incorporation, new peaks emerged in the MALDI spectrum (Fig. 5.2a in blue) at 7260 m/z and 7127 m/z. The separation between these peaks is 133 m/z, which corresponds to the mass difference between Au and Cu atoms ($m_{Au} - m_{Cu}$ = 133.42 u). These signals can thus be assigned to $Au_{25-x}Cu_x(2\text{-PET})_{18}$ clusters with x = 1 and x = 2, respectively, thereby confirming the doping level of the nanoclusters. The low Cu concentration is in accordance with the literature as it has already been reported that doping Au clusters with Cu atoms via the coreduction methods leads to low Cu intercalation in the cluster (generally $x < 5$) [26]. This result again confirms the purity of the synthesized clusters.

UV-DRS

UV-DRS measurements were carried out to monitor the modification of the cluster absorption in the UV-Vis region as well as the generation of optically active defects in the ZnO lattice (e.g. V_O, Zn_i) at different stages of the thermal processes. The spectra of bare ZnO and clusters deposited on ZnO as prepared, post pretreatment and post catalysis are plotted using the Kubelka-Munk equation vs the wavelength of the incident light.

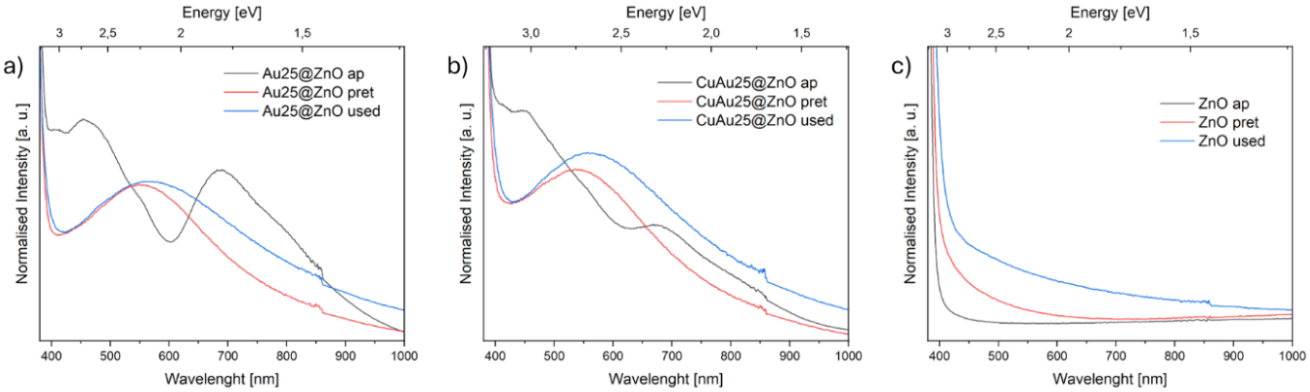

Fig. 5.3: UV-DRS spectra of a) Au NCs on ZnO; b) CuAu NCs on ZnO; c) bare ZnO during the different steps of the thermal treatment: as prepared (ap), after pretreatment (pret), after catalysis (used)

In Fig. 5.3 some general trends can be observed. Firstly, when the clusters are only deposited on the ZnO surface the same bands detected in the UV-Vis spectrum of bare clusters (Fig. 5.3 a, b black lines) can be noticed. This underlines the absence of reaction between ZnO and the clusters before pretreatment thus signalling their deposition on the ZnO surface and the need for a pretreatment to bind them directly to the oxide. Upon pretreatment a band centered at ~ 540 nm appears for both the clusters (Fig. 5.3 a, b red lines), indicating the presence of Localised Surface Plasmon Resonance (LSPR) thus revealing the generation of small metal nanoparticles on the surface of the ZnO due to the ligands being burn out. However, after catalysis, the LSPR peak red-shifts and broadens signalling the increase in size of the metal nanoparticles that started to coalesce due to high temperature treatments (Fig. 5.3 a, b blue lines).

It has also to be observed that upon thermal treatment a modification of the energy gap of ZnO is noticeable (Tauc plot, Fig. 5.4), which decreases from 3.23 eV in the as-prepared sample to 3.21 eV and 3.18 eV in the pretreated and post-catalysis samples, respectively. This shift indicates the potential formation of intra-gap defects (e.g., V_O, Zn_i, V_{Zn}) induced by the thermal treatment.

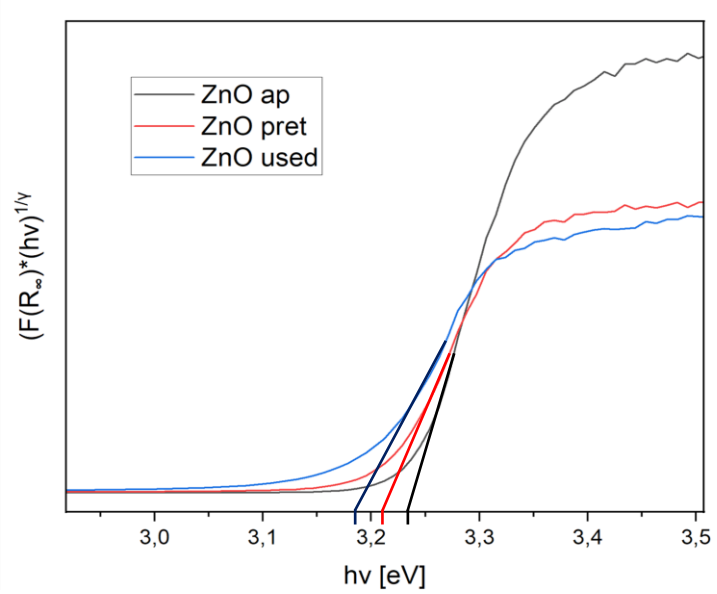

Fig. 5.4: Tauc plot of bare ZnO as prepared (black line); after pretreatment (red line) and after reaction (blue line)

DRIFTS

In-situ DRIFTS experiments were employed to monitor the structural modifications of the samples during the pretreatment process. Specifically, the same reaction mixture and temperature ramp used for the pretreatment were applied within the DRIFTS cell, alternated with CO dosing measurements to detect the presence of metallic species on the catalyst surface. The key parameter monitored was CO desorption, using CO as a probe molecule to track surface changes. Figure 5.5 illustrates the progressive depletion of the CO signal (a doublet due to the two main rotovibrational branches of gaseous CO [30]) after each pretreatment step. Notably, following H_2 treatment (Fig, 5.5c), a shoulder appears at 2077 cm^{-1}, which has previously been attributed to the adsorption of CO on an $Au^{\delta-}$ site [2].

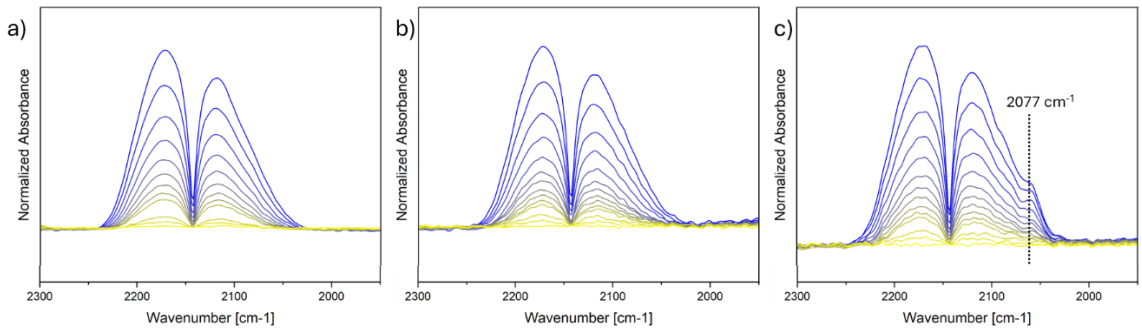

Fig. 5.5: DRIFTS spectra of CO desorption on a) Au25@ZnO as prepared, b) post O_2 treatment; c) post H_2 treatment. Highlighted is the CO-$Au^{\delta-}$ shoulder.

The presence of partially negative Au sites might be related to the loose nature of the oxygen in the ZnO lattice, which can easily escape leaving electrons behind. In particular, the presence of Au metal on the surface of the oxide generates V_O in the neighbouring site of the metal which can than influence the partial charge of the metal centres by giving up electrons to the Au atoms, thus negatively charging them.

In-situ DRIFTS was also used to monitor CO desorption from CuAu@ZnO, and, in this case, the picture looks very different. Firstly, it can be observed that a distinct shoulder at 2070 cm^{-1} (Fig. 5.6b), which has been previously attributed to CO-$Au^{\delta-}$ species [31], already emerges following oxygen treatment. More interestingly, after H_2 treatment, this shoulder shifts to 2058 cm^{-1} (Fig. 5.6c). Studies in the literature on Cu containing systems have reported several times this signal as corresponding to the CO-Cu^0 bond [32], [33], [34], and its presence underlines two peculiar phenomena.

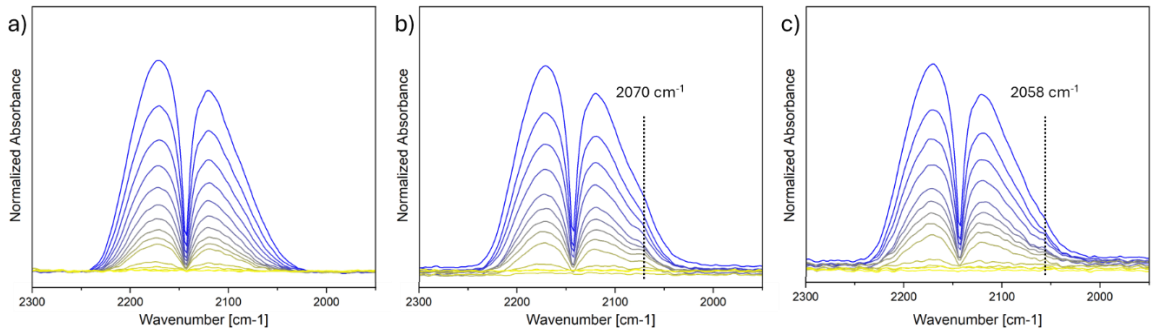

Fig. 5.6: DRIFTS spectra of CO desorption on a) CuAu25@ZnO as prepared, b) post O_2 treatment; c) post H_2 treatment.

The first is connected to the fact that Cu(0) species can be available to CO binding only after H_2 treatment, either because before H_2 reduction their oxidation state was closer to Cu(I) (See section about EPR later) or because the staple units were protecting Cu atoms from interacting with gases. The second and more interesting phenomenon, involves the CO-Cu(0) band at 2058 cm^{-1}, which becomes visible and does not allow the CO-$Au^{\delta-}$ band at 2070 cm^{-1} to be visible anymore. This suggests that when Cu is present, CO molecules bind more easily and more strongly (therefore the DRIFTS signal is more intense) to Cu than to Au. To confirm this hypothesis, DRIFTS was also used to monitor the tendency of the catalysts to bind the active gas, and in particular, CO binding strength was monitored as a function of time. CO DRIFTS signals were integrated in the region 2250-2000 cm^{-1} to calculate the "amount" of CO present on the sample. This integration was then monitored while the signal decreased during the gas desorption and plotted as a function of time. What can be seen in Fig. 5.7 is that the presence of Cu atoms in the clusters binds CO better than the pure Au cluster, as it gets purged off more slowly.

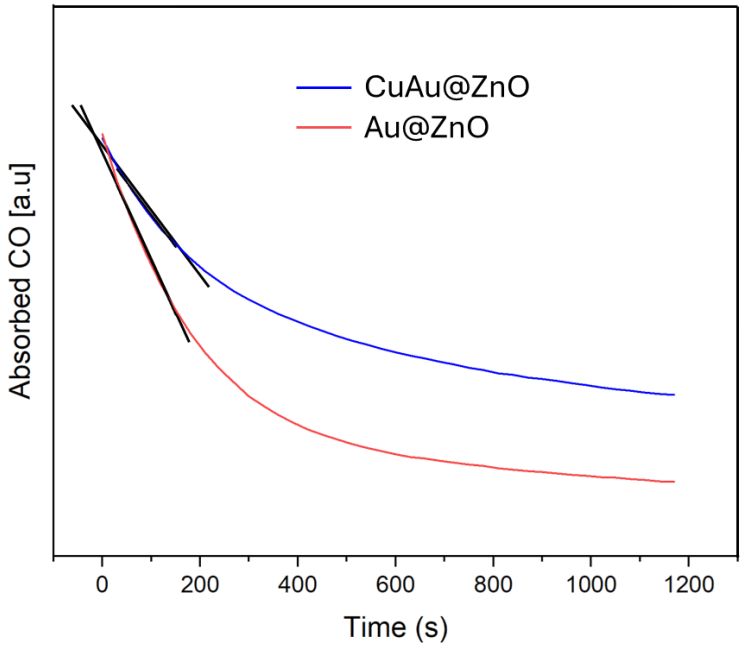

Fig. 5.7: CO DRIFTS integration signal decrease as a function of time for AuCu@ZnO and Au@ZnO

However, it is worth mentioning that this behaviour might be due both to the presence of Cu atoms which are more selective for CO binding, as well as to the higher concentration of defects on the catalyst with copper, as testified by UV-DRS (Fig. 5.3) and EPR (see next session).

5.3.2 Preliminary catalytic test

The catalytic performance of AuCu@ZnO and Au@ZnO was evaluated for the conversion of CO_2 to methanol under ambient pressure, under the experimental conditions reported in section 5.2.3. The preliminary results are summarized in Figure 5.8

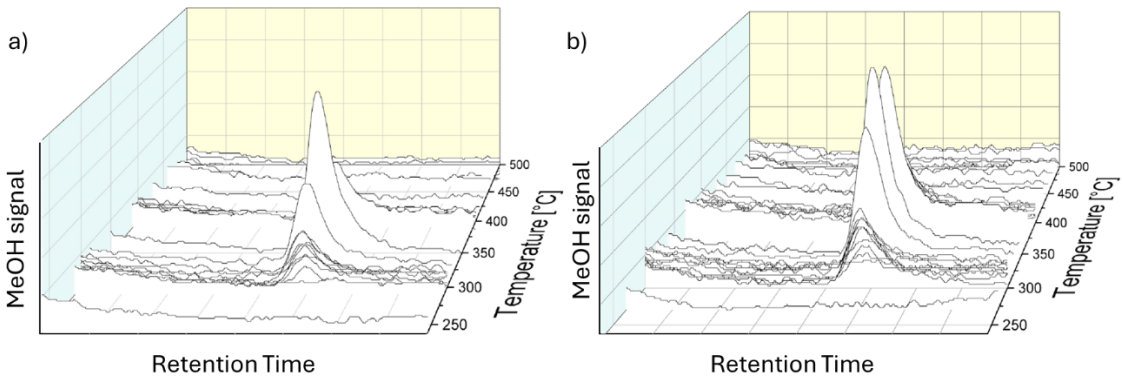

Fig. 5.8: Micro-GC chromatograms of the reaction outlet gas during CO_2 hydrogenation to methanol over the prepared catalyst. Peak corresponds to CH_3OH is presented as a function of reaction Temperature for a) Au@ZnO and b) CuAu@ZnO

Both catalysts exhibited selectivity toward methanol formation. Analysis of the retention time region corresponding to methanol on the polar column revealed a distinct peak arising at approximately 300°C (Fig. 5.8a b). The intensity of this peak increased with temperature, reaching a maximum near 350 °C, before decreasing at higher temperatures. This trend is consistent with the exothermic nature of the CO_2-to-methanol reaction, where elevated temperatures thermodynamically disfavor methanol formation [4], [35], [36].

Interestingly, the CuAu@ZnO catalyst, produced a more intense methanol signal over a broader temperature range compared to Au@ZnO. This behavior suggests that defect sites detected by UV-DRS and DRIFTS may play a key role in enhancing the catalytic activity and overall methanol yield of the Cu–Au-modified system. To further substantiate this hypothesis and to try to draw possible relations between defectivity and catalytic performance, a comprehensive EPR investigation on the prepared catalysts has been also carried out.

5.3.3 EPR monitoring

EPR was used to get an insight into the defectivity of the samples at different stages of the thermal treatments as well as their behaviour under gas contact. Experiments on the spent catalysts were also performed.

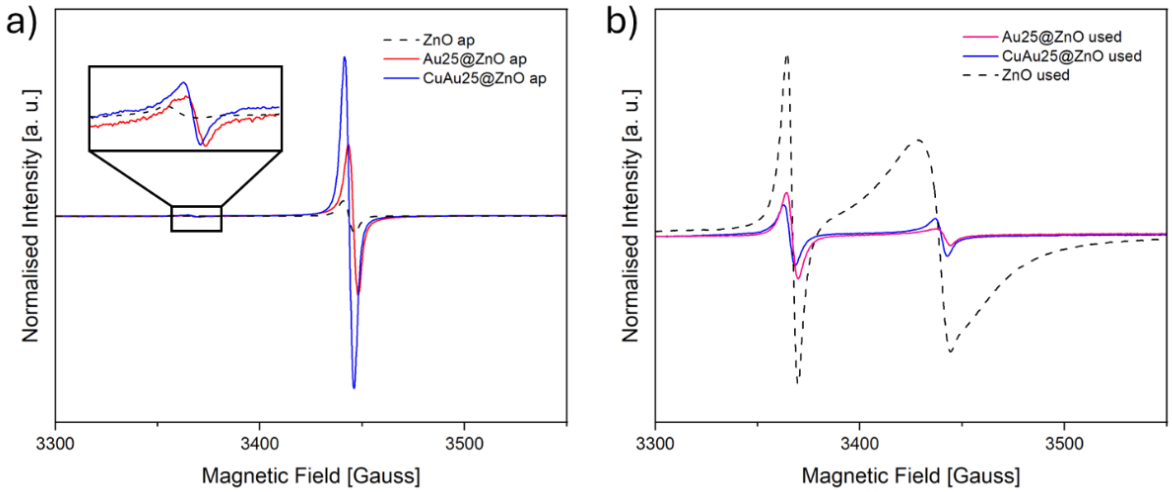

Fig. 5.9: EPR spectra at 130 K, 10mW under vacuum conditions (P ≈ 10^{-4} mbar) of: a) as prepared samples and b) spent samples

As an initial step, the as prepared samples were examined (Fig. 5.9a). Two distinct features can be observed in the spectra: the first, located at g = 2.004 and whose attribution is still under debate, is commonly associated to oxygenated species present on the ZnO surface; the second signal appears at

a higher field (g ≈ 1.96). The origin of this resonance is also debated in the literature [37], [38], [39] and is most often relatable either to singly ionized oxygen vacancy defects ($V_O^{\bullet}$) or to shallow donor centers, such as ionized impurity atoms within the ZnO crystal lattice [38], [39]. Other studies, however, suggest that this EPR signal may instead arise from an electron weakly bound to Zn ionized impurities, such as Zn_i centres [40]. Upon UV irradiation, these centres are expected to become excited, thus generating paramagnetic species [41]. To clarify he origin of the features at g ≈ 1.96, measurements under UV photoexcitation were carried out by directly irradiating the samples inside the EPR cavity at 130 K.

Interestingly, Au@ZnO appears to be unaffected by UV irradiation (Fig. 5.10a), whereas the signal intensity of CuAu@ZnO increases slightly (Fig. 5.10b). This suggests that the observed signal may be partially associated also with electrons originating from shallow donor levels located at impurity sites, such as Zn_i centers, which seems to be completely absent in the Au@ZnO sample [41], [42]. However, even when present, these defects account for only a minor fraction of the overall signal detected for CuAu@ZnO. Additional experiments (i.e. CO gas dosing) helped to fully grasp the nature of the defect at g ≈ 1.96. The samples were initially placed under high vacuum conditions ($P < 10^{-4}$ mbar) directly in the EPR quartz tube, subsequently, 20 mbar of CO gas was introduced into the tube for 2 minutes. After restoring the vacuum and lowering the pressure, the EPR spectrum was recorded at 130 K.

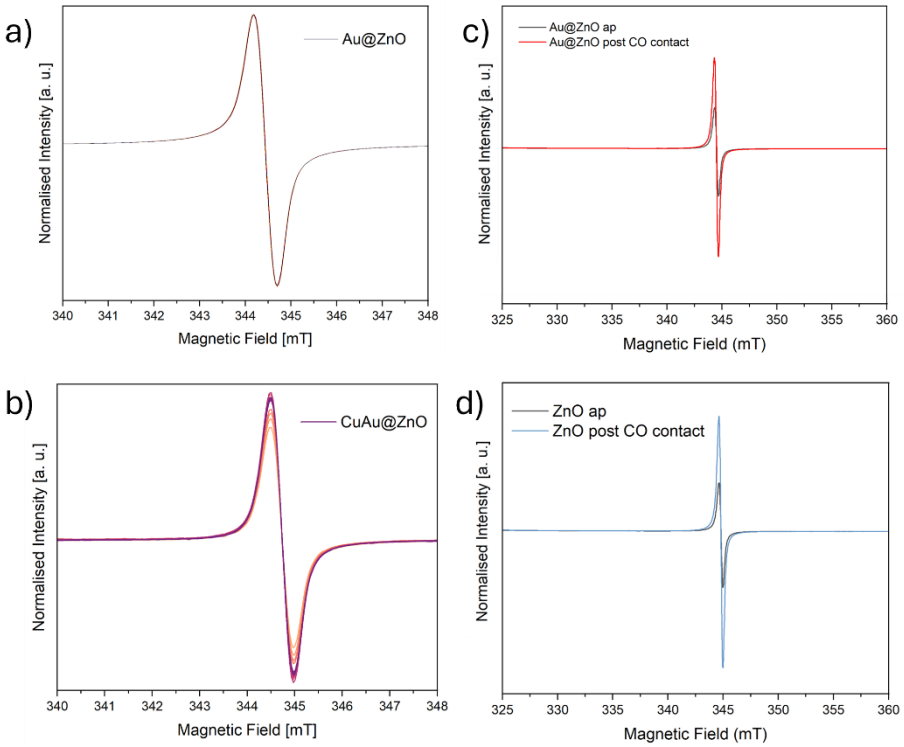

Fig. 5.10: EPR spectra of: a,b) UV kinetic measurements of respectively Au@ZnO and CuAu@ZnO; c,d) CO dosing respectively on Au@ZnO and CuAu@ZnO

In detail, for both the catalysts, the intensity of the signal increases after CO exposure (Fig. 5.10c, d) though more pronounced increase in the signal is visible for CuAu@ZnO sample (Fig. 5.10d). As widely described in the literature [43], CO can interact with lattice oxygen in ZnO, resulting in the formation of oxygen vacancies whose further ionization results in the generation of $V_O^{\bullet}$ species, according to the reactions:

$$CO + O_O \leftrightarrows CO_2 + V_O$$
$$V_O \leftrightarrows V_O^{\bullet} + e^-$$

$V_O^{\bullet}$ species are paramagnetic and therefore can be detected by EPR. These considerations indicate that the resonance observed at g ≈ 1.96 in CuAu@ZnO can be primarily attributed to the presence of $V_O^{\bullet}$ centers, along with the possible contribution of other defect sites (such as Zn interstitial or impurity sites).

The intensities of these EPR signals, normalized to the sample mass, provide indirect insights into the reactivity of the studied systems. Indeed, Bruckner et al. (2021) [2], investigated analogous systems, specifically Au nanoparticles supported on ZnO with varying particle sizes and evaluated their performance in CO_2 hydrogenation to methanol. Interestingly, they observed a direct correlation between methanol selectivity and the intensity of an EPR signal at g ≈ 1.96 attributed to oxygen vacancy defects located in the subsurface region, generated at the interfacial zone between Au and ZnO. This defect-induced interfacial environment correlates with catalytic reactivity, as a result on a charge transfer mechanism from the oxygen vacancies to the metal nanoparticles.

In our case, evidence of similar charge transfer can be inferred considering the appearance in the DRIFTS spectrum of the shoulders at 2070 cm^{-1} and 2058 cm^{-1} attributed to the CO–$Au^{\delta-}$ species and to the CO–Cu^0 bond, respectively, supporting the role of these defects in facilitating enhanced catalytic activity of Au@ZnO and, markedly, of CuAu@ZnO in the methanol generation.

After the catalytic reaction, the EPR spectra exhibit further changes (Fig. 5.9b). In particular, bare ZnO shows more intense signals than the samples containing clusters. This effect can be attributed to the presence of metal nanoparticles on the oxide surface, which act as electron sinks, withdrawing electrons from the substrate and thereby mitigating the formation of defects under the reducing conditions of the catalytic reaction.

The long-term stability of the catalysts was also investigated. Fig. 5.11 shows the EPR spectra of the CuAu@ZnO as prepared sample and after six months of storage in air at room temperature.

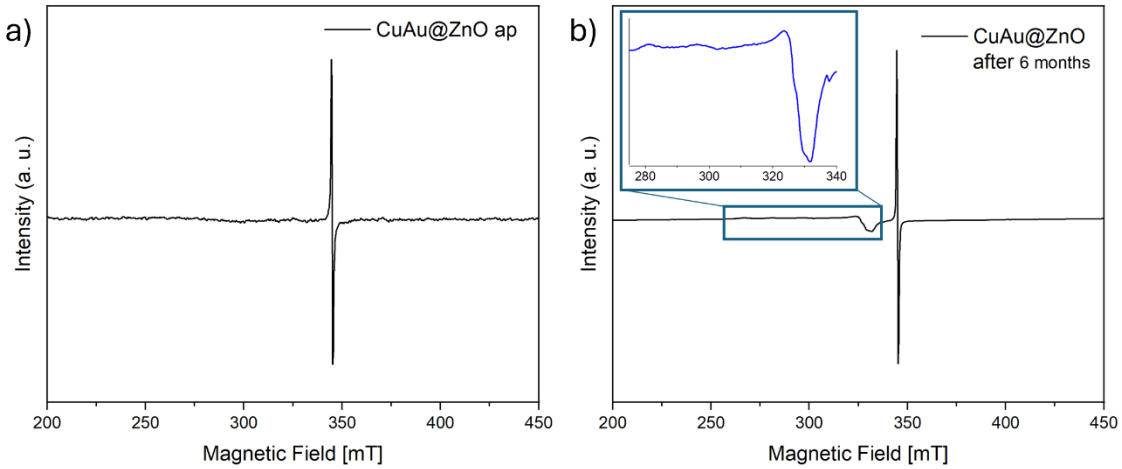

Fig. 5.11: a) EPR spectrum of CuAu@ZnO as prepared, b) EPR spectrum of CuAu@ZnO after six months of aging at room temperature and exposed to air

As previously discussed, Cu(II) is a highly sensitive EPR probe, detectable even at low concentrations. In Fig. 5.11a, no Cu(II) signal is observed, indicating that the Cu species in the clusters are in reduced states, either Cu(I) or Cu(0). After six months, however, a Cu(II) signal emerges in the lower-field region, attributable to Cu(II) centers with axial symmetry (Fig. 5.11b). This observation highlights both the relative stability of the material and its ability to stabilize reduced Cu species over a long period of time.

The partial oxidation and structural changes of the catalyst may stem from the intrinsic mismatch between Cu and Au. Although both metals adopt a face-centered cubic (fcc) lattice, their lattice constants differ significantly (0.361 nm for Cu versus 0.408 nm for Au, corresponding to an 11.4% deviation relative to Au) [44]. This lattice mismatch likely contributes to the structural evolution of $Au_{25-x}Cu_x(2\text{-PET})_{18}$ nanoclusters. Additionally, the higher chemical reactivity of Cu compared to Au makes Cu-containing clusters more prone to oxidation, promoting spontaneous de-alloying over time.

5.4 Conclusion

In this chapter, we investigated ZnO-supported Au and CuAu nanoclusters (NCs) in the catalytic hydrogenation of CO_2 to methanol, as a possible model system for the study of this reaction. Particular attention has been given to the structural, electronic, and defect-related features that govern their reactivity. The synthesis and characterization of $Au_{25}(2\text{-PET})_{18}$ and $Au_{25-x}Cu_x(2\text{-PET})_{18}$ clusters confirmed successful synthesis of both the clusters and the Cu incorporation at low doping levels, consistent with prior reports. Deposition of these clusters on ZnO nanoparticles provided model systems for probing metal–support interactions and their consequences for catalysis.

Spectroscopic analyses demonstrated that Cu doping subtly modifies the electronic structure of the clusters, while thermal pretreatments induce the formation of localized surface plasmon resonances, reflecting the generation of small metallic particles on ZnO. Importantly, both DRIFTS measurements revealed the dynamic interplay between cluster composition, ZnO defect formation, and gas adsorption. DRIFTS results showed that Au@ZnO favours CO binding to partially negative $Au^{\delta-}$ sites, whereas CuAu@ZnO preferentially binds CO through Cu^0 centres, reflecting a shift in active-site character upon alloying.

The catalytic tests under CO_2/H_2 revealed that both Au@ZnO and CuAu@ZnO are selective toward methanol production, with maximum yields near 350 °C. However, CuAu@ZnO exhibited higher methanol signals and sustained activity over a broader temperature window, consistent with its greater initial defect concentration and stronger CO adsorption capacity. The enhanced performance of CuAu@ZnO underscores the synergistic role of Cu in modulating both the electronic properties of Au sites and the defect chemistry of ZnO, thereby promoting more effective metal–support charge transfer and improved stabilization of reactive intermediates.

EPR confirmed the presence of oxygen vacancy ($V_O^{\bullet}$) defects and shallow donor states in ZnO, whose concentration was further enhanced by the presence of Cu. These defects, particularly subsurface $V_O^{\bullet}$ species, appear central to catalytic activity, as supported by correlations with methanol selectivity reported in the literature.

Overall, this study highlights that methanol formation over ZnO-supported nanoclusters is not solely dictated by the metallic component but also by the dynamic generation and utilization of ZnO defects at the metal–oxide interface. The results provide valuable insights into how heteroatom doping of Au NCs and controlled defect engineering in ZnO can be leveraged to design catalysts with higher activity, selectivity, and stability for CO_2 hydrogenation. These findings contribute to a deeper understanding of

structure–function relationships in complex nanocatalysts and suggest promising directions for advancing CO_2 valorisation technologies.

Bibliography

[1] H. Zada, J. Yu, and J. Sun, “Active Sites for CO2 Hydrogenation to Methanol: Mechanistic Insights and Reaction Control,” *ChemSusChem*, vol. 18, no. 4, p. e202401846, Feb. 2025, doi: https://doi.org/10.1002/cssc.202401846.

[2] S. Chen *et al.*, “Controlling the O-Vacancy Formation and Performance of Au/ZnO Catalysts in CO2 Reduction to Methanol by the ZnO Particle Size,” *ACS Catal*, vol. 11, no. 15, pp. 9022–9033, Aug. 2021, doi: 10.1021/acscatal.1c01415.

[3] R. Burch, S. E. Golunski, and M. S. Spencer, “The role of copper and zinc oxide in methanol synthesis catalysts,” *Journal of the Chemical Society, Faraday Transactions*, vol. 86, no. 15, pp. 2683–2691, 1990, doi: 10.1039/FT9908602683.

[4] K. C. Waugh, “Methanol Synthesis,” *Catal Letters*, vol. 142, no. 10, pp. 1153–1166, 2012, doi: 10.1007/s10562-012-0905-2.

[5] S. M. Fehr, K. Nguyen, and I. Krossing, “Realistic Operando-DRIFTS Studies on Cu/ZnO Catalysts for CO2 Hydrogenation to Methanol – Direct Observation of Mono-ionized Defect Sites and Implications for Reaction Intermediates,” *ChemCatChem*, vol. 14, no. 3, p. e202101500, Feb. 2022, doi: https://doi.org/10.1002/cctc.202101500.

[6] M. Behrens and R. Schlögl, “How to Prepare a Good Cu/ZnO Catalyst or the Role of Solid State Chemistry for the Synthesis of Nanostructured Catalysts,” *Z Anorg Allg Chem*, vol. 639, no. 15, pp. 2683–2695, Dec. 2013, doi: https://doi.org/10.1002/zaac.201300356.

[7] R. van den Berg *et al.*, “Structure sensitivity of Cu and CuZn catalysts relevant to industrial methanol synthesis,” *Nat Commun*, vol. 7, no. 1, p. 13057, 2016, doi: 10.1038/ncomms13057.

[8] G. Pacchioni, “From CO2 to Methanol on Cu/ZnO/Al2O3 Industrial Catalyst. What Do We Know about the Active Phase and the Reaction Mechanism?,” Feb. 16, 2024, *American Chemical Society*. doi: 10.1021/acscatal.3c05669.

[9] M. Yang *et al.*, “Probing the Nature of Zinc in Copper-Zinc-Zirconium Catalysts by Operando Spectroscopies for CO2 Hydrogenation to Methanol,” *Angewandte Chemie - International Edition*, vol. 62, no. 7, Feb. 2023, doi: 10.1002/anie.202216803.

[10] S. Chen *et al.*, “Performance of Au/ZnO catalysts in CO2 reduction to methanol: Varying the Au loading / Au particle size,” *Appl Catal A Gen*, vol. 624, p. 118318, 2021, doi: https://doi.org/10.1016/j.apcata.2021.118318.

[11] J. Strunk *et al.*, “Au/ZnO as catalyst for methanol synthesis: The role of oxygen vacancies,” *Appl Catal A Gen*, vol. 359, no. 1, pp. 121–128, 2009, doi: https://doi.org/10.1016/j.apcata.2009.02.030.

[12] A. M. Abdel-Mageed, A. Klyushin, A. Knop-Gericke, R. Schlögl, and R. J. Behm, “Influence of CO on the Activation, O-Vacancy Formation, and Performance of Au/ZnO Catalysts in CO2 Hydrogenation to Methanol,” *J Phys Chem Lett*, vol. 10, no. 13, pp. 3645–3653, Jul. 2019, doi: 10.1021/acs.jpclett.9b00925.

[13] Y. Hartadi, D. Widmann, and R. J. Behm, “CO2 Hydrogenation to Methanol on Supported Au Catalysts under Moderate Reaction Conditions: Support and Particle Size Effects,”

ChemSusChem, vol. 8, no. 3, pp. 456–465, Feb. 2015, doi: https://doi.org/10.1002/cssc.201402645.

[14] Y. Du, Y. Fang, P. Wang, and M. Zhu, "Synergistic effects of atomically precise Au-based bimetallic nanocluster on energy-related small molecule catalysis," *Chem Sci*, vol. 16, no. 24, pp. 10642–10664, 2025, doi: 10.1039/D5SC01108F.

[15] Q. Yao, T. Chen, X. Yuan, and J. Xie, "Toward Total Synthesis of Thiolate-Protected Metal Nanoclusters," *Acc Chem Res*, vol. 51, no. 6, pp. 1338–1348, Jun. 2018, doi: 10.1021/acs.accounts.8b00065.

[16] Y. Guo, M. Wang, Q. Zhu, D. Xiao, and D. Ma, "Ensemble effect for single-atom, small cluster and nanoparticle catalysts," *Nat Catal*, vol. 5, no. 9, pp. 766–776, 2022, doi: 10.1038/s41929-022-00839-7.

[17] X. Cai *et al.*, "Reversible Switching of Catalytic Activity by Shuttling an Atom into and out of Gold Nanoclusters," *Angewandte Chemie International Edition*, vol. 58, no. 29, pp. 9964–9968, Jul. 2019, doi: https://doi.org/10.1002/anie.201903853.

[18] Z.-J. Guan, J.-J. Li, F. Hu, and Q.-M. Wang, "Structural Engineering toward Gold Nanocluster Catalysis," *Angewandte Chemie International Edition*, vol. 61, no. 51, p. e202209725, Dec. 2022, doi: https://doi.org/10.1002/anie.202209725.

[19] J. Zhao and R. Jin, "Heterogeneous catalysis by gold and gold-based bimetal nanoclusters," *Nano Today*, vol. 18, pp. 86–102, 2018, doi: https://doi.org/10.1016/j.nantod.2017.12.009.

[20] G. X. Pei, L. Zhang, and X. Sun, "Recent advances of bimetallic nanoclusters with atomic precision for catalytic applications," *Coord Chem Rev*, vol. 506, p. 215692, 2024, doi: https://doi.org/10.1016/j.ccr.2024.215692.

[21] C. L. Bracey, P. R. Ellis, and G. J. Hutchings, "Application of copper–gold alloys in catalysis: current status and future perspectives," *Chem Soc Rev*, vol. 38, no. 8, pp. 2231–2243, 2009, doi: 10.1039/B817729P.

[22] T. MURAYAMA, T. ISHIDA, and C. MOCHIZUKI, "UCARBON DIOXIDE REDUCTION CATALYST AND CARBON DIOXIDE REDUCTION METHOD," US 2023/0166242 A1, Jun. 2023

[23] M. Dhifallah, M. Iachella, A. Dhouib, F. Di Renzo, D. Loffreda, and H. Guesmi, "Support Effects Examined by a Comparative Theoretical Study of Au, Cu, and CuAu Nanoclusters on Rutile and Anatase Surfaces," *The Journal of Physical Chemistry C*, vol. 123, no. 8, pp. 4892–4902, Feb. 2019, doi: 10.1021/acs.jpcc.8b11812.

[24] A. A. Mikhailova, S. V Lepeshkin, V. S. Baturin, A. P. Maltsev, Y. A. Uspenskii, and A. R. Oganov, "Ultralow reaction barriers for CO oxidation in Cu–Au nanoclusters," *Nanoscale*, vol. 15, no. 33, pp. 13699–13707, 2023, doi: 10.1039/D3NR02044D.

[25] E. Ibáñez-Alé *et al.*, "Structural Evolution of Stapes Controls the Electrochemical CO2 Reduction on Bimetallic Cu-doped Gold Nanoclusters," *Small*, vol. 21, no. 2, p. 2408531, Jan. 2025, doi: https://doi.org/10.1002/smll.202408531.

[26] Y. Negishi, K. Munakata, W. Ohgake, and K. Nobusada, "Effect of Copper Doping on Electronic Structure, Geometric Structure, and Stability of Thiolate-Protected Au25 Nanoclusters," *J Phys Chem Lett*, vol. 3, no. 16, pp. 2209–2214, Aug. 2012, doi: 10.1021/jz300892w.

[27] S. Lee, S. Jeong, D. Kim, S. Hwang, M. Jeon, and J. Moon, “ZnO nanoparticles with controlled shapes and sizes prepared using a simple polyol synthesis,” *Superlattices Microstruct*, vol. 43, no. 4, pp. 330–339, 2008, doi: https://doi.org/10.1016/j.spmi.2008.01.004.

[28] E. Gottlieb, H. Qian, and R. Jin, “Atomic-Level Alloying and De-alloying in Doped Gold Nanoparticles,” *Chemistry – A European Journal*, vol. 19, no. 13, pp. 4238–4243, Mar. 2013, doi: https://doi.org/10.1002/chem.201203158.

[29] A. Dass, A. Stevenson, G. R. Dubay, J. B. Tracy, and R. W. Murray, “Nanoparticle MALDI-TOF Mass Spectrometry without Fragmentation: Au25(SCH2CH2Ph)18 and Mixed Monolayer Au25(SCH2CH2Ph)18−x(L)x,” *J Am Chem Soc*, vol. 130, no. 18, pp. 5940–5946, May 2008, doi: 10.1021/ja710323t.

[30] “Analysis of the IR Spectrum of Carbon Monoxide.” [Online]. Available: https://chem.libretexts.org/@go/page/96247

[31] H. Tang *et al.*, “Classical strong metal–support interactions between gold nanoparticles and titanium dioxide,” *Sci Adv*, vol. 3, no. 10, p. e1700231, Sep. 2025, doi: 10.1126/sciadv.1700231.

[32] E. Shaaban and G. Li, “Probing active sites for carbon oxides hydrogenation on Cu/TiO2 using infrared spectroscopy,” *Commun Chem*, vol. 5, no. 1, p. 32, 2022, doi: 10.1038/s42004-022-00650-2.

[33] M. L. Smith, N. Kumar, and J. J. Spivey, “CO Adsorption Behavior of Cu/SiO2, Co/SiO2, and CuCo/SiO2 Catalysts Studied by in Situ DRIFTS,” *The Journal of Physical Chemistry C*, vol. 116, no. 14, pp. 7931–7939, Apr. 2012, doi: 10.1021/jp301197s.

[34] L. Cai, Z. Hu, P. Branton, and W. Li, “The effect of doping transition metal oxides on copper manganese oxides for the catalytic oxidation of CO,” *Chinese Journal of Catalysis*, vol. 35, pp. 159–167, Feb. 2014, doi: 10.1016/S1872-2067(12)60699-8.

[35] M. T. Khalil *et al.*, “Recent advancements in catalytic CO2 conversion to methanol: strategies, innovations, and future directions,” Jul. 28, 2025, *Royal Society of Chemistry*. doi: 10.1039/d5gc01906k.

[36] M. Behrens, “Promoting the Synthesis of Methanol: Understanding the Requirements for an Industrial Catalyst for the Conversion of CO2,” *Angewandte Chemie International Edition*, vol. 55, no. 48, pp. 14906–14908, Nov. 2016, doi: https://doi.org/10.1002/anie.201607600.

[37] S. M. Evans, N. C. Giles, L. E. Halliburton, and L. A. Kappers, “Further characterization of oxygen vacancies and zinc vacancies in electron-irradiated ZnO,” *J Appl Phys*, vol. 103, no. 4, p. 043710, Feb. 2008, doi: 10.1063/1.2833432.

[38] B. K. Meyer *et al.*, “Bound exciton and donor–acceptor pair recombinations in ZnO,” *physica status solidi (b)*, vol. 241, no. 2, pp. 231–260, Feb. 2004, doi: https://doi.org/10.1002/pssb.200301962.

[39] A. Janotti and C. G. Van de Walle, “Fundamentals of zinc oxide as a semiconductor,” *Reports on Progress in Physics*, vol. 72, no. 12, p. 126501, 2009, doi: 10.1088/0034-4885/72/12/126501.

[40] S. Polarz *et al.*, “Structure–Property–Function Relationships in Nanoscale Oxide Sensors: A Case Study Based on Zinc Oxide,” *Adv Funct Mater*, vol. 17, no. 8, pp. 1385–1391, May 2007, doi: https://doi.org/10.1002/adfm.200700139.

[41] D. M. Hofmann *et al.*, “Hydrogen: A Relevant Shallow Donor in Zinc Oxide,” *Phys Rev Lett*, vol. 88, no. 4, p. 45504, Jan. 2002, doi: 10.1103/PhysRevLett.88.045504.

[42] V. Ischenko, S. Polarz, D. Grote, V. Stavarache, K. Fink, and M. Driess, “Zinc Oxide Nanoparticles with Defects,” *Adv Funct Mater*, vol. 15, no. 12, pp. 1945–1954, Dec. 2005, doi: https://doi.org/10.1002/adfm.200500087.

[43] M. D’Arienzo, F. Morazzoni, R. Ruffo, and R. Scotti, “Using the electron spin resonance to detect the functional centers in materials for sensor devices,” *Ionics (Kiel)*, vol. 27, no. 5, pp. 1839–1851, 2021, doi: 10.1007/s11581-021-03996-0.

[44] A. F. Alvarez-Paneque, B. Rodríguez-González, I. Pastoriza-Santos, and L. M. Liz-Marzán, “Shape-Templated Growth of Au@Cu Nanoparticles,” *The Journal of Physical Chemistry C*, vol. 117, no. 6, pp. 2474–2479, Feb. 2013, doi: 10.1021/jp3062724.

Chapter 6

Other case studies

Index of the chapter

This chapter presents a comprehensive description of the synthesis procedures, characterization techniques, and testing methods employed to investigate two distinct catalytic systems. On the one hand, both commercial and synthetic CZA catalysts were thoroughly characterized and tested in the CO_2 conversion to methanol to gain insights into the current state of the art of this reference material. On the other hand, Cu and Zn co-doped STO catalysts were synthesized and evaluated in the same reaction as a model system to better assess the synergistic effect arising from the occurrence of a Cu/Zn interface

6.1 CZA

As already mentioned in the Introduction of this dissertation, the commercially available catalyst for CO_2 conversion to MeOH is called CZA which stands for $CuO/ZnO/Al_2O_3$. Generally speaking, this catalyst is composed as follows: CuO ca. 60% wt, ZnO ca. 30% wt, Al_2O_3 ca. 10% wt. In the present work, the first attempts have been devoted to characterize and to test in the CO_2 conversion to methanol a commercially available CZA sample (labelled as CZA-comm). Afterwards, a CZA catalysts (called CZA-synt) was synthesized by a tailor-made co-precipitation approach. The sample was then characterized, tested and the performances compared with CZA-comm.

6.1.1 Synthesis of CZA

To produce the in-house catalyst a coprecipitation method has been employed [1]. A 1M solution of $Zn(NO_3)_2$, $Cu(NO_3)_2$, $Al(NO_3)_3$ was heated up till 90°C, and then a 1M solution of $NaCO_3$ was added dropwise until the pH reached 6.9. After the addition was completed, the reaction was kept stirring for 90 more minutes and then filtered and washed with distilled water. The powder was the dried in an oven at 80°C overnight and subsequently calcination was carried out in air. After several trials an optimized calcination procedure was adopted consisting of: a heating ramp of 10 °C min^{-1} from room temperature to 150 °C, followed by a 30-minute isothermal hold at this temperature; the temperature was then increased to 200 °C at the same rate, with another 30-minute isothermal step. This procedure was then repeated in 50 °C increments up to 350 °C, temperature at which the sample was finally maintained under isothermal conditions for 3 h (see Fig. 6.1).

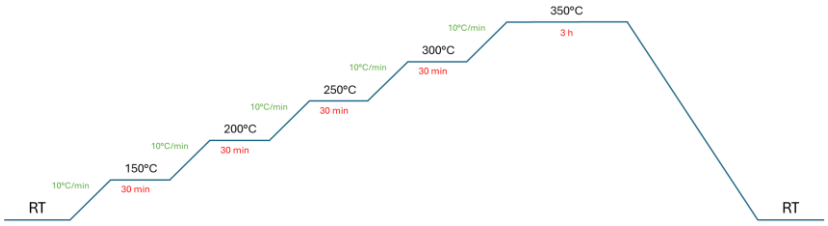

Fig. 6.1: Schematic temperature ramp for the final calcination procedure used for CZA-synt

6.1.2 Characterization

CZA-synt was fully characterized and compared to the CZA commercial catalyst. A multi-technique approach was employed to obtain a comprehensive understanding of the samples' characteristics from different perspectives. Usually, these kinds of materials are activated before catalysis via a strong reductions step in H_2 (either pure or 20% in Ar/N_2) at relatively low pressure (4 bar) and temperature (400°C). Whenever possible and, particularly, when relevant, the samples were analyzed at all three stages of the process: as-prepared (ap), activated, and spent. However, some characterization techniques could not be applied at every stage. During the activation and catalytic testing steps, the catalysts were physically mixed with quartz wool and quartz sand, which made any subsequent quantitative analysis unreliable.

TEM

TEM imaging was performed on both samples to assess the shape and morphology, and it was also coupled with EDX analyses (Fig. 6.2).

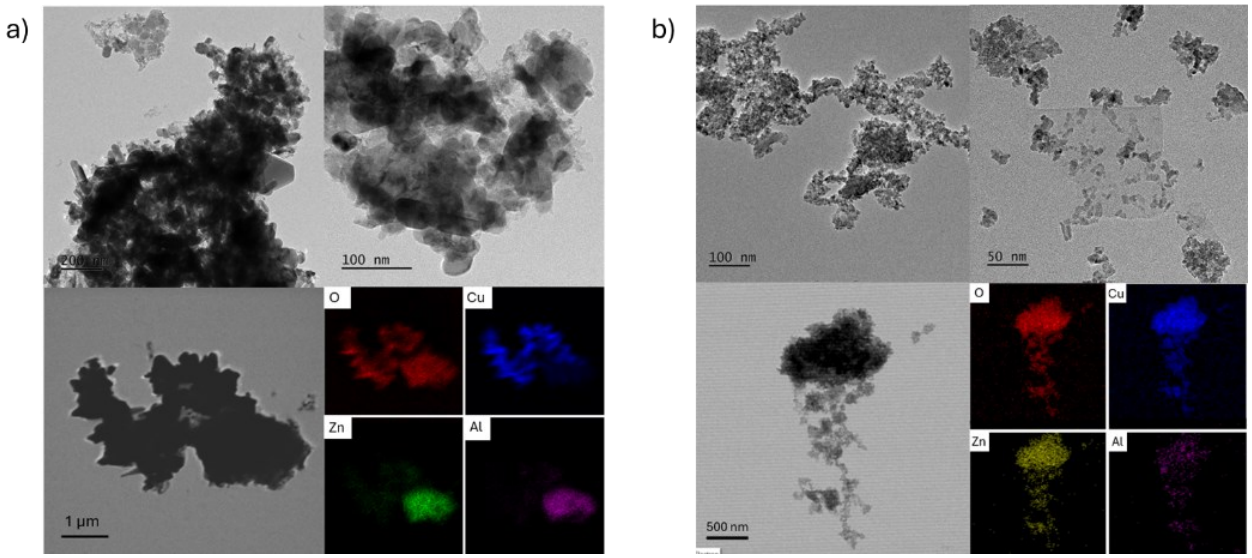

Fig. 6.2: a) TEM images and EDX mapping of CZA-synt; b) TEM images and EDX mapping of CZA-comm

A clear difference in the morphological features can be observed from the obtained images. The synthesized catalyst (CZA-synt) is composed of relatively large particles, with sizes ranging from approximately 20 to 100 nm (Fig. 2a), whereas the commercial catalyst (CZA-comm) consists predominantly of smaller particles, around 10 nm in length (Fig. 2b). This morphological variation is further reflected in the EDX elemental mapping of the two materials. In CZA-comm, the elemental distribution appears homogeneous across aggregates extending over several hundred nanometers, suggesting a uniform dispersion of the constituent metals. In contrast, CZA-synt exhibits regions of compositional inhomogeneity, where only two of the three metallic elements are detected, indicating a less uniform distribution within the catalyst structure.

XRD

PXRD analyses were performed on both samples before and after catalysis (Fig. 6.3).

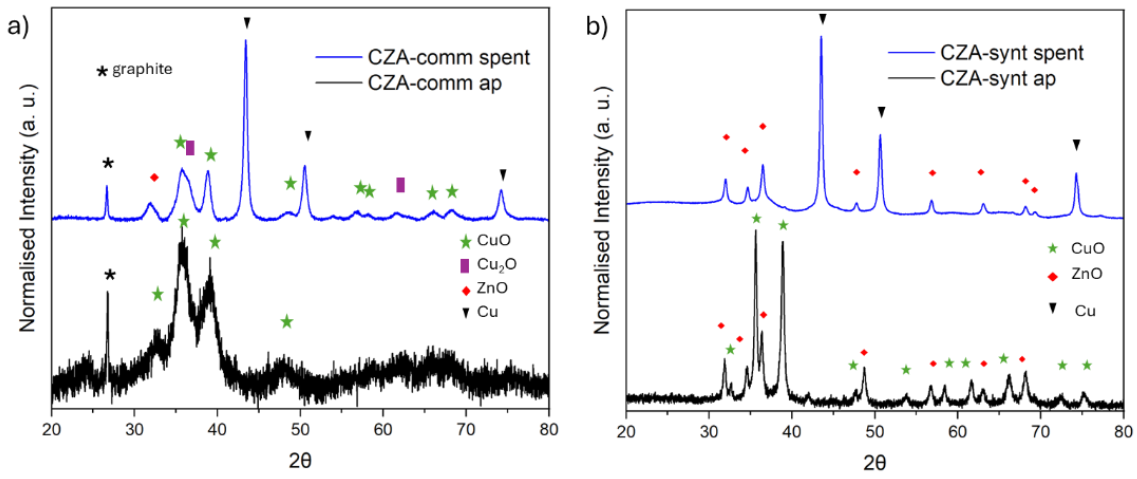

Fig. 6.3: PXRD diffraction pattern of a) CZA-comm as prepared (black line) and after catalysis (blue line), b) CZA-synt as prepared (black line) and after catalysis (blue line)

Firstly, the as-prepared samples of CZA-comm and CZA-synt were compared. The CZA-comm diffractogram appears considerably noisier than that of CZA-synt, indicating a lower degree of crystallinity. This can likely be attributed to the smaller particle size of the commercial catalyst, as confirmed by TEM imaging. In contrast, the synthesized sample exhibits sharper diffraction peaks, suggesting a more crystalline structure and the presence of multiple well-defined phases even prior to catalytic testing. Conversely, CZA-comm primarily shows reflections corresponding to CuO, with no evidence of additional crystalline phases.

After the catalytic reaction, the overall trends remain consistent: CZA-synt retains higher crystallinity and displays sharper diffraction features compared to CZA-comm. Notably, post-reaction analysis of CZA-comm reveals the occurence of peaks corresponding to Cu_2O, indicating the partial reduction of Cu species during catalysis. Such phases are absent in the post-reaction pattern of CZA-synt, suggesting greater structural stability under reaction conditions.

Finally, in the XRD pattern of CZA-comm, an additional peak is observed at 2θ = 26°, which, based on phase analysis, can be attributed to graphite. This finding is consistent with the TEM observations described earlier.

ICP & CHNS

Elemental analyses were conducted to quantify the metal content by inductively coupled plasma (ICP) spectroscopy (Table 6.1) and to evaluate the presence of organic residues by CHNS elemental analysis (Table 6.2).

Table 6.1: ICP results for CZA-comm and CZA-synt

Sample	Cu %	Zn%	Al %
CZA-comm	46.9	3.72	17.7
CZA-synt	49.1	3.52	16.8

The ICP analysis revealed that the metal loadings of the two samples are comparable and fall within the range typically reported for CZA catalysts [2], [3]. CHNS elemental analysis was further employed to investigate possible differences between the samples in terms of organic residue content. In addition, TGA measurements were carried out to correlate the CHNS results with the thermal stability of the materials (Fig. 6.4). The corresponding results are presented in the following section.

Table 6.2: CHNS results for CZA-comm and CZA-synt

Weight [mg]	**Name**	**C [%]**	**H [%]**	**N [%]**	**S [%]**
1.4700	CZA-synt	0.25	0.118	0.00	0.000
1.5300	CZA-comm	13.69	3.655	0.00	0.000

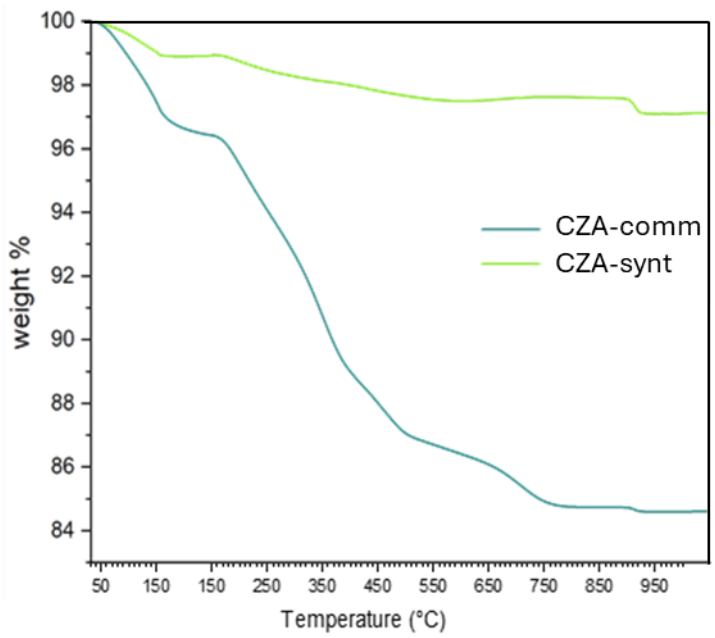

Fig. 6.4: TGA curves for CZA-comm and CZA-synt

An interesting observation is that CZA-comm contains approximately 14 wt% of carbon, as determined by CHNS analysis (Table 2). According to the TGA profile, this carbonaceous fraction decomposes gradually between 250 °C and 700 °C. Such behavior is consistent with the presence of graphitic material, previously identified by TEM and XRD, and explains why the total oxide content of CZA-comm, as determined by ICP analysis, accounts for only about 84 wt% of the total mass.

In contrast, CZA-synt does not exhibit a comparable carbon signal or significant mass loss in this temperature range, confirming the absence of graphitic species. However, when calculating the total oxide contribution for CZA-synt, approximately 10 wt% of the mass remains unaccounted. This discrepancy may be attributed to the presence of amorphous impurities, such as residual sodium ionic species or carbonate species (CO_3^{2-}), originating from the synthesis process.

XAS

Cu-Edge

The Cu K-shell spectra of copper (Fig. 6.5a) show that both the CZA-synt and CZA-comm, are mainly composed of CuO. As for what concerns the activated and spent CZA-comm, we can see that the former appears to be very similar to the metallic copper sample, although the oscillations are less intense, while the latter shows a slight shift in threshold (of 0.4 eV) which could be due to slight oxidation. Finally, the activated and spent samples obtained from CZA-synt appear to be mainly composed of metallic copper.

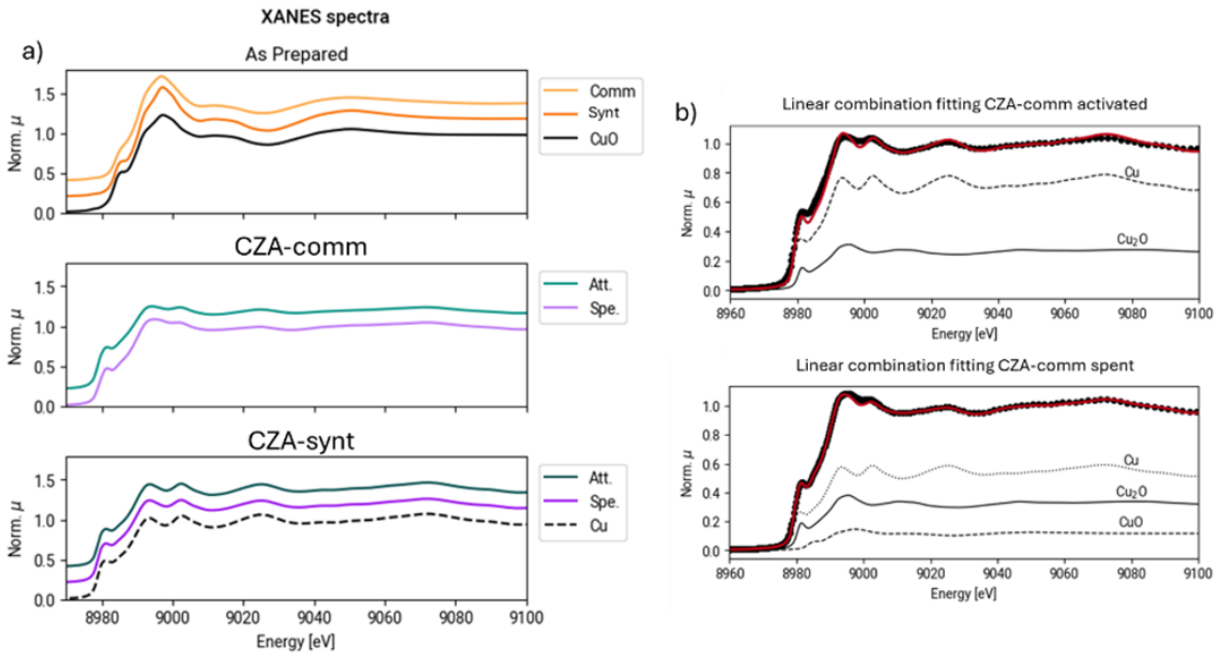

Fig. 6.5: a) XANES spectra of Cu edge for the different samples at different stages; b) LCF of XANES spectra for CZA-comm and CZA-synt

By Linear Combination Fitting (LCF) Fig. 6.5b, the amount of metallic and oxidated Cu in CZA-comm can be retrieved. It can be observed that the spent catalyst contains a mixture of Cu(0), Cu(I), and Cu(II) species, whereas the activated catalyst consists solely of Cu(0) and Cu(I), with no detectable presence of Cu(II) (Table 6.3).

Table 6.3: LCF weight for each Cu species in CZA-comm samples. In brackets the error

Species	CZA-comm activated	CZA-comm spent
Cu	72(3)	56(1)
Cu_2O	28(4)	30(1)
CuO	4	14(1)

The EXAFS spectra (Figure 6.6a) provide very similar indications. At the top, the spectra of the as prepared samples, compared with the CuO standard, show the signal due to scattering between collinear Cu atoms in the region between 6 and 10 $Å^{-1}$ (as shown in the top right-hand representation); this signal is very intense for the CZA-synt sample and very weak for the CZA-comm, indicating a less ordered structure as already seen in the XRD (less crystallinity = less order in the sample). In the middle and bottom graphs, respectively, CZA-comm and CZA-synt are compared with the Cu standard, since no oxide oscillations are visible and the trend is similar to metallic copper.

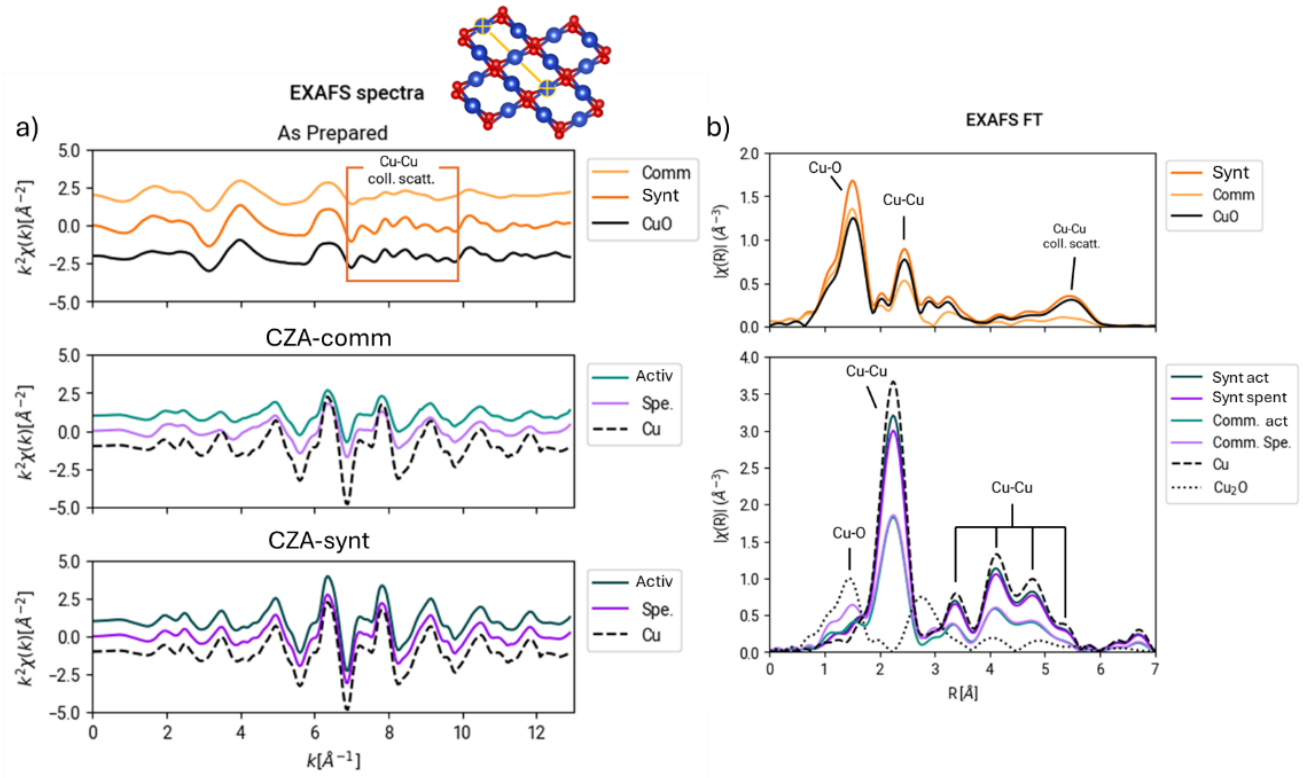

Fig. 6.6: a) EXAFS spectra of Cu edge for CZA-comm and CZA-synt in different stages of the process; b) FT of EXAFS spectra

The Fourier transforms of the EXAFS spectra (Figure 6.6b) were calculated for all spectra in the range 3–12.5 $Å^{-1}$. A qualitative analysis allows us to see that the as-prepared samples show Cu-O and Cu-Cu bond peaks as found in copper (II) oxide; again, the collinear scattering peak is very intense in CZA-synt and less intense in CZA-comm. The other samples all show oscillations related to metallic copper, while in the commercial sample, a rather intense band related to the Cu-O bond is also observed. What can therefore be hypothesised is a reduction of Cu during activation, which goes from Cu^{2+} to Cu^0, followed by a slight re-oxidation during catalysis, as also shown in the LCF, and by the increase in intensity of the Cu-O bond. What is noticeable is that, despite being identified in the LCF, no peaks related to copper(I) oxide are observable. A quantitative analysis of the EXAFS data confirms what has been commented so far. The spectra of the as-prepared samples were fitted using the structural data of CuO up to the second shell (R max fit of 3Å). In the case of CZA-comm, it can be observed that the structure at higher R is not present, indicating a greater amorphous component. From the point of view of interatomic distances, the two samples show no differences from the CuO standard. By observing the signal amplitudes, it can be seen that in the case of CZA-synt, the copper is completely present in the CuO crystalline phase, while in CZA-comm, the crystalline CuO phase is approximately 50% of the whole Cu(II) content.

By looking at the fittings for the activated and spent samples of both CZA we can see that in CZA-synt, the amount of copper in the metallic structure is close to 100%, while for CZA-comm the value is lower

(compatible with the data found with the LCF). In particular, for the spent CZA-comm sample, a Cu-O bond is clearly visible, which has the same distance as the bond with oxygen in the case of a bi-coordinated Cu(I), with a copper-metal, copper-oxide ratio of 1:1. In the case of the activated commercial sample, 50% metallic copper is observed, although it was not possible to fit the remaining 50%.

Zn-Edge

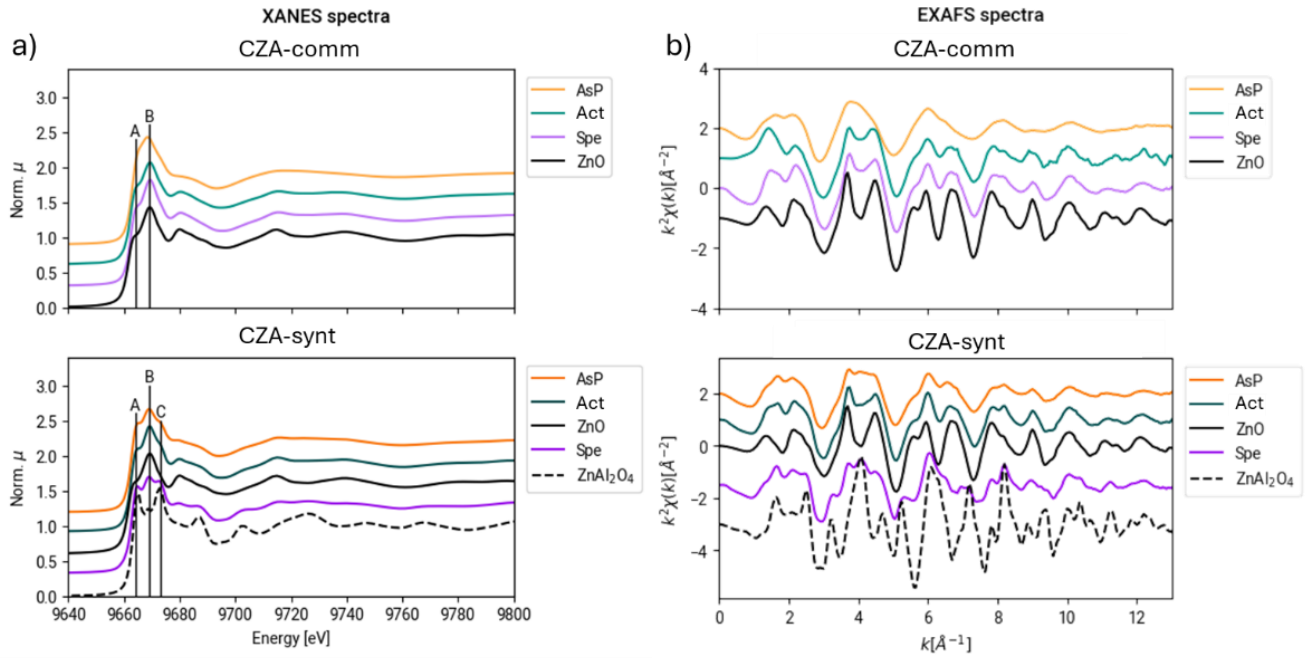

Fig. 6.7: a) XANES spectra of CZA-comm and CZA-synt at different stages of the process, b) EXAFS spectra of the two samples

In the case of CZA-comm, the XANES spectra (Fig. 6.7a) of the activated and spent samples closely resemble the ZnO spectrum, and the absorption bands are well reproduced, while for spectrum of CZA-comm as prepared much less distinct bands are visible. For the CZA-synt samples, on the other hand, the difference is more marked, bands A and B (Fig. 6.7a) are much more resolved, and a third band C also appears. These bands can be attributed to the presence of a crystalline form of $ZnAl_2O_4$, the spectrum of which is shown at the bottom of Fig. 6.7a. It is therefore possible to hypothesise a combination of zinc oxide with alumina during reaction, leading to the formation of this structure like already suggested in the literature [4], [5]. The same observations can be made for the EXAFS data, Fig. 6.7b. In particular, for the spectra of spent CZA-synt, oscillations at 2.5, 4, 6 and 8 $Å^{-1}$, characteristic of the $ZnAl_2O_4$ structure, can be observed. For further confirmation, LCF (not shown) were calculated for

the EXAFS spectrum of the spent CZA-synt, from which a ratio of 60% ZnO and 40% $ZnAl_2O_4$ was calculated.

The Fourier transforms reported in Figure 7b, (calculated in the range 3-12.6 $Å^{-1}$), show a very intense peak linked to the Zn-O bond in all samples, with an intensity equal to or greater than that observed in the ZnO standard, and a much less intense peak linked to the Zn-Zn bond (indicating a different degree of crystallinity). For CZA-comm, this peak increases in intensity after activation, while upon catalysis, both the Zn-O and Zn-Zn bond peaks increase equally. These observations suggest that, initially, ZnO is highly dispersed within the matrix, likely in an amorphous form, which gradually becomes more crystalline upon activation and during the catalytic reaction. In the spent catalyst, the peaks around 4Å also begin to have intensity ratios similar to those of ZnO, also indicating an increase in order in the sample.

In the case of CZA-synt, on the other hand, an extremely intense Zn-O bond peak is observed, and the Zn-Zn bond increases with activation and then decreases with reaction. The peaks of the activated sample are very similar to those of ZnO, although less intense, a situation that is then lost with reaction.

The EXAFS data were fitted in a window from 1 to 3.5 Å, thus fitting the first two shells (also including multiple scattering). It was not possible to fit the spent CZA-synt due to the number of bonds present and the overlap between the peaks of the two structures. Although the bond distances are always equivalent to those of zinc oxide in tetrahedral form (zincite), the concentration of Zn-O and Zn-Zn bonds changes significantly (as also observed from the qualitative analysis of the peaks). The number of Zn-O bonds remains virtually constant, while for the commercial sample there is an increase in Zn-Zn bonds throughout the transformation: 10% in the case of the as-prepared sample, 20% for the activated sample and 30% for the deactivated sample (10% error). For CZA-synt, on the other hand, there is an increase between the as-prepared and activated structures, with an increase in Zn-Zn bonds from 20 to 30%.

XPS

The spectral region of the Cu2p3/2 signal and the following “shake up” has been used for copper (II)/(copper (I) + copper (0)) evaluation. The use of the Cu2p3/2 component in the deconvolution analysis neglecting the 2p1/2 component is preferred since the Cu2p1/2 accounts quantitatively for the half of the Cu2p3/2 area [6]. The components at binding energies lower than 933.0 eV can be attributed either to copper (I) or to metallic copper. From literature the binding energy of the metallic copper is 932.63 eV while for Cu_2O is 932.18 eV but are also reported and employed different binding energies for them [7], [8]. The fitting curve used is centred at energy below 933.0 eV, and is broader than the two separated

contribute reported in literature [6]. Copper (II) Cu2p3/2 peaks are reported to be fitted using more than a component, especially for CuO and Cu(OH)2. Three curves have been used, accounting for copper oxide/copper carbonate (first, around 933.9 eV), copper hydroxide/copper carbonate (the latter expected at 935.1eV) and the extension of the main Cu2p3/2 signal toward the shake up (third, around 937.4 eV), that is reported, at higher binding energies, for copper hydroxide. In addition, to account the variation in the distribution of different species among the samples, the component has been centred at the same binding energy (±0.2 eV), but the FWHM has been left free to widen. The "shake up" signal has been fitted using three curves and this high number of components can be attributed to the presence of copper oxide, copper hydroxide and copper carbonate (or even malachite), also known to possess "shake up" with a different shape. The use of a third curve in the "shake up" is needed to avoid the use of broad curves that risked contributing in the fitting of the Cu2p3/2 signal, becoming an overfit of the data. These curves are employed to perform the analysis of the copper (II)/(copper (0) + copper (I)) abundance (data are summarized in Fig. 6.8)

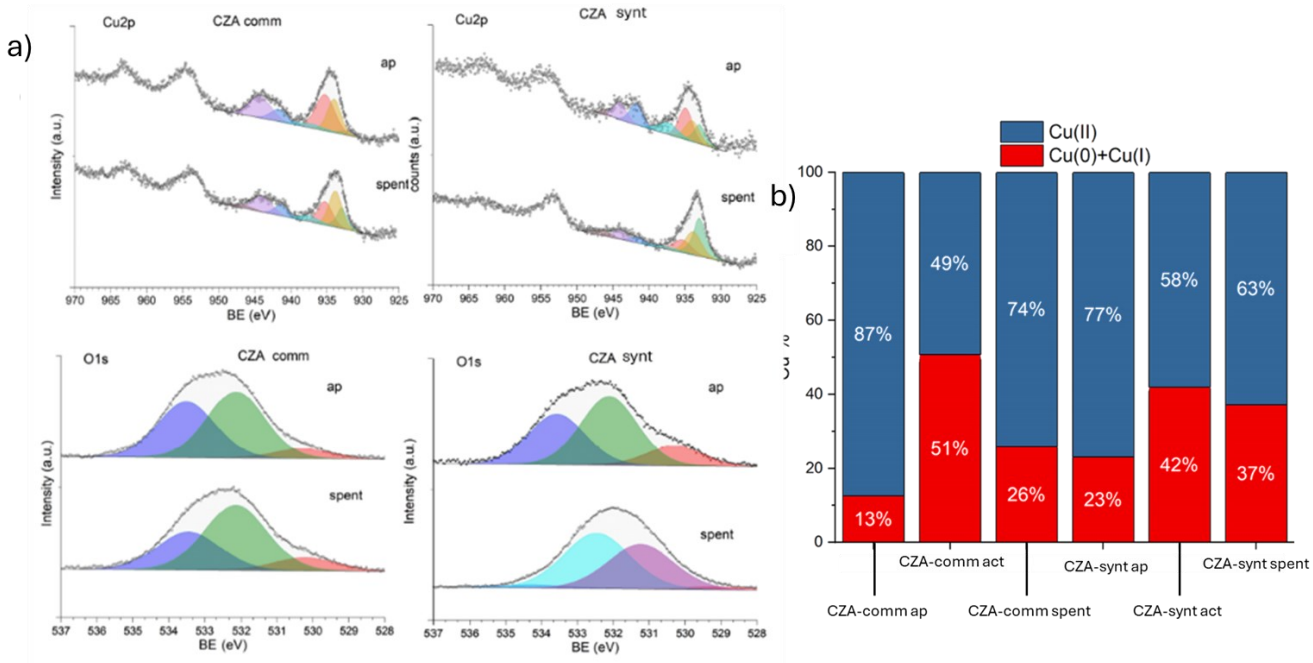

Fig. 6.8: a) XPS spectra of Cu2p region (top) and O1s region (bottom); b) schematic summary of different oxidation states of Cu content in the two samples at different steps of the reaction

The O1s region (Fig. 8a, bottom) has been fitted using three components for all the samples but the spent CZA-synt, that required 4 components. O1s peak fitted with three components presents a contribute at 530.2 eV that is attributed to lattice oxygen bounded to metal (copper), one at 532.1 eV and attributed to carbonates (copper carbonate, zinc carbonate and more in general carboxylic carbon), and one at 533.5 eV attributed to water [9]. Sample CZA-synt spent presents 4 contributions, a small

one centred around 529.1 eV and attributable to copper (II) oxide, one at 531.2 eV and attributable to either zinc oxide, copper hydroxide or zinc hydroxide, one at 532.5 and attributable to carbonates and/or hydroxides and a small component at 534.2 eV attributable to water.

Regarding the other regions, the C1s signal has been fitted using 4 curves (Fig. 6.9 a), one identified as adventitious carbon, and used to calibrate the spectrum (centred at 285.0 eV), one identified as (C-O) at around 286.2 eV and attributed to C-O from the sample but also from the carbon tape, one at 288.7 eV that has been identified as C from CO_3^{2-} (copper carbonate, zinc carbonate [10]), and one very small component at 290.4 eV identifiable as carbon from HCO_3^- [11]. These four components are equally present in all the sample with the exception of spent CZA-synt, which presented a smaller contribution from C-O and CO_3^{2-} and a slightly increase in the HCO_3^- one (Fig. 9a).

The Zn 2p region (Fig. 9b) is characterized by the two 1/2 and 3/2 spin orbit peaks, separated by 22.97 eV, with the one at lower binding energy located around 1022.4 eV for the CZA-synt series, and 1022.7eV for the CZA-comm series, and in both cases attributable to $ZnO/Zn(OH)_2/ZnCO_3$ [12]. Also the Auger transitions of both Cu and Zn were thoroughly analysed (Fig. 6.9c and 6.9d), but the information retrieved are the same as the analysis done on the main transitions of the spectra and therefore are not presented here.

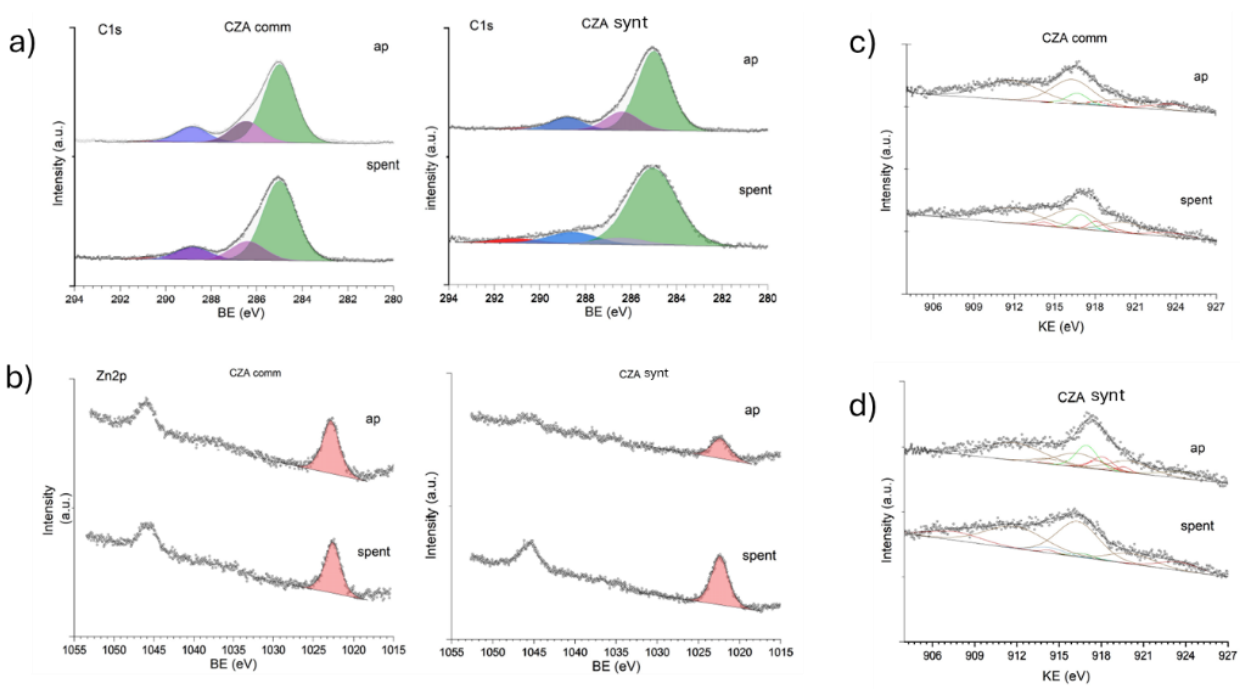

Fig.6.9: XPS spectra of CZA-comm and CZA-synt: a) C1s region; b) Zn2p region; c,d) Cu $L_3M_{45}M_{45}$ Auger peak

6.1.3 Catalytic tests

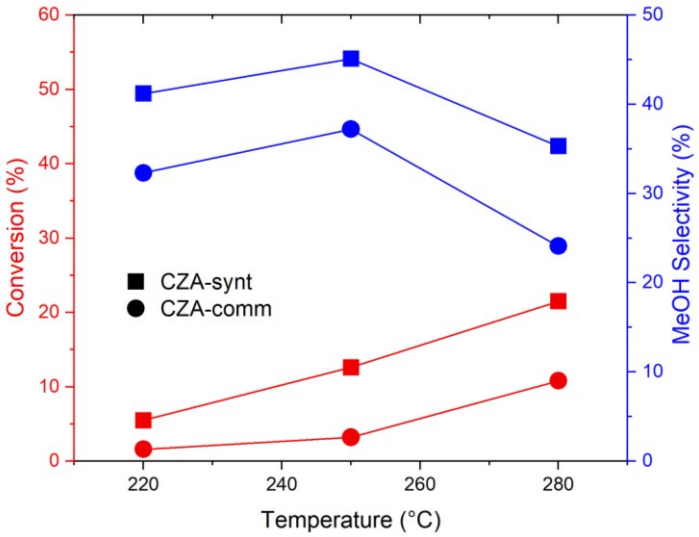

Fig. 6.10: Catalytic results of CZA-synt and CZA-comm

Both samples were tested for CO_2 conversion to MeOH in a lab scale catalytic plant at three different temperatures (220, 250, 280°C), at a pressure of 20 bar with a gas inlet mixture of CO_2 and H_2 with ratio H_2: CO_2 of 3:1. Reactions were carried out for 71h, and at the end of the reactions the cold trap containing the MeOH was weighted to assess the amount of product obtained and calculate the carbon balance.

Interestingly, the CZA-synt catalyst exhibits both higher CO_2 conversion and greater selectivity toward methanol compared to CZA-comm (Fig. 6.10). The experiment was repeated twice, yielding consistent results. However, the overall carbon balance for CZA-synt consistently showed an error of approximately 20%. When this discrepancy is taken into account, the performance data of the two catalysts can be considered broadly comparable. Nevertheless, as shown in Figure 6.4, CZA-comm contains approximately 13 wt% of graphitic carbon. To enable a more accurate comparison of the catalytic activity between the two samples, a new batch of CZA-synt was prepared, and graphite was added to account for 13% of its total weight.

Table 6.4: Catalytic results of CZA-synt + C

SAMPLE	PRESSURE [bar]	T [°C]	% Conversion	%CO selectivity	%MeOH selectivity	%MeOH Yield
CZA-synt+C	20	220	<1	-	-	-
CZA-synt+C	20	250	<1	-	-	-
CZA-synt+C	20	280	3.0	40.0	25.0	0.8

Interestingly, when graphitic carbon is added to the CZA-synt catalyst, its CO_2 conversion drops drastically, and virtually no reaction is observed (see Table 6.4). This behavior is likely due to the graphite covering the active sites, thereby preventing the catalytic reaction from occurring. While in some cases the addition of a small amount of graphite can improve heat and water dispersion, favoring direct reactions over reverse reactions, this effect is not observed in the present study. Notably, CZA-comm, despite containing approximately 13 wt% graphite, exhibits catalytic activity comparable to CZA-synt without graphite, indicating that the remaining "active" material in CZA-comm is sufficient to sustain reaction performance.

6.1.4 Conclusion

In summary, extensive effort was devoted to the full characterization of the CZA-comm catalyst in order to gain new insights into the behaviour of this highly dynamic system. Our attempt to reproduce it (CZA-synt) did not fully succeed, as evident from several analyses. TEM images clearly show a significant difference in particle size between CZA-synt and CZA-comm, while more complex spectroscopic techniques (e.g., XAS, XPS) also reveal distinct behaviours between the two materials. These discrepancies likely originate from differences in the synthetic pathways. In particular, the smaller particle size of CZA-synt may result from an alternative synthesis route, such as flame synthesis, which could also have influenced the crystallinity of the sample (Fig. 6.3a, 6.6a).

The two samples differ not only morphologically but also in their behaviour under reaction conditions. For instance, Zn K-edge EXAFS of CZA-synt (Fig. 6.7) indicates the formation of a new phase, $ZnAl_2O_4$, after catalysis, consistent with previous literature reports [4], [13], whereas this phase is absent in CZA-comm. Moreover, XPS data on the Cu content and oxidation state (Fig. 6.8a) highlighted differences in the reduced carbon species between the two catalysts, as well as during different stages of the reaction.

Overall, the findings presented in this chapter reflect well-known properties and peculiarities of this type of catalyst. However, they represent only a partial picture of the complex modifications these materials can undergo, since variations in activation and reaction conditions (e.g., temperature and pressure) are known to induce different structural and chemical changes [14], [15], [16]. Despite these limitations, the study and testing of these systems have been crucial for advancing the understanding of the state of the art in CO_2-to-methanol conversion catalysis, and for identifying the key structural and functional characteristics of such catalytic systems.

6.2 Cu/Zn-STO

As discussed in previous chapters, the interface between Cu and Zn or ZnO, as well as the presence of Zn-related defects [4], [17], [18], [19], play a crucial role in designing effective catalysts for CO_2 conversion to methanol. Additionally, earlier chapters demonstrated an unconventional method for producing monometallic or bimetallic nanoparticles on oxide supports via a redox exsolution process. The present work aims to combine these two strategies in a single "model" material. To achieve this, Cu- and Zn-co-doped $SrTiO_3$ was synthesized, thoroughly characterized, and evaluated for its performance in CO_2 conversion to methanol.

6.2.1 Synthesis

1.42 g of Ti isopropyoxide were added to 15 g of glycerol and allowed to react under agitation for 60 minutes. Then 7.82 g of citric acid were added to the mixture, and the solution was heated to 60°C for 1 hour. A solution containing 1.04 g $Sr(NO_3)_2$ in 2 g H_2O was added and left to react for 30 minutes. Then, the reducible metals (i. e. Cu and Zn) were added, either both or just one as follows. 1 mL solution of Zn acetate (0.031 g in 1 mL of H_2O) was added, and, after 30 minutes, a solution of 1 mL of Cu acetate (0.021 mg in 1 mL) and left to react for 2 hours. The temperature is then raised to 130°C and left to react for another 2 hours. The product is finally calcined with a ramp heat treatment at 120°C/h up to 400°C and left isothermal for 2 hours, then the temperature is raised again to 900°C and maintained for another 2 hours. In this way three samples were produced: $SrTi_{1-x+y}Zn_xCu_yO_{3-\delta}$, respectively named STCO (x = 0, y = 2) STZO (x = 2, y = 0), STCZO (x = 2, y = 2). The doping level chosen was 2% of the B site for both the metals, and the reason for it lies in the solubility of the metals in the perowskite lattice, Cu solubility can reach up to 5% in moles [20], while for Zn it is around 1% molar [21]. This means that higher metal loadings would most certainly lead to oxide phase segregation.

6.2.2 Characterization

The three doped samples were characterized in order to assess the effect on the properties of the co-doping of the metals. For the characterization of the undoped STO see Chapter 3.

Firstly, PXRD was used to determine the purity of the phase and assess no side phases are present in the samples. Fig. 6.11a shows the three diffractograms

a)

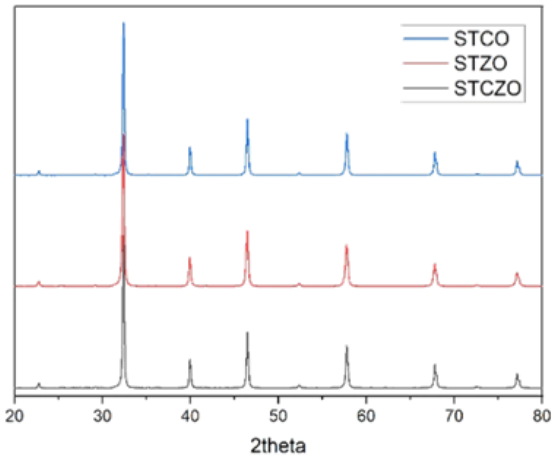

b)

Sample	Cu (mol% Sr)	Zn (mol% Sr)
STCO	2,12	0,01
STZO	0,02	1,94
STCZO	2,07	1,89

Fig. 6.11: a) XRD patterns for STZO, STCO, STCZO; b) ICP results of Cu and Zn for the three samples

All the samples display the same correct phase of a cubic perovskite $Pm\bar{3}m$ with no side phases except a small peak at around $2\theta \approx 28°$ attributable probably to TiO_2. ICP-MS (Fig. 6.11b) was used to assess the doping metal content and confirmed that the nominal metal loadings are correct for all the samples.

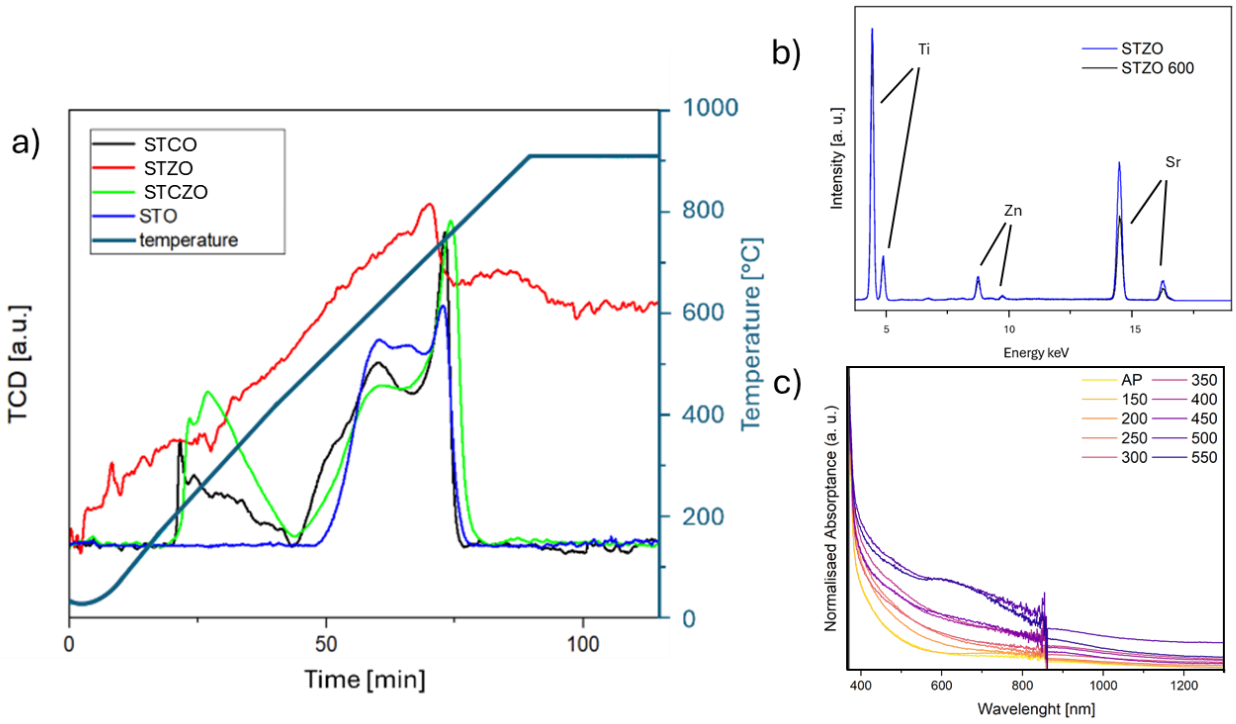

Fig. 6.12: a) TPR curves of all the samples; b) XRF spectra of STZO as prepared and after reduction at 600°C; c) UV-DRS spectra of STCZO after reduction at different temperatures

The reduction behaviour of these materials was the studied via exploiting different techniques, namely TPR, XRF and UV-DRS. TPR (Fig. 6.12a) was employed to monitor the reduction temperatures of the samples. For the Cu-doped sample, two small peaks are observed at relatively low temperatures (214 °C and 301 °C), which are typically attributed to Cu(II) in the form of amorphous CuO located on the

grain boundaries of the particles or on the surface of $SrTiO_3$ (STO) [22]. The reduction of CuO generally occurs in two consecutive steps, namely Cu(II) → Cu(I) followed by Cu(I) → Cu(0), so each observed peak often represents a double-step process [23]. At higher temperatures, around 614 °C, Cu(II) ions substituting Ti(IV) in the STO lattice begin to reduce, primarily from the surface or sub-surface regions. Finally, reduction in the bulk occurs at approximately 750 °C, facilitated by the increased oxygen mobility at elevated temperatures. For the sample only containing Zn, no useful information could be retrieved due to the highly noisy measurement probably due to some issues in the TCD set-up. Nevertheless, a peak at around 760°C is still visible which is commonly attributed to Zn(II) reducing to Zn(0). However, at these temperatures Zn also evaporated and therefore a fair attribution of this signal remains complicated. Interestingly, when both metals are incorporated into the lattice, the TPR profile retains the same overall shape as the Cu-only sample, but the total H_2 consumption increases, and all reduction events are shifted to higher temperatures.

XRF measurements were performed exclusively on STZO to obtain a clearer assessment of the Zn signals, which could overlap with Cu signals in the same region. As shown in Figure 6.12b, the Zn signal remains unchanged after reduction at 600 °C, confirming the thermal stability of the material up to this temperature. Based on this observation, 600 °C was selected as the reduction temperature for catalytic testing.

UV–DRS was employed to monitor changes in the spectroscopic behavior of the samples and to assess the formation of nanoparticles (NPs) via the localized surface plasmon resonance (LSPR) effect (Fig. 6.12c). STCZO was reduced at different temperatures, and spectra were recorded to track the arising of the LSPR band. Upon reduction at 500 °C, a band attributable to LSPR begins to appear. Subsequently, a further reduction was performed at 600 °C, a temperature commonly chosen for the activation of such materials in catalytic applications. UV–DRS (and XRF) was used to confirm the presence of NPs and to verify that the Zn content remained stable under high-temperature conditions. The UV–DRS spectra indicate that the LSPR band remains visible, confirming the persistence of NPs on the oxide surface.

6.2.3 Preliminary catalytic testing

The three samples, together with bare $SrTiO_3$ (named STO) were tested in CO_2 conversion to MeOH via the use of a fixed bed reactor at high pressure (30 bar) and relative low temperature (250°C). Before the reaction all the samples were reduced in 5% H_2 atmosphere in Ar for 5h at 600°C and then tested for 7 hours. The total flow for the reaction was 30 ml/min and the gas ratio was as follows 70,5% H_2, 23.5% CO_2, 6% N_2. Results are presented in Fig. 6.13.

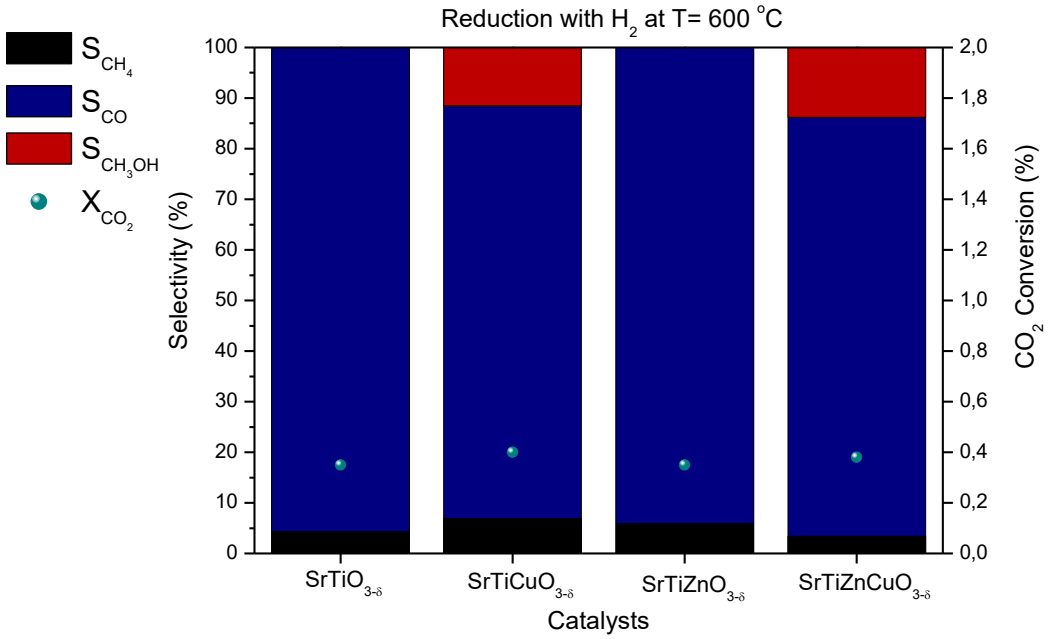

Fig. 6.13: catalytic results in terms of selectivity for MeOH, CO, CH_4 and CO_2 conversion of the four samples activated at 600°C

Though the absolute conversion of the catalysts is pretty low, what is interesting to notice is the change in selectivity. While STO and STZO produce no MeOH, when Cu is introduced (STCO) the selectivity for methanol increases to around 11%, but when both are used (STCZO), the selectivity increases to 14%. This underlines the synergy that is present between Zn and Cu and shows how both metals are needed in order to produce a better catalyst.

After this catalytic test, the thermal reduction was also tested via reducing the catalysts at different temperatures in H_2 to see if there actually is an effect in the overall reactivity.

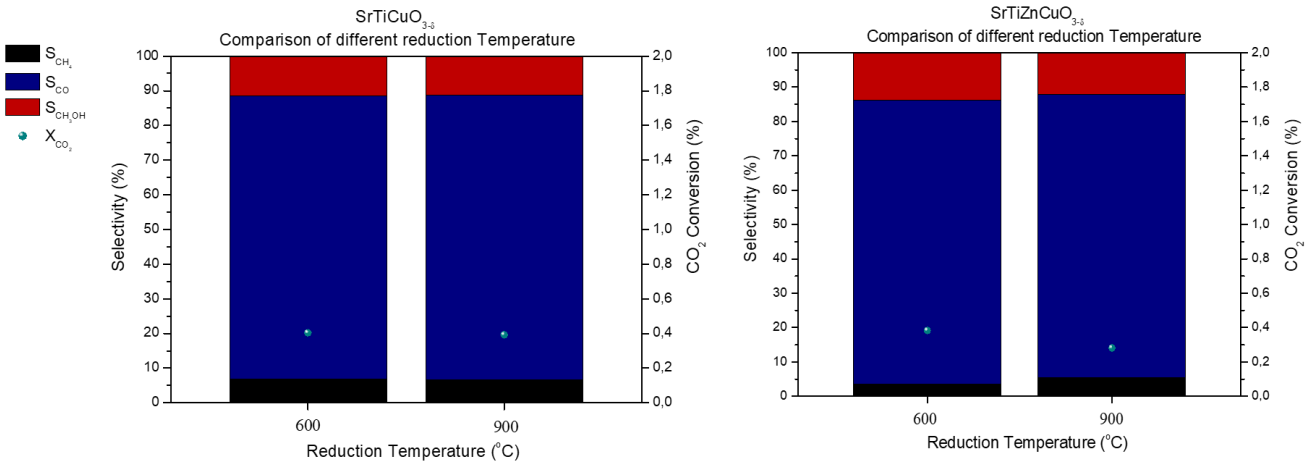

Fig. 6.14: catalytic results in terms of selectivity for MeOH, CO, CH_4 and CO_2 conversion of a) STCO, b) STCZO reduced at two different temperatures

The observations indicate that for STCO, the selectivity (≈11%) and CO_2 conversion remain unaffected by the reduction temperature. In contrast, for STCZO, increasing the reduction temperature results in a decrease in both selectivity and conversion, from 14% to 12.2% and from 0.38% to 0.28%, respectively. This decline in catalytic performance can be attributed to the volatilization of Zn species, as previously reported in the literature, where surface Zn in oxides begins to volatilize at temperatures above 550 °C [24].

6.2.4 Conclusions

In conclusion, the materials were successfully synthesized and characterized, and their catalytic activity follows a trend consistent with both literature reports and current understanding of the methanol production mechanism. Moreover, the Cu/Zn synergy has been confirmed as a key factor for achieving high selectivity toward methanol. However, it is worth mentioning that the low doping level makes this whole material study a somewhat exercise in style. Looking at the conversion of these catalysts it is clear that improvements are needed to increase the activity of the materials. To explore this further, new materials have been synthesized and are currently under investigation. Although the results are not yet mature enough to be included in this thesis, it is worth noting the ongoing work. The strategy is to employ a similar class of materials but with larger lattice parameters, specifically $BaZrO_3$ as the parent perovskite structure. Ba and Zr were chosen because they occupy the same groups as Sr and Ti, but one period lower, resulting in larger ionic radii. Consequently, $BaZrO_3$ retains the perovskite crystal structure of $SrTiO_3$ but with expanded unit cell parameters. This expansion enhances the solubility of larger dopant atoms, such as Cu and Zn, allowing doping levels up to approximately 10 mol%. Increased solubility permits a higher concentration of active metals within the lattice. When subjected to the exsolution process, this leads to a larger number and size of metal nanoparticles on the surface, which is expected to enhance catalytic activity in methanol production.

Bibliography

[1] R. G. Herman, K. Klier, G. W. Simmons, B. P. Finn, J. B. Bulko, and T. P. Kobylinski, “Catalytic synthesis of methanol from COH2: I. Phase composition, electronic properties, and activities of the Cu/ZnO/M2O3 catalysts,” *J Catal*, vol. 56, pp. 407–429, 1979, [Online]. Available: https://api.semanticscholar.org/CorpusID:94367802

[2] D. Sheldon, “Methanol production - A technical history,” Jul. 01, 2017, *Johnson Matthey Public Limited Company*. doi: 10.1595/205651317X695622.

[3] T. Lunkenbein, J. Schumann, M. Behrens, R. Schlögl, and M. G. Willinger, “Formation of a ZnO Overlayer in Industrial Cu/ZnO/Al2O3 Catalysts Induced by Strong Metal–Support Interactions,” *Angewandte Chemie International Edition*, vol. 54, no. 15, pp. 4544–4548, Apr. 2015, doi: https://doi.org/10.1002/anie.201411581.

[4] G. Pacchioni, “From CO2 to Methanol on Cu/ZnO/Al2O3 Industrial Catalyst. What Do We Know about the Active Phase and the Reaction Mechanism?,” Feb. 16, 2024, *American Chemical Society*. doi: 10.1021/acscatal.3c05669.

[5] S. Pin *et al.*, “Role of Interfacial Energy and Crystallographic Orientation on the Mechanism of the ZnO + Al2O3 → ZnAl2O4 Solid-State Reaction: I. Reactivity of Films Deposited onto the Sapphire (110) and (012) Faces,” *The Journal of Physical Chemistry C*, vol. 117, no. 12, pp. 6105–6112, Mar. 2013, doi: 10.1021/jp3124956.

[6] M. C. Biesinger, “Advanced analysis of copper X-ray photoelectron spectra,” *Surface and Interface Analysis*, vol. 49, no. 13, pp. 1325–1334, Dec. 2017, doi: https://doi.org/10.1002/sia.6239.

[7] M. Romand, M. Roubin, and J. P. Deloume, “ESCA studies of some copper and silver selenides,” *J Electron Spectros Relat Phenomena*, vol. 13, no. 3, pp. 229–242, 1978, doi: https://doi.org/10.1016/0368-2048(78)85029-4.

[8] L. Meda and G. F. Cerofolini, “A decomposition procedure for the determination of copper oxidation states in Cu-zeolites by XPS,” *Surface and Interface Analysis*, vol. 36, no. 8, pp. 756–759, Aug. 2004, doi: https://doi.org/10.1002/sia.1757.

[9] D. W. Shoesmith, S. Sunder, M. G. Bailey, G. J. Wallace, and F. W. Stanchell, “Anodic oxidation of copper in alkaline solutions: Part IV. Nature of the passivating film,” *J Electroanal Chem Interfacial Electrochem*, vol. 143, no. 1, pp. 153–165, 1983, doi: https://doi.org/10.1016/S0022-0728(83)80261-7.

[10] J. F. Moulder, W. F. Stickle, P. E. ’ Sobol, K. D. Bomben, and J. Chastain, “Handbook of X-ray Photoelectron Spectroscopy AReference Book of Standard Spectra for Identification and Interpretation of XPS Data.”

[11] C. Unger, M. Petsovits, and P. A. Lieberzeit, “Investigation and Optimization of a Dual Electrode QCM Set-up for Sensing Biospecies in Liquids,” *ECS Meeting Abstracts*, vol. MA2021-01, no. 58, p. 1558, 2021, doi: 10.1149/MA2021-01581558mtgabs.

[12] E. A. Redekop *et al.*, “Zn Redistribution and Volatility in ZnZrOx Catalysts for CO2 Hydrogenation,” *Chemistry of Materials*, vol. 35, no. 24, pp. 10434–10445, Dec. 2023, doi: 10.1021/acs.chemmater.3c01632.

[13] X. Huang *et al.*, “Visualizing Structural and Chemical Transformations of an Industrial Cu/ZnO/Al2O3 Pre-catalyst during Activation and CO2 Reduction,” *ChemCatChem*, vol. 14, no. 24, p. e202201280, Dec. 2022, doi: https://doi.org/10.1002/cctc.202201280.

[14] R. van den Berg *et al.*, “Structure sensitivity of Cu and CuZn catalysts relevant to industrial methanol synthesis,” *Nat Commun*, vol. 7, no. 1, p. 13057, 2016, doi: 10.1038/ncomms13057.

[15] N. J. Divins *et al.*, “Operando high-pressure investigation of size-controlled CuZn catalysts for the methanol synthesis reaction,” *Nat Commun*, vol. 12, no. 1, p. 1435, 2021, doi: 10.1038/s41467-021-21604-7.

[16] A. Beck, M. Zabilskiy, M. A. Newton, O. Safonova, M. G. Willinger, and J. A. van Bokhoven, “Following the structure of copper-zinc-alumina across the pressure gap in carbon dioxide hydrogenation,” *Nat Catal*, vol. 4, no. 6, pp. 488–497, 2021, doi: 10.1038/s41929-021-00625-x.

[17] Malte Behrens et al., “The Active Site of MethanolSynthesis over Cu/ZnO/Al 2 O3Industrial Catalysts,” *Science (1979)*, vol. 336, no. 6083, pp. 893–897, May 2012, doi: 10.1126/science.1219468.

[18] H. Zada, J. Yu, and J. Sun, “Active Sites for CO2 Hydrogenation to Methanol: Mechanistic Insights and Reaction Control,” *ChemSusChem*, vol. 18, no. 4, p. e202401846, Feb. 2025, doi: https://doi.org/10.1002/cssc.202401846.

[19] G. Bonura, M. Cordaro, C. Cannilla, F. Arena, and F. Frusteri, “The changing nature of the active site of Cu-Zn-Zr catalysts for the CO2 hydrogenation reaction to methanol,” *Appl Catal B*, vol. 152–153, pp. 152–161, 2014, doi: https://doi.org/10.1016/j.apcatb.2014.01.035.

[20] P. Gwóźdź, A. Łącz, A. Mizera, and E. Drożdż, “Some aspects of Cu incorporation into SrTiO3 structure,” *J Therm Anal Calorim*, vol. 147, no. 18, pp. 9949–9958, 2022, doi: 10.1007/s10973-022-11306-7.

[21] G. WANG, Y. QIN, J. CHENG, and Y. WANG, “Influence of Zn doping on the photocatalytic property of SrTiO3,” *Journal of Fuel Chemistry and Technology*, vol. 38, no. 4, pp. 502–507, 2010, doi: https://doi.org/10.1016/S1872-5813(10)60042-4.

[22] A. Mizera, A. Kowalczyk, L. Chmielarz, and E. Drożdż, “Catalysts Based on Strontium Titanate Doped with Ni/Co/Cu for Dry Reforming of Methane,” *Materials*, vol. 14, no. 23, 2021, doi: 10.3390/ma14237227.

[23] L. Rizzato, J. Cavazzani, A. Osti, M. Scavini, and A. Glisenti, “Cu-Doped SrTiO3 Nanostructured Catalysts for CO2 Conversion into Solar Fuels Using Localised Surface Plasmon Resonance,” *Catalysts*, vol. 13, no. 10, 2023, doi: 10.3390/catal13101377.

[24] E. A. Redekop *et al.*, “Zn Redistribution and Volatility in ZnZrOx Catalysts for CO2 Hydrogenation,” *Chemistry of Materials*, vol. 35, no. 24, pp. 10434–10445, Dec. 2023, doi: 10.1021/acs.chemmater.3c01632.

Conclusions

The work presented in this PhD thesis addressed some of the open questions surrounding the nature of the active sites and the role of defects in catalysts for CO_2 conversion to methanol. Given the intrinsic complexity, dynamicity, and inhomogeneity of catalytic systems such as $Cu/ZnO/Al_2O_3$ and perovskite-type oxides, the study aimed to establish a clearer link between defect chemistry, metal dispersion, and catalytic functionality. The unifying methodological approach throughout this research was the use of Electron Paramagnetic Resonance (EPR) spectroscopy, supported by complementary structural and spectroscopic techniques, to monitor defects and their evolution under reaction or pseudo-catalytic conditions.

The first part of the work presented in Chapters 3 and 4, focused on $SrTiO_3$ based systems, exploring the exsolution of doping transition metals as a novel route to produce dispersed and strongly anchored nanoparticles onto an oxide lattice. For Cu-doped $SrTiO_3$, EPR, XANES, and UV-DRS revealed that copper species occupy different sites with distinct local environments, exhibiting complex redox dynamics and strong coupling with oxygen vacancies. The results highlighted that the exsolution process is far more heterogeneous than typically assumed, and that standard structural characterization alone fails to capture its chemical complexity. Extending this investigation to Fe–Ni co-doped systems demonstrated how co-doping can modulate defect formation and redox behaviour, thereby influencing catalytic activity in the RWGS reaction. The combined use of EPR and XAS elucidated the cooperative effects between Fe and Ni and provided a methodological framework for tailoring exsolved materials with tuneable composition and catalytic performance.

The second major focus (Chapter 5) involved model catalysts for CO_2 hydrogenation to methanol, based on thiol-protected Au and CuAu NCs supported on ZnO nanoparticles. These systems allowed a more controlled exploration of metal–support interactions and defect-mediated reactivity. The results demonstrated that Cu incorporation in Au nanoclusters significantly alters the electronic structure and enhances the creation of ZnO surface defects, which were identified via a combination of EPR measurements. DRIFTS and catalytic testing revealed that these defects actively participate in CO_2 activation and methanol formation, with CuAu@ZnO exhibiting superior performance due to the synergistic interplay between alloy composition and defect chemistry. This study underscored that catalytic efficiency is dictated not only by the metallic phase but also by the dynamic response of the oxide support, particularly the reversible generation and healing of oxygen vacancies.

Finally, Chapter 6 bridged these findings by investigating Cu/Zn-based systems, comparing commercial and synthesized CZA catalysts and introducing Cu, Zn co-doped $SrTiO_3$ as a hybrid between conventional and exsolved materials. The results reaffirmed the importance of the Cu–Zn synergy for methanol selectivity and pointed toward new directions for enhancing activity through lattice engineering. Preliminary work on $BaZrO_3$-based analogues, characterized by larger lattice parameters and higher dopant solubility, was identified as a promising pathway to increase active metal loading and surface nanoparticle density, ultimately aiming to boost CO_2 conversion rates.

In summary, this thesis demonstrated that defects are not merely spectators but active participants in CO_2 hydrogenation catalysis, influencing metal dispersion, oxidation states, and catalytic selectivity. The combination of EPR spectroscopy with complementary structural and electronic characterization proved essential in uncovering these relationships, offering a more complete understanding of structure–function correlations. The insights gained here contribute to the rational design of next-generation catalysts, where defect engineering and exsolution strategies can be exploited to develop more efficient, stable, and selective systems for sustainable CO_2 valorisation.

Appendix
Characterization Techniques

UV-Vis Spectroscopy (UV-Vis)

UV–Vis spectroscopy is a widely used analytical technique for both qualitative and quantitative analysis, based on the interaction between a solution-phase sample and electromagnetic radiation in the wavelength range of 190–1000 nm. In this region, absorption of light promotes transitions of valence electrons and can be correlated to the concentration of absorbing species in the sample. This relationship follows the Lambert–Beer law, which expresses a linear dependence between absorbance (A) and concentration (c):

$$A = \varepsilon c l \qquad \text{(A.1)}$$

where ε is the molar extinction coefficient characteristic of each compound, l is the optical path length, and c is the concentration of the solution. The law is valid for monochromatic radiation and dilute solutions (typically < 0.01 M) in the absence of strong electrolyte effects, as electrostatic interactions can lead to deviations from linearity. Besides quantitative determinations, UV–Vis spectroscopy also provides qualitative insights into the presence of functional groups that absorb within the 180–1000 nm region. In this work, absorption spectra of clusters dissolved in THF were recorded using a PerkinElmer Lambda 750 UV–Vis spectrometer in range from 1000 to 250 nm.

Transmission Electron Microscopy (TEM)

TEM is a highly effective technique for the morphological characterization of nanostructured materials, offering significantly higher resolution than Scanning Electron Microscopy (SEM). TEM employs a high-energy electron beam, typically accelerated up to 300 kV, combined with electromagnetic lenses to produce high-resolution images. Samples, usually supported on 3 mm copper or nickel grids, are exposed to the electron beam, which interacts with the material to generate transmitted and elastically scattered electrons. These electrons form diffraction patterns that are projected via lenses to produce detailed two-dimensional images of the sample. TEM can resolve fine structural features, making it ideal for powders, nanostructures, and ultrathin sections of composites, with spatial resolution below 1 nm. In this study, TEM images were acquired using a JEOL JEM-2100Plus operating at 200 kV and equipped

with an 8-megapixel Gatan Rio CMOS camera. Samples were prepared by drop-casting dilute nanoparticle dispersions in ethanol onto carbon-coated Cu or Ni TEM grids.

Scanning Electron Microscope (SEM)

Scanning Electron Microscopy (SEM) is a powerful technique for morphological characterization, allowing high-resolution imaging of large specimens at magnifications far beyond those achievable with light microscopy. SEM operates by directing a focused high-energy electron beam onto the sample under vacuum. The interactions between the electrons and the sample generate signals that are detected and processed into images. The electron beam is produced by an electron gun, which can be either thermionic or field emission based. SEM is widely used to investigate surface morphology, defects, topography, and chemical composition, often in combination with Energy Dispersive X-ray (EDX) analysis. In this study, SEM images were acquired using a Vega TS5136 XM Tescan microscope in high-vacuum mode, with an electron beam of 30 kV, a beam current of 25 pA, a working distance of 12 mm, and a beam spot size of 38 nm. Samples were prepared by dispersing the material in ethanol, drop-casting onto an aluminum substrate, and coating with gold to enhance conductivity.

Energy Dispersive X-Rays (EDX)

Both TEM and SEM can be coupled with Energy Dispersive X-ray Spectroscopy (EDX), which enables the identification and quantification of elements in a sample. In EDX, the high-energy electron beam excites the core electrons of atoms, creating vacancies in their electronic configuration. Electrons from higher energy levels then decay to fill these vacancies, emitting X-ray photons in the process. The energy of these emitted photons is characteristic of each element, as it depends on the specific electronic structure and nuclear charge. By detecting and analyzing these X-rays, EDX provides both qualitative and quantitative information about the elemental composition of the material [1].

Thermogravimetric Analysis (TGA)

TGA was performed using a Mettler Toledo TGA/DSC1 STARe system under a constant air flow of 50 mL min^{-1}. Samples were heated from 30°C to 150°C at 10°C min^{-1}, held isothermally at 150°C for 10 minutes, and then heated to 1000°C at the same rate, with a final hold at 1000°C for 5 minutes. Analyses were conducted in a 75 µL alumina pan, filled to at least half its volume. The TGA recorded the percentage weight loss of the samples, reflecting decomposition, oxidation, vaporization, and

desorption processes. This technique was primarily applied to CZA catalysts to evaluate their thermal stability and to determine the effects of high temperatures on sample integrity.

CHNS analysis

CHNS analysis is a rapid technique for determining the concentrations of carbon, hydrogen, nitrogen, and sulphur in solids, liquids, and viscous samples. It finds applications across pharmaceuticals, polymers, environmental science, food, and energy research. The method involves high-temperature combustion, typically around 1000°C, in an oxygen-rich environment, often assisted by catalysts. During combustion, carbon is converted to CO_2, hydrogen to H_2O, nitrogen to N_2 or nitrogen oxides, and sulphur to SO_2. The resulting gases are carried by an inert gas (helium) through a heated copper tube to remove residual oxygen and convert nitrogen oxides to molecular nitrogen, then separated and quantified using absorbent traps and detectors such as infrared or thermal conductivity cells. Quantification is achieved via calibration with high-purity standards like acetanilide and benzoic acid. In this study, CHNS measurements were performed using an Elementar VarioMICRO analyzer in CHNS configuration, with a combustion column at 1150°C and a reduction column at 850°C, normalized to a sulphanilamide standard. This technique was employed to evaluate the carbon content of catalytic materials with a measurement uncertainty of 0.1%.

Powder X-Rays Diffraction (PXRD or XRD)

XRD is an analytical technique used to investigate the crystalline structure of materials. It relies on the diffraction of high-energy photons (X-rays) by the atomic lattice planes of a crystal. An XRD instrument typically consists of an X-ray source, a sample holder, and a detector. X-rays are generated when a heated filament emits electrons via the thermionic effect, which are then accelerated by a potential difference and directed onto a metal target, commonly copper (Cu). Upon striking the target, electrons can either be deflected by atomic nuclei—producing a broad spectrum of Bremsstrahlung radiation—or eject inner-shell electrons, creating vacancies. Electrons from higher energy levels subsequently fill these vacancies, emitting X-ray photons of fixed energy in the process. The most intense and commonly used radiation, known as Kα radiation, arises from the electronic transition between the L (2p or 2s) and K (1s) orbitals. This monochromatic X-ray beam is then directed onto the sample, where diffraction occurs when the incident and reflected angles satisfy Bragg's law:

$$n\lambda = 2d \sin\theta \qquad \text{(A.2)}$$

where n is an integer, λ the wavelength of the X-rays ($\lambda_{K\alpha}$ = 1.542 Å), d the spacing between the crystal planes of the sample and θ the angle of incidence, a diffracted intensity is recorded on the detector.

When the sample is struck by X-ray radiation, which has a wavelength comparable to the distance between the crystal planes, it diffracts the X-rays in all directions, and it is therefore necessary to have a detector that can move to find the points in space where the diffracted intensity is different from zero and maximum. To do this, there are different instrument geometries, typically with either a fixed source and rotating sample holder and detector, or a fixed sample holder and rotating source and detector. The instrument used was a Rigaku MINIFLEX 600 HR with a θ, 2θ configuration for powder analysis.

XRD patterns were collected using a Cu Kα radiation source operated at 40 kV and 15 mA, scanning over the 2θ range of 10–90°, with a step size of 0.02° and a scan rate of 1.0° min^{-1}. Phase identification was carried out using the PDXL-2 software package in comparison with reference diffraction data from the ICDD database. The average crystallite size was estimated from the full width at half maximum (FWHM) of the most intense diffraction peak using the Scherrer equation.

UV Diffuse Reflectance Spectroscopy (UV-DRS)

UV-DRS is a surface analysis technique that employs UV-Visible radiation to gather information about the structural characterization and optoelectronic properties of solid-state samples. It specifically measures the light scattered by the sample when exposed to radiation in the 200 to 800 nm range and represents it as a percentage of reflectance. In general, light scattering (R) is always accompanied by ab- sorption (A) and transmission (T) phenomena, adhering to the following law:

$$A + T + R = 1 \qquad \text{(A.3)}$$

Similar to UV–Vis spectroscopy, Diffuse Reflectance Spectroscopy (DRS) relies on the interaction between electromagnetic radiation and the material, leading to electronic transitions involving both bonding and valence electrons. Spectra were collected in the spectral range from 300 to 1600 nm using a PerkinElmer Lambda 1050+ UV/vis/NIR spectrophotometer equipped with a 10 cm diameter integrating sphere. Powder samples were analysed using a Teflon sample holder and quartz glass. The resulting spectra are typically represented as percent reflectance (R%) versus wavelength or converted using the Kubelka–Munk function, defined as

$$\frac{k}{s} = \frac{(1-R_\infty)^2}{2R_\infty} \qquad \text{(A.4)}$$

Where R_∞ represents the reflectance of an infinitely thick substrate which can be approximated with the R% read by the instrument when the sample is a thick enough solid layer. This approximation allows to

look at a spectrum which resembles the absorbance spectrum. The derivation of the Kubelka-Munk equation from the absorbance is not reported as is of little use for the understanding of the spectra and can be found elsewhere [2].

Diffuse Reflectance InfraRed Fourier Transformed Spectroscopy (DRIFTS)

Just like UV-DRS is not more than a UV-Vis spectrometer that measures in diffusion, the DRIFTS is an FTIR spectroscopy measuring in diffusion. It measures the surface modifications in terms of IR signals (i.e. vibration of chemical bonds). It comes in particularly handy when is used in-situ coupled to gaseous atmosphere and temperature variations. It can give insight into the binding of reactive species to the surface of the catalysts or the modification of superficial species with gas and temperature. In-situ Diffuse Reflectance Infrared Fourier Transform Spectroscopy (DRIFTS) analyses were performed using a Bruker Vertex 70 spectrometer equipped with an MTC detector cooled with liquid nitrogen and operating at a resolution of 4 cm^{-1}. The catalyst samples were placed in a DiffusIR flow cell (PIKE Technologies) fitted with CaF_2 windows and connected to a PIKE Technologies liquid recirculator. Gas flow and composition were precisely regulated using a MULTIGAS CONTROLLER 647C. Infrared spectra were collected at 3-minute intervals, averaging 256 scans per spectrum to ensure optimal signal-to-noise ratio and temporal resolution.

Inductively Coupled Plasma-Mass Spectroscopy (ICP-MS)

ICP-MS is a highly sensitive analytical technique used to determine the presence and concentration of elements, particularly metals, in a sample, with detection limits down to the parts-per-billion (ppb) level. Samples are introduced as an aerosol into an argon plasma, where they are dried, dissociated, and ionized, generating predominantly singly charged ions. These ions are then directed into a mass spectrometer, commonly a quadrupole system, which scans the mass-to-charge ratios sequentially. Upon exiting the mass spectrometer, ions strike an electron multiplier, producing cascades of electrons that are amplified into measurable pulses. Element concentrations are determined by comparing these signal intensities with calibration curves obtained from high-purity standards. [3]. Approximately 0.2 g of each powdered sample was finely ground and transferred into a Teflon beaker, where it was dissolved in an acid mixture consisting of 4 mL HNO_3, 3 mL HCl, and 1 mL HF. The resulting suspension was subjected to microwave mineralization. After digestion, the solutions were diluted with 12 mL of Milli-Q water and centrifuged. A 15 mL aliquot of the clarified solution was then diluted 1:100 with Milli-Q water and introduced into the ICP for analysis. During measurement, a steady argon flow of 20 L min^{-1} was used in the quartz plasma torch to transport the aerosolized sample.

X-Rays Fluorescence (XRF)

XRF, similar to EDX, is a non-destructive technique used to determine the elemental composition of materials by exploiting the natural fluorescence of elements under X-ray irradiation. High-energy X-rays excite the atoms in the sample, causing the emission of secondary (fluorescent) X-rays at characteristic energies unique to each element. This allows for both qualitative and quantitative analysis of solids, powders, and liquids, providing bulk compositional information. In this study, XRF measurements were performed using a Bruker ARTAX 200 micro-XRF spectrometer equipped with a Mo anode X-ray tube and a 0.65 mm collimated beam, corresponding to an excited sample area of 0.33 mm^2.

EPR

See chapter 2.

X-Rays Photoelectron Spectroscopy (XPS)

XPS analysis is a surface analysis used to determine the elemental composition, chemical state and electronic structure of materials. By measuring the kinetic energy of electrons emitted from the sample upon X-ray irradiation, XPS allows the identification of the elements and their oxidation states. The analyses were performed using a home-built apparatus consisting of an analysis chamber and a hemispherical analyser (VSW-HA100) equipped with a 16-channel detector. The source was the non-monochromatic MgKα (1253.6 eV) (VSW-TA10). Surveys spectra have been recorded using a pass energy of 44 eV and a resolution of 0.4 eV, while for the regions of interest (ROI) the pass energy was 22 eV and 0.05 eV the resolution, in both cases the source total power is 144W (12kV, 12mA). The base pressure of the chamber before the analysis was 1×10-9 mbar. Samples have been prepared by pressing powders onto carbon adhesive tape mounted on Kapton tape. This strategy was adopted to isolate the sample from the ground, avoiding differential charging issue. Data have been processed using CASA XPS software v2.36, spectra are calibrated using the component assigned to the adventitious carbon and conventionally fixed at 285.0 eV [4].

Matrix Assisted Laser Desorption and Ionization (MALDI-MS)

MALDI-MS is a useful technique to study the fragmentation of organic molecules caused by laser radiation. It has been used to monitor the NCs fragmentation in order to gain insight into their atomic

composition and ligand structure. An RTOF mass spectrometer from Shimadzu was used to conduct the MALDI-MS measurements and 2,4,6-Trihydroxyacetophenone was used as the MALDI-MS matrix. To produce mass spectra of sufficient resolution [3000-5000, FWHM], MALDI-RTOF-MS were used near the boundary laser intensity. Every mass spectrum consisted of an average of 300–600 single and not selected laser pulses (lambda = 337 nm at 50 Hz).

Temperature-programmed Reduction (TPR)

Temperature-Programmed Reduction (TPR) measurements were performed to evaluate the reducibility of catalytic systems as a function of temperature using a BELCAT II catalytic analyser (Microtrac Retsch GmbH). For each experiment, at least 40 mg of sample was used. Prior to measurement, the thermal conductivity detector (TCD) was stabilized at room temperature for a minimum of 90 minutes. TPR analyses were conducted with a 5% H_2/N_2 gas mixture at a flow rate of 20 sccm, applying a heating ramp of 10 K/min up to 900°C, followed by an isothermal hold for 30 minutes. The TCD signal was baseline-corrected, and the resulting curves were normalized for visualization. Hydrogen consumption was quantified using ChemMaster II software (Microtrac Retsch GmbH).

X-ray Absorption Spectroscopy (XAS)

X-ray Absorption Spectroscopy (XAS) is a versatile and element-specific analytical technique used to probe the oxidation state, electronic configuration, and local atomic environment of selected elements within a material [5]. By precisely tuning the energy of the incident X-rays, it is possible to excite core-level electrons and monitor their interactions with the surrounding atomic structure. The method is inherently bulk-sensitive due to the deep penetration of high-energy X-rays (2–35 keV), enabling studies of solids, liquids, and amorphous systems under realistic or even in situ conditions. Governed by the Beer–Lambert law, XAS measures the attenuation of X-ray intensity as a function of photon energy, providing an energy-dependent absorption coefficient, μ(E). The behaviour of μ depends on the atomic number (Z), density, and energy, and exhibits abrupt increases at element-specific absorption edges corresponding to the excitation of core electrons [6]. These edges mark transitions such as 1s → unoccupied orbitals and serve as fingerprints for element identification. The spectrum is divided into two main regions: the X-ray Absorption Near Edge Structure (XANES), extending roughly 30–40 eV above the edge, and the Extended X-ray Absorption Fine Structure (EXAFS), which spans up to 1000 eV above the edge. XANES is sensitive to oxidation state, coordination geometry, and electronic structure, while EXAFS provides quantitative information about interatomic distances, coordination numbers, and types

of neighbouring atoms. The combination of these regions allows a simultaneous understanding of both electronic and structural aspects of a material.

In transition metals, the main absorption feature (the white line) originates from 1s → 4p transitions, while weaker pre-edge peaks arise from dipole-forbidden or quadrupole-allowed transitions (e.g., 1s → 3d), often enabled by p–d orbital hybridization. The position of the white line shifts to higher energy with increasing oxidation state, providing a reliable indicator of valence changes. Because of its sensitivity, element selectivity, and compatibility with time-resolved measurements, XAS has become an essential technique for studying catalytic processes, redox transformations, and structure–function relationships in complex and dynamic materials. XAS measurements were collected at the Italian CRG beamline of ESRF, BM08 LISA [7]. Spectra were recorded using a Si-111 double crystal monochromator and a pair of silicon mirrors for high-order harmonic rejection (E cutoff ≈15 keV) and beam collimation on the sample. The samples were analyzed in fluorescence mode using a 4-element Peltier-cooled SDD detector, while the beam flux was measured with a 1 bar N 2 -filled ionization chamber. At the same time as the samples, metal foils, placed downstream the beamline, were also measured as energy reference in transmission mode, using a pair of ionization chambers. The data analysis was performed using the Demeter package and Larch.

Bilbliography

[1] P. J. Goodhew, J. Humphreys, and R. Beanland, *Electron Microscopy and Analysis Third edition*. 2001.

[2] P. Kubelka and F. Munk, “An Article on Optics of Paint Layers,” 1931.

[3] PerkinElmer, “The 30-Minute Guide to ICP-MS,” 2011.

[4] J. F. Moulder, W. F. Stickle, P. E. ’ Sobol, K. D. Bomben, and J. Chastain, “Handbook of X-ray Photoelectron Spectroscopy AReference Book of Standard Spectra for Identification and Interpretation of XPS Data.”

[5] M. Wang, L. Árnadóttir, Z. J. Xu, and Z. Feng, “In Situ X-ray Absorption Spectroscopy Studies of Nanoscale Electrocatalysts,” *Nanomicro Lett*, vol. 11, no. 1, p. 47, 2019, doi: 10.1007/s40820-019-0277-x.

[6] M. Newville, “Fundamentals of XAFS,” *Rev Mineral Geochem*, vol. 78, no. 1, pp. 33–74, Jan. 2014, doi: 10.2138/rmg.2014.78.2.

[7] F. d’Acapito *et al.*, “The LISA beamline at ESRF,” *J Synchrotron Radiat*, vol. 26, no. 2, pp. 551–558, Mar. 2019, doi: 10.1107/S160057751801843X.